

**EVOLUTIONARY OPTIMIZATION FOR CONTINUOUS,  
BINARY, MIXED-VARIABLE AND CONSTRAINED  
ELECTROMAGNETIC PROBLEMS**

by

Maria Kovaleva



Dissertation submitted in fulfilment of the requirements

for the degree of

**DOCTOR OF PHILOSOPHY**

School of Engineering  
Faculty of Science and Engineering  
Macquarie University  
Sydney, Australia

16<sup>th</sup> of February 2018



Copyright © 2018 Maria Kovaleva

All Rights Reserved





MACQUARIE UNIVERSITY

GRADUATE COMMITTEE APPROVAL

of a Dissertation submitted by

Maria Kovaleva

This dissertation has been read by each member of the following graduate committee and by majority vote has been found to be satisfactory.

---

Date

---

Prof. Karu P. Esselle, Chair  
Macquarie University, Australia

---

Date

---

Prof. Christophe Fumeaux, Reviewer  
The University of Adelaide, Australia

---

Date

---

Dr. Cristina Ponti, Reviewer  
Roma Tre University, Italy

---

Date

---

Dr. Guido Lombardi, Reviewer  
Polytechnic University of Turin, Italy



## MACQUARIE UNIVERSITY

As a chair of the candidate's graduate committee, I have read the dissertation of Maria Kovaleva in its final form and have found that (1) its format, citations, and bibliographical style are consistent and acceptable and fulfill university and department style requirements; (2) its illustrative materials including figures, tables, and charts are in place; and (3) the final manuscript is satisfactory to the graduate committee and is ready for submission to the University Library.

---

Date

---

Prof. Karu P. Esselle  
Chair, Graduate Committee

Accepted for the Department

---

Prof. Darren Bagnall, Dean  
School of Engineering

Accepted for the Division

---

Tracy Rushmer, Associate Professor  
Faculty of Science and Engineering



## ABSTRACT

Evolutionary optimization algorithms are a type of computational intelligence. Their application to electromagnetic (EM) engineering problems open exciting possibilities of improving the performance of existing solutions, finding novel complex configurations and, ultimately, having the potential to fully automate the design of antennas, filters and other electronic devices. This thesis focuses on extending the functionality that is provided by evolutionary algorithms to the field of electromagnetics. A detailed study is undertaken to identify the needs of real-world EM engineering problems and propose methodologies that enhance the available capabilities.

The EM problems optimized in this thesis include compact high-gain wide-band resonant cavity antennas (RCAs), wideband aperture-coupled microstrip patch antennas (ACMPAs), pixelated EM surfaces and microstrip filters. In order to obtain accurate performance prediction of the designed devices, all considered designs are simulated using a full-wave EM solver. The optimization process is automated by interfacing simulation software with evolutionary algorithms.

Particle swarm optimization (PSO), the cross-entropy (CE) method and covariance matrix adaptation evolutionary strategy (CMA-ES) are the evolutionary algorithms used in this thesis. By means of PSO, improved designs of a new class of compact RCAs are obtained that outperform the designs reported in the literature. Four antennas of only  $1.7\text{--}2.2\lambda_0$  in diameter have a directivity 17.6–19.6 dBi and a 3-dB radiation bandwidth of 24%, 50%, 55% and 70%. An ACMPA with 53% bandwidth is proposed as a new planar feed solution for RCAs. The designed RCA with an ACMPA feed has a peak directivity of 19 dBi and a 3-dB radiation bandwidth of 40%.



The most important outcome of this thesis are the proposed methodologies for the optimization of continuous, mixed-variable, binary and constrained EM problems. It is shown that various design requirements can be incorporated in optimization using the CE method, which is not possible with PSO or CMA-ES. In contrast to the previous CE applications, which only utilise the normal distribution, this thesis makes use of probability distribution functions that model the design space, such as the beta, Dirichlet, Bernoulli and discrete probability distribution families. Thus, the flexibility and broader potential of the CE method is exploited and demonstrated.

By encoding the metallic patterns printed on thin pixelated EM surfaces into binary strings, single- and dual-frequency artificial magnetic conductors and phase-shifting metasurfaces are designed. The methodology of handling equality and inequality constraints is demonstrated on the design of a 5-pole microstrip low-pass filter, which has a selectivity of 60 dB and an 8.5 GHz rejection bandwidth.

All the designs in this thesis are obtained by an automated optimization process. In comparison with the initial designs or existing alternative solutions, the optimized designs exhibit improved desired characteristics.





## STATEMENT OF ORIGINALITY

I certify that the work in this thesis has not previously been submitted for a degree nor has it been submitted as part of the requirements for a degree to any other university or institution.

I also certify that the thesis is an original piece of research and it has been written by me.

To the best of my knowledge and belief, the thesis contains no material previously published or written by another person except where due reference is made in the thesis itself.

.....

Maria Kovaleva



## ACKNOWLEDGMENTS

I would like to express sincere gratitude and appreciation to my project advisers for the support that they provided during my Ph.D. candidature. I am blessed to have Dr. David Bulger as a collaborator, a teacher and a friend. I am extremely grateful to Prof. Karu P. Esselle for giving me the most liberating encouragement that a Principal Supervisor can ever give, which is “do what you love”. Thank you for trusting my abilities in the first place and giving unconditional support to all my endeavours! I am deeply indebted to Dr. Basit Ali Zeb for maintaining an expectation of a high academic standard and for spending enormous amount of time mentoring me. Thanks to the supportive environment that they have created, I was able to extend my professional interests beyond academia. Together, we had organised a session “Aerial Combat: Survival of the Fittest” as a part of the Macquarie Minds Showcase conference and went through the CSIRO ON Prime pre-accelerator program.

I gratefully acknowledge the financial support from the Australian government and Macquarie University that went well beyond sponsoring my research. I was lucky to have received the encouragement to commercialise my research and to develop my entrepreneurial skills. Also, I attended several prestigious national and international conferences. It was an outstanding experience to visit the Computational Electromagnetics and Antennas Research Laboratory directed by Dr. Douglas Werner at Pennsylvania State University and to attend the 2016 IEEE Symposium on Antennas and Propagation in Fajardo, Puerto Rico, and the 16th International Symposium on Antenna Technology and Applied Electromagnetics in Montreal, Canada. These experiences have broadened my horizons.

Thanks to my colleagues at the School of Engineering for their generous support and respect. I am thankful to each and every member of the Centre for Collaboration in Electromagnetic and Antenna Engineering for making my postgraduate life a memorable one. Special thanks go to Dr. Raheel Hashmi and Dr. Syed Abbas for guiding me in the initial stages of my candidature, Dr. Muhammad Usman Afzal and Rajas Prakash Khokle for sharing their technical and life knowledge with me and Roy Simorangkir for the occasional fruitful discussions and being in sync with me for the most nerve-racking milestones.

Thanks to the CST Support Team, and especially Dr. Frank Demming-Janssen, for the timely responses and the Faculty of Science and Engineering IT Support member Richard Miller for addressing the needs of this project. Thanks to Dr. Keith Imrie for editing this thesis.

I am enormously honoured to thank Dr. Trevor Bird for inspiring and keeping my spirits up during difficult times.

This thesis would not have been possible without my supportive partner. Last but not least I would like to express the very deep gratitude to my family and friends for being always there for me while being so far away.

*Maria Kovaleva*

*February 2018*

*Macquarie University*

*Sydney, New South Wales*

*To my mother, whose name means “love”, and also to love itself...*



# Contents

<b>Table of Contents</b>	<b>xix</b>
<b>List of Figures</b>	<b>xxv</b>
<b>List of Tables</b>	<b>xxxv</b>
<b>List of Acronyms</b>	<b>xxxvii</b>
<b>1 Introduction</b>	<b>1</b>
1.1 Evolutionary Optimization in Antenna Design . . . . .	1
1.2 Research Motivation . . . . .	3
1.3 Current State of the Art . . . . .	5
1.4 Research Framework and Objectives . . . . .	8
1.5 Overview of Contents . . . . .	10
1.6 Thesis Contributions . . . . .	11
<b>2 Evolutionary Optimization Algorithms in Electromagnetics</b>	<b>15</b>
2.1 Introduction . . . . .	15
2.2 Particle Swarm Optimization (PSO): Theory and Applications . . . . .	17
2.2.1 PSO Algorithm . . . . .	18
2.2.2 Applications of PSO to EM problems . . . . .	20
2.3 Cross-Entropy (CE) Method: Theory and Applications . . . . .	25
2.3.1 CE Algorithm . . . . .	26
2.3.2 Applications the CE method to EM problems . . . . .	33

2.4	Covariance Matrix Adaptation Evolutionary Strategy (CMA-ES): Theory and Applications . . . . .	35
2.4.1	CMA-ES Algorithm . . . . .	35
2.4.2	Applications of CMA-ES to EM problems . . . . .	39
2.5	Comparisons of the Algorithms . . . . .	42
2.5.1	Benchmarks for Optimization . . . . .	42
2.5.2	Antenna Engineering Designs . . . . .	45
2.6	Limitations and Challenges of Evolutionary Optimization . . . . .	46
2.6.1	Objective Function . . . . .	46
2.6.2	Design Constraints . . . . .	47
2.6.3	Computational Time . . . . .	48
2.6.4	Algorithm Selection . . . . .	48
2.7	Summary . . . . .	49
<b>3</b>	<b>Application of PSO to the Design of High-Gain Compact RCAs</b>	<b>51</b>
3.1	Introduction to RCAs . . . . .	51
3.2	Methods of Analysis . . . . .	53
3.2.1	Ray-Tracing Model . . . . .	54
3.2.2	EBG Defect Model . . . . .	56
3.2.3	Transmission-Line Model . . . . .	58
3.2.4	Leaky-Wave Model . . . . .	59
3.3	PSO Implementation Details . . . . .	59
3.4	Wideband RCAs with Dielectric Superstrates of Concentric Sections . . .	62
3.4.1	Uniform-Superstrate Compact RCA . . . . .	62
3.4.2	Design I: Ten-Sectional Superstrate . . . . .	64
3.4.3	Design II: Four-Sectional Superstrate . . . . .	67
3.4.4	Design III: Three-Sectional Superstrate . . . . .	74
3.5	Extremely Wideband RCA With a Slot Feed . . . . .	79
3.5.1	Design Parameters and Objective . . . . .	79
3.5.2	Results and Discussion . . . . .	80



---

3.6	Summary . . . . .	84
<b>4</b>	<b>CE for Optimization With Constraints and Mixed Variables</b>	<b>87</b>
4.1	Introduction . . . . .	88
4.2	Optimization Approach using the CE Method . . . . .	89
4.2.1	Convergence Properties of the CE Method . . . . .	90
4.2.2	Basic Principle of the CE Method . . . . .	90
4.3	RCAs Optimized by the CE Method . . . . .	94
4.3.1	Algorithm Implementation . . . . .	94
4.3.2	Fitness Function Definition . . . . .	97
4.3.3	Stopping Criterion . . . . .	99
4.3.4	Optimization Case-I: RCA with Three-Sectional TPG . . . . .	100
4.3.5	Optimization Case-II: RCA with Six-Sectional TPG . . . . .	103
4.4	Experimental Results . . . . .	107
4.5	Summary . . . . .	112
<b>5</b>	<b>CE, PSO and CMA-ES in the Design of Wideband Antennas</b>	<b>113</b>
5.1	Introduction . . . . .	113
5.2	Optimization of an ACMPA . . . . .	115
5.2.1	Problem Formulation . . . . .	115
5.2.2	Optimization Methodology . . . . .	120
5.2.3	Optimization Results . . . . .	123
5.3	Optimization of RCA with ACMPA Feed . . . . .	126
5.3.1	Design of an RCA with an ACMPA Feed . . . . .	127
5.3.2	Optimization Details . . . . .	128
5.3.3	Results . . . . .	129
5.4	Discussion . . . . .	133
5.5	Summary . . . . .	136

<b>6</b>	<b>Optimization of Thin Pixelated EM Surfaces</b>	<b>137</b>
6.1	Introduction . . . . .	137
6.2	The Theory of Thin EM Surfaces . . . . .	139
6.3	Method of Analysis . . . . .	140
6.3.1	Periodic Analysis . . . . .	140
6.3.2	Symmetry Planes . . . . .	142
6.3.3	Vertices-Removal Technique . . . . .	143
6.4	Optimization Approach . . . . .	145
6.4.1	Sampling Binary Variables . . . . .	145
6.4.2	CE Algorithm for Optimization of Binary Problems . . . . .	146
6.5	Optimization Results . . . . .	149
6.5.1	Single-Frequency AMC Surface . . . . .	149
6.5.2	Dual-Frequency AMC Surface . . . . .	156
6.5.3	Thin Phase-Correcting Metasurfaces . . . . .	160
6.6	Summary . . . . .	163
<b>7</b>	<b>Optimization of Microstrip Low-Pass Filters</b>	<b>165</b>
7.1	Introduction . . . . .	165
7.2	The CE Method for LPF Optimization . . . . .	167
7.2.1	Non-Uniform Microstrip Transverse Resonance LPF . . . . .	168
7.2.2	Optimization Approach . . . . .	169
7.3	Optimization Results . . . . .	172
7.4	Summary . . . . .	175
<b>8</b>	<b>Conclusions</b>	<b>177</b>
8.1	Summary . . . . .	177
8.2	Avenues for Future Work . . . . .	179

---

<b>A</b>	<b>Interfacing MATLAB and CST MWS</b>	<b>181</b>
<b>B</b>	<b>Sample Code for the Implementation of the CE method</b>	<b>185</b>
<b>C</b>	<b>VBA Program for the Optimization of Pixelated Unit-Cells</b>	<b>189</b>
<b>D</b>	<b>List of Publications</b>	<b>193</b>
	<b>Bibliography</b>	<b>195</b>



# List of Figures

1.1	Genetically evolved crooked wire antennas for the 2006 NASA ST5 spacecraft [15]. . . . .	2
1.2	Academic publications related to the application of evolutionary optimization algorithms to antenna engineering according to the Scopus database. . . . .	3
1.3	The most common evolutionary optimization algorithms in EM applications from 1960 to 2017 according to Scopus. *The category <i>Others</i> include CE, CMA-ES and BBO. . . . .	6
1.4	Evolutionary optimization algorithms applied to EM engineering problems. . . . .	7
2.1	A few examples of group intelligence behaviour. . . . .	16
2.2	Schematic representation of the motion of a particle pulled by the global best, personal best and its inertia in a two-dimensional space with parameters $t$ and $\varepsilon$ . . . . .	18
2.3	PSO algorithm flowchart. . . . .	19
2.4	A dual-band handset patch antenna design problem with a mixed-parameters vector. (a) Antenna geometry. (b) Convergence curve with antenna prototype in the inset (from [46]). . . . .	21
2.5	A parasitically coupled microstrip antenna array for the IEEE 802.11a WLAN 5–6 GHz frequency band. (a) The prototype of the optimized antenna. (b) Reflection coefficient of the original and optimized antenna (from [18]). . . . .	22

2.6	Ka-band single-feed reflectarray system was optimized for a number of quad-beam requirements using PSO. (a) Fabricated reflectarray prototype. (b) Convergence curves for four radiation pattern mask requirements (from [77]). . . . .	23
2.7	L-shaped folded monopole antenna array optimized under five inequality constraints. (a) Antenna deployment on a substrate and the geometry under optimization with eleven continuous variables. (b) Convergence of the elite particle $X$ minimizing the goal function equal to the sum of $G_1(X)$ , $G_2(X)$ and $G_3(X)$ (from [78]). . . . .	24
2.8	Normal probability density functions of a random variable $x$ , $N_1(4, 0.5)$ , $N_2(4, 0.5)$ , $N_3(4, 0.5)$ . . . . .	27
2.9	CE method flowchart. . . . .	28
2.10	2D Eggholder test function, best location is at $\mathbf{x}^* = (512, 404.2319)$ . . . .	30
2.11	(continues on next page) CE optimization process demonstrated on the 2D Eggholder function. The global best solution is located at $x_1 = 512$ , $x_2 = 404.2319$ (red pentagram). . . . .	31
2.11	(cont.) CE optimization process demonstrated on the 2D Eggholder function. Five iterations were required for the algorithm to converge to the global best solution located at $x_1 = 512$ , $x_2 = 404.2319$ (red pentagram). . . . .	32
2.12	The optimized planar sparse antenna array, a single element and the prototype of simplified antenna array [89]. . . . .	34
2.13	Bivariate normal distribution (contours) and a sample of 100 points from this distribution (blue dots). Mean and variance for each marginal normal distribution are given in a textbox. . . . .	36
2.14	Flowchart of CMA-ES [96]. . . . .	36
2.15	Illustration of CMA-ES (a) selection process with the generation of a new mean and (b) movement and reshaping of the search distribution over several iterations on a 2D Rotated Hyperellipse test function [97]. . . . .	38

2.16	Parameterized geometry of a folded shorted patch antenna with a meandered slot: side view ( <i>left</i> ) and top view ( <i>right</i> ) [97]. . . . .	39
2.17	Simulated and measured reflection coefficient of the optimized antenna design. Vertical dashed lines indicate the targeted frequencies [97]. . . . .	40
2.18	Mixed-parameter optimization problem of multilayer dielectric filter design [48]. . . . .	41
2.19	Optimization test functions used in a comparative benchmark study: (a) Sum of squares, (b) Ackley. . . . .	42
2.20	Convergence comparison between PSO and CE method on 5D Ackley test function. . . . .	44
2.21	Box-and-whisker plots of MNFEs for 60 optimization runs by CMA-ES and CE on a $d$ -dimensional Ackley function: (a) $d = 10$ , (b) $d = 20$ . The blue boxes are drawn around the 25th and 75th percentiles and divided (by the red thick line) at the 50th percentile. The whiskers (black dashed line) extend out to the 10th and 90th percentiles. The outliers are plotted individually using the ‘+’ symbol. . . . .	45
3.1	Elementary geometry of an RCA along with its advantages and limitations in comparison to other antenna types. . . . .	52
3.2	A simple ray-tracing model of an RCA. . . . .	55
3.3	The concept of the EBG defect model for the analysis of periodic RCAs. . . . .	57
3.4	A profile of a fully dielectric superstrate and its equivalent circuit [129]. . . . .	58
3.5	Pseudocode for particle swarm optimization. . . . .	60
3.6	Simplified RCA model with HED cavity excitation. . . . .	62
3.7	Boresight directivity of an RCA with a single-slab superstrate, dielectric constant of the the slab $\varepsilon_{ri} = \{2; 3.8; 5.6; 7.4; 9.2; 11; 12; 20; 40\}$ , $i = 1, 2, \dots, 9$ . . . . .	63
3.8	Cross-sectional view of the optimized RCA with $D = 48 \text{ mm} = 2.2\lambda_0$ , $H_{cav} = 11 \text{ mm}$ , $\lambda_0 = 22 \text{ mm}$ . . . . .	64
3.9	Boresight directivity and side lobe levels of the optimized RCA. . . . .	65
3.10	Permittivity profile of the optimized RCA with ten-sectional superstrate. . . . .	66

3.11 Boresight directivity comparison of the optimized RCA and a non-optimized RCA with a uniform superstrate. . . . .	67
3.12 (a) A slot with dimensions $(W_s, L_s)$ . (b) Cross-sectional view of the RCA with $D = 48 \text{ mm} = 1.85\lambda_0$ , $t = 6.35 \text{ mm}$ , $H_{cav} = 13 \text{ mm}$ , $\lambda_0 = 26 \text{ mm}$ . . .	68
3.13 Evolution of the swarm of 15 particles over 20 iterations for one of the optimization trials. . . . .	69
3.14 Input impedance matching of the four-sectional RCA (Design II). . . . .	70
3.15 Illustration of two full optimization runs emphasizing $\hat{f}(x_{pop}^{g=0})$ (green), $\hat{f}(x_{pop}^{g=10})$ (cyan) and $\hat{f}(x_{pop}^{g=20})$ (red). . . . .	71
3.16 Enlarged view of the trade-off between the peak directivity and 3-dB bandwidth provided by an RCA with a four-sectional all-dielectric superstrate. . . . .	71
3.17 E-field phase distribution probed 3 mm above the optimized supersrate of the four-sectional RCA (Design II). . . . .	72
3.18 Cross-sectional view of the RCA structure with three-sectional TPG superstrate: $(\varepsilon_1, \varepsilon_2, \varepsilon_3) = (7.26, 5.2, 3.16)$ , $t = 10 \text{ mm}$ . $H_{cav} = \lambda_0/2$ , $D = 2\lambda_0$ , $\lambda_0 = 24 \text{ mm}$ . . . . .	75
3.19 Convergence curve for the completed optimization run. Objective function is given in Eq. (3.9). . . . .	75
3.20 Boresight gain of the optimized RCA in comparison with a slot antenna in the ground plane, $D = 48 \text{ mm}$ . Inset provides the parameters of the optimal RCA design. . . . .	76
3.21 Normalized radiation patterns of the optimized high-gain wideband RCA in the E- and H-planes at five frequencies within the bandwidth. . . . .	77
3.22 Input impedance matching of the four-sectional RCA (Design III). . . . .	77
3.23 E-field phase distribution above the optimized supersrate of the three-sectional RCA (Design III). . . . .	78
3.24 Cross-sectional view of the RCA with a superstructure from concentric dielectric sections of width $w = 0.086\lambda_0$ , $D = 1.7\lambda_0$ , $t = 0.3\lambda_0$ , $H_{cav} = 0.5\lambda_0$ , $\lambda_0 = 28 \text{ mm}$ . . . . .	79



3.25	Boresight directivity and gain of the optimized RCA. . . . .	81
3.26	Input impedance matching of the optimized RCA. . . . .	81
3.27	E-field phase distribution probed 3 mm above the optimized supersrate of the extremely wideband RCA. . . . .	82
3.28	Normalised radiation patterns of the optimized RCA at six frequencies within the operating frequency range. . . . .	83
3.29	Summary of the RCA design parameters and their performance character- istics presented in this chapter. . . . .	85
4.1	Flow chart of a common general approach to optimization of constrained antenna design problems [154]. . . . .	88
4.2	Beta distribution PDF of a random variable bounded between $[-10, 10]$ for various shape parameters $(\alpha, \beta)$ . . . . .	91
4.3	Illustration of selection and evaluation procedure in the CE method. The figure shows the first four iterations in the optimization of the univariate Ackley test function, with PDF shown on the left and fitness function on the right. . . . .	92
4.4	(a) Side view and (b) top view of an RCA with a TPG superstrate. The superstrate is made out of five dielectric segments. . . . .	95
4.5	Three possible combinations of widths. . . . .	96
4.6	Convergence results of the CE method for Case-I optimization of three compact RCAs with TPG superstrates, where $t$ is the superstrate thickness and $D$ is its diameter. For each optimization run, “best” is the best result observed so far, and “average” is the mean of all results observed at each iteration. . . . .	101
4.7	Evolution of design variables for Case-I optimization with superstrate thick- ness $t_2 = 6.99$ mm shows the gradual convergence of the population. . . .	102

4.8	Convergence results of the CE method for Case-II optimization of three compact RCAs with TPG superstrates, where $t$ is the superstrate thickness and $D$ is its diameter. For each optimization run, “best” is the best result observed so far, and “average” is the mean of all results observed at each iteration. . . . .	105
4.9	Case-II total section widths over iterations. . . . .	105
4.10	Evolution of design variables for Case-II optimization with $D_3$ over the progress of optimization shows the gradual convergence of the population. . . . .	106
4.11	Fabricated prototype of the optimized RCA from Case-I study with superstrate thickness $t_1=6.35$ mm. Two nylon spacers support the superstrate above the ground plane. . . . .	107
4.12	Measured reflection coefficient of the RCA prototype from Case-I study with superstrate thickness $t_1=6.35$ mm. Impedance matching of the slot is shown for comparison. . . . .	108
4.13	Measured boresight directivity of the prototype of the optimized RCA with the fitness function $f(x)=624.6$ . Measured peak directivity is 17.6 dBi, and measured 3-dB directivity bandwidth is 51%. . . . .	109
4.14	Predicted and measured radiation patterns of the prototyped antenna at 13 GHz, 15 GHz and 17 GHz. . . . .	110
4.15	E-field phase distribution probed 3 mm above the optimized RCA from Case-I study with $t_1 = 6.35$ mm. . . . .	111
5.1	Geometry of the optimized ACMPA. Inset table shows the lower and upper limits of the design variables. . . . .	116
5.2	Theoretical dimensions of a microstrip patch. . . . .	117
5.3	Sensitivity analysis of the design variables. Grey dashed lines show the desired $S_{11}$ response. . . . .	119
5.4	Reflection coefficients of the ACMPAs optimized by PSO, CE and CMA-ES. . . . .	123
5.5	Boresight directivity of the optimized ACMPAs. . . . .	124
5.6	Radiation patterns of the CE-optimized ACMPA. . . . .	125

5.7	Geometry of the RCA with an ACMPA feed. The PRS is an all-dielectric TPG superstrate of diameter $D=60$ mm and thickness $t=6.985$ mm. . . .	127
5.8	Reflection coefficient of the CE-optimized ACMPA (Table 5.3) before and after placing the PRS on top. . . . .	128
5.9	Reflection coefficient of the RCAs optimized by PSO, CE and CMA-ES. .	130
5.10	Boresight directivity comparison of the slot-fed RCA and the ACMPA-fed RCA optimized by CE (shown in an inset). . . . .	131
5.11	Radiation patterns of the CE-optimized RCA with ACMPA. . . . .	132
5.12	CE, PSO and CMA-ES convergence curves for two design cases. . . . .	135
6.1	Illustration of a periodic structure having a pixelated unit-cell with $n = 8$ . By assuming perfect walls surrounding a single unit-cell, infinite repetitions in the $x$ and $y$ directions are realised. . . . .	141
6.2	A quarter of a unit-cell can be converted into three different configurations by applying different symmetry planes. Reducing the unit-cell to a quarter decreases the dimensionality of the optimization problem by a factor of four.	143
6.3	(a) Conventional unit-cell with square pixels causing problematic connections of Type 1; (b) unit-cell with octagonal pixels; (c) square-to-octagonal pixel conversion for the elimination of diagonal infinitesimal intersection of pixels. . . . .	144
6.4	Illustration of the exponential increase in the complexity of binary optimization problems. . . . .	146
6.5	The flowchart for optimization of binary problems using the CE method.	147
6.6	A model of the square unit-cell under optimization. . . . .	149
6.7	A part of the optimized single-frequency AMC: top pattern ( <i>left</i> ) and bottom pattern ( <i>right</i> ) of 9 unit-cells. . . . .	151
6.8	Reflection phase of TE-polarised incident wave from the top and bottom sides of the optimized AMC, as well as the transmission magnitude. . . .	151
6.9	A part of the optimized single-frequency AMC with $a = 0.1\lambda_0$ : top pattern ( <i>left</i> ) and bottom pattern ( <i>right</i> ) of 9 unit-cells. . . . .	153

6.10	Reflection phase of TE-polarised incident wave from the top and bottom sides of the AMC with $a = 0.1\lambda_0$ , as well as the transmission magnitude. . . . .	153
6.11	Convergence curve for the optimization of a single-frequency AMC with $a = 0.1\lambda_0$ . . . . .	154
6.12	Distribution of the F.F. value (Eq. (6.9)) over all candidates for the first and the last iteration of the optimization of the AMC with $a = 0.27\lambda_0$ . . . . .	154
6.13	A part of the optimized dual-frequency AMC showing 9 unit-cells: top view ( <i>left</i> ) and bottom view ( <i>right</i> ) of the optimized patterns. . . . .	156
6.14	Reflection phase of TE-polarised incident wave from the top and bottom sides of the optimized AMC, as well as the transmission magnitude. . . . .	157
6.15	Convergence curves for the optimization of a dual-frequency AMC. The stopping criterion was satisfied after (a) 47 iterations for the first run and (b) 58 iterations for the second run. The unit-cell with octagonal pixels has the side length $a=8$ mm and thickness $t=3.15$ mm. . . . .	158
6.16	Transmission coefficient magnitude and phase of the phase correcting meta-surface. Optimized design meets the target of $\angle S_{12,obj} = 200^\circ$ , $ S_{12}  \geq 0.9$ at 20 GHz. . . . .	162
6.17	The phase of the transmission coefficient of the optimized phase-shifting unit-cells with $ S_{12}  \geq 0.9$ . . . . .	162
7.1	Layout of a 5-pole transverse resonance Butterworth microstrip LPF. . . . .	168
7.2	Transmission characteristics of the designed 5-pole TR-LPF with a cut-off frequency at 3.3 GHz using the traditional cost function formulation. . . . .	171
7.3	Comparison of the optimized TR-LPF and the linear TR-LPF. The transmission mask ( <i>red line</i> ) defines the desired filter response. The optimization goal was to minimise the squared difference between the mask and the result. . . . .	173
7.4	Convergence curve for the optimization of a 5-pole TR-LPF. . . . .	173
A.1	The flowchart for interfacing MATLAB and CST MWS. . . . .	181

---

C.1 Initial unit-cell model with only the quarter of the pixels on each side of the superstrate. . . . .	190
---	-----



# List of Tables

2.1	Alternative terminology and the meaning of the key terms used in evolutionary optimization algorithms. . . . .	17
2.2	Additional coefficients used in the CMA-ES algorithm. . . . .	38
2.3	Comparison of the mean number of function evaluations (MNFE) required for CE, PSO and CMA-ES on two test functions. . . . .	43
3.1	Recent advances in gain-bandwidth enhancement of compact RCAs. . . .	54
3.2	Simulation-time reduction using parameter sweep. . . . .	61
3.3	Radiation characteristics of the RCA with a quarter-wavelength dielectric superstrate of diameter $D = 2\lambda_0$ , $\lambda_0=24$ mm. . . . .	63
3.4	Results of six sequential optimization trials of the design problem given in Fig. 3.12. . . . .	73
4.1	Design parameters for RCA optimization. . . . .	97
4.2	Optimization Case-I results for three predefined superstrate thickness values.	100
4.3	Catalogue of RF laminates for Case-II optimization. . . . .	103
4.4	Optimization Case-II Results for Three Predefined Superstrate Diameter Values ( $\lambda_0=26$ mm). . . . .	104
4.5	Measured SLLs of the RCA prototype. . . . .	109
5.1	Fixed ACMPA parameters. . . . .	116
5.2	Input parameters for CE, PSO and CMA-ES. . . . .	122
5.3	Dimensions and F.F. of the best ACMPA solutions. . . . .	124
5.4	Input parameters for CE, PSO and CMA-ES. . . . .	129

---

5.5	Dimensions and F.F. of the best ACMPA-fed RCA solutions. . . . .	131
5.6	Best obtained fitness function value and NFE of each algorithm applied to the optimization of the ACMPA and the ACMPA-fed RCA. . . . .	134
6.1	A comparison table of the presented work with the GA-optimized single- frequency AMC surfaces. . . . .	155
6.2	A comparison table of the presented work with the GA-optimized dual- frequency AMC surfaces. . . . .	159
6.3	Obtained phase shifts of the optimized pixelated unit-cells. . . . .	161
7.1	The CE method parameters for optimization of 5-pole LPF problem. . .	170
7.2	Parameter values for the 5-pole TR-LPF before and after optimization. .	174



# List of Acronyms

ACMPA	Aperture-Coupled Microstrip Patch Antenna
ACO	Ant Colony Optimization
AMC	Artificial Magnetic Conductor
BBO	Biogeography-Based Optimization
CE	Cross-Entropy
CMA-ES	Covariance Matrix Adaptation Evolution Strategy
CS	Cuckoo Search
CST MWS	Computer Simulation Technology Microwave Studio
CWA	Conventional Weighted Aggregation
DBP	Directivity-Bandwidth Product
DE	Differential Evolution
EA	Evolutionary Algorithm
EBG	Electromagnetic Band Gap
EDA	Estimation of Distribution Algorithm
EM	Electromagnetic
EO	Evolutionary Optimization
ES	Evolutionary Strategy
FSS	Frequency-Selective Surface
GA	Genetic Algorithm
HED	Horizontal Electric Dipole
HIS	High-Impedance Surface
IWO	Invasive Weed Optimization

LPF	Low-Pass Filter
MPA	Microstrip Patch Antenna
NFL	No Free Lunch
PBC	Periodic Boundary Condition
PEC	Perfect Electric Conductor
PMC	Perfect Magnetic Conductor
PRS	Partially Reflecting Surface
PSO	Particle Swarm Optimization
RCA	Resonant Cavity Antenna
SA	Simulated Annealing
SLL	Side Lobe Level
TPG	Transverse Permittivity Gradient
WDO	Wind-Driven Optimization

*It was the best of times, it was the worst of  
times...*  
— Charles Dickens, "A Tale of Two Cities"

# Chapter 1

## Introduction

### 1.1 Evolutionary Optimization in Antenna Design

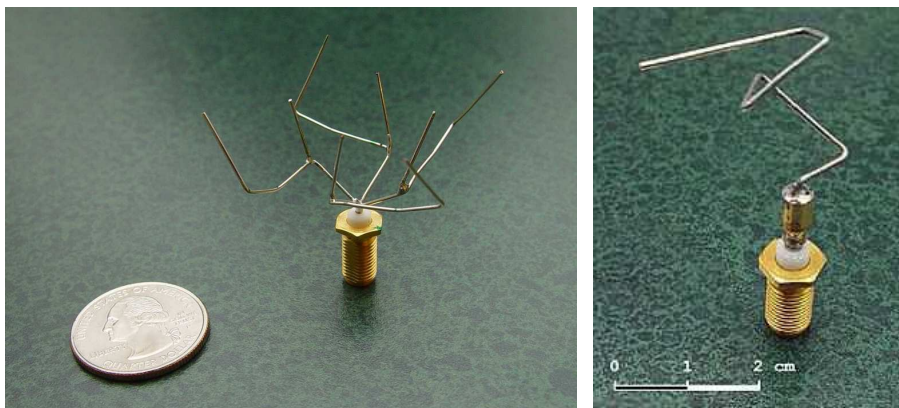
Optimization is everywhere. It is a fundamental aspect of problem solving. Even in our everyday life, we strive to make decisions that are optimal in terms of time, cost, effort or other factors. In simple terms, to optimize means to find such design parameters of a system which result in its best possible performance. Optimization is a truly interdisciplinary research topic merging mathematics with practical problems from various application areas. It has been effectively used in such applications as design of gas and water supply networks, distributed energy systems, wind farm turbine positions and aircraft structural components [1, 2].

Life on Earth has been evolving for almost four billion years, and she has found various ingenious problem-solving methods and the ways to adapt to ever-changing environments [3]. Interpreting the genetic theory of evolution as a population-based optimization process inspired the creation of evolutionary algorithms (EAs). The first attempts to simulate genetic systems using automatic digital computers were made in the 1950s [4]. Later studies were conducted on adaptation in natural and artificial systems through reproduction, mutation, competition and selection. The proposed algorithmic expressions of these processes resulted in the creation of genetic algorithms (GAs). The core principle of almost all EAs is the collective intelligence of populations of agents that must contin-

ually obtain information from sometimes uncertain, changing environments and use it to improve performance and enhance the chance of survival [5,6]. GAs have inspired many related methods and led to the thriving field of evolutionary computation.

Evolutionary optimization algorithms are global search methods that have the potential to find the universally best solution(s) in the presence of multiple suboptimal, local solutions under the specified constraints [7]. They have been widely used in many real-world engineering applications [8], including electromagnetic and antenna design. Modern electromagnetic (EM) optimization problems have complex geometries with multiple design parameters and multimodal search spaces, and therefore, global optimization methods, which are more computationally intensive than local ones, have to be used. Previously, the lack of computing power limited the range of problems that could have been solved by EAs. As the computing technology advances, more practical problems become tractable [9–11].

The antenna design process requires the adjustment of its geometry and material parameters to ensure that the response satisfies performance specifications with respect to certain characteristics, such as input impedance, radiation pattern, antenna efficiency [12]. Therefore, EAs are exceptionally suitable for application to antenna design. One of the first applications of EAs to antenna engineering is a crooked wire antenna, shown in Fig. 1.1. It is also known as an evolved or genetic antenna because it was designed by an automated procedure using GAs [13–15].

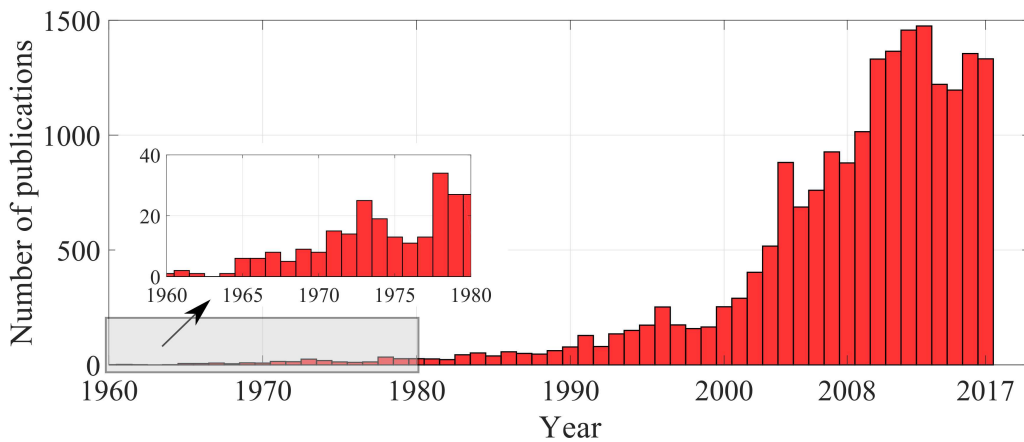


**Figure 1.1:** Genetically evolved crooked wire antennas for the 2006 NASA ST5 spacecraft [15].

## 1.2 Research Motivation

As an industry and academic standard, antenna design is realised by a manual or semi-manual adjustment of selected geometrical dimensions guided by engineering experience [16]. Such a trial-and-error approach often leads to a satisfactory result but is time-consuming and does not produce the best possible solution. As the number of design parameters increases, the complexity of the design problems grows exponentially. This phenomenon, known as the curse of dimensionality, limits the success of manual design methods. A genuinely optimal solution can be obtained with a high probability by means of numerical optimization algorithms, such as EAs.

Progress in evolutionary optimization (EO) has led to a tremendous increase in the interest in EAs within the EM community. The search by the keywords “*antennas*” and “*optimization*” or “*evolutionary algorithm*” in the Scopus database shows a total number of 19568 papers published from 1960 to 2017 year [17]. Fig. 1.2 shows the distribution of these publications over the last 57 years, where a five-fold increase is observed from the year 2000 to 2010. A dramatic change in modern antenna design approaches in the field of EM can be observed. The areas where EAs have been implemented and advanced our knowledge of EM design problems include microstrip antennas [18–20], antenna arrays of arbitrary shapes [21–23] and electromagnetic bandgap (EBG) structures and EBG-based antennas [24–26].



**Figure 1.2:** Academic publications related to the application of evolutionary optimization algorithms to antenna engineering according to the Scopus database.

The growth of interest in the application of EO to antenna engineering problems is motivated by the following factors [7, 27]:

- There is a high probability of finding the optimum or near-to-optimum solution.
- Significantly reduced overall design time compared to manual trial-and-error approach can be achieved.
- In contrast to classic optimization methods such as gradient descent and quasi-newton methods, there is no need for the optimization problem to be differentiable.
- No assumptions about the problem topology are required, as multi-extremal, multi-objective and multi-variable optimization problems can be solved.
- Educated trade-off analysis can be conducted based on several performance figures (in multi-objective optimization).
- Employing EO allows the exploration of designs that might not be identified using traditional techniques. Non-intuitive designs may be found, allowing new possibilities in antenna engineering.
- They have an advantage of a convenient parallel implementation, which can reduce optimization time when multiple computers are available.
- Real-world problems with continuous, discrete and mixed variables can be optimized.
- In conjunction with numerical simulation packages, an accurate optimized result can be directly obtained, reducing the engineering design cycle.
- The potential to automate antenna design process by means of advanced computational resources and thus significantly decrease the cost of antenna components in wireless communication systems.

Automated design optimization technology is being rapidly adopted by engineers in all major industries [11]. The potential for delivering better designs in less time compared

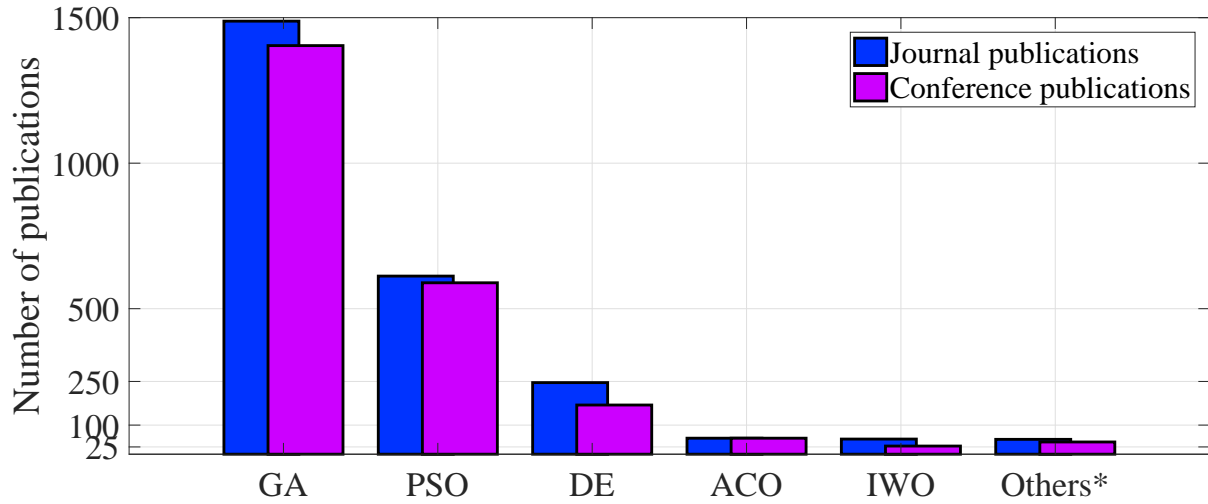
to manual optimization approaches makes automated design optimization very attractive from both technical and business points of view [28]. It would be highly convenient if the antenna design process could be reduced to defining the design variables, objectives and constraints, followed by an automatic process producing a satisfactory solution. A framework for numerical optimization can be defined as specifying the space of all possible designs with optimization parameters and specifying the design criteria. For a seamless automation, the required solvers have to be connected to optimization strategies.

A significant challenge lies in handling the design parameters and constraints of practical designs. Electronic and EM engineering design problems are often constrained and include discrete parameters. The designs are traditionally realised using commercially available materials and components, such as dielectric materials, available in limited thickness and permittivity values, or resistors, available in specific resistance values. Also, overall dimensions of many modern designs are constrained by space limitations. Therefore, mixed-variable (continuous and discrete) design parameters and constraints have to be handled by optimization methods.

## 1.3 Current State of the Art

The collection of EAs is evolving so rapidly that decades of research will be needed to utilise its potential in EM engineering [29–31]. According to the classification proposed in [32], there are four types of EAs: biology-based, physics-based, chemistry-based and mathematics-based. As shown in Fig. 1.4, the algorithms based on biological phenomena have been investigated in EM applications the most.

The first methods implemented on EM problems were GAs [33–37], particle swarm optimization (PSO) and differential evolution (DE). Currently, the number of optimization methods known to the EM community is gradually increasing [38–41]. Fig. 1.3 shows the most popular EAs in EM applications from 1960 to 2017. After GAs, PSO and DE, novel algorithms such as ant-colony optimization (ACO), invasive weed optimization (IWO), cross-entropy (CE), covariance matrix adaptation evolutionary strategy (CMA-ES) and



**Figure 1.3:** The most common evolutionary optimization algorithms in EM applications from 1960 to 2017 according to Scopus. \*The category *Others* include CE, CMA-ES and BBO.

biogeography-based optimization (BBO) gain popularity.

“No free lunch” (NFL) theorems for optimization state that there is no universally better algorithm [42, 43]. However, experience shows that some algorithms outperform others for given types of optimization problems. Most EAs are well-suited for unconstrained continuous search spaces, but require some modifications or real-binary conversions to handle discrete or mixed-integer variables. In terms of design parameters, GAs and ACO handle *discrete* variables intrinsically, while other EAs, including PSO, DE, cuckoo search (CS), IWO and evolutionary strategies (ESs), were originally developed for problems with a *continuous* domain.

The demand for practical combinatorial, mixed-variable and constrained optimization is clear. To optimize problems with discrete variables, binary modifications of popular optimization algorithms were proposed, such as binary DE [44] and binary PSO [45]. For mixed-integer problems, hybrid real-binary techniques have been developed, such as hybrid real-binary PSO [46], mixed-integer GA [47], mixed-integer CMA-ES [48], mixed-variable ACO [49] and hybrid real-binary DE [50]. The constraints are still a very challenging requirement that is usually handled outside of the algorithm update procedures [51].



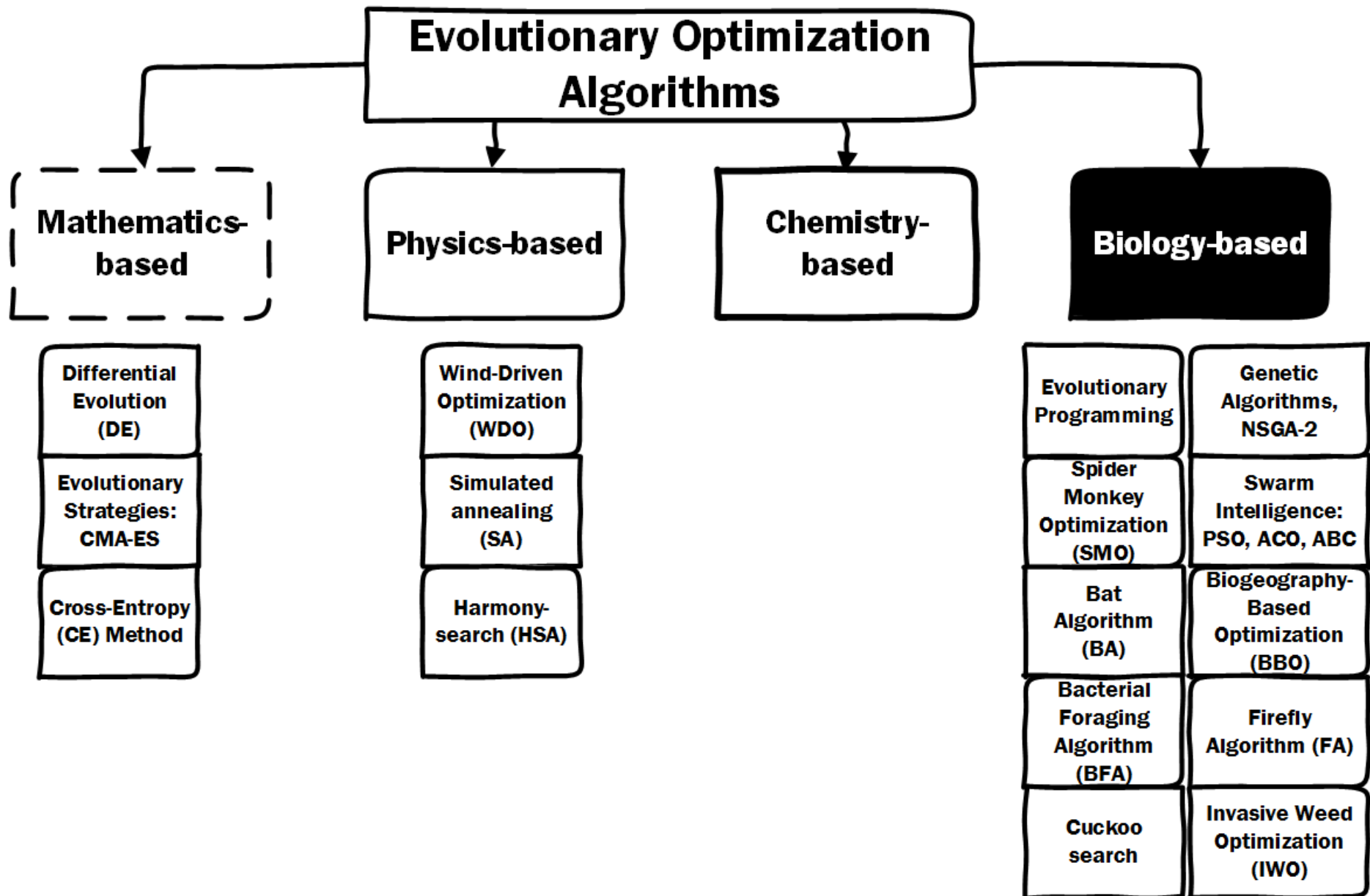


Figure 1.4: Evolutionary optimization algorithms applied to EM engineering problems.

## 1.4 Research Framework and Objectives

Taking into account the variability in terminology in the field of evolutionary computation, some terms that are used throughout this thesis have to be defined. *Evolutionary optimization* (EO) implies that the optimization is performed by an EA. According to [52], any algorithm that optimizes the objective function by evolving, i.e., by an iterative process, can be called an EA. EAs are not necessarily inspired by the theory of natural evolution, such as ESs or GAs, which are just a specific case of EAs. EAs can be population-based, as PSO or IWO, or single-individual algorithms, such as SA. Although EAs are quite often referred to as nature-inspired or bio-inspired optimization algorithms, this terminology excludes DE or EDA, which are not directly motivated by nature. Therefore, we accept the term “*evolutionary algorithm*” as a broad term that includes non-biologically motivated algorithms.

In mathematics, algorithms are usually evaluated on test functions in order to compare their performance. Since EM problems are usually evaluated via simulation, it is time-consuming to perform such studies on them, especially in the competitive engineering environment, where the focus is on a better design rather than on research. Moreover, NFL theorems for optimization show that a “one-size-fits-all” optimization algorithm does not exist [42]. Instead of comparing the algorithms, the research is focused on how the problem specifics govern the choice of the optimization method. A diverse range of EM problems with continuous, discrete and mixed-integer design parameter is considered, such as wideband high-gain resonant cavity antennas of compact size, wideband planar microstrip patch antennas, pixelated EM surfaces and low-pass microstrip filters. The literature review is accompanied by a benchmark study conducted on two common test functions using one well-known and two novel optimization algorithms that will later be implemented on EM problems.

Simulations of all EM designs in this thesis are conducted via the full-wave commercial solver CST Microwave Studio (MWS). The optimization is automated by interfacing the solver with *MATLAB* using macro programming. *MATLAB* and its statistics toolbox were used to generate the code for the CE method and PSO.

Engineering problems are mostly multiobjective. There are two possible ways to optimize for multiple objectives. First, conduct a multi-objective optimization procedure to find multiple trade-off optimal solutions with a wide range of values for objectives and then choose a single solution from the obtained solutions using higher-level information [53]. Second way is to start from prioritising objectives and then combine them according to their weights to form a composite objective function. This method of scaling an objective vector into a composite objective function converts the multi-objective optimization problem into a single-objective optimization problem. Some authors name it as a preference-based multi-objective optimization procedure, others refer to it as a conventional weighted aggregation (CWA). Multiobjective optimization provides a set of non-dominated solutions, a Pareto front, which might be useful to have in case of uncertain priorities. CWA gives only one outcome and is much simpler and more practical because usually only one solution is needed for a problem instead of a set of solutions. Therefore, CWA gained more popularity in engineering applications and EM problems in particular.

In this thesis, multiple design objectives are handled by a CWA. Although multiobjective versions of the implemented optimization algorithms have been proposed, such as multiobjective PSO [45], multiobjective CE [54] and multiobjective CMA-ES [48], their investigation is out of the scope. It is assumed that in many engineering applications the decision about the relative importance of the objectives can be made in advance, and, therefore, the objectives can be combined into a single objective.

The objective of this research is to identify the limitations of the most advanced optimization algorithms for EM applications and propose the solutions that would enable the required capabilities. This thesis provides methodologies that respond to the requirements of real-world EM engineering optimization, and that are flexible enough to be adapted to any other EM problem with similar design requirements.

## 1.5 Overview of Contents

The thesis consists of eight chapters, including this introductory chapter (**Chapter 1**). The contents of the following chapters are briefly described below.

**Chapter 2** provides the theory of three evolutionary algorithms considered in this thesis, PSO, CE and CMA-ES, and reviews their previous applications to EM optimization problems. Following the conventional approach in optimization research, their implementation on common optimization test problems is conducted. The results of the benchmark study are presented and performance comparison is provided. Finally, the difficulties of EO are discussed, as well as the techniques to overcome them.

In **Chapter 3**, the application of the PSO method to the design of a new type of resonant cavity antennas (RCAs) is described. The superstrates of the RCAs, made out of concentric dielectric sections, are optimized for different objectives. The considered optimization problems have continuous variables. Four optimized compact designs with  $\approx 19$  dB gain and radiation bandwidths of 24–70% are presented. The parameters of each superstrate are provided, and the reason for the wideband phenomenon is explained by looking at near-field phase distribution. Optimization methodologies are described in detail.

**Chapter 4** presents the application of the CE method to the design of RCAs. The formulated optimization problems exhibit two unique features. The first is that the overall diameter of the superstrates remains fixed, while the concentric sections composing them vary in size, thus, imposing an equality constraint on the design. The second is that the design variables comprise both continuous and discrete values. The parameters of six compact resonant cavity antennas with improved performance as compared to the initial design are provided. Measurement results of a prototype antenna are presented.

**Chapter 5** presents the optimization results of aperture-coupled microstrip patch antennas obtained using PSO, CE and CMA-ES. The optimization problems consist of continuous design variables. Two scenarios are considered: a stand-alone aperture-coupled microstrip patch and a resonant cavity with an aperture-coupled microstrip patch as a feed. Optimization methodology is described in detail, and performance of each

algorithm, along with the advantages of the CE method, are discussed.

In **Chapter 6**, a novel optimization methodology for the design of pixelated EM surfaces is presented. The fast convergence properties of the CE method and its flexibility to handle various types of design parameters are employed to optimize unit-cell problems with binary variables. The proposed approach is demonstrated on the designs of single- and dual-frequency artificial magnetic surfaces for X-band operation, as well as thin phase shifting metasurfaces for K-band.

**Chapter 7** presents an application of the CE method to the design of a microstrip low-pass filter. The optimization problem consists of continuous variables as well as equality and inequality constraints. The importance of the constrained design requirements is discussed. The optimized microstrip filter with the cut-off frequency at 2.5 GHz has a significantly improved rejection bandwidth as compared to the initial design, preserving its selectivity and size.

Finally, **Chapter 8** summarises the thesis and suggests avenues for future work.

## 1.6 Thesis Contributions

The main contributions of this thesis are presented in five chapters. The major outcomes are listed below.

1. In Chapter 3, a new class of high-gain wideband RCAs with single planar superstrates is considered. Four different configurations of dielectric superstrates, optimized using the PSO method, are proposed. It is shown that by formulating an objective function that reflects the design requirements, radiation bandwidths of 24%, 50% or 70% can be obtained from the RCA. All designs have a high gain of 17.6–19.6 dB and a very compact size ranging between  $1.7 - 2.2\lambda_0$ . The presented RCA designs have radiation parameters outperforming the latest advances found in the literature.
- **M. Kovaleva**, D. Bulger and K.P. Esselle, “Directivity-Bandwidth Enhancement of EBG Resonator Antennas Using a Particle Swarm Optimization Algo-

rithm”, *Fourteenth Australian Symposium on Antennas (ASA 2015)*, Sydney, Australia, Feb. 18-19, 2015.

- **M. Kovaleva**, B.A. Zeb, D. Bulger, K.P. Esselle, “Radiation Performance Enhancement of a Compact Fabry-Perot Cavity Antenna Using Particle Swarm Optimization”, *2015 IEEE International Symposium on Antennas and Propagation (ISAP)*, Hobart, Australia, Nov. 9-12, 2015.
- **M. Kovaleva**, B.A. Zeb, D. Bulger, K.P. Esselle, “Simulation-Driven Optimization of a Compact Fabry-Perot Cavity Antenna”, *2016 IEEE International Symposium on Antennas and Propagation (AP-S/USNC-URSI)*, Fajardo, Puerto Rico, June 26-July 1, 2016.
- **M. Kovaleva**, B.A. Zeb, D. Bulger, K.P. Esselle, “An Extremely Wideband Fabry-Perot Cavity Antenna for Superfast Wireless Backhaul Applications”, *2016 International Symposium on Antenna Technology and Applied Electromagnetics (ANTEM)*, Montreal, Canada, July 10-13, 2016.
- **M. Kovaleva**, D. Bulger and K.P. Esselle, “Efficient Optimization of a Simple Compact Resonant Cavity Antenna”, *2017 IEEE International Symposium on Antennas and Propagation (AP-S/USNC-URSI)*, San Diego, California, July 9-14, 2017, pp. 345-346.

2. In Chapter 4, a novel methodology is developed for the optimization of mixed-integer constrained EM problems. It differs from the previously reported optimization approaches by using flexible updating rules of the CE method. The methodology is implemented on an RCA optimization problem in order to demonstrate its advantages in application to mixed-integer problems with constraints. Simulation results are confirmed by measurement of the prototype, which has the peak directivity of 17.6 dBi and the 3-dB directivity bandwidth of 51%.

- **M. Kovaleva**, D. Bulger, K.P. Esselle, B.A. Zeb, Australian Patent Application (AU) 2016903249. *Title: Optimisation of designs of electromagnetic devices*, date of filing: 16 August 2016.

- **M. Kovaleva**, D. Bulger, K.P. Esselle, B.A. Zeb, International Patent Application PCT/AU2017/050873. *Title: Optimisation of designs of electromagnetic devices*, date of filing: 16 August 2017.
  - **M. Kovaleva**, D. Bulger, B.A. Zeb and K.P. Esselle, “Cross-Entropy Method for Electromagnetic Optimization with Constraints and Mixed Variables”, *IEEE Transactions on Antennas and Propagation*, vol. 65, no. 10, pp. 5532-5540, Oct. 2017.
3. In Chapter 5, a new feed is proposed for achieving wideband impedance matching in compact RCAs. An aperture-coupled microstrip patch antenna (ACMPA) is designed using CE, PSO and CMA-ES optimization methods. The ACMPA has the peak directivity of 9.5 dBi and 45% common bandwidth, and the RCA with the ACMPA feed has the peak directivity of 19 dBi and 40% common bandwidth. A performance comparison of the aforementioned algorithms is provided in order to evaluate the effectiveness of the aforementioned methods in optimization of continuous unconstrained EM problems.
- **M. Kovaleva**, D. Bulger and K. P. Esselle, “A Comparative Study of CE, PSO and CMA-ES in Wideband Antenna Design”, *IEEE Transactions on Evolutionary Computation*, in preparation.
4. In Chapter 6, a new methodology is proposed for optimizing pixelated printed EM surfaces. The CE method has not previously been used for the optimization of binary EM problems. Single- and dual-frequency artificial magnetic conductors obtained using the CE method have a comparable performance to that obtained using GAs but their optimization took much less time. Using the proposed methodology, novel thin phase-shifting metasurfaces are designed with the desired transmission and reflection magnitude and phase. A novel shape of pixels is proposed that prevents a very common issue related to vertices connection in fabricated EM surfaces.
- **M. Kovaleva**, D. Bulger and K. P. Esselle, “A Novel Fast Optimization Method for Pixelated Metasurface Design”, *IEEE Transactions on Antennas*

*and Propagation*, in preparation.

5. In Chapter 7, it is shown how the CE method can be applied to EM problems with constrained continuous design variables. As compared to previously described methods to tackle constraints, the method proposed in this thesis ensures efficient implementation for both inequality constraints, usually obtained by discarding unsatisfactory solutions, and equality constraints, which cannot be handled by the previous methods. The success of the methodology is demonstrated via optimization of a low-pass microstrip filter. The optimized filter outperforms the initial design by improving the rejection bandwidth from 0.5 to 8.5 GHz.

- **M. Kovaleva**, D. Bulger, R. P. Khokle, K.P. Esselle, “Application of the Cross-Entropy Method to Electromagnetic Optimisation Problems”, *2018 IEEE International Symposium on Antennas and Propagation (AP-S/USNC-URSI)*, Boston, MA, pp. 1595-1596.

The code for the PSO and CE optimization algorithms and macro programs for interfacing with software packages in this thesis are the work of the author. The work presented in this thesis has been carried out by the author, and the role of the thesis supervisors was primarily advisory.

A complete list of the author’s publications is given in **Appendix D**.



*Evolution advances, not by a priori design, but by the selection of what works best out of whatever choices offer. We are the products of editing, rather than of authorship.*

— George Wald

## Chapter 2

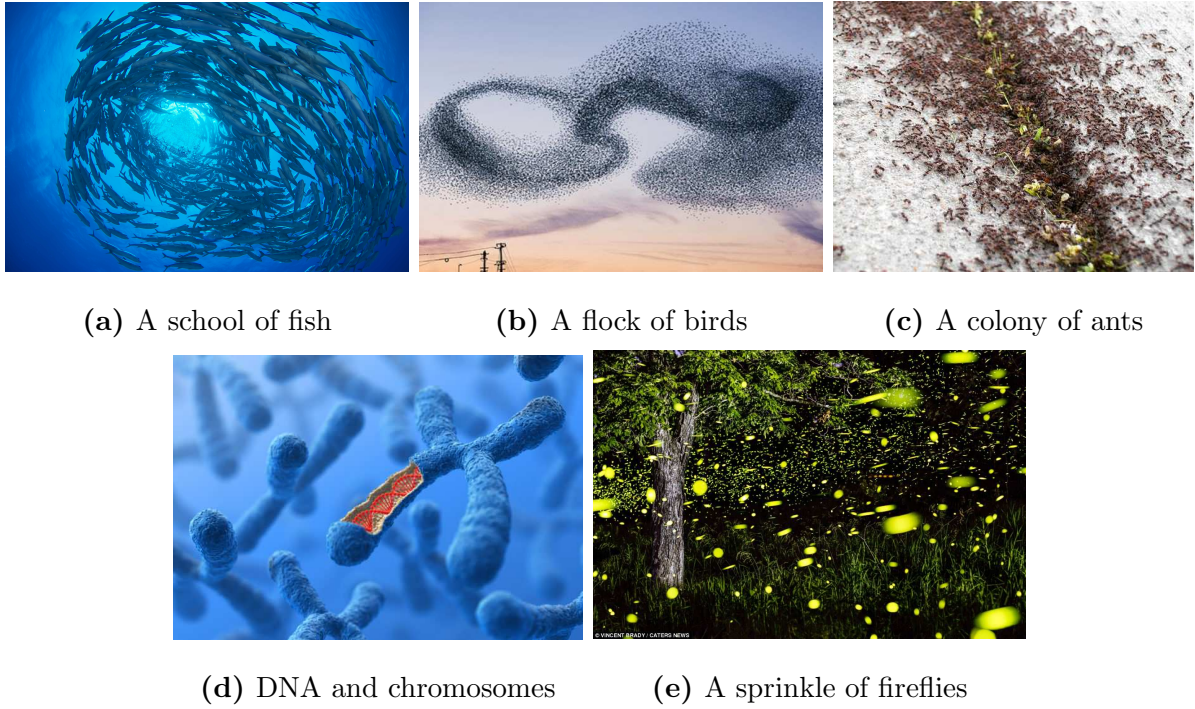
# Evolutionary Optimization

# Algorithms in Electromagnetics

## 2.1 Introduction

Biological studies of group intelligence of animals, plants, bacteria, fungi, etc. show that their survival behaviour (such as foraging, migration, mating, etc.) can be mathematically formulated as optimization algorithms. The algorithms that imitate this behaviour are called nature-inspired optimization algorithms. The inspiration for some well-known nature-inspired techniques came from such phenomena as schooling of fish, flocking of birds, the movements of ants or fireflies, as well as the sophisticated gene combinations in human DNA (Fig. 2.1).

Nature-inspired optimization techniques found its application in electromagnetics (EM) back in 1960s. The complexity of the problems in EM engineering make it impractical to search every possible solution manually. For such problems evolutionary computational techniques can yield globally optimized solutions in an acceptable timescale that are not attainable by traditional gradient-based local-search optimization methods. EO algorithms can be classified as population-based and trajectory-based. For example, GA and PSO use multiple search agents (or candidates) that explore the solution space, while SA is a single-individual algorithm. Table 2.1 summarizes the alternative terminology



**Figure 2.1:** A few examples of group intelligence behaviour.

that will be interchangeably used in this thesis.

EO algorithms are stochastic, which means that a certain degree of randomness is involved in the search process. Therefore, every optimization run produces a slightly different result. Randomisation is a crucial step that provides an opportunity to move away from local search and to search on a global scale. Every EO algorithm has a certain trade-off between randomisation and local search [3]. While increasing randomisation encourages diversification of the solutions, decreasing it allows for intensification of the search around the already found good solutions.

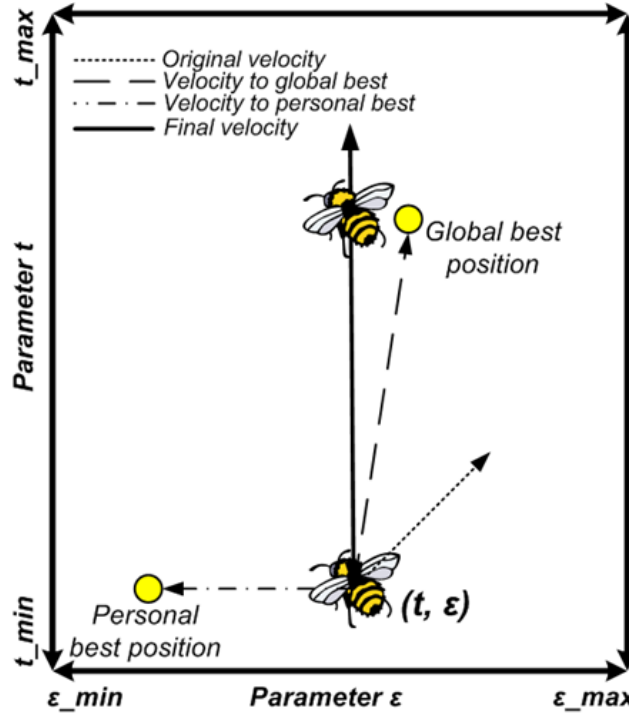
In this chapter, PSO, CE and CMA-ES along with their recent applications to EM optimization problems will be reviewed. The biggest challenges that EM applications pose to EAs will be identified and discussed. The need for efficient optimization methods capable of solving optimization problems of special types, such as mixed-variable and constrained, will be demonstrated.

**Table 2.1:** Alternative terminology and the meaning of the key terms used in evolutionary optimization algorithms.

Key term	Meaning
<i>Search/Solution space, Design region</i>	User-defined region with the dimensionality of the optimization problem
<i>Particle, Candidate, Agent, Solution</i>	An individual design expressed as a vector of design parameters
<i>Generation, Population, Iteration, Swarm</i>	Each time the candidates move to a new location in a search space
<i>Fitness, Score, Objective, Cost function</i>	A single number reflecting the goodness (or badness) of each candidate
<i>Ranking, Elitism, Sorting, Scoring</i>	Arranging the candidates in ascending (or descending) order of their fitness and keeping only $N_{el}$ best for reproduction

## 2.2 Particle Swarm Optimization (PSO): Theory and Applications

Particle swarm optimization (PSO) was developed by a social psychologist James Kennedy and an electrical engineer Russell Eberhart in 1995 [55, 56]. Simple in implementation, it has demonstrated great robustness and speed of convergence in many applications. The method uses the memory of the particles and their cooperation within a swarm in order to find the best position in a field. The fundamental difference between PSO and other EAs is that it modifies the movement of the particles in the search space and not the positions directly. Since its development, about 20 versions of modified PSO have been proposed to improve its search capabilities, including the concept of neighbourhoods or by hybridising it with other optimization methods [3, 57–60]. The classical version of PSO, which has been used in this thesis, is described below.



**Figure 2.2:** Schematic representation of the motion of a particle pulled by the global best, personal best and its inertia in a two-dimensional space with parameters  $t$  and  $\varepsilon$ .

### 2.2.1 PSO Algorithm

The algorithm searches for the best location in the domain of an objective function by adjusting the trajectories of individual particles. Fig. 2.2 gives a schematic representation of the forces that affect the movement of a single particle. Flying around the search space, the particles are attracted by the best positions they have observed  $p_{(t)}^n$  (cognition), the best position observed by the whole swarm  $b_{(t)}$  (socialising) and by their previous directions  $v_{(t)}^n$  (inertia).

The position of each particle  $x_{(t)}^n$  is updated at each iteration using the equation [56]:

$$x_{(t+1)}^n = x_{(t)}^n + \Delta t * v_{(t+1)}^n, \quad (2.1)$$

where  $n = 1, \dots, N_{pop}$  is a particle index,  $N_{pop}$  is a swarm size, and  $t$  is an iteration count with a step  $\Delta t=1$ . In a classical PSO with an inertia weight  $w$ , the velocity  $v_{(t+1)}^n$  of each particle, which is a sum of inertia, social and cognitive components, has the following

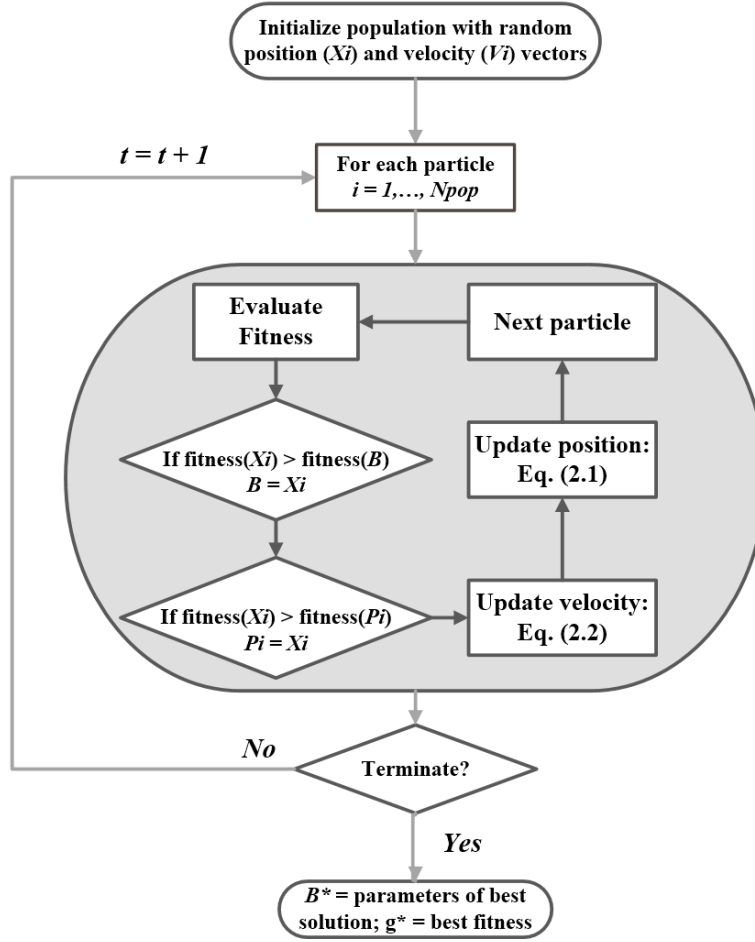


Figure 2.3: PSO algorithm flowchart.

expression:

$$v_{(t+1)}^n = wv_{(t)}^n + c_1 * rand_1 * (p_{(t)}^n - x_{(t)}^n) + c_2 * rand_2 * (b_{(t)} - x_{(t)}^n), \quad (2.2)$$

where  $rand_1$  and  $rand_2$  are random coefficients taking any value between (0,1). The factors  $c_1$  and  $c_2$  will be described in the following discussion.

The essential steps of the PSO can be summarized in the flowchart in Fig. 2.3. The first step is to assign initial values of positions and velocities to each particle. If there is no prior knowledge of the problem, the values are assigned randomly. It is highly recommended though to initialize the algorithm from a meaningful result as, in this case, the time taken by the algorithm to converge can be significantly reduced [61]. The following steps should be repeated for each particle in a population: evaluate fitness, find  $b_{(t)}$  and  $p_{(t)}^n$ , update velocity and position. The cycle is repeated until the termination

criterion is met.

The swarm behaviour can be controlled by the adjustment of the swarm size  $N_{pop}$ , the weight of the inertia component  $w$ , cognitive constant  $c_1$ , social constant  $c_2$  and the maximum number of iterations  $N_{it}$ . Although other stopping criteria are possible,  $N_{it}$  should be specified if a linearly decreasing inertia component is used. The speed of decreasing  $w$  depends on the maximum number of iterations. As suggested in [62], acceleration constants should be  $c_1 = c_2 = 1.49$ . The value of the inertia weight is usually decreased over iterations from 0.9 to 0.4. The convergence rate of the algorithm can be increased (therefore, the overall number of evaluations can be decreased) by setting the lowest value of  $w$  equal to 0.1 [63]. The randomness is introduced to the algorithm by  $rand_1$  and  $rand_2$ , which are uniformly distributed coefficients taking values between 0 and 1. The swarm size  $n$  and the maximum number of iterations  $N$  “are somewhat arbitrary” [64] and depend of the optimization problem but a “rule of thumb” is that  $n$  is at least two to four times larger than the problem dimensionality.

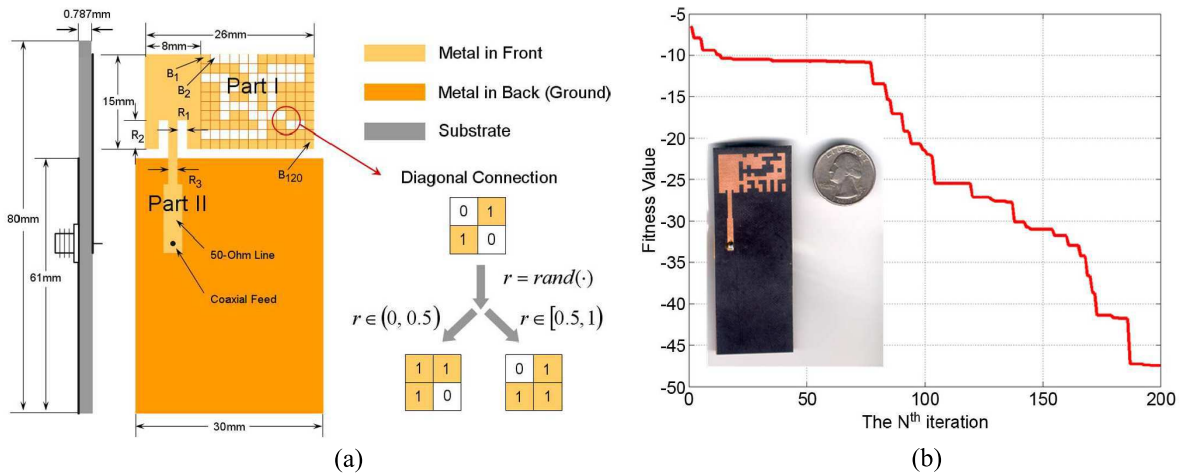
It can be seen that the algorithm is extremely simple to implement, which is one of the reasons it has gained significant popularity in EM applications. Compared to GAs, PSO does not require an artificial binary encoding of the problem domain, and it has fewer parameters to be tuned. PSO does not naturally keep the particles inside any defined solution space. Therefore, boundary conditions have been introduced to prevent the particles from flying out of the solution space and, therefore, violating the design constraints. For example, penalties can be used, assigning a bad fitness value to any infeasible particle [45, 62, 65]. This measure however reduces the efficiency of the optimizer because it causes a temporary loss of search agents.

### 2.2.2 Applications of PSO to EM problems

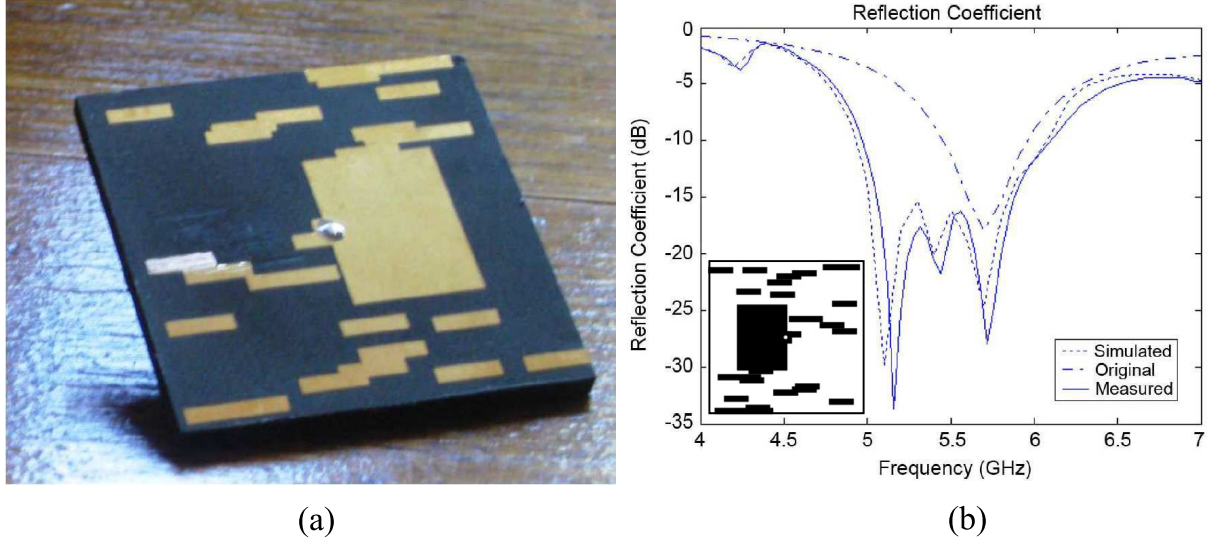
The classical version of PSO described above operates only with *continuous* design variables. It has found numerous applications in EM, such as in the design of multiband and wide-band microstrip patch antennas [66, 67], reconfigurable and conformal E-shaped antennas [68, 69], as well as EBG-based antennas [26] and UWB antennas [70]. Many

successful applications of PSO to linear and planar antenna array synthesis problems have been demonstrated for the purpose of side lobe suppression, null placement or dynamic phased-array control [46, 71–73]. A significant advantage of array synthesis problems is that they are very fast to analyse and, therefore, the optimization results can be obtained within several hours, giving a designer a chance to repeat multiple optimization runs and tune the internal parameters of optimization algorithms. A binary version of PSO that can handle *discrete* design variables has been proposed in [74]. It has found applications in array thinning [75], adaptive phased-arrays control [72], microstrip antenna design [76] and many others. Below, some recent PSO applications will be reviewed in detail.

To tackle optimization problems with mixed variables and constraints, a hybrid real-binary PSO has been proposed [46]. Highlighting that the rounding-off operation, which has been previously used to handle mixed-integer problems, significantly deteriorates convergence of PSO, the authors proposed concatenating real and binary variables into a single parameter vector. One application of the proposed methodology was a handset patch antenna shown in Fig. 2.4(a). The challenge of the design was to obtain required dual-band impedance matching in a limited design space. The space was divided into two parts, where one part served to hold a 15 mm × 8 mm rectangular patch, and



**Figure 2.4:** A dual-band handset patch antenna design problem with a mixed-parameters vector. (a) Antenna geometry. (b) Convergence curve with antenna prototype in the inset (from [46]).

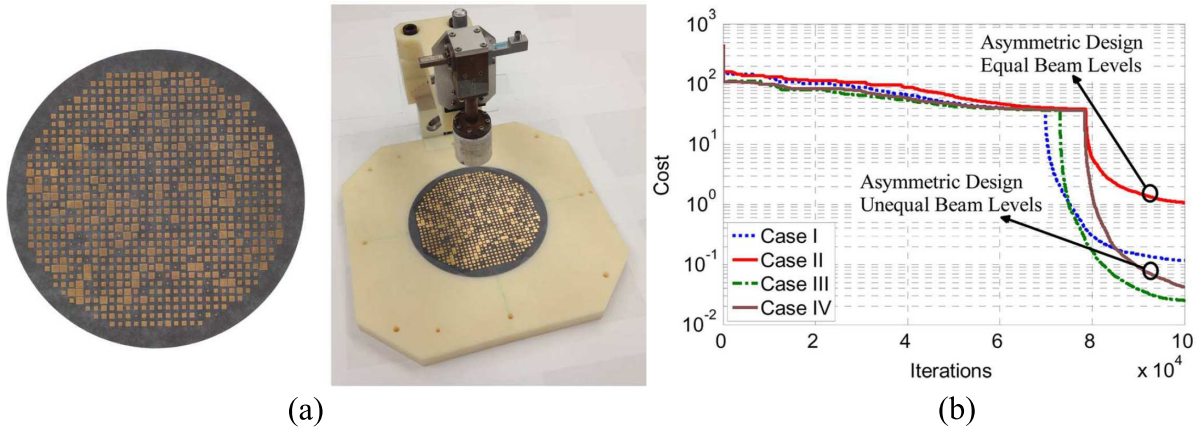


**Figure 2.5:** A parasitically coupled microstrip antenna array for the IEEE 802.11a WLAN 5–6 GHz frequency band. (a) The prototype of the optimized antenna. (b) Reflection coefficient of the original and optimized antenna (from [18]).

the second was discretized into  $12 \times 10$  square pixels with a side length of 1.5 mm. The design was represented by 3 continuous variables and a 120-bit binary string to identify dielectric/metal status of each pixel. The cost function included  $S_{11}$  at two frequencies of interest, 1.8 GHz and 2.4 GHz. Fig. 2.4(b) shows the optimized design and the convergence curve of the optimization. The optimal design that has satisfactory input impedance appeared at the 190th iteration. It is interesting to note that after first 10 iterations the algorithm showed very little improvement for around 50 iterations but then escaped stagnation.

Another EM problem was described in [18], where a microstrip patch antenna without predefined geometry was optimized by PSO. The aim of the design was to increase the impedance bandwidth of a standard rectangular microstrip patch antenna. The hypothesis was that small parasitic rectangular dipoles placed around the driven patch could create strong mutual coupling resulting in additional resonances at frequencies slightly lower than that of the main patch. The methodology employed classic PSO to place the sub-patches of  $8 \text{ mm} \times 2 \text{ mm}$  on the substrate at the positions corresponding to a particle's position in the solution space. The constraints of the design were the area of



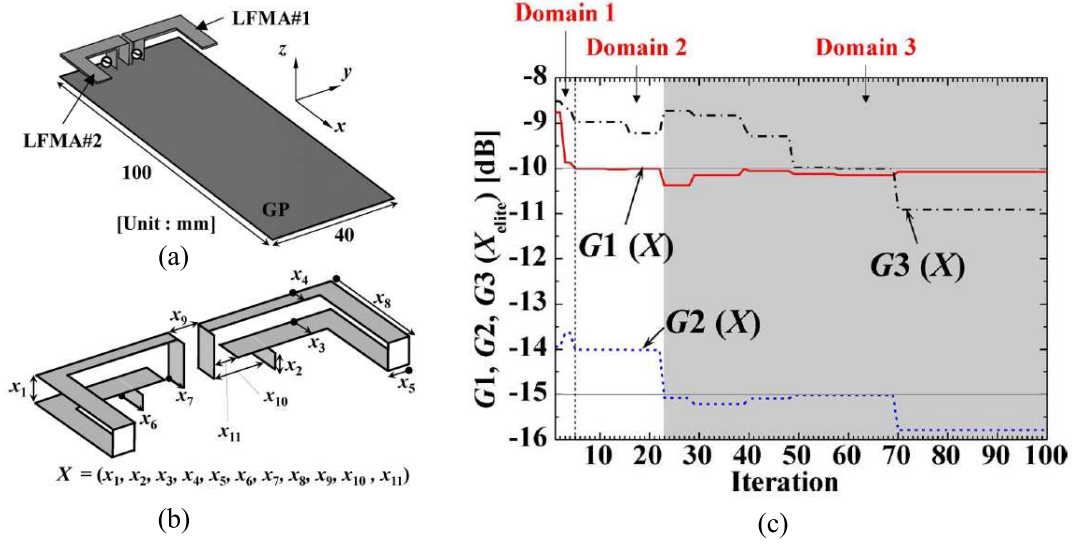


**Figure 2.6:** Ka-band single-feed reflectarray system was optimized for a number of quad-beam requirements using PSO. (a) Fabricated reflectarray prototype. (b) Convergence curves for four radiation pattern mask requirements (from [77]).

the substrate, the shape of the sub-patches and selection of the driven patch. The results confirmed the initial assumption, and the bandwidth of the antenna increased from the original 7% to 19%.

PSO has also been implemented to optimize the phase of the elements in asymmetric multibeam reflectarrays with arbitrary beam directions and gain levels [77]. This is a very challenging design problem due to the very large solution spaces. In particular, the optimization problem in [77] has 848 continuous variables. To achieve a multibeam pattern, a far-field mask based on the design requirements was defined for the optimization. A swarm population of 400 particles performed 100 000 iterations, corresponding to 40 million fitness evaluations. Due to the use of a custom analysis code, the radiation pattern calculations were fairly fast, with total computation time of about 44 hours. The prototype of the optimized reflectarray is shown in Fig. 2.6(a), and the convergence curves for four different design cases are given in Fig. 2.6(b). It can be seen that for 70 000–80 000 iterations the algorithm struggled to find a satisfactory performance but it eventually escaped the stagnation. Convergence rates can potentially be increased by using larger swarm populations, however, this would come at a cost of longer optimization runs.

It is very common that specifications for antenna design problems include multiple requirements, such as impedance matching, gain, axial ratio, radiation pattern, etc. There



**Figure 2.7:** L-shaped folded monopole antenna array optimized under five inequality constraints. (a) Antenna deployment on a substrate and the geometry under optimization with eleven continuous variables. (b) Convergence of the elite particle  $X$  minimizing the goal function equal to the sum of  $G_1(X)$ ,  $G_2(X)$  and  $G_3(X)$  (from [78]).

are two alternative ways to optimize for multiple objectives. First, by a multi-objective optimization procedure that finds multiple trade-off optimal solutions (known as Pareto-optimal solutions) with a wide range of values for objectives. It is then the designer's task to choose a single solution from the obtained solutions using higher-level information [53]. Second way is to start from prioritising objectives and combining them according to their weights to form a composite objective function. These methods will be discussed in more detail in Section 2.6.1. In a recent implementation of continuous PSO [78], it is proposed to include multiple objectives by performing multi-level optimization instead of using conventional weighted aggregation or Pareto dominance method. The design problem consists of two L-shaped folded monopole antennas (Fig. 2.7(a)) that are to be installed in a handset and, therefore, miniaturisation is one of the most important criteria. Other design requirements were low mutual coupling reduction between two antennas and a sufficient resonant bandwidth covering the IEEE 802.11 b/g WLAN band. Parametrized antenna geometry, shown in Fig. 2.7(b), had 11 variables and 5 constraints. To satisfy the design targets, the optimization goals were expressed by three equations that were

minimized one by one. Convergence curves for each goal are shown in Fig. 2.7(b). The optimized design achieves the specified goals and outperforms the previous solutions.

It can be seen that PSO has been a successful optimization method for EM applications. However, to incorporate problem-specific information, some modifications were required. Particularly, to tackle the problem with mixed variables and constraints (Fig. 2.4), a novel methodology had to be derived. The updating procedure was separate for continuous and binary parts of the design vector. The position of continuous part was updated by the Eq. (2.1), and the binary part was updated using sigmoid transformation [46]. This approach converts discrete variables into binary strings, which adds complexity and, therefore, might prevent the methodology from being widely used.

## 2.3 Cross-Entropy (CE) Method: Theory and Applications

The cross-entropy (CE) method was proposed by Rubinstein in 1997 [79] as an adaptive importance sampling procedure for estimating the probabilities of rare events, such as earthquakes, hurricanes or financial market crashes. The distinctive feature of the CE method is in the use of parametrized probability distributions in the updating rules. The name of the method comes from the fact that it uses Kullback-Leibler divergence, also known as cross-entropy, as a measure of closeness between two sampling distributions [80]. In later work by the same author, it was shown that the CE method can be used as a stochastic optimization algorithm because optimization problems can be represented as rare-event estimation problems. The idea of the method is that the probability of locating an optimal or near optimal solution using naive random search is a rare-event probability [81]. Searching for the global optimal solution, the CE method iteratively reshapes the sampling distribution of a random search to place more emphasis on the rare-event occurrence.

### 2.3.1 CE Algorithm

To operate with the CE method, knowledge of basic principles from statistics and information theory is required [82, 83]. Before getting into the details on how exactly the distance between two probability distributions is measured, we will introduce some necessary notations. As mentioned above, in optimization using the CE method, updating rules iteratively modify the shape parameters of probability distributions instead of the solutions of the optimization problem itself. Probability density functions (for continuous variables) or probability mass functions (for discrete variables) are the functions whose value at any given point in the sample space can be interpreted as providing a relative likelihood that the value of the random variable would equal that sample.

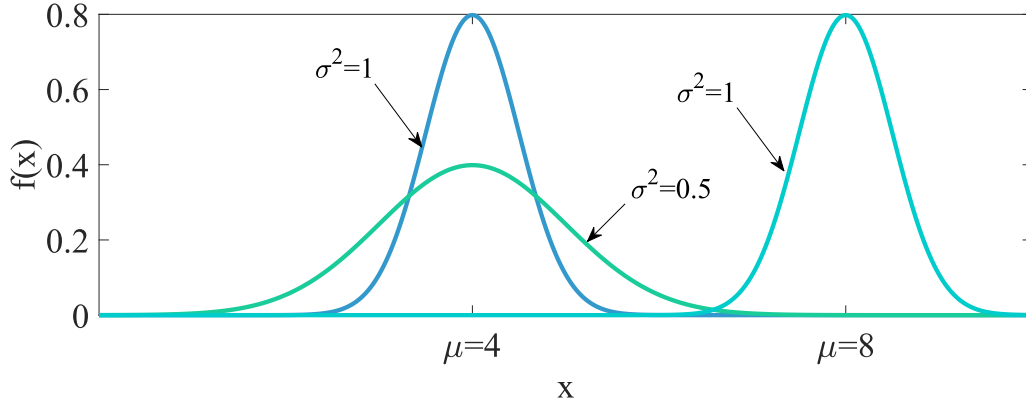
All possible outcomes of a random experiment constitute the **sample space** of the experiment. A sample space is **discrete** if it consists of a finite or countably infinite set of outcomes and **continuous** if it contains an interval (either bounded or unbounded) of real numbers.

Continuous random variables can be modelled by probability density functions (PDFs), such as Gaussian, beta or Gamma distribution. Each PDF is uniquely identified by its parameters. For example, Gaussian distribution is characterised by its mean  $\mu$  and variance  $\sigma$  and has the notation  $N(\mu, \sigma^2)$ . A normal random variable  $X$  has a PDF as in Eq. (2.3) with parameters  $-\infty < \mu < \infty$  and  $\sigma > 0$ .

$$f(x; \mu, \sigma) = \frac{1}{\sigma\sqrt{2\pi}} e^{-(x-\mu)^2/2\sigma^2}, -\infty < x < \infty \quad (2.3)$$

From Fig. 2.8, which illustrates three normal PDFs with selected values of  $\mu$  and  $\sigma$ , it can be seen that  $\mu$  determines the center of the distribution, and  $\sigma$  determines its width.

In CE, at each iteration, a population is drawn by sampling from any given PDF that is defined by its distributional parameters. The distributions are also called *models* in the literature, and, therefore, the CE algorithm belongs to a class of *model-based* optimization methods along with CMA-ES (see Section 2.4) and Estimation of Distributions. Another important concept used in CE is parameter estimation, which is used to update the shape parameters of PDF for the next iteration. In order to generate the parameters of a



**Figure 2.8:** Normal probability density functions of a random variable  $x$ ,  $N_1(4, 0.5)$ ,  $N_2(4, 0.5)$ ,  $N_3(4, 0.5)$ .

new sampling distribution, the updating procedure looks at the current best performing individuals and generates the parameters of a new sampling distribution that closely describes them. The estimation of the parameters of this new sampling distribution is the key task in the CE method.

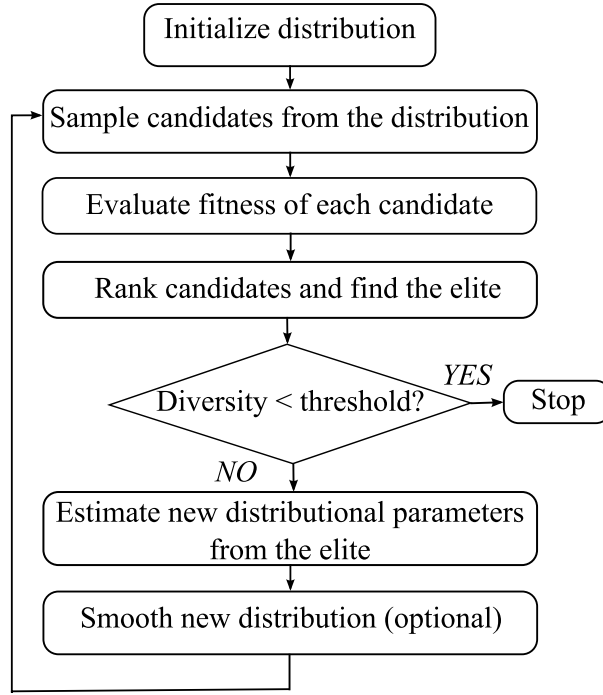
In statistics, there are two well-known methods, the method of moments and the method of maximum likelihood [82], that perform this estimation. In information theory, this is performed using a measure of dissimilarity (or “distance”) between two PDFs,  $f(\mathbf{y})$  and  $g(\mathbf{y})$ , called cross-entropy, that can be expressed as:

$$D(f, g) = \int f(\mathbf{y}) \ln \frac{f(\mathbf{y})}{g(\mathbf{y})} d\mathbf{y}. \quad (2.4)$$

The above expression holds for continuous variables, and for the discrete variables, the integration should be substituted by summation (alternatively, the continuous and discrete cases could be notationally unified with a measure-theoretic treatment). Minimising Eq. (2.4) gives  $D(f, g) = 0$  and, therefore,  $f = g$  assuring a perfect fit of two PDFs. Essentially, maximum likelihood estimation and cross-entropy minimisation is the same procedure, and either of them can be performed for CE optimization method depending on which is easier to obtain. It should be noted that  $D$  from Eq. (2.4) is not a distance in the formal sense, since in general  $D(f, g) \neq D(g, f)$  [84].

The flowchart in Fig. 2.9 summarizes the operating principle of the CE method for optimization. The settings of three parameters, i.e. population size  $N_{pop}$ , elite subpop-

ulation size  $N_{el}$  and smoothing parameter  $\alpha_S$ , have to be supplied by a user to begin optimization.



**Figure 2.9:** CE method flowchart.

The algorithm is initialized by sampling the population from an initial (usually uniform) distribution, in a so-called random start. After the population is sampled, the performance of each candidate is evaluated by calculating  $f(x)$ , and each candidate in the population is assigned a fitness value. If the optimization problem is maximisation, the fitness function values are sorted in a descending order, and an elite subpopulation is created by taking the first  $N_{el}$  samples. Similarly, if the optimization aims at minimizing the objective function, the candidates are sorted in an ascending order of their performance, and the top  $\rho\%$  are chosen for an elite subpopulation, where  $\rho = N_{el}/N_{pop} * 100\%$ . Then, the termination criterion is evaluated. If the algorithm is not converged, the iterations continue. Based on the elite subpopulation, a new sampling distribution is defined. It is this crucial point when the algorithm applies cross-entropy minimisation (or maximum likelihood estimation) to fit a new sampling distribution as close as possible to the current empirical distribution of elite candidates. A smoothing procedure is usually introduced to the algorithm to prevent a premature convergence and ensure the balance

between intensification and diversification. With a smoothing parameter  $\alpha_S$  set to 0.7, the algorithm converged after 5 iterations. The smoothing is applied as follows:

$$v_s^{t+1} = \alpha_S * v_{un}^{t+1} + (1 - \alpha_S)v_s^t, \quad (2.5)$$

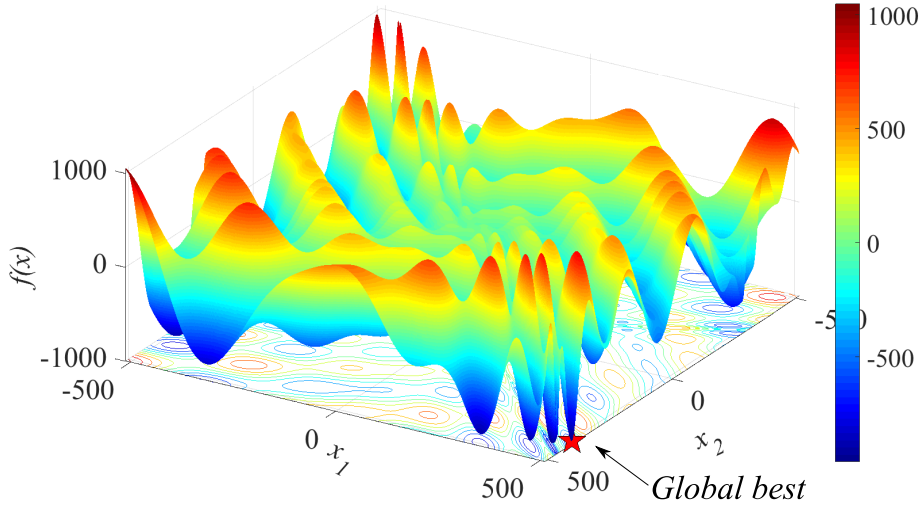
where  $v_{un}^{t+1}$  is a vector of reconstructed distributional parameters at the current population, and  $v_s^t$  is a vector of smoothed distributional parameters from a previous population. Setting smoothing closer to 1 increases the speed of convergence but results in lower success rates, while lower values of  $\alpha_S$  slow down convergence (increase the number of iterations) but also increase the chance of locating the global optimum.

A couple of comments should be made about possible modifications in the given flowchart. Although it is typical for EO to initialize with a random population, it might be beneficial to start the optimization from a seed containing close-to-optimum solutions if such *a priori* knowledge exists. Further information with valuable practical examples can be found in [52]. In Fig. 2.9, a stopping criterion that compares the diversity of the elite subpopulation with a user-defined threshold is evaluated. If the elite subpopulation consists of identical or very similar results, then the algorithm has reached convergence, and the optimization is terminated. Other stopping criteria are also possible, such as a maximum number of iterations or the distance between the best found solution and the target result.

To demonstrate the fast convergence properties of the CE method, we visualize an optimization process of a 2D Eggholder function that is characterised by a very difficult terrain. The function contains multiple local minima, some of which pose difficulties by being deep and narrow or diagonally oriented, while the global solution is located at the boundary of the solution space. Eggholder function has the following mathematical expression:

$$f(\mathbf{x}) = -(x_2 + 47) \sin \left( \sqrt{\left| x_2 + \frac{x_1}{2} + 47 \right|} \right) - x_1 \sin \left( \sqrt{|x_1 - (x_2 + 47)|} \right), \quad (2.6)$$

and its multiple local minima can be seen in Fig. 2.10. The function is usually evaluated in the domain  $x_i \in [-512, 512]$ , for  $i = 1, 2$ . The well-hidden global optimum is located at  $\mathbf{x}^* = (512, 404.2319)$  with the value  $f(\mathbf{x}^*) = -959.6407$  [85].



**Figure 2.10:** 2D Eggholder test function, best location is at  $\mathbf{x}^* = (512, 404.2319)$ .

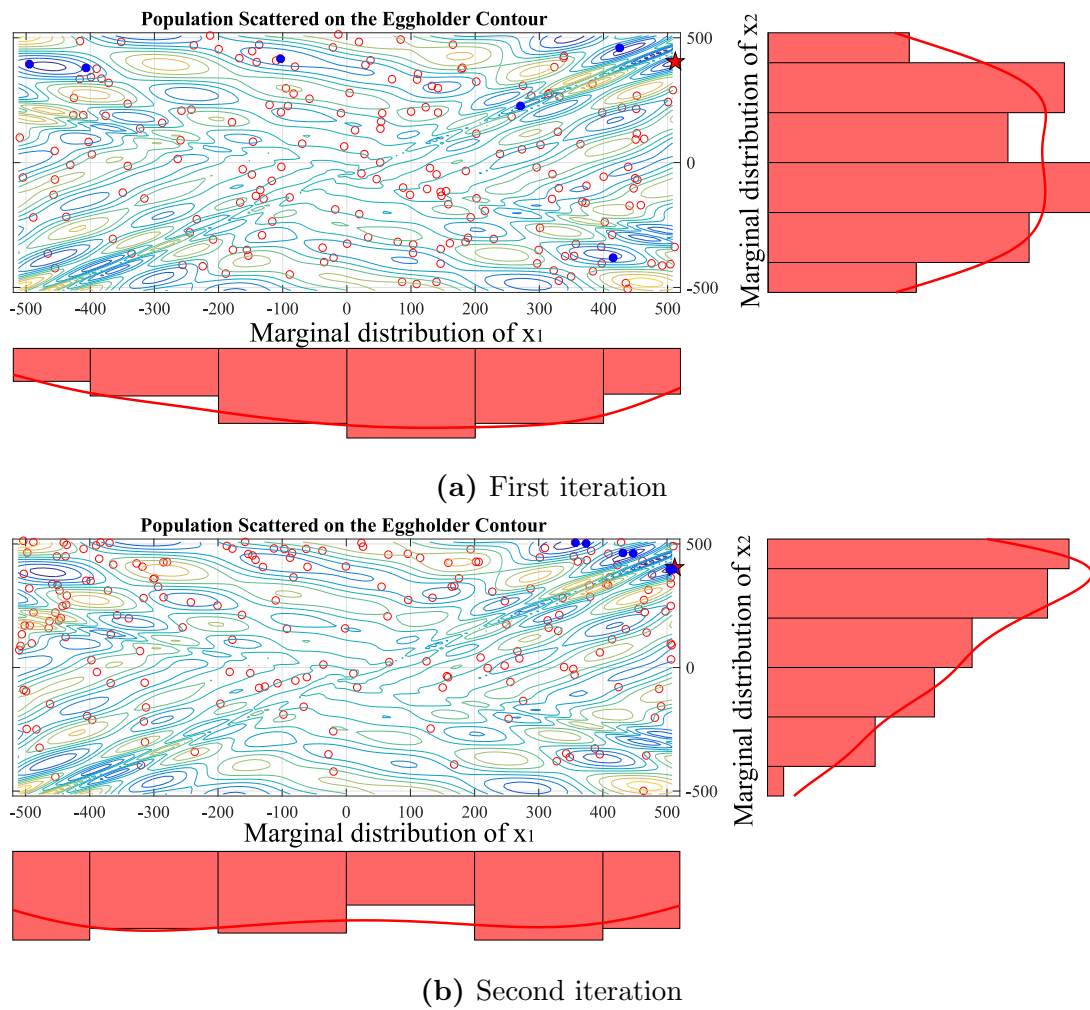
For a bounded solution space, the beta PDF with distributional parameters  $\alpha$  and  $\beta$  is a natural choice. Its equation is provided below:

$$B(x; v) = \frac{x^{\alpha-1}(1-x)^{\beta-1}}{\int_0^1 x^{\alpha-1}(1-x)^{\beta-1} dx}, \quad v = (\alpha, \beta). \quad (2.7)$$

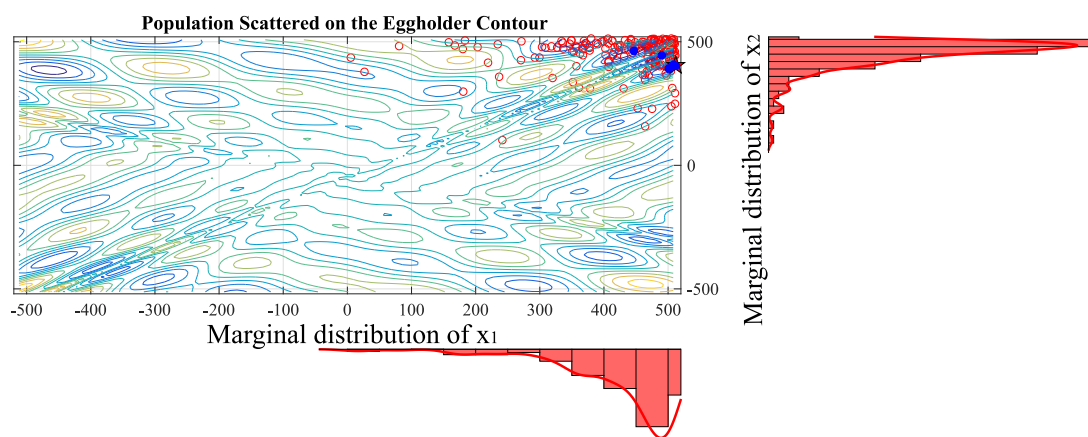
Unlike the normal distribution  $N(\mu, \sigma)$ , which has unbounded support, the beta PDF has the support  $[0; 1]$ . This ensures that the parameters of the candidates sampled from the beta distribution are located within the defined bounds of the solution space. If the solution space bounds are different from  $[0; 1]$ , a simple transformation is applied to scale the parameters of all samples to the solution space bounds. Marginal distributions  $B(\alpha, \beta)$  are generated for every optimization parameter.

A full optimization process of the Eggholder function is shown in Fig. 2.11. Beside the contour plot of the design space, the marginal distributions for each variable are provided. The populations of  $N = 200$  candidates are depicted in red circles, while elite subpopulations of  $N_{el} = 6$  candidates are highlighted by blue dots. It can be observed from Fig. 2.11 that the PDFs for each variable gradually concentrate around the best results. In Section 4.2, the CE method will be further discussed from the application point of view.

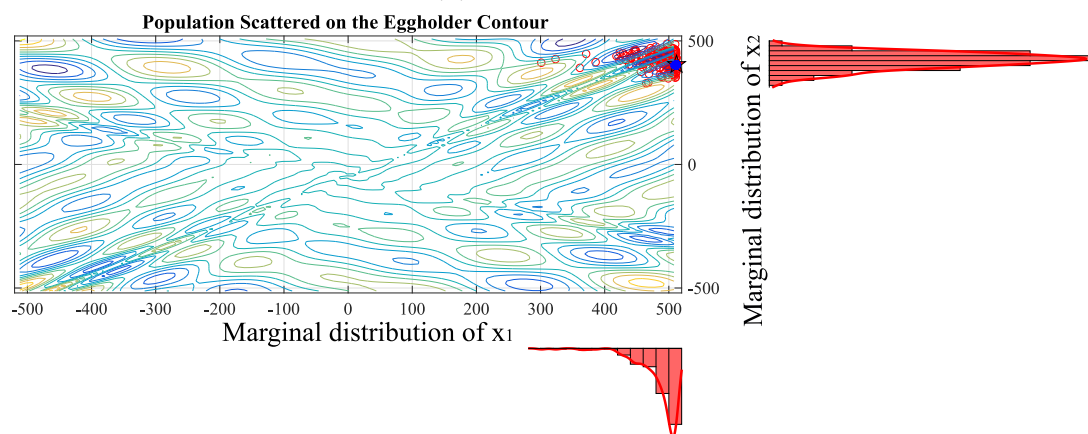




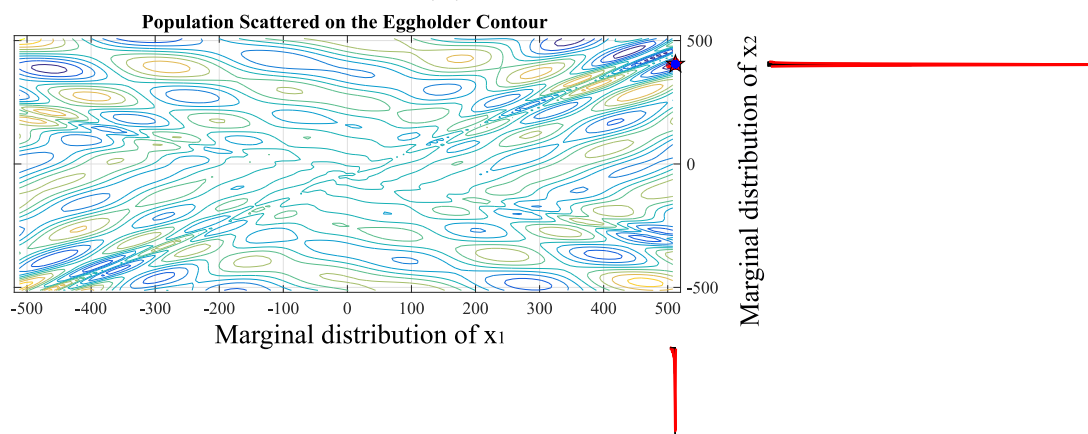
**Figure 2.11:** (continues on next page) CE optimization process demonstrated on the 2D Eggholder function. The global best solution is located at  $x_1 = 512$ ,  $x_2 = 404.2319$  (red pentagram).



(c) Third iteration



(d) Fourth iteration



(e) Fifth iteration

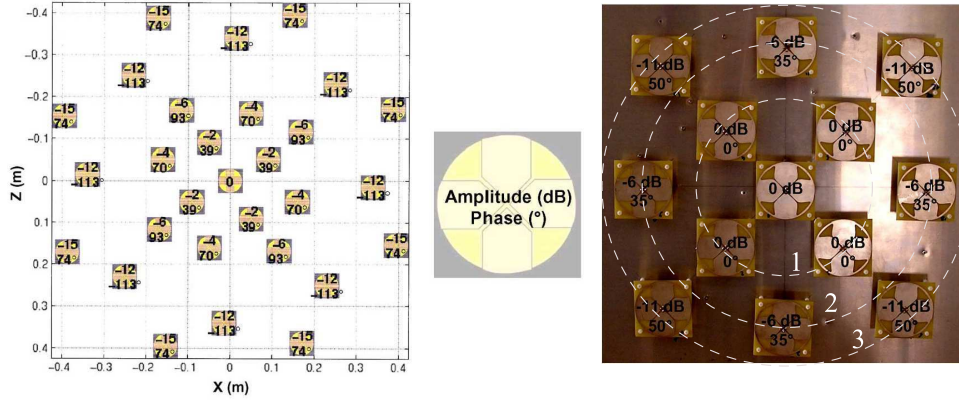
**Figure 2.11:** (cont.) CE optimization process demonstrated on the 2D Eggholder function. Five iterations were required for the algorithm to converge to the global best solution located at  $x_1 = 512$ ,  $x_2 = 404.2319$  (red pentagram).

### 2.3.2 Applications the CE method to EM problems

The CE method has been successfully applied to a diverse range of optimization problems, including multi-modal and multi-dimensional problems [86]. For EM applications this method is still new and has only been applied to a few problems [87–90]. The first work where CE has been used to optimize EM design problems is by Connor [7,91]. Particularly, the method has been explored in application to continuous and combinatorial problems of aperiodic and phased antenna array synthesis. Both single objective and multi-objective problems were considered, and the conclusion was reached that the CE method is a competitive alternative to such popular techniques as PSO or GA. Other EM applications of the CE method include antenna selection for multiple-input multiple-output systems [92], superconductive magnetic energy storage optimization benchmark [54] and radiation pattern null steering in phased arrays [93].

A more recent application of the CE method to a continuous constrained EM problem has been reported in [89]. To the best of author’s knowledge, it is the only previous application of the CE method that resulted in a built antenna prototype. The work addresses the design problem of a sparse planar array for radar cross section measurement under various constraints. The array shown in Fig. 2.12 (left) is composed of identical bipolar antennas made of two folded dipoles. A single element of the array is shown in the middle of Fig. 2.12. The optimization problem is an array of 29 elements spaced on 5 circles with the the radius and angle as the design parameters. The optimization goals were to produce a “quiet zone” where the variation of the amplitude of the EM field is less than 0.2 dB and to reduce the coupling between the array and a scatterer. To optimize the described problem with 10 design variables, a population size was set to 500, and the algorithm converged after 38 iterations. The fabricated optimized antenna array prototype with reduced number of elements (for simplicity) is shown in Fig. 2.12 (right). It can be seen that in addition to the central element, 12 array elements are placed on 3 circles, 4 antennas on each circle, resulting in non-uniformly spaced array. The optimization produced results that satisfy the design requirements. After comparison to other evolutionary paradigms, it was concluded that CE features the advantages of a

straightforward application and relatively fast convergence.



**Figure 2.12:** The optimized planar sparse antenna array, a single element and the prototype of simplified antenna array [89].

The **advantages** of the CE method include:

- Global search method;
- Inherently flexible for any types of variables;
- Fast convergence properties [94];
- No derivative information is required;
- Population-based method, so that the evaluation of the designs can be arranged in a parallel way using high-performance computers (as opposed to SA).

The known **limitations** of the CE method are:

- Large number of samples is required for an accurate estimation of distribution;
- In case the sample size is not large enough, the algorithm can be trapped in a local optimum.

In this thesis, all considered design problems are evaluated using EM software in order to obtain more accurate results. Moreover, in contrast to the previously reported applications, which only utilize the normal distribution for the CE method, this thesis makes use of PDFs that model the design space such as beta, Dirichlet and discrete

probability distribution families. Thus, the flexibility and broader potential of the CE method is exploited and demonstrated.

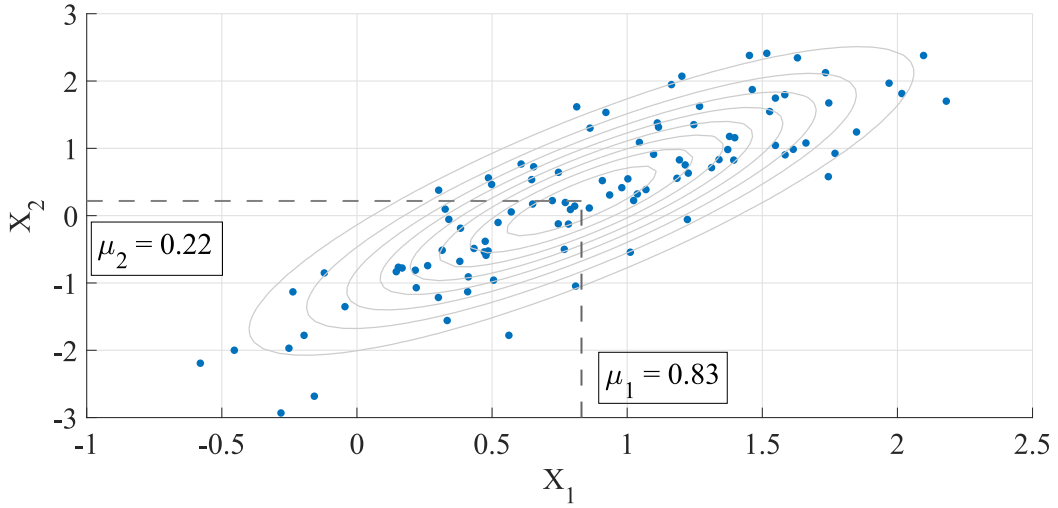
## 2.4 Covariance Matrix Adaptation Evolutionary Strategy (CMA-ES): Theory and Applications

The covariance matrix adaptation evolutionary strategy (CMA-ES) is a very popular and successful evolutionary algorithm for continuous optimization introduced by Hansen and Ostermeier in 2001 [95]. It was introduced to EM community in 2011 [96] as an attractive alternative to GA and PSO because of the minimal number of required user-defined algorithm parameters. The search in CMA-ES is performed by evolving a normal distribution that approximates the contours of the objective function. It differs from other *model-based* optimization methods in the way it moves and reshapes the sampling distributions. As its name suggests, CMA-ES makes use of a full covariance matrix and not only a variance vector.

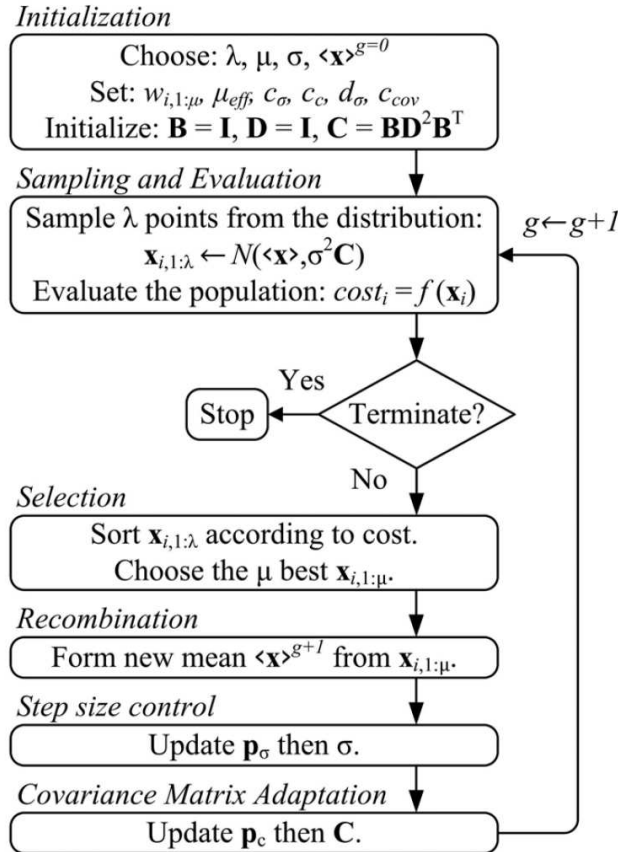
### 2.4.1 CMA-ES Algorithm

Optimization problems usually have multiple design variables, and therefore a multi-dimensional design space. CMA-ES employs general multivariate normal distributions, i.e. it models the design variables as normally distributed and correlated with each other. For the convenience of illustration, the contours of a two-dimensional (bivariate) PDF along with a random sample of 100 candidates is shown in Fig. 2.13. It can be seen that the shape of the bivariate normal distribution is ellipsoid. For higher dimensions, the distribution takes the form of a hyper-ellipse. Therefore, the algorithm has the potential to adjust to the terrain of the optimization problem.

The flowchart of the CMA-ES is shown in Fig. 2.14. The algorithm is initialized by setting a population size  $\lambda$  and a number of selected children  $\mu = \lambda/2$ , which can also be called an elite subpopulation. The parameters of the initial normal distribution, that is the mean  $\langle \mathbf{x} \rangle^{g=0}$ , step-size  $\sigma^{g=0}$  and covariance matrix  $C^{g=0}$ , where  $g$  is an iteration



**Figure 2.13:** Bivariate normal distribution (contours) and a sample of 100 points from this distribution (blue dots). Mean and variance for each marginal normal distribution are given in a textbox.



**Figure 2.14:** Flowchart of CMA-ES [96].

count, are set automatically to the recommended values. Then, the designs are sampled from this distribution, evaluated and sorted according to their performance. These steps are common for CE and CMA-ES. If the termination criterion is not satisfied, the best  $\mu^{g=0}$  designs are then chosen for the creation of a new mean using a weighted average method (Table 2.2).

To iteratively update the step-size and the covariance matrix, two parameters are calculated, i.e., the conjugate evolution path  $\mathbf{p}_\sigma$  and evolution path  $\mathbf{p}_C$ :

$$\mathbf{p}_\sigma^{g+1} = (1 - c_\sigma) \cdot \mathbf{p}_\sigma^g + \sqrt{c_\sigma(2 - c_\sigma)} \cdot \frac{\sqrt{\mu_{eff}}}{\sigma^g} (C^g)^{-1/2} (\langle \mathbf{x} \rangle^{g+1} - \langle \mathbf{x} \rangle^g) \quad (2.8)$$

$$\mathbf{p}_C^{g+1} = (1 - c_c) \cdot \mathbf{p}_C^g + \sqrt{c_c(2 - c_c)} \cdot \frac{\sqrt{\mu_{eff}}}{\sigma^g} (C^g)^{-1/2} (\langle \mathbf{x} \rangle^{g+1} - \langle \mathbf{x} \rangle^g) \quad (2.9)$$

The coefficients used in the equations (2.8) and (2.9) are collected in Table 2.2. Finally, the step-size and covariance matrix can be updated by:

$$\sigma^{g+1} = \sigma^g \cdot \exp \left( \frac{c_\sigma}{d_\sigma} \left( \frac{\|\mathbf{p}_\sigma^{g+1}\|}{\sqrt{N} \left(1 - \frac{1}{4N} + \frac{1}{21N^2}\right)} - 1 \right) \right) \quad (2.10)$$

$$\begin{aligned} C^{g+1} = & (1 - c_{cov}) \cdot C^g + \frac{c_{cov}}{\mu_{eff}} \mathbf{p}_C^{g+1} (\mathbf{p}_C^{g+1})^T + \\ & + \left( 1 - \frac{1}{\mu_{eff}} \right) \frac{c_{cov}}{(\sigma^g)^2} \sum_{i=1}^{\mu} w_i (\mathbf{x}_i^{g+1} - \langle \mathbf{x} \rangle^g) (\mathbf{x}_i^{g+1} - \langle \mathbf{x} \rangle^g)^T \end{aligned} \quad (2.11)$$

These parameters take into account the learning rates  $c_\sigma$ ,  $c_{cov}$  (also in Table 2.2) and keep the history of the evolution for the distributional parameters at the previous iterations. A population size depends on the problem dimensionality  $N$ , and the recommended minimum value for it is:

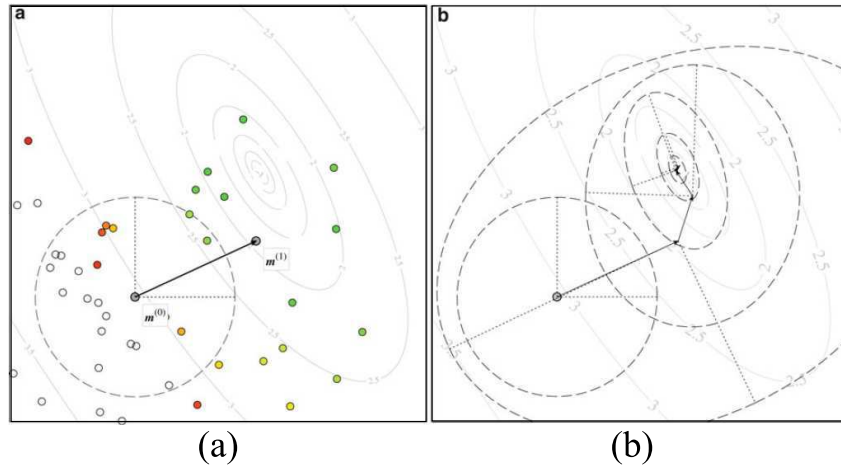
$$\lambda = 4 + [3 \ln(N)]. \quad (2.12)$$

An illustration of CMA-ES procedure is shown in Fig. 2.15. The assignment of different weights to the candidates depending on their performance is colour-coded, and the solutions that are the closest to the global optimum are coloured in green. Fig. 2.15(b) shows the evolved contours of the sampling distributions over iterations. CMA-ES is attractive for EM optimization problems due to its adaptive properties that make the

**Table 2.2:** Additional coefficients used in the CMA-ES algorithm.

Parameter	Equation
Mean	$\langle \mathbf{x} \rangle^{g+1} = \sum_{i=1}^{\mu} w_i \mathbf{x}_i^g$
Recombination weight	$w_i = \frac{\log_2(\mu+0.5) - \log_2(i))}{\sum_{j=1}^{\mu} (\log_2(\mu+0.5) - \log_2(j))}, i = 1, 2, \dots, \mu$
Effective number of children	$\mu_{eff} = \left( \sum_{i=1}^{\mu} w_i^2 \right)^{-1}$
Step-size learning rate	$c_{\sigma} = \frac{\mu_{eff} + 2}{N + \mu_{eff} + 3}$
Step-size damping factor	$d_{\sigma} = 1 + 2 \max \left( 0, \sqrt{\frac{\mu_{eff} - 1}{N + 1}} - 1 \right) + c_{\sigma}$
Covariance learning rate	$c_c = \frac{4}{N + 4}$
Covariance damping factor	$c_{cov} = \frac{1}{\mu_{eff}} \frac{2}{(N + \sqrt{2})^2} + \left( 1 - \frac{1}{\mu_{eff}} \right) \min \left( 1, \frac{2\mu_{eff} - 1}{(N + 2)^2 + \mu_{eff}} \right)$

algorithm almost user-independent. Although the tuning of some internal parameters of the algorithm can be performed by a user to manipulate the behaviour of the algorithm, the preference is to minimize the interaction between the user and the algorithm. Also, it will be shown later that CMA-ES demonstrates fast convergence properties.



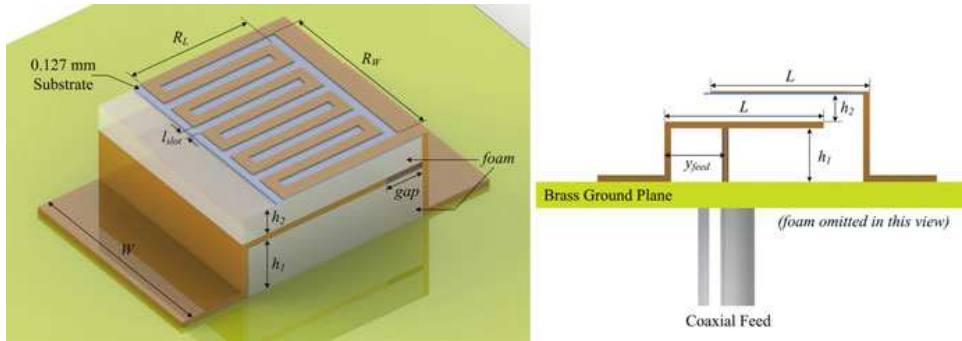
**Figure 2.15:** Illustration of CMA-ES (a) selection process with the generation of a new mean and (b) movement and reshaping of the search distribution over several iterations on a 2D Rotated Hyperellipse test function [97].



### 2.4.2 Applications of CMA-ES to EM problems

Although CMA-ES is a relatively new paradigm for the EM community, it has been proven to have robust and efficient performance. The range of its applications is quite broad, including microstrip antennas [98], slot antennas, Yagi-Uda antennas [48], ultra wideband (UWB) and non-uniform antenna arrays [99], dielectric resonator antennas [100] and EBG structures [41].

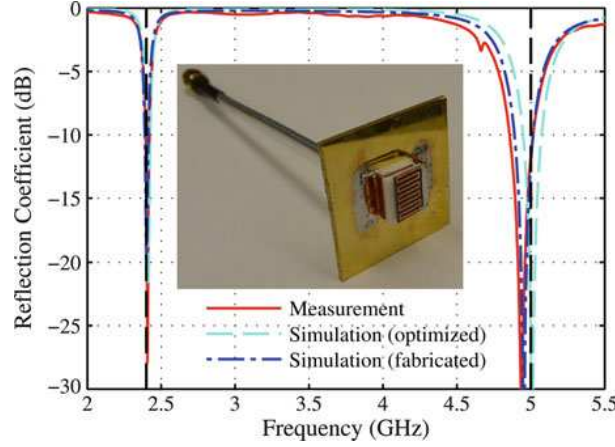
An interesting antenna optimization problem has been described in [97]. The antenna geometry is shown in Fig. 2.16. It is a modified folded patch antenna with a meandered slot and a short. The requirements for the antenna is to provide a miniaturised solution operating at two Wi-Fi frequencies, 2.4 and 5.0 GHz. The optimization problem has 9 design variables  $\mathbf{x} = (L, W, gap, R_L, R_W, h_1, h_2, l_{slot}, y_{feed})$  with defined bounds. The goal of the optimization is to achieve less than  $-12$  dB reflection coefficient and more than 6 dBi broadside gain at the two specified frequencies.



**Figure 2.16:** Parameterized geometry of a folded shorted patch antenna with a meandered slot: side view (*left*) and top view (*right*) [97].

A population size was set to 16, which is a little larger than recommended by Eq. (2.12), and converged after 24 iterations. The targeted reflection coefficient was achieved at both frequencies, and the broadside gain was 2.9 and 5.9 dBi at 2.4 and 5.0 GHz, respectively. Due to the physical limitations, the value of 6 dBi gain at 2.4 GHz in such a compact footprint is probably not attainable. During optimization, the performance of each candidate was evaluated using Ansoft HFSS. The fabricated antenna and its measured and simulated characteristics are shown in Fig. 2.17. It can be seen that the optimized results

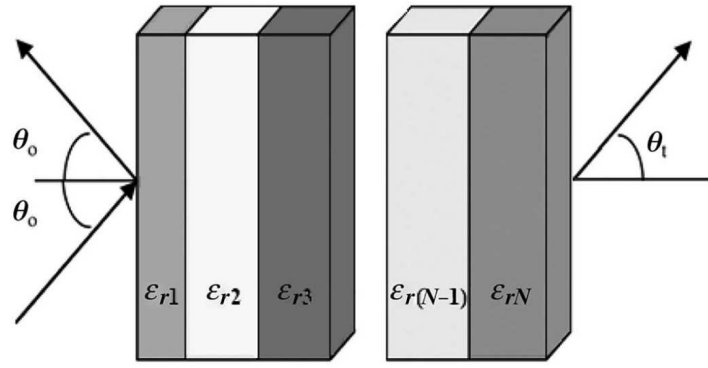
satisfy the design requirements. Such a complex antenna design with multiple design parameters and strong mutual coupling effects would be impractical to design using the traditional manual approach. Optimization in this case helped to obtain the solution within the practical time frames.



**Figure 2.17:** Simulated and measured reflection coefficient of the optimized antenna design. Vertical dashed lines indicate the targeted frequencies [97].

As CMA-ES is inherently suitable for solely continuous problems, attempts have been made to overcome this limitation. Two schemes were proposed in [48] for the optimization of the design problems with mixed-variables using a Poisson mutation (*Scheme I*) and an integer mutation (*Scheme II*). The techniques were tested on a dielectric band-pass filter problem and a novel design of a printed UWB antenna.

The geometry of a multilayer dielectric filter is given in Fig. 2.18. For optimization, a filter with seven layers ( $N = 7$ ) of permittivity  $\varepsilon_{ri}$  and thickness  $d_i$  each was considered. The optimization problem involves 14 variables, where the thickness of each layer  $d_i$  is a continuous bounded variable, and the permittivity  $\varepsilon_{ri}$  is a discrete variable sampled from a library of 14 elements. The optimization goal was to achieve band-pass performance with the reflection coefficient less than  $-15$  dB in the frequency band  $f_{pass} = 28 - 32$  GHz and greater than  $-5$  dB in the bands  $f_{stop} = 24 - 26.5$  GHz. The results of both mixed-parameter CMA-ES schemes were compared with mixed-parameter GA and mixed-parameter EP, and, after the same number of function evaluations, CMA-ES located better results with the second scheme providing the overall best performance.



**Figure 2.18:** Mixed-parameter optimization problem of multilayer dielectric filter design [48].

An UWB antenna optimization problem considered in [48] has a complex geometry with the continuous parameters describing the dimensions of the antenna and binary parameters indicating whether the segments in the patch should be filled with metal or air. The optimization goal was to obtain the reflection coefficient less than  $-10$  dB and a boresight gain above 0 dBi in the frequency band 1 – 10 GHz. Due to the long simulation time (21 min per 1 out of 20 frequency points per generation on a 3-GHz P4 PC), only CMA-ES with *Scheme II* was implemented. The algorithm converged after 60 generations producing a design with significantly enhanced performance as compared to the original design.

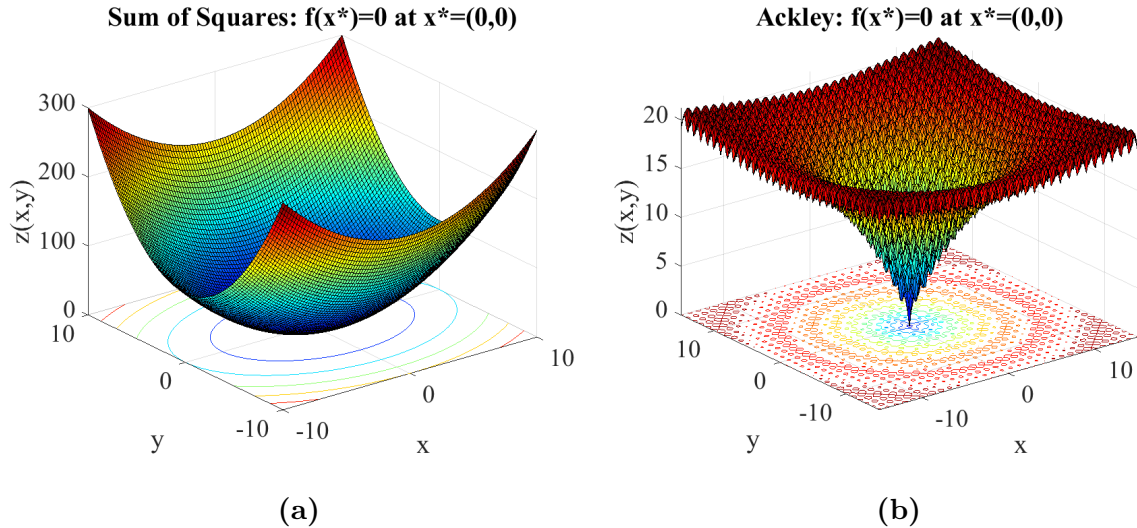
CMA-ES has definite advantages for EM applications, i.e., it is a quasi-parameter-free algorithm with a robust performance. It should be noted that, though inherently suitable for the problems with continuous variables, it requires additional modifications in order to be applicable to problems with discrete and mixed variables. Another consideration is that the elements in the covariance matrix that need to be stored increase quadratically ( $O(n^2)$ ) with the problem dimensionality. Therefore, large scale optimization problems might be challenging for CMA-ES [101].

## 2.5 Comparisons of the Algorithms

Although the NFL theorems [42, 43] state that “all optimization algorithms perform equally well when averaged over all possible problems”, it is still worth providing the comparisons of several algorithms on the same problems. The meaning of this is two-fold: first, it can serve as a test of the algorithmic implementations and, second, it can help the designer to develop intuition for the algorithms.

### 2.5.1 Benchmarks for Optimization

Benchmark problems for optimization are artificial landscapes with known locations and fitness of global optimal positions. The results of a short comparison study of PSO, CE and CMA-ES are provided further. The performance of these algorithms has been compared on two classical multidimensional test functions, unimodal Sum of Squares and multimodal Ackley function [85], in order to provide a basis for an educated decision when choosing the one for the implementation on EM problems. Both functions in their 2D versions are shown in Fig. 2.19.



**Figure 2.19:** Optimization test functions used in a comparative benchmark study:

(a) Sum of squares, (b) Ackley.

The first function has a single minimum, and the second has multiple local optima along with the global minimum in the middle. Both test functions were restricted to the

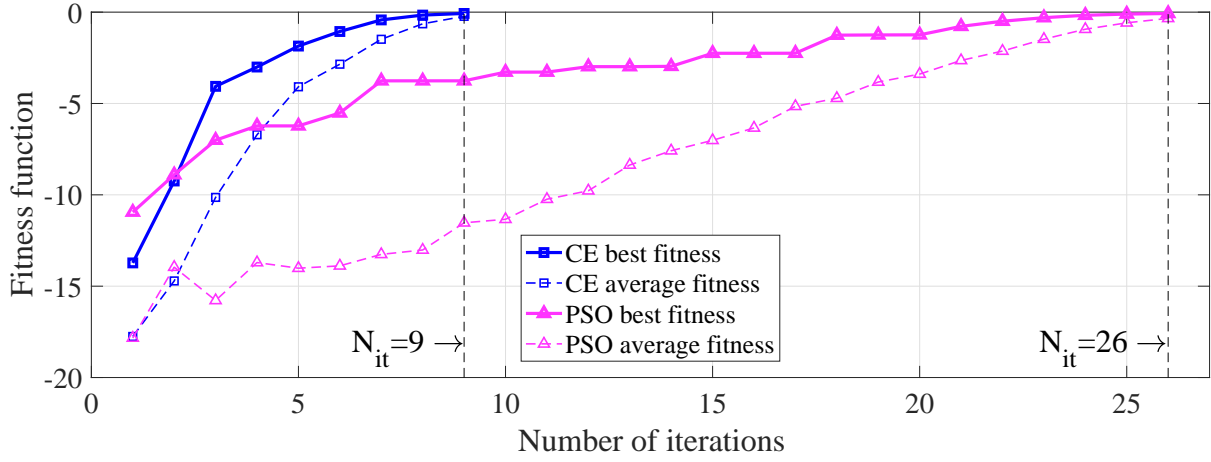
domain  $x_i = [-10, 10]$  for all  $i = 1, \dots, d$ , where  $d$  is the problem dimensionality, set to 5, 10, 15, 20 and 30. The mean number of function evaluations (MNFE) required for each algorithm to reach the fitness function values less than the threshold  $\delta = 0.01$  was calculated over 200 Monte-Carlo simulations.

The results are summarized in Table 2.3. For each problem, the internal parameters of CE and PSO were adjusted to ensure that the algorithms perform with 100% success rate. Presented PSO results were acquired with population sizes from 20 (for low-dimensional cases) to 300 (for high-dimensional cases), absorbing wall boundary condition and inertia weight [102] with  $w_{min} = 0.01$  for low-dimensional cases and  $w_{min} = 0.4$  for high-dimensional cases. The population sizes were selected using a rule of thumb for PSO which states that the minimum number of candidates should be four times the dimensionality of the problem [62]. CE results were achieved with Gaussian distribution and population sizes from 50 to 140, elite sizes from 10 to 15 and smoothing parameter  $\alpha_S$  within the recommended range of  $(0.4 - 0.7)$ .

It can be seen that CE and CMA-ES converge much faster than PSO, especially for high-dimensional and multimodal problems. A significant speed advantage can be observed in Fig. 2.20 showing the convergence curves of PSO and CE optimization of 5D

**Table 2.3:** Comparison of the mean number of function evaluations (MNFE) required for CE, PSO and CMA-ES on two test functions.

Test functions	$d$	CE	PSO	CMA-ES
Sum of Squares (Fig. 2.19 (a))	5	567	573	623
	10	1771	2325	1706
	15	3255	5155	2919
	20	4864	12413	4157
	30	7059	62340	6711
Ackley (Fig. 2.19 (b))	5	853	1384	994
	10	1908	6636	2281
	15	3090	13708	3531
	20	4628	20310	4704
	30	6512	78380	6810

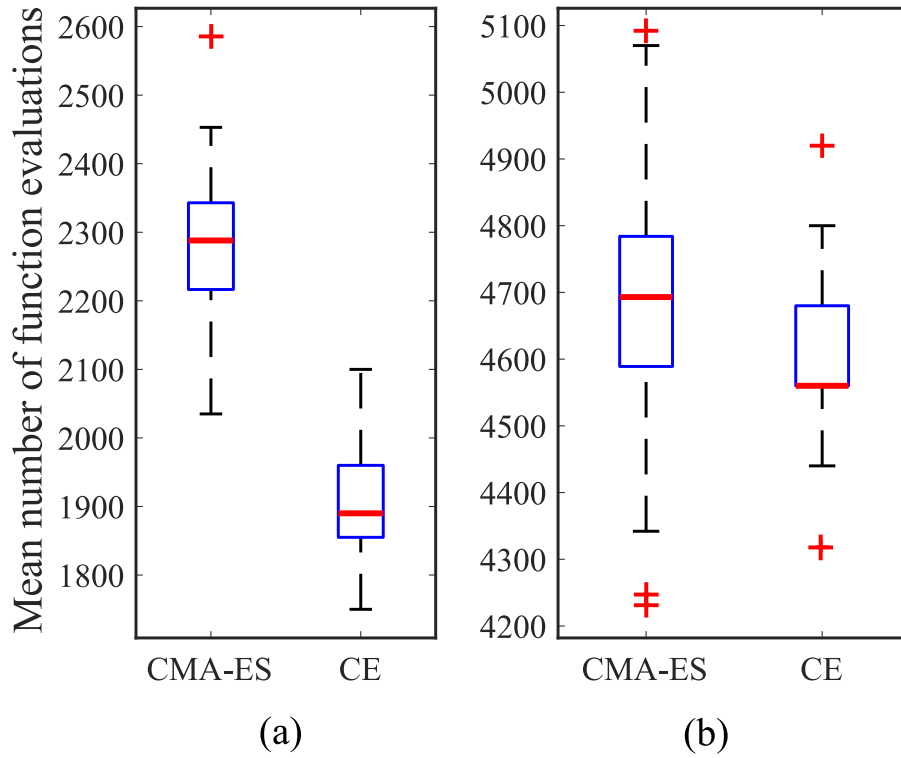


**Figure 2.20:** Convergence comparison between PSO and CE method on 5D Ackley test function.

Ackley function. In both cases, the population size  $N_{pop}=100$ , and the stopping criterion was  $-0.1$ . It can be seen that while PSO needs 26 iterations to converge, CE needs only 9, which can be a very significant time reduction in case of practical applications.

The convergence rates of CE and CMA-ES are comparable. This can be explained by the similarities in the nature of their updating rules on continuous problems, i.e. both methods manipulate the parameters of a Gaussian distribution. CMA-ES outperformed CE on the unimodal test problem, and CE outperformed CMA-ES on the multimodal function. This is expected because CMA-ES is very similar to a gradient descent local optimizer [103].

The comparison of MNFE for CE and CMA-ES on 10- and 20-dimensional Ackley functions is shown in Fig. 2.21 using a box-and-whisker plot. This graph is useful for illustrating variations in large datasets, and is used here to demonstrate that the performance of CE is steadily faster than that of CMA-ES. The results for CMA-ES in Table 2.3 agree well with those reported in [41]. This comparison study is not thorough but it demonstrates that the PSO, CE and CMA-ES algorithms, implemented in this thesis, converge to the global optimum under the provided settings. Sample code for a CE implementation on two test functions is given in Appendix B.



**Figure 2.21:** Box-and-whisker plots of MNFEs for 60 optimization runs by CMA-ES and CE on a  $d$ -dimensional Ackley function: (a)  $d = 10$ , (b)  $d = 20$ . The blue boxes are drawn around the 25th and 75th percentiles and divided (by the red thick line) at the 50th percentile. The whiskers (black dashed line) extend out to the 10th and 90th percentiles. The outliers are plotted individually using the ‘+’ symbol.

### 2.5.2 Antenna Engineering Designs

Multiple comparative studies of evolutionary optimization algorithms in application to antenna design problems have been reported [20, 104–110]. In [104], SA, GA and PSO, as well as their hybrids, have been applied to antenna far-field radiation pattern reconstruction from planar near-field data. All methods achieved accurate results, but PSO and SA excel in simplicity, accuracy, and computational cost. Self-adaptive DE and classical PSO were compared on a number of common antenna problems in [105]. Linear antenna array, E-shaped patch and microstrip filter optimization problems were chosen, and DE demonstrated a slightly better performance. A recent comparative study of PSO, DE, Taguchi, IWO and adaptive IWO on a log-periodic dipole array showed that although PSO has

fast convergence properties, IWO can find secluded locations of better performance [106].

As expected, no universal algorithm has been found for antenna applications. The preference is usually given to methods that tend to require fewer fitness function evaluations, because in EMs, fitness functions are usually evaluated through computationally expensive full-wave simulations and, thus, NFEs determine the overall optimization time. An important note was made in [108], which investigated the use of SA, ACO and GA for self-structuring antennas. The authors refrained from selecting the best performing algorithm and instead noted that “performance of the various algorithms depends on the configuration of the antenna model and the fitness objectives used, as well as on the details of algorithm implementation”.

## 2.6 Limitations and Challenges of Evolutionary Optimization

A great variety of evolutionary optimization algorithms is available for EM design problems. No matter what method is used, there are common hurdles that might be faced during the set-up of an optimization procedure.

### 2.6.1 Objective Function

The definition of an objective function is a crucial part of any optimization process. It has more influence on the result of optimization process than the selection of an optimization algorithm. Unfortunately, there are no guidelines on how to define the right objective function, and usually it is found by trial and error. The most common performance parameters in antenna engineering are the reflection coefficient, directivity/gain, the shape of radiation patterns and axial ratio, but other requirements are of course possible. Although the formulation of an objective function greatly depends on whether the performance parameters need to be achieved in narrow, wide or multiple bands, in many cases, the least mean square difference between the current solution and the objective was found to be an effective way to evaluate the fitness [7, 97, 109].



To accommodate multiple objectives, a conventional weighted aggregation (CWA) method is usually used as it is a simple way as opposed to multiobjective versions of the applied optimization methods. In CWA, the fitness function is a sum of all objectives each multiplied by a coefficient reflecting its relative importance. This method of scaling an objective vector into a composite objective function converts the multi-objective optimization problem into a single-objective optimization problem. Some authors name it as a preference-based multi-objective optimization procedure, others refer to it as a weighted sum method. Multiobjective optimization provides a set of non-dominated solutions, a Pareto front, which might be useful to have in case of uncertain priorities. Weighted sum method gives only one outcome and is much simpler and more practical because usually only one solution is needed for a problem instead of a set of solutions. Therefore, weighted sum method is more preferred and gained more popularity in engineering applications and electromagnetic problems in particular.

Some recommendation for the choice of weights in a combined objective function can be found in [53]. First, it is important to identify if objectives take different orders of magnitude and normalize them. Then, the weights can be assigned according to each objective according to their relative importance. A disadvantage of the CWA approach is that it often requires extensive tuning of the weighting coefficients to find the most effective combination of for the set of sub-objective functions. This is especially difficult in problems where the objectives of design targets are unrelated or employ different physical units.

### 2.6.2 Design Constraints

Practical EM optimization problems have equality and inequality constraints, such as overall size limitations or physical limitations, which are desirable to include in the optimization process. Several methods exist in optimization to deal with constraints. A *direct approach* intends to find the feasible solutions enclosed by the constraints. If the solution does not satisfy one or more constraints, it is discarded and a new solution is generated. However, this method is often slow and inefficient. Another common approach

to constraint handling in EO is to apply a *penalty function* to bias the search toward a feasible solution [111]. It implies that the solution's fitness function is evaluated even if the constraints are not satisfied but receives a penalty to reduce the chance that the offspring of this solution appear in next generations [112, 113].

### 2.6.3 Computational Time

Full-wave EM simulations nowadays are used in industry and academia as a standard approach to obtain a reliable evaluation of antenna structures. Therefore, to acquire a reliable optimized design, the optimization algorithms are interfaced with full-wave EM solvers [114, 115]. Appendix A provides an interface scheme used in this thesis.

In order to minimize the simulation time, the use of “low-fidelity” surrogate-based models that can substitute time-consuming EM simulation has been investigated [16, 116]. This approach was found useful but its general-case implementation is not yet automated.

### 2.6.4 Algorithm Selection

With the variety of existing optimization methods [30–32], it is often not clear which one is the most suitable for which problem, and it becomes a challenge to select the one to be applied to the given problem. The choice of a suitable optimization method for a given problem depends on the type of the design space that this problem has. However, the characteristics of the design space are not known in advance for real-world problems, and can be explored by means of the optimization algorithms. Some useful and interesting comments about this topic are provided in [28], calling this a “chicken and egg” problem.

Another important criterion to consider when choosing an optimization algorithm is the design variables, the knowledge of the problem (local methods might work better than EO) and the availability of the optimization code. Applying several optimization methods to the same problem can give the confidence that the global optimum is found [98].

It is also important to justify the use of global optimization algorithms (the class where EAs belong to) as opposed to local ones. Local optimization methods can find a more accurate solution in a shorter time if applied to a problem with a single minimum.

The existing knowledge of the problem is essential for the choice of the optimization algorithm and for the decision whether global optimization is required or local will be sufficient. An example when preliminary analysis shows that the problem has only a single minimum can be found in [117].

## 2.7 Summary

Three state-of-the-art evolutionary optimization algorithms (PSO, CE and CMA-ES) that will be applied to EM problems have been introduced. A review of the application of these methods to antenna design problems with diverse requirements and comparative studies on common benchmarks have been provided. The significance of probability-based methods, such as CE and CMA-ES, is that they define a precise mathematical framework for deriving fast and robust learning rules. Appealing features of the CE, such as the exponential convergence rate and inherent ability to optimize mixed-variable design problems, have been identified. The next chapter presents an application of PSO to the design of an all-dielectric high-gain resonant cavity antenna.



*What we once enjoyed and deeply loved we can  
never lose, For all that we love deeply becomes  
a part of us.*

— Helen Adams Keller

## Chapter 3

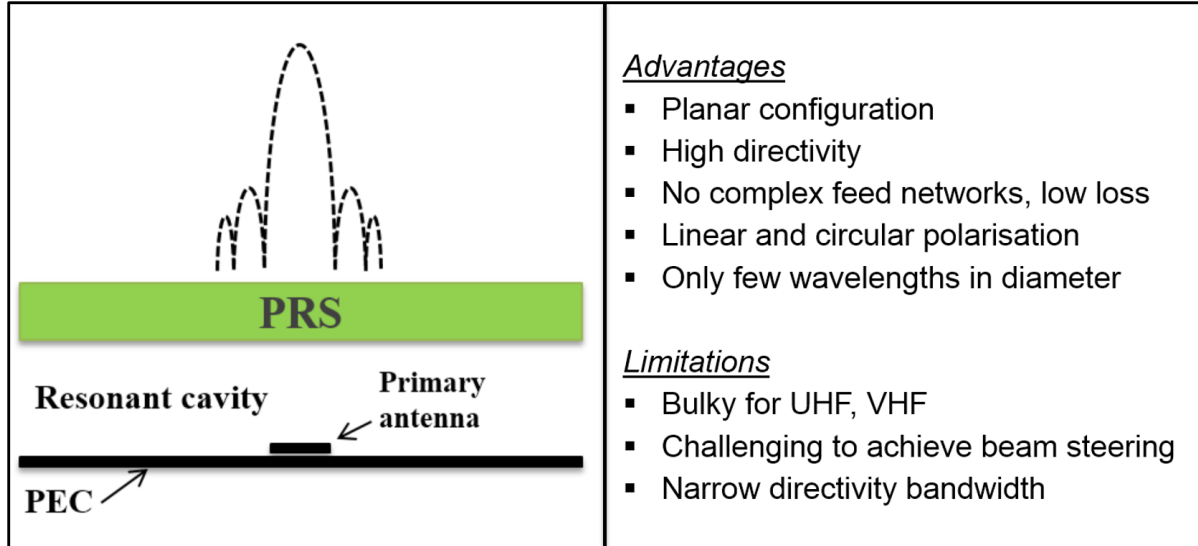
# Application of PSO to the Design of High-Gain Compact RCAs

Achieving high gain and broadband performance in a compact-size antenna is challenging but desirable in many advanced wireless applications. This chapter addresses the issue of designing compact resonant cavity antennas (RCAs) with increased boresight directivity and radiation bandwidth for high-speed communication applications. The PSO algorithm is applied in the design process to obtain the desired radiation characteristics.

### 3.1 Introduction to RCAs

Low-profile high-directivity antennas at microwave and millimeter-wave frequencies have been an ongoing research topic for decades. Applications of these antennas include high-speed wireless local area networks, satellite reception and various point-to-point radio links [118]. RCAs, also called Fabry-Perot antennas, electromagnetic bandgap (EBG) resonator antennas, partially reflective surface (PRS) antennas and leaky-wave antennas, offer an appealing solution for the aforementioned applications. Their simple planar configuration and highly directive radiation at boresight offer a more cost-effective option than antenna arrays, which require feed networks that often are expensive and heavy. Moreover, both linear and circular polarisation can be provided by RCAs [119].

The elementary geometry of an RCA is shown in Fig. 3.1. It consists of a primary low-



**Figure 3.1:** Elementary geometry of an RCA along with its advantages and limitations in comparison to other antenna types.

gain antenna, which serves the purpose of a cavity excitation, a ground plane and a PRS placed at a resonance distance from the ground. The ground plane is usually just a fully reflective metal screen, which can be considered as a perfect electric conductor (PEC). The PRS is an all-dielectric, metallic or metallo-dielectric surface with tailored reflection and transmission properties. In the first studies by Trentini [120] an open waveguide was used as a primary antenna, and metallic strips with various separations were employed as PRSs.

Afterwards, many geometries of RCAs have been devised that provide significantly improved performance compared to their predecessor. Over time, PRSs underwent the transformation from wires or strips to single-layered dense dielectric sheets, multi-layered dielectric sheets, EBG materials, FSSs and, finally, metamaterials [121]. Gain enhancement techniques by single-layer and multi-layer quarter-wavelength dielectric slabs were described in [122–124]. In [125,126], the PRS was composed of periodically disposed cylindrical dielectric rods of high permittivity, and the measured antenna has 19 dB gain with 3% bandwidth. In earlier RCAs, resonant cavities with high Q-factors were used, which resulted in narrow directivity bandwidths on the order of 0.1–3.0% [24, 127]. Over the last decade, research efforts have been focused on methods of achieving high directivity

in a wide radiation bandwidth, and several techniques have been proposed [128–130].

The performance of one-, two- and three-layer printed PRSs was studied in [118, 131–133], and a directivity of 20 dBi with 15% fractional bandwidth was achieved. However, the high directivity of the three-layer PRS comes at a cost of high antenna profile. The RCA with a decreased profile presented in [134] has a peak directivity of 19.52 dBi and a fractional 3-dB bandwidth of 8%. The bandwidth was increased through the use of a tapered printed surface as a PRS, and the height of the resonant cavity was reduced by using an artificial magnetic conductor surface as a ground. The design in [129] further increased the radiation bandwidth by using a complementary printed PRS, resulting in a fractional 3-dB gain bandwidth of 28% with a peak gain of 13.8 dBi. Later, the authors presented a design with two layers of dielectric slabs that has a fractional 3-dB gain bandwidth of 25.8% with a peak gain of 15 dBi. A theoretical study by [135] demonstrated the bandwidth enhancement of unprinted RCAs with a directivity of 17.5 dBi and a fractional bandwidth of 18%. In [130], a three-layer dielectric RCA with 18.2 dBi directivity and 22% fractional bandwidth was presented. The outstanding feature of the antenna is that its area is only  $1.5\lambda_0 \times 1.5\lambda_0$ , which is much smaller than all previously presented RCAs. Recently, [136] introduced superstructures with transverse permittivity gradients (TPG), which provide extremely large directivity bandwidths, in the order of 50%. The antenna in [136] has a very small footprint area of  $1.54\lambda_0^2$  and a measured peak directivity of 16.4 dBi.

The latest advances in directivity-bandwidth enhancement of compact RCAs are summarised in Table 3.1. We take the ratio of gain-bandwidth product per area ( $\text{dB}\cdot\%/ \lambda_0^2$ ) as a figure of merit for the comparison. It can be seen that [136] and [139] outperform the previous solutions due to the large 3-dB gain bandwidths that were achieved.

## 3.2 Methods of Analysis

To predict the radiation performance of RCAs, four main analytical models have been proposed. Based on different approximations, they have been used throughout the history

**Table 3.1:** Recent advances in gain-bandwidth enhancement of compact RCAs.

Year of publication	Ref.	Peak Gain (dB)	3-dB BW (%)	Side length ( $\lambda_0$ )	Area ( $\lambda_0^2$ )	GBP/Area (dB·%/ $\lambda_0^2$ )
2006	[137]	19.1	7	2.9	8.4	15.9
2010	[138]	18.7	15.4	2.2	4.84	59.5
2013	[135]	16.9	19.3	2.6	6.76	48.25
2014	[129]	13.8	28	2.4	5.8	66.6
2014	[130]	18.2	22	1.5	2.25	177.9
2016	[139]	17.15	51	1.62	2.06	424.6
2016	[136]	16.4	53	1.5	1.76	493.9

of RCAs' development, partially due to the absence of accurate numerical methods and required computing power, and also for simplicity and time reduction of the analysis. They are important for an understanding of the physical effects causing the high-directivity properties of RCAs. Each model will be briefly discussed below.

### 3.2.1 Ray-Tracing Model

The first model applied for the analysis of RCAs resembles a Fabry-Perot cavity, shown in Fig. 3.2, where two highly reflecting surfaces are replaced by a PRS and a perfectly reflecting ground plane. The source is placed inside the cavity instead of outside [140]. While the reflection characteristics of the ground plane are independent of frequency, i.e.,  $\Gamma_{PEC} = 1, \phi_{PEC} = -\pi$ , for the PRS they depend on frequency. The cavity can be excited by a small antenna such as a dipole, patch or open waveguide. The waves from the primary radiator bounce in the created cavity, travelling outwards from the centre and accumulating phase delays  $\mathbf{d}$ . The transmitted power can be calculated by the interference of the waves partially transmitted through the PRS, and the power pattern can be represented by an analytical equation [118]:

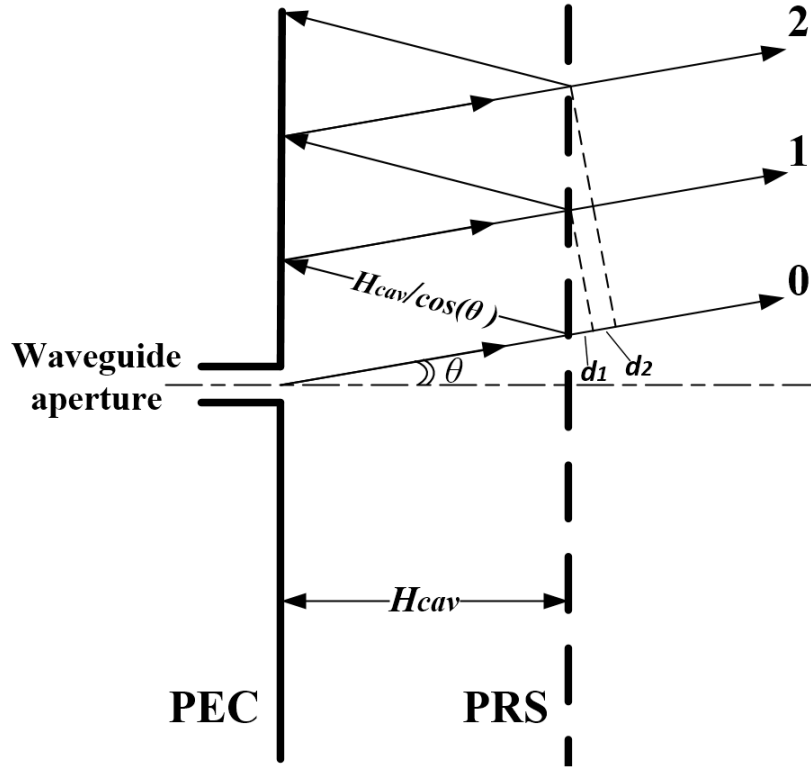
$$P(\theta) = \frac{[1 - R(\theta)^2]}{1 + R(\theta)^2 - 2R(\theta) \cos[\phi(\theta) - \pi - \frac{4\pi H_{cav}}{\lambda_0}]} F(\theta)^2, \quad (3.1)$$



where  $R(\theta)e^{j\phi_{PRS}(\theta)}$  the complex reflection coefficient of the PRS as a function of  $\theta$ ,  $\lambda_0$  is the free-space wavelength, and  $F(\theta)$  is the radiation pattern of the primary antenna. The maximum power condition at boresight is then

$$\phi_{PRS} + \phi_{PEC} - \frac{4\pi H_{cav}}{\lambda_0} = 2N\pi, \quad (3.2)$$

where  $\phi_{PEC}$  and  $\phi_{PRS}$  are the reflection phases of the ground plane and the PRS, respectively, and  $N$  is an integer.



**Figure 3.2:** A simple ray-tracing model of an RCA.

Simple equations have been derived in [118] for the estimation of the gain enhancement and half-power fractional bandwidth as functions of reflectivity:

$$G_{PRS} = \frac{1 + |\Gamma_{PRS}|}{1 - |\Gamma_{PRS}|}, \quad BW = \frac{\lambda(1 - |\Gamma_{PRS}|)}{2\pi H_{cav} \sqrt{|\Gamma_{PRS}|}}. \quad (3.3)$$

It was shown in [141] that the bandwidth and Q-factor of the cavity are related by

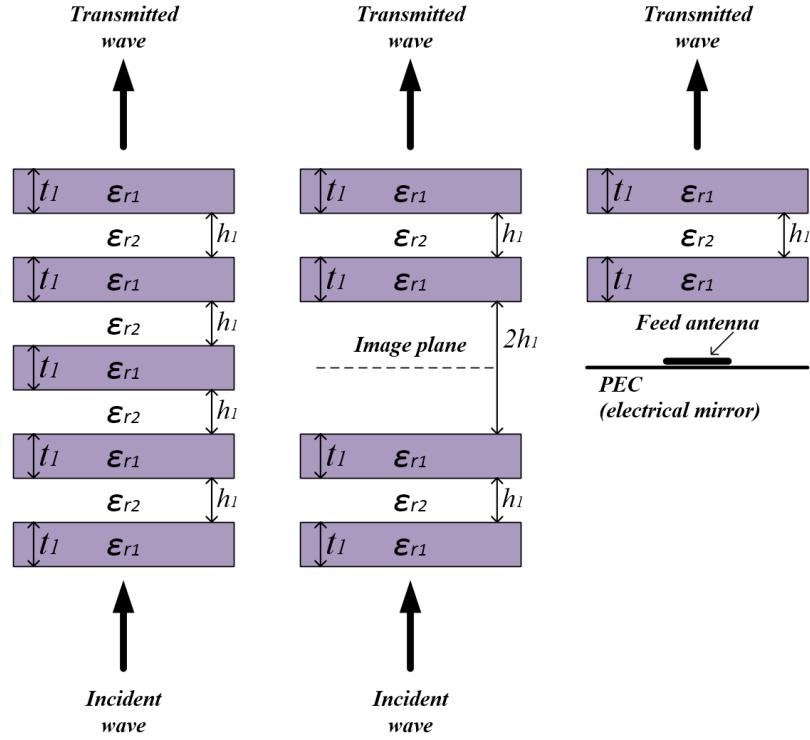
$$\Delta\theta_{3dB,min} \approx \sqrt{\frac{2}{Q}}. \quad (3.4)$$

### 3.2.2 EBG Defect Model

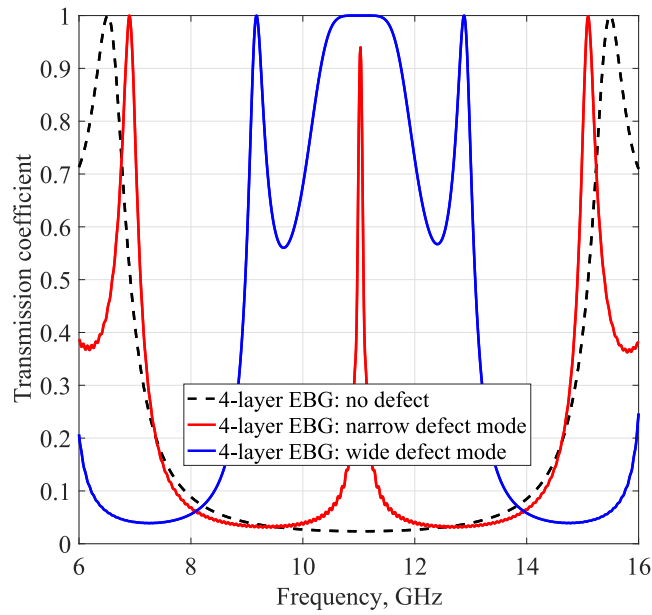
With the advent of photonic band gap structures, the phenomenon of forbidden wave propagation became a part of the state-of-the-art research in electromagnetics. Although the operational principle is the same as in photonics, these structures were named electromagnetic band gap (EBG) structures due to the different frequency of operation. The EBG defect model was derived in [125, 126] to predict the performance of RCAs with EBG structures as PRSs. By disturbing the periodicity in the EBG material lattice, a localised transmission window is introduced within a forbidden frequency band. This transmission window is characterised by a high spatial selectivity that forces the EM field to propagate in a specific direction at the defect frequency [142, 143]. This results in an increase of the effective aperture of the antenna, which is the reason for directivity enhancement in EBG RCAs.

Fig. 3.3(a) shows the transformation from a 4-layer EBG material to an RCA with a 4-layer EBG-PRS. A defect is introduced in the EBG material (two layers of  $\varepsilon_{r1}$  and two layers of  $\varepsilon_{r2}$ , where  $\varepsilon_{r2}$  is usually air) by removing a dielectric slab from the centre. Thus, if a PEC is placed at the image plane in the middle, an EBG resonator antenna can be constructed with highly directive boresight radiation at the frequency of the defect mode. The predicted transmission coefficient of the EBG structure constructed of lossless dielectric materials with  $\varepsilon_{r1}=9.2$ ,  $\varepsilon_{r2}=1$  and  $t_1 = h_1 = 0.25\lambda_g$  that create a bandgap in the frequency range 7–15 GHz is shown in Fig. 3.3(b). Also, a defect mode that is generated at 11 GHz by removing the middle slab is shown. In the same figure, a wide defect mode that is generated when  $t_1 = 0.5\lambda_g$  is provided.

The defect-mode theory is applicable to RCAs under two assumptions. First, the PRS is assumed to be infinitely large, and second, the superstrate is illuminated by a normal-incidence uniform plane wave. Numerical analysis of the EBG defect model can be realised using a waveguide-simulation method. The method predicts reflection and transmission characteristics of a unit-cell EBG structure by illuminating it by an open-ended waveguide and assigning perfect electric and perfect magnetic boundary conditions around a unit-cell [144].



(a) Transformation from a 4-layer EBG material to a 4-layer EBG resonator antenna.



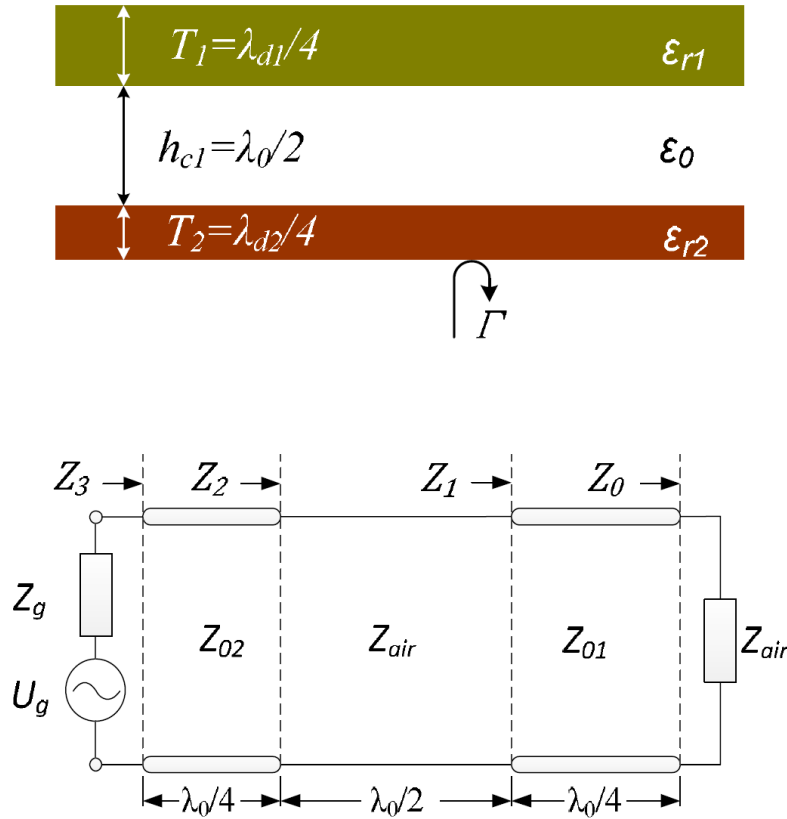
(b) Transmission coefficient of a 4-layer EBG structure. Narrow and wide defect modes can be created by manipulating the parameters of the periodic layers, such as  $\epsilon_{ri}$ ,  $h_i$  and  $t_i$ ,  $i = 1, 2$ .

**Figure 3.3:** The concept of the EBG defect model for the analysis of periodic RCAs.

### 3.2.3 Transmission-Line Model

The transmission-line model for the analysis of RCAs with both all-dielectric and metallo-dielectric superstrates has been described in [129, 145, 146]. The reflection and transmission characteristics of the PRS in Fig. 3.4 (top) can be predicted by considering an equivalent circuit that represents the layered structure as a cascade of transmission lines. Each layer can be represented by a transmission line with characteristic impedance, such as  $Z_{0i} = Z_{air}/\sqrt{\epsilon_{ri}}$ . The reflection coefficient of the EBG PRS is equivalent to that at the plane of  $Z_3$ . In case of printed superstrates, the cascades of circuit elements  $L$  and  $C$  represent metallic patches and slots in an equivalent circuit.

The transmission-line model is based on the assumption of uniform plane-wave illumination and does not take into account the diffraction effects caused by the finite superstrates.



**Figure 3.4:** A profile of a fully dielectric superstrate and its equivalent circuit [129].

### 3.2.4 Leaky-Wave Model

A highly directive boresight radiation in dielectric RCAs was shown to be attributed to the excitation of weakly attenuated leaky waves on the superstrate [123,124]. A radiated power pattern described by the equation

$$R(\theta) = \left| \frac{\cos \theta}{\sin^2 \zeta_p - \sin^2 \theta} \right|^2 \quad (3.5)$$

is predicted using scalar diffraction theory, where  $\zeta_p$  is a  $\zeta$ -plane angle. It is applicable for the H-plane because the dipole pattern at this plane is identical to that for the two-dimensional infinite line source. The radiation field can then be calculated from the amplitude distribution of the leaky-wave on the layer surface. More recent studies of the field distribution within the cavity showed the excitation of an even and odd mode in the operating frequency band of the RCA [147–149].

The aforementioned models give accurate predictions only under certain conditions. The assumptions that each of the models make put significant limitations on the parameters that can be extracted from the analysis [150]. Ray-tracing, EBG defect and the leaky-wave model assume infinite lateral dimensions of the ground plane and PRS in at least one direction. It will be shown later in this chapter that the diffraction from the edges significantly contributes to the directivity and radiation bandwidth of the compact RCAs. Moreover, none of the analytical models predict the input impedance of RCAs, which in practice must be matched to the feed network. Therefore, in order to base the optimization on accurate predictions, the full-wave numerical analysis of the complete RCA models is considered.

## 3.3 PSO Implementation Details

The principle of the PSO algorithm has been described in Chapter 2. We implemented its classic version for continuous variables [55] in order to optimize several designs of compact RCAs. Particularly, the parameters of TPG superstrates have been optimized, while the dimensions of the feed antenna and the ground plane have been kept constant.

PSO has been chosen for this optimization problem because, as shown in Chapter 2, it is an easily implemented and robust method for optimization problems with continuous variables. The pseudocode for PSO is given in Fig. 3.5. For each optimization case, the input parameters include the minimal and maximal bounds of each design parameter and the maximum number of iterations  $N_{it}$ , which must be specified when the decreasing inertia weight is used, even if another stopping criterion is defined. Depending on the dimension of a problem,  $N_{it}$  can be from 30 to 100 000, and it must be large enough to ensure proper exploration of the design space in all dimensions.

---

**Particle Swarm Optimization**


---

**Inputs:***Objective function  $f(X^*)$* *Population size  $N_{pop}$ , max number of iterations  $N_{it}$* *Inertia weight  $w^t = 0.9 - 0.4$ , acceleration constants  $c_1 = c_2 = 1.49$* **Initialization:***Generate locations  $X_i^0 \in [X_L; X_U]$ ,  $i=1 \dots N_{pop}$ ;  $X_L, X_U$  – solution space boundaries**Initial velocities  $V_i^0 \leftarrow \text{zeros}$* *Find global best value  $g^* \leftarrow \max \{f(X_1^0), \dots, f(X_{N_{pop}}^0)\}$ ;  $B^0 \leftarrow X_{i=best}^0$ ;  $P_i^0 \leftarrow X_i^0$* **Main loop****for**  $t \leftarrow 1, \dots, N_{it}$     **for**  $i \leftarrow 1, \dots, N_{pop}$         *Generate new velocities  $V_i^{t+1} = w^t V_i^t + c_1 \varepsilon_1 * [P_i^t - X_i^t] + c_2 \varepsilon_2 * [B^t - X_i^t]$ ,*         *$\varepsilon_1, \varepsilon_2$  – random vectors from  $(0, 1)$*          *$w^t = 0.4 + (N_{it} - t) * (0.9 - 0.4) / (N_{it} - 1)$*         *Generate new locations  $X_i^{t+1} = X_i^t + V_i^{t+1}$*         *Make sure particles are within the range (specify boundary conditions)*        *Evaluate objective functions at new locations*        *Find personal best for each particle  $P_i^t$*     **end for**    *Find the current global best  $B^*$* **end for***Output the final result  $B^*$ , which gives  $g^*$* 

**Figure 3.5:** Pseudocode for particle swarm optimization.

Instead of using analytical models to evaluate the fitness function of each design, an EM simulator has been used. The integration of the optimization algorithm and CST Microwave Studio (MWS) was organized as described in Appendix A. Different fitness functions were considered in order to examine the potentially attainable gain and

bandwidths of RCAs with TPG superstrates. To reduce the computation complexity, a cavity excitation by an infinitely small horizontal electric dipole (HED) was assumed, and the symmetry of the RCA was utilised.

The optimization time can be significantly reduced by using high-performance computing (HPC). It is due to the parallel nature of searching agents in population-based optimization algorithms that the fitness evaluations can be performed in parallel. Thus, ideally, the overall optimization time depends only on the number of iterations that is required for an algorithm to converge. However, for low-mesh geometries ( $< 800\,000$  hexahedrons), the job allocation and scheduling to the computing nodes in CST MWS is as time-consuming as the evaluation of one candidate and, therefore, the actual time reduction is less than expected. For low-mesh geometries, another method has been found to reduce the total optimization time by a factor of four. Instead of sending the models for a simulation separately, fitness function evaluation of the full batch of candidates can be performed by a parameter sweep (Appendix A). Table 3.2 illustrates that the total optimization time decreased by a factor of four compared to the case when each model is simulated by a separate software call. The reason for this higher computation efficiency is that the CST MWS environment is launched only once for the entire population, thus, less time is spent on intermediate processes. Simulation results are then written into a single ASCII file by a *user-defined watch* within CST MWS.

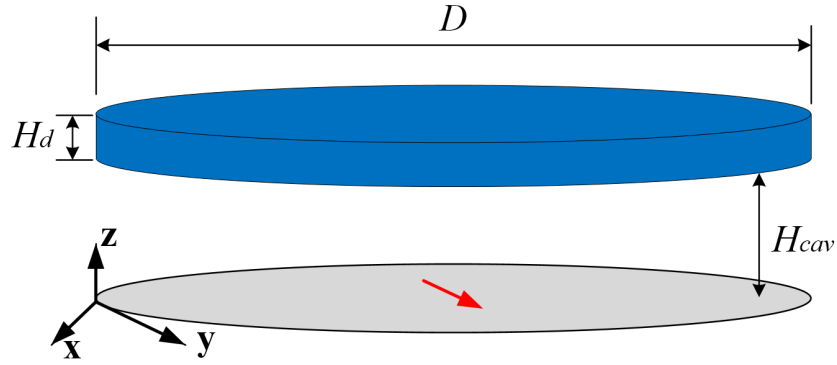
**Table 3.2:** Simulation-time reduction using parameter sweep.

	Without parameter sweep	Using parameter sweep
One model evaluation time (1 simulation)	4 min	4 min
Population evaluation time (15 simulations)	1 hour	14 min
Total optimization time (300 simulations)	20 hours	4.5 hours

## 3.4 Wideband RCAs with Dielectric Superstrates of Concentric Sections

### 3.4.1 Uniform-Superstrate Compact RCA

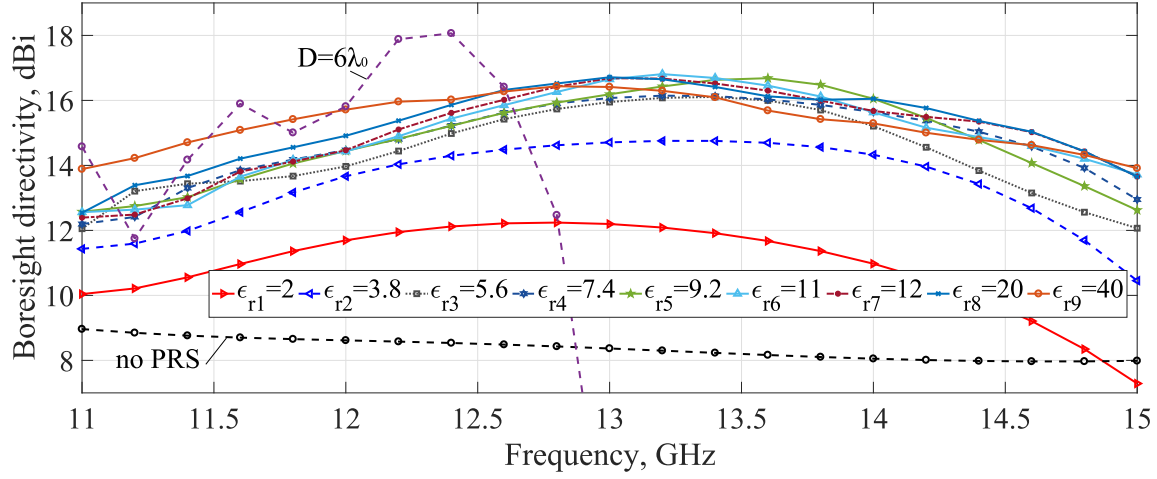
To provide a basis for the comparison of optimized designs, a classical single-layer RCA with a uniform dielectric superstrate of thickness  $t$  and diameter  $D$  is considered. A fully-reflective ground plane of the same diameter  $D$  is placed at the cavity distance  $H_{cav}$  from the superstrate. The cavity is excited by an infinitesimal HED, that is, an equivalent numerical model of a theoretical Hertzian electric dipole. The RCA model is shown in Fig. 3.6 with fixed parameters  $H_{cav} = 0.5\lambda_0 = 12$  mm,  $D = 2\lambda_0 = 48$  mm,  $t = 0.25\lambda_g = 0.25\lambda_0/\sqrt{\epsilon_r}$  at the operating frequency of  $f_0=12.5$  GHz. With increasing permittivity of the superstrate  $\epsilon_r$ , its reflectivity increases, which, as analytical models predict, increases the directivity of the RCA. It was explained in [150] that the directivity bandwidth cannot be predicted using any of the aforementioned analytic models.



**Figure 3.6:** Simplified RCA model with HED cavity excitation.

Fig. 3.7 shows the boresight directivity in the band 11–15 GHz for an RCA with a uniform quarter-wavelength dielectric slab with  $\epsilon_{ri} = \{2; 3.8; 5.6; 7.4; 9.2; 11; 12; 20; 40\}$ . For comparison, the boresight directivity of a classical RCA of  $6\lambda_0$ -diameter with  $\epsilon_r=9.2$  is also provided. Table 3.3 provides a summary of the peak directivity, half-power fractional bandwidth (3-dB bandwidth) and directivity-bandwidth product resulting from varying the superstrate permittivity. The ideal source antenna above the ground has a spherical





**Figure 3.7:** Boresight directivity of an RCA with a single-slab superstrate, dielectric constant of the the slab  $\varepsilon_{ri} = \{2; 3.8; 5.6; 7.4; 9.2; 11; 12; 20; 40\}$ ,  $i = 1, 2, \dots, 9$ .

radiation pattern with maximum directivity equal to 8.5 dBi at boresight. When a superstrate of permittivity  $2 \leq \varepsilon_r \leq 11$  is placed at a resonance distance above the source, the boresight directivity increases to 12.3 dBi for the lowest permittivity and to 17.1 dBi for the highest permittivity. For permittivity  $\varepsilon_r > 11$ , the increase in the peak directivity is almost negligible. Therefore, to reduce the cost of the designs, commercially available materials of permittivity less than 11 will be considered for optimization. The 3-dB bandwidth of this RCA varies in the range 21.5–28.5%.

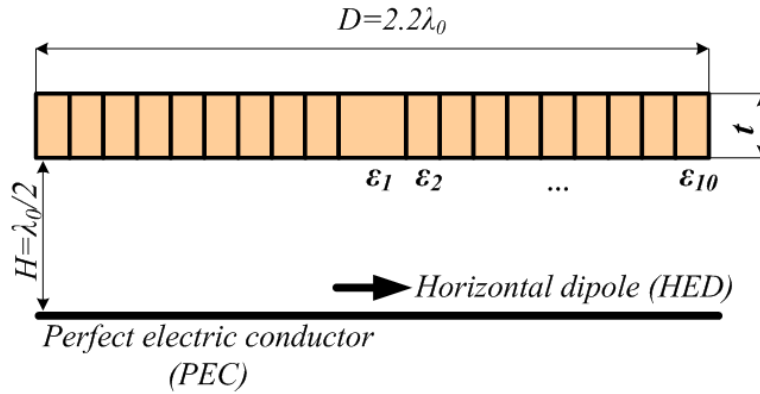
**Table 3.3:** Radiation characteristics of the RCA with a quarter-wavelength dielectric superstrate of diameter  $D = 2\lambda_0$ ,  $\lambda_0 = 24$  mm.

$\varepsilon_r$	$t$ (mm)	$f_0$ (GHz)	$Dir_{f_0}$ (dBi)	$Dir_{peak}$ (dBi)	$BW$ (GHz)	$BW$ (%)	DBP (dBi·%)
2	4.2	12.5	12.24	<b>12.3</b>	3.62	<b>28.3</b>	348.09
3.8	3.1		14.45	<b>14.8</b>	3.45	<b>25.7</b>	380.36
5.6	2.5		15.35	<b>16.2</b>	3.54	<b>26.4</b>	427.68
7.4	2.2		15.58	<b>16.2</b>	3.79	<b>28.5</b>	461.7
9.2	1.9		15.56	<b>16.9</b>	2.95	<b>21.5</b>	363.35
11	1.8		15.45	<b>17.1</b>	3.14	<b>23.6</b>	403.56
20	1.3		15.9	<b>17.1</b>	3.18	<b>24.8</b>	424.08
40	0.9		16.1	<b>16.9</b>	3.52	<b>27.0</b>	456.3

### 3.4.2 Design I: Ten-Sectional Superstrate

Very few RCAs have previously been optimized using evolutionary optimization methods [24],[151]. In [24], a superstructure based on a printed double-sided frequency-selective surface was designed using a microgenetic algorithm with the goal of achieving a high-Q resonant cavity. A result of 22.15 dBi peak gain over a narrow frequency band was achieved. In [151], a real-value coding hybrid genetic algorithm was applied to design an RCA for a mobile base station by optimizing the dimensions of square patches and loops on its double-sided superstructure. A peak gain of 13.8 dBi and a 10% 3-dB gain bandwidth was reported.

The design in [152] has a flat superstrate and offers a large directivity bandwidth. For the objective of higher peak directivity in a compact-size wideband RCA, we optimize the geometry shown in Fig. 3.8 with a dielectric single-layer superstrate consisting of ten concentric annular sections.



**Figure 3.8:** Cross-sectional view of the optimized RCA with  $D = 48 \text{ mm} = 2.2\lambda_0$ ,  $H_{cav} = 11 \text{ mm}$ ,  $\lambda_0 = 22 \text{ mm}$ .

The antenna model to be optimized consists of a PEC ground plane, a flat dielectric superstrate and an HED as a feed. The superstructure is  $2.2\lambda_0$  in diameter and consists of ten concentric dielectric sections of equal width. The design vector includes ten permittivities and the superstrate thickness:  $\mathbf{x} = (\varepsilon_{ri}, t), i = 1, 2 \dots 10$  with the boundary constraints  $\varepsilon_{ri} = [2; 11]$  for permittivities and  $t = [2; 6] \text{ mm}$  for the superstrate thickness.

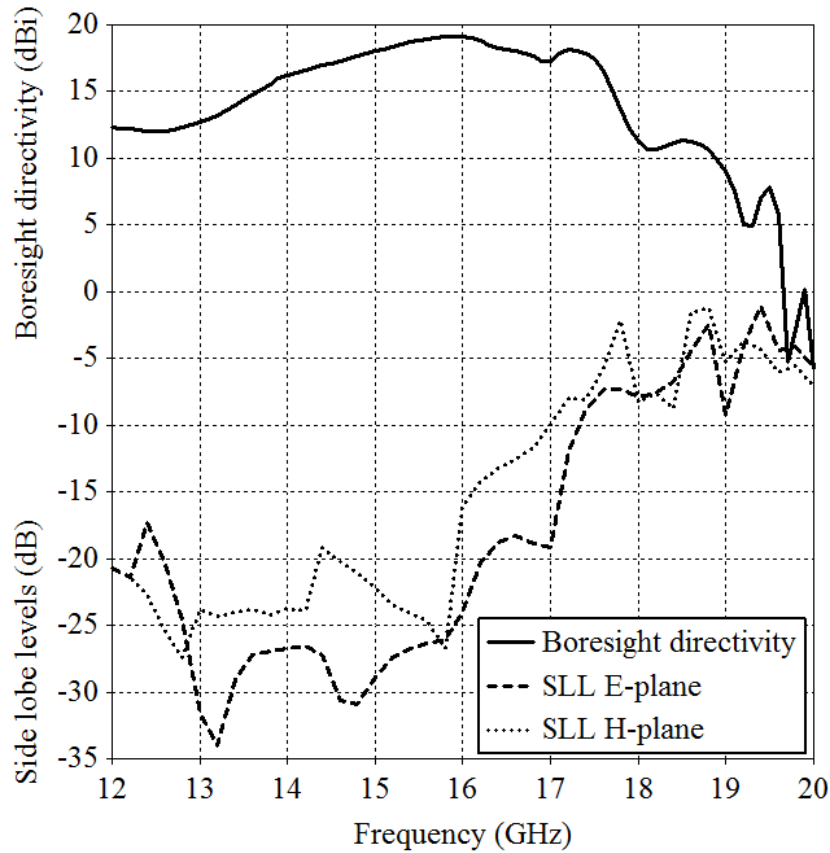
The objective function is an important figure of merit, which determines the solution

that will be reached by the algorithm. In order to achieve higher peak directivity while keeping the bandwidth reasonably large, the objective function was defined as a sum of the directivity at three particular frequencies given by

$$F.F. = \sum_{i=1}^3 Dir(f_i), \quad (3.6)$$

where  $Dir(f_i)$  is the boresight directivity at the  $i^{th}$  frequency and  $f_1 = 16$  GHz,  $f_2 = 16.8$  GHz,  $f_3 = 17.6$  GHz. This choice of frequencies in the objective function was found to be useful in extending the bandwidth.

The algorithm converged after 15 generations of 20 agents. The boresight directivity and side lobe levels (SLLs) of the optimized design are shown in Fig. 3.9. The peak directivity and 3-dB directivity bandwidth are 19.1 dBi and 24%, respectively. It is similar to the result in [130], but the superstructure is much thinner and employs only one layer. As compared to [152], the peak directivity is improved by 1.5 dBi. The SLLs remain lower than  $-20$  dB for the H-plane and  $-25$  dB for the E-plane in the frequency



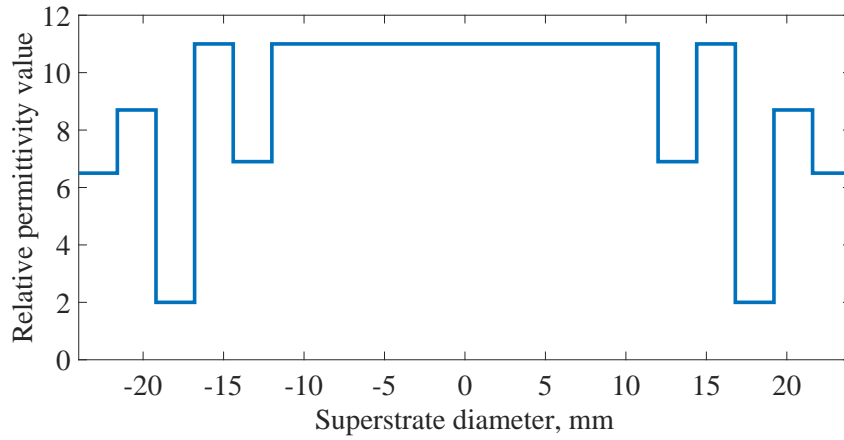
**Figure 3.9:** Boresight directivity and side lobe levels of the optimized RCA.

range from 14 to 16 GHz. However, the SLL increases to  $-7$  dB at the high edge of the operating frequency band. Although the increase in SLLs is common for many RCAs, it comes at the expense of reduced effective bandwidths.

The optimized superstrate has the parameters

$$\varepsilon_{ri} = (11, 11, 11, 11, 11, 6.9, 11, 2, 8.7, 6.5); t = 4.2 \text{ mm}. \quad (3.7)$$

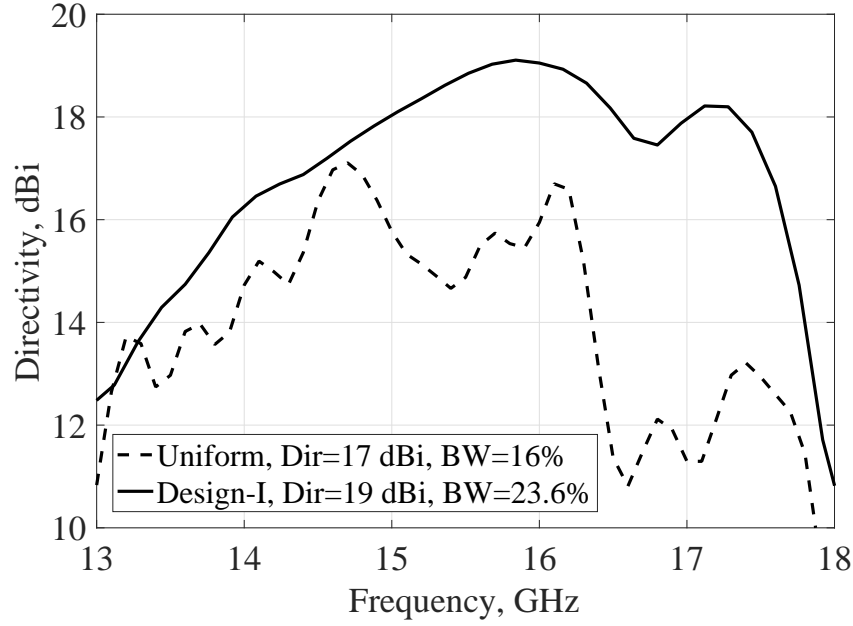
The optimized permittivity profile of the superstrate is shown in Fig. 3.10. It can be seen that the permittivity in the centre is high but decreases non-linearly towards the edges.



**Figure 3.10:** Permittivity profile of the optimized RCA with ten-sectional superstrate.

Compared to an RCA with a uniform superstrate of  $\varepsilon_r = 11, t = 4.2$  mm, which has peak directivity and 3-dB bandwidth equal to 17 dBi and 16%, respectively, the performance of the optimized RCA is superior. As shown in Fig. 3.11, the peak directivity is 19 dBi and the 3-dB bandwidth is 24%. This is higher than for the design presented in [130] in addition to the advantage of the thinner profile.

The limitation of the ideal feed used for the cavity excitation is that the impedance matching of the antenna cannot be calculated. Therefore, in the next section, a real feed antenna will be considered.



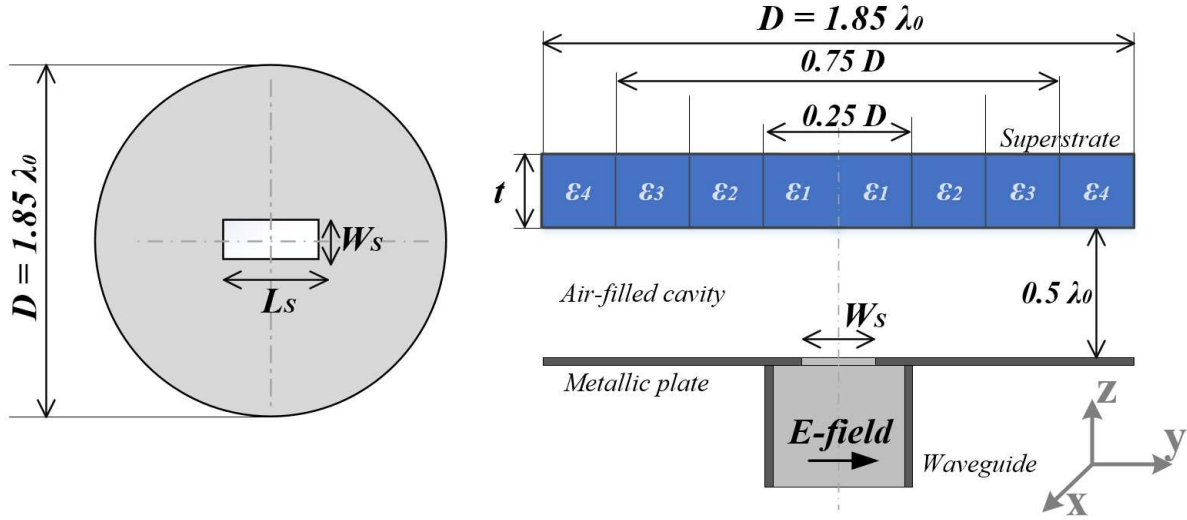
**Figure 3.11:** Bore sight directivity comparison of the optimized RCA and a non-optimized RCA with a uniform superstrate.

### 3.4.3 Design II: Four-Sectional Superstrate

In order to achieve a wider bandwidth from the compact RCA with the flat superstrate made of concentric sections, a different approach is taken in the formulation of the fitness function. A directivity-bandwidth product (DBP), calculated as the product of a peak directivity (in dBi) and half-power bandwidth (fractional bandwidth in %), is maximized. Assuming that a peak directivity appears at any frequency between 10 and 20 GHz, we evaluate the boresight directivity in this band with a 0.2 GHz frequency step and then find the values of the peak directivity and half-power bandwidth. The objective of optimization is then to maximize the following fitness function:

$$F.F. = \max \left( Dir_{dBi}(f \in [10 - 20GHz]) \right) \cdot \frac{200(f_h - f_l)}{(f_h + f_l)}, \quad (3.8)$$

where the peak directivity is multiplied by the fractional 3-dB directivity bandwidth (in %) calculated using the lowest  $f_l$  and the highest  $f_h$  frequencies of the band. The peak directivity is found from the  $Dir_{dBi}$  curve using ‘max’ operator in MATLAB.



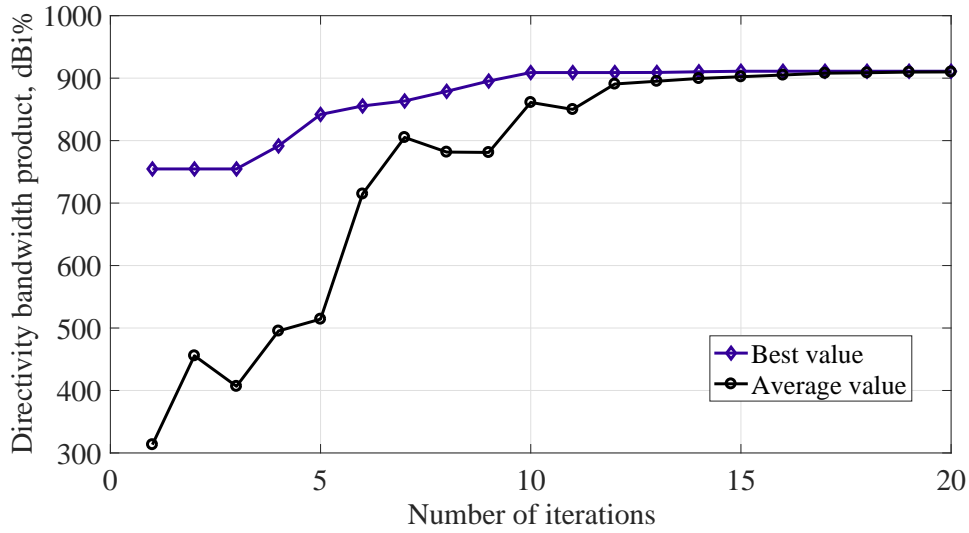
**Figure 3.12:** (a) A slot with dimensions  $(W_s, L_s)$ . (b) Cross-sectional view of the RCA with  $D = 48 \text{ mm} = 1.85\lambda_0$ ,  $t = 6.35 \text{ mm}$ ,  $H_{cav} = 13 \text{ mm}$ ,  $\lambda_0 = 26 \text{ mm}$ .

The geometry of the optimization problem is shown in Fig. 3.12. A slot with the dimensions  $(W_s, L_s) = (9, 12.5) \text{ mm}$  is cut in a ground plane and excited by a rectangular waveguide. As the slot parameters mostly affect the input impedance matching and not the boresight directivity, its dimensions are not considered in the optimization. The optimization goal is to find the optimal permittivity distribution in an all-dielectric superstrate made out of four concentric sections of equal widths with overall diameter equal to 48 mm, which is  $\approx 1.85\lambda_0$ ,  $\lambda_0 = 26 \text{ mm}$ . Therefore, the parameter vector for optimization is given by  $\mathbf{x} = (\varepsilon_1, \varepsilon_2, \varepsilon_3, \varepsilon_4)$ .

Six sequential optimization trials were performed to keep a reasonable trade-off between the statistical certainty of performance and the computational cost. For every trial, a population of 15 particles was optimized for a maximum of 20 iterations. The approximate time required per simulation on an Intel Core i7-4790 processor and 32 GB of memory was 4 minutes. Following the guideline given in Chapter 2, acceleration constants were chosen to be  $c_1 = c_2 = 1.49$ , and the inertia weight gradually decreased from 0.9 to 0.1. The evolution of the swarm for one of the optimization trials is shown in Fig. 3.13, and the results of six optimization trials in the same order as obtained by PSO

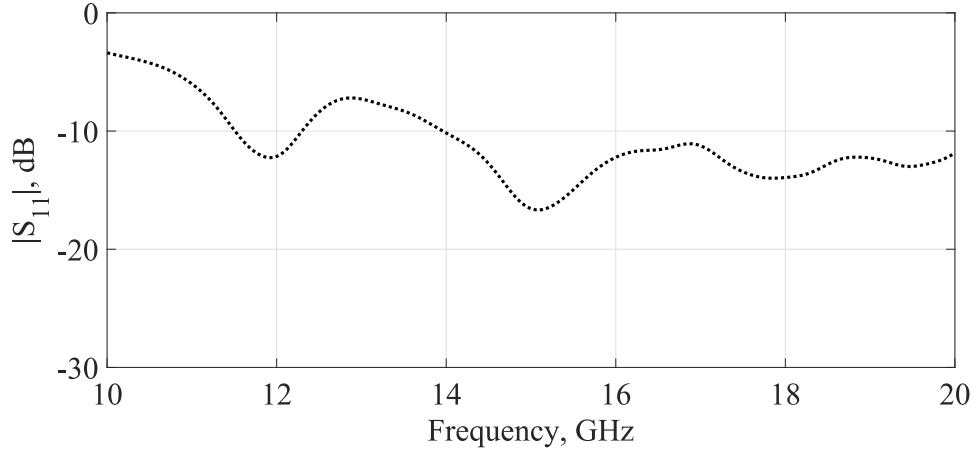
are summarized in Table 3.4 (given at the end of Section 3.4.3).

The maximum value of the objective function formulated in Eq. (3.8) is 911.87 dBi\*%. It is interesting to note that there are only two significantly distinct designs, i.e. the one with  $\text{mean}(\mathbf{x}_1)=(10, 10, 6.7, 3.32)$  and another with  $\text{mean}(\mathbf{x}_2)=(9.6, 7.14, 4.59, 2.1)$ , where  $\mathbf{x}_1$  and  $\mathbf{x}_2$  represent the average parameter vectors of two noticeable clusters of solutions. The three out of six times optimizer gave the same suboptimal result, with an average DBP of around 875 dBi\*%, which leads us to the conclusion that this is a high local maximum, where PSO was trapped. Three other times the solutions varied around  $\text{mean}(\text{DBP}) = 910$  dBi\*%.



**Figure 3.13:** Evolution of the swarm of 15 particles over 20 iterations for one of the optimization trials.

The input impedance matching, given in Fig. 3.14, shows that the reflection coefficient is less than  $-10$  dB for the majority of the frequency band of interest and rises to  $-7$  dB around the resonance frequency of the cavity, which is a common issue in the RCAs. The impedance improvement was out of the scope of this study, but can be achieved by fine-tuning  $W_S$  and  $L_S$  of the rectangular slot that feeds the cavity.

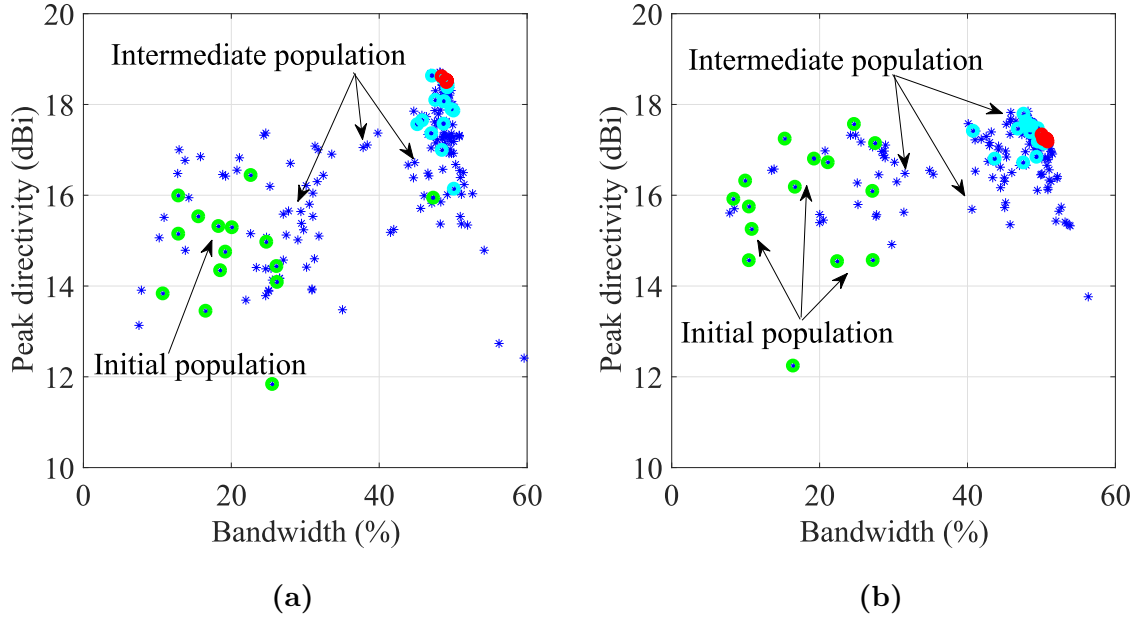


**Figure 3.14:** Input impedance matching of the four-sectional RCA (Design II).

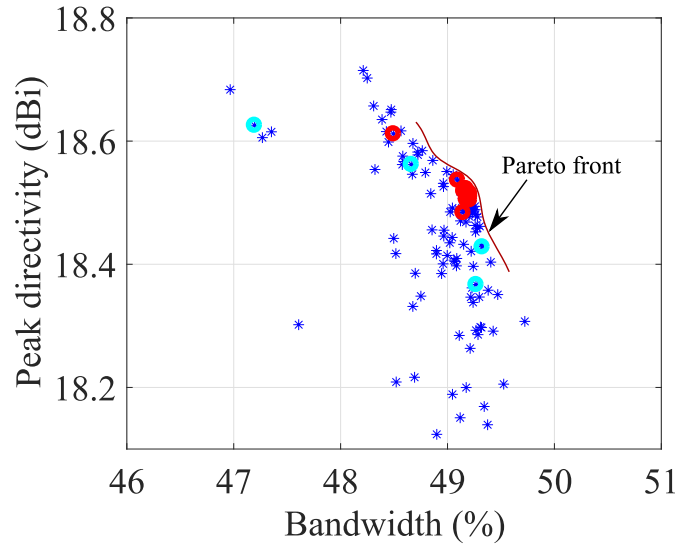
The movement of the particles in the solution space for two distinct solutions is shown in Fig. 3.15 (a) and (b), respectively. Each figure contains 300 points representing a solution  $\hat{f}(x_i^{g=j})$ , where  $i = 1...15$  is a particle number, and  $j = 0...20$  is an iteration number. As the fitness function contains two objectives, each point provides information about the peak directivity and 3-dB bandwidth. Initially, the particles were generated randomly and, therefore, their fitness is low (shown in green). However, with every next iteration, the population moved to better positions with higher fitness values. The plot emphasises the particles at  $g = 10$  (cyan) and at the final iteration  $g = 20$  (red).

Fig. 3.16 provides an enlarged view of the solutions reached at the last iteration. It can be seen that there is a trade-off between peak directivity and bandwidth which forms a Pareto front, and the solutions with the highest fitness function are concentrated on it. It can be concluded that if larger bandwidths are not required from the RCA but, instead, designs with higher peak directivity are preferable, the fitness function should be adjusted to prioritise one objective over another. One way to prioritise peak directivity over bandwidth in the calculation of DBP will be described in Chapter 4.





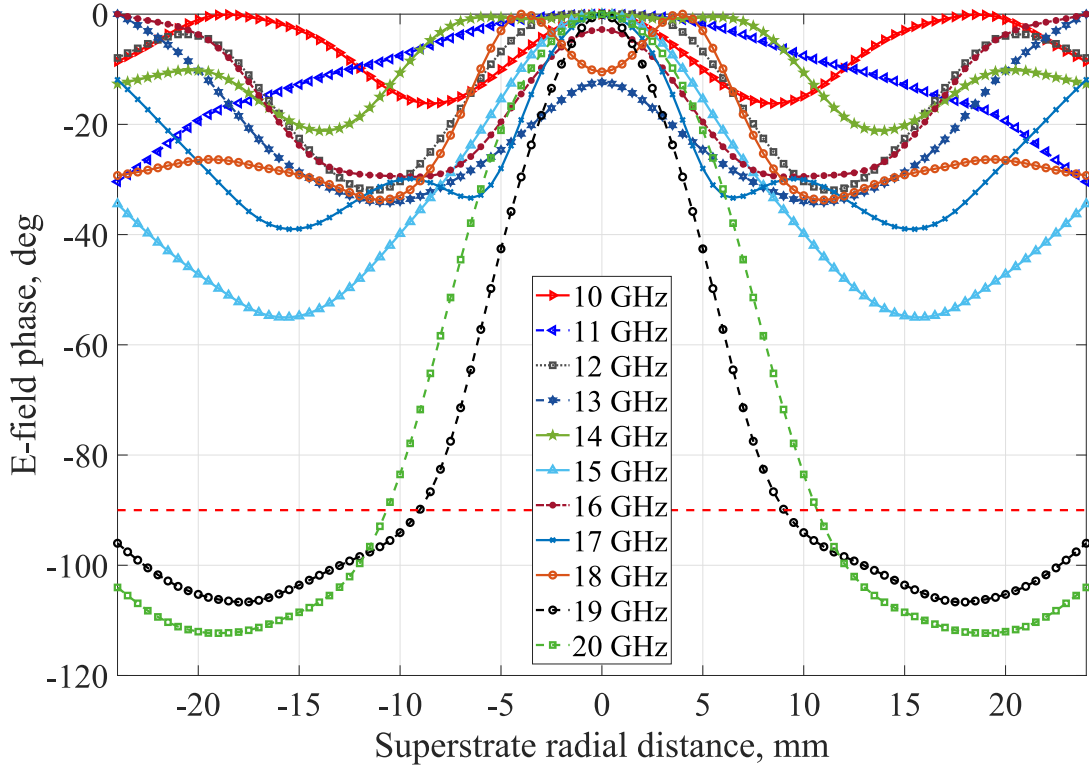
**Figure 3.15:** Illustration of two full optimization runs emphasizing  $\hat{f}(x_{pop}^{g=0})$  (green),  $\hat{f}(x_{pop}^{g=10})$  (cyan) and  $\hat{f}(x_{pop}^{g=20})$  (red).



**Figure 3.16:** Enlarged view of the trade-off between the peak directivity and 3-dB bandwidth provided by an RCA with a four-sectional all-dielectric superstrate.

The best optimized antenna design is Solution 3 with a peak directivity of 18.3 dBi and bandwidth of 49.8%. Although stochastic optimization methods never guarantee convergence to the global maximum, the repeated trials suggest that the best solution found is most probably near-optimal, and no significantly better solution can be found.

We note that for a maximum DBP of the RCA, two central sections of the superstructure should have equally high permittivities, and starting from the middle of the superstrate a permittivity gradient is required. The effect of decreasing the permittivity towards the edge of the slab is similar to what tapered printed superstructures provide, which results in improving the distribution of the E-field on the aperture while maintaining strong reflections in the middle region of the cavity. Particularly, the phase of E-field at every point above the superstrate lies between  $0$  and  $90^\circ$ , creating an effective in-phase aperture [136]. It can be seen in Fig. 3.17 that the phase difference is less than  $90^\circ$  in the area covering the entire superstrate for the frequencies 10–18 GHz, and increases slightly towards the edge of the superstrate at 19 and 20 GHz.



**Figure 3.17:** E-field phase distribution probed 3 mm above the optimized superstrate of the four-sectional RCA (Design II).

**Table 3.4:** Results of six sequential optimization trials of the design problem given in Fig. 3.12.

	<b>Solution 1</b>	<b>Solution 2</b>	<b>Solution 3</b>	<b>Solution 4</b>	<b>Solution 5</b>	<b>Solution 6</b>
$\varepsilon_1$	10.00	9.81	10.00	9.47	9.99	9.52
$\varepsilon_2$	10.00	7.17	10.00	7.14	9.27	7.12
$\varepsilon_3$	7.24	4.61	6.60	4.64	6.28	4.52
$\varepsilon_4$	3.36	2.00	3.03	2.32	3.57	2.00
<b>Peak Directivity, dBi</b>	<b>18.61</b>	<b>17.20</b>	<b>18.30</b>	<b>16.99</b>	<b>18.52</b>	<b>17.10</b>
<b>Directivity Bandwidth, %</b>	<b>48.75</b>	<b>51.00</b>	<b>49.84</b>	<b>51.71</b>	<b>49.20</b>	<b>51.14</b>
<b>DBP, dBi*%</b>	<b>907.28</b>	<b>874.58</b>	<b>911.87</b>	<b>878.77</b>	<b>911.05</b>	<b>874.40</b>

### 3.4.4 Design III: Three-Sectional Superstrate

An RCA with a three-sectional superstrate has been optimized for maximal DBP. The reduction in the number of sections as compared to the previous design problems is for fabrication simplicity. The configuration of the RCA with overall diameter  $D=48$  mm and cavity height  $H_{cav}=12$  mm is shown in Fig. 3.18. The thickness of the superstrate is fixed at  $t=10$  mm. The cavity is fed by a rectangular slot of length  $L_s=12$  mm and width  $W_s=9.525$  mm.

The classic version of PSO with decreasing inertia weight described in Section 2.2.1 has been implemented to optimize the permittivity distribution in the superstrate, i.e.  $(\varepsilon_1, \varepsilon_2, \varepsilon_3)$ , where each variable is bounded between  $\varepsilon_{min}=2$  and  $\varepsilon_{max}=11$ . As the optimization problem has only three variables, the population size is reduced to 7 particles with the stopping criterion of a maximum number of iterations equal to 30.

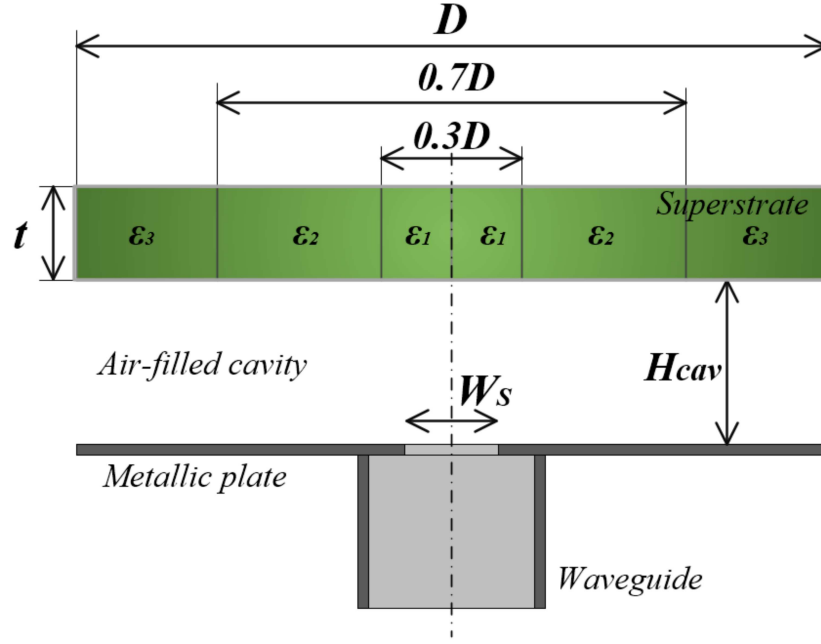
The optimization goal was to maximise the product of peak directivity (linear scale) and 3-dB directivity bandwidth (%), expressed as

$$F.F. = 10^{(Dir_{dB}/10)} \cdot BW_{\%}. \quad (3.9)$$

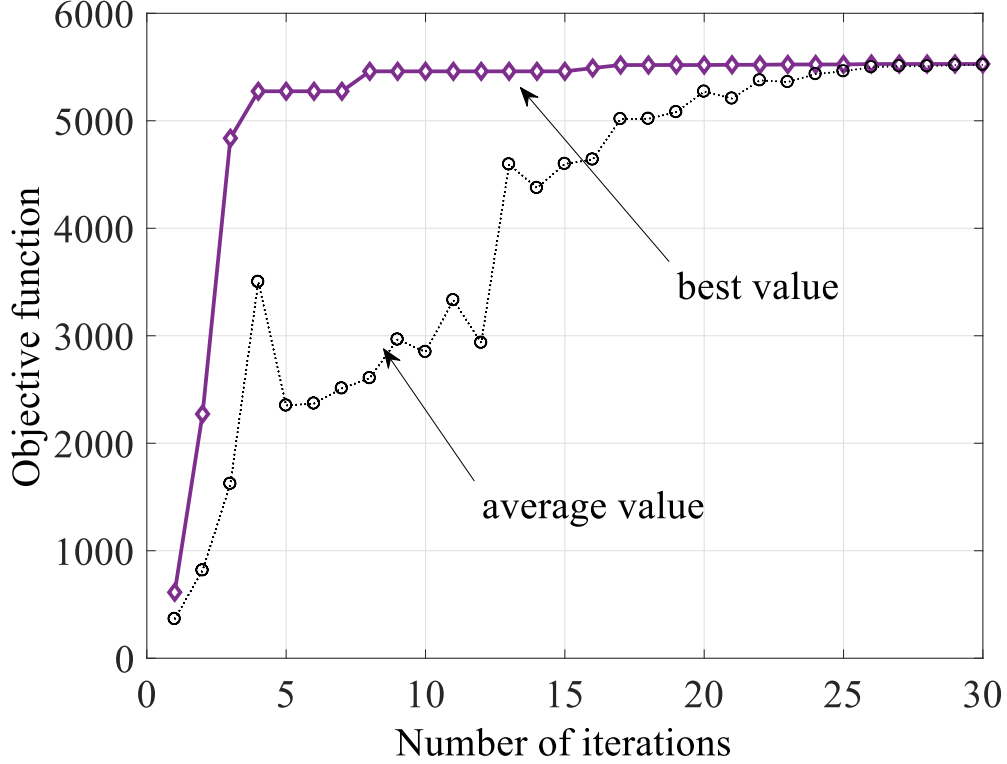
To evaluate the fitness of each design, the boresight directivity was calculated in the frequency band 12–26 GHz with a 0.1 GHz step. The approximate time required to complete a full optimization run is 9 hours on an Intel Core i7, 3.6 GHz processor with 32 GB of RAM. From the convergence curve shown in Fig. 3.19, it can be seen that the optimal design was found at the 17th iteration. The optimal design vector consists of the following permittivity values:

$$\mathbf{x}^* = (\varepsilon_1, \varepsilon_2, \varepsilon_3) = (7.26, 5.2, 3.16).$$

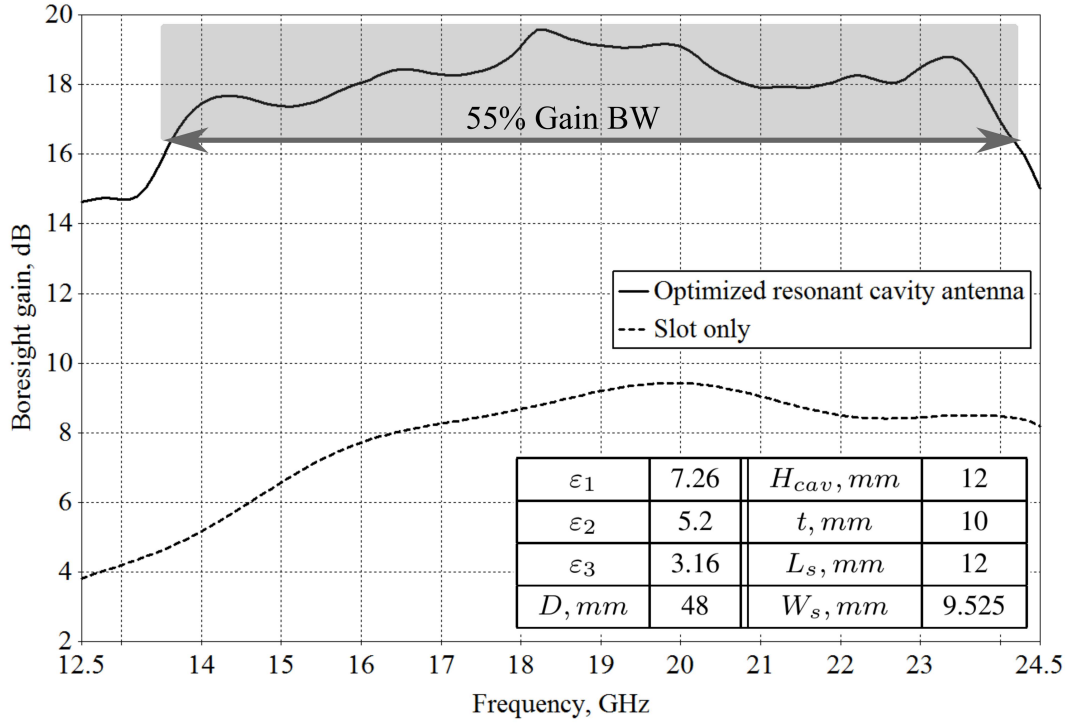
The boresight gain and the parameters (inset) of the best RCA design found by PSO is shown in Fig. 3.20. For comparison, the gain of the slot antenna fed by a waveguide is shown in the graph. The value of the best fitness function is DBP=5526.79, which is calculated using Eq. (3.9). The RCA's peak gain is 19.78 dB and the 3-dB gain bandwidth is from 13.7 to 24.1 GHz, which is a 58% fractional bandwidth.



**Figure 3.18:** Cross-sectional view of the RCA structure with three-sectional TPG superstrate:  $(\varepsilon_1, \varepsilon_2, \varepsilon_3) = (7.26, 5.2, 3.16)$ ,  $t = 10$  mm.  $H_{cav} = \lambda_0/2$ ,  $D = 2\lambda_0$ ,  $\lambda_0 = 24$  mm.



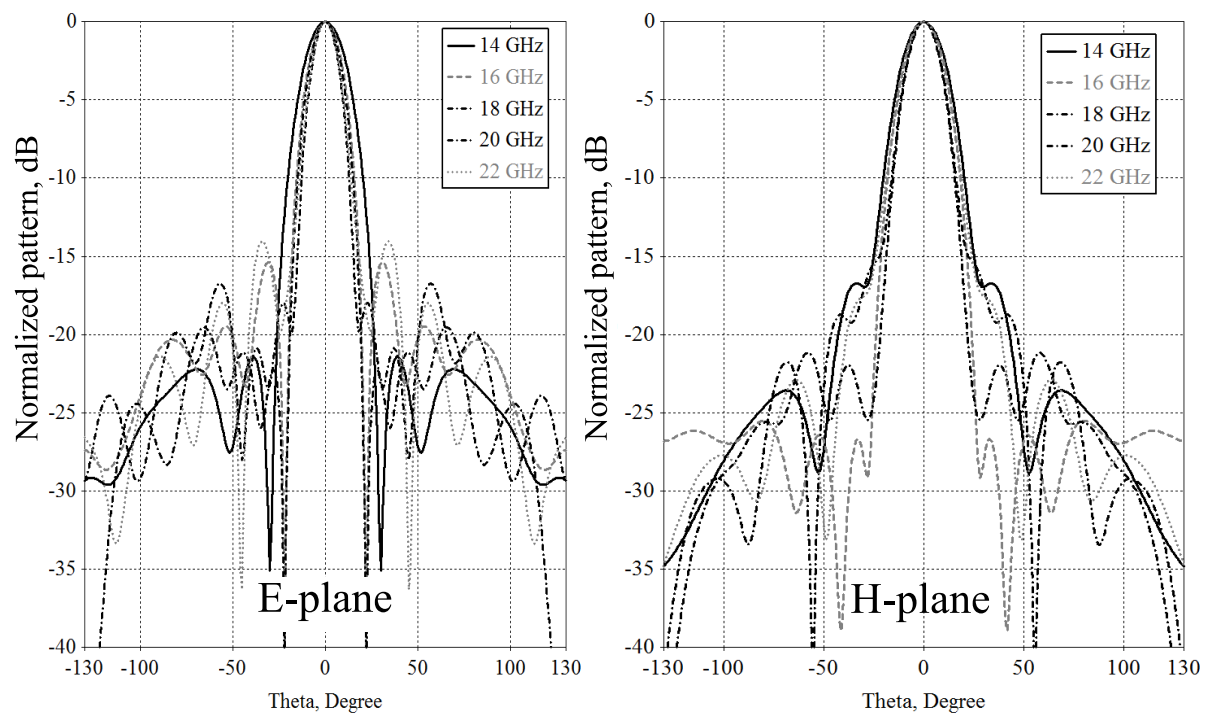
**Figure 3.19:** Convergence curve for the completed optimization run. Objective function is given in Eq. (3.9).



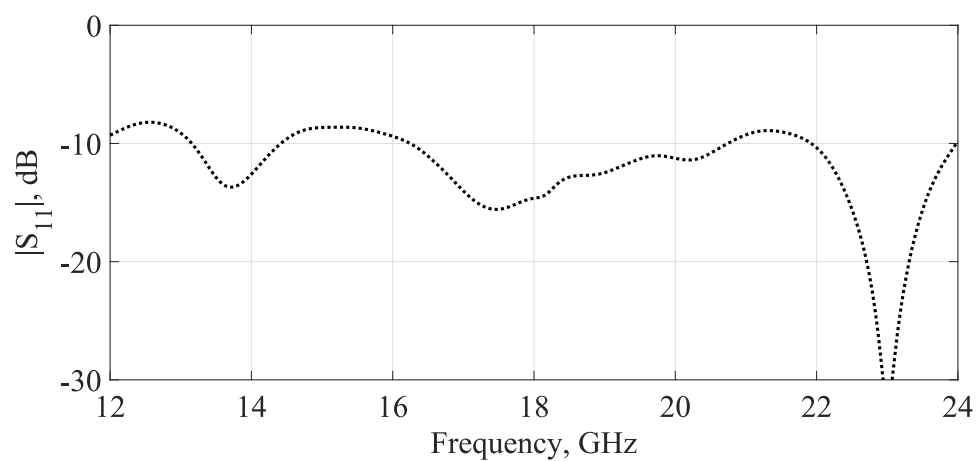
**Figure 3.20:** Boresight gain of the optimized RCA in comparison with a slot antenna in the ground plane,  $D=48$  mm. Inset provides the parameters of the optimal RCA design.

The impedance bandwidth covers well the gain bandwidth, as shown in Fig. 3.22, with  $|S_{11}| < -8.5$  dB. The voltage standing wave ratio (VSWR) in this frequency range is below 2.2. Radiation patterns at five frequencies in both planes are provided in Fig. 3.21, and it can be seen that SLLs in the entire bandwidth are below  $-14$  dB.

Compared to the RCAs with four-sectional superstrates and thickness  $t = 6.35$  mm (Section 3.4.3), the optimized antenna with three-sectional superstrate and thickness  $t = 10$  mm has a higher value of DBP. In [136], parametric studies on TPG superstrates showed that with thick superstrates of up to  $t = \lambda_0/\sqrt{\epsilon_r}$  a peak directivity of 19.1 dBi can be obtained using a nine-sectional superstrate, where  $\epsilon$  is the permittivity of the innermost section in the TPG superstrate. The maximum peak directivity of 16.7 dBi was obtained from a three-sectional superstrate in [136] using manual search methods. This is 3 dB lower than that of the optimized design presented here.

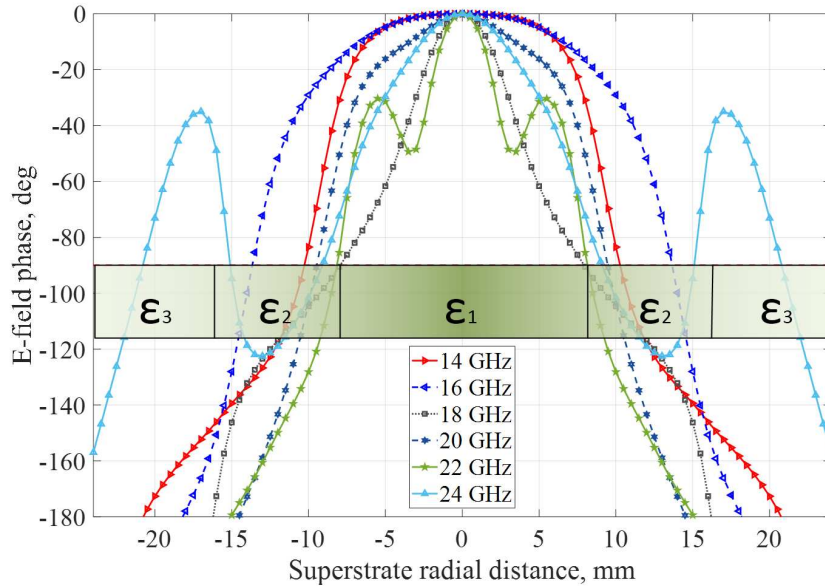


**Figure 3.21:** Normalized radiation patterns of the optimized high-gain wideband RCA in the E- and H-planes at five frequencies within the bandwidth.



**Figure 3.22:** Input impedance matching of the four-sectional RCA (Design III).

The spatial E-field phase distribution above the superstrate at frequencies 14, 16, 18, 20, 22 and 24 GHz is given in Fig. 3.23. It can be seen that compared to the previous case, this superstrate (which is significantly thicker) generates less than 100% effective in-phase aperture as defined in [136]. The cross-section view of the superstrate has been overlapped with the E-field phase distribution to observe the radial distance where the phase changes its value. It can be noticed that in the middle of the superstrate the phase is within  $90^\circ$ . The phase is below  $-90^\circ$  for the middle and outer dielectric sections. In this design, the 100% in-phase aperture might not been achieved due to the low level of discretization of this superstrate and its large thickness. The high value of the directivity-bandwidth product might be due to the diffraction from the edge of the superstrate. This is arguably one of the advantages of optimization-generated designs that a high-performing solution can be obtained without understanding of the physics of the problem.



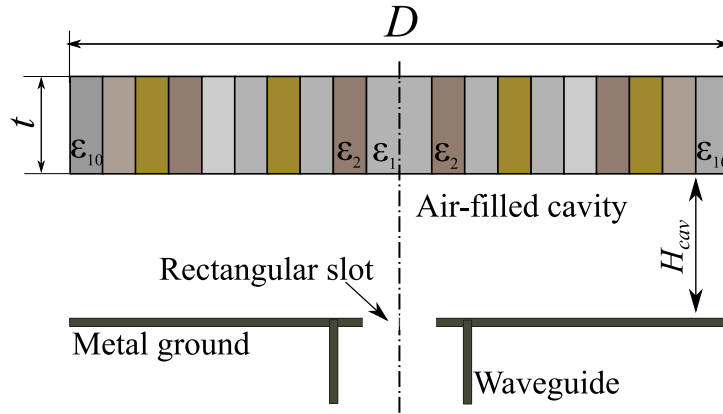
**Figure 3.23:** E-field phase distribution above the optimized superstrate of the three-sectional RCA (Design III).



### 3.5 Extremely Wideband RCA With a Slot Feed

An RCA with a ten-sectional superstrate and an HED for cavity excitation has been presented in Section 3.4.2, with a peak directivity of 19 dBi and a 3-dB bandwidth of 24%. In this section, an RCA with a ten-sectional superstrate and a real feed antenna is optimized with the goal to maximize the DBP in the frequency band 10–23 GHz.

#### 3.5.1 Design Parameters and Objective



**Figure 3.24:** Cross-sectional view of the RCA with a superstructure from concentric dielectric sections of width  $w = 0.086\lambda_0$ ,  $D = 1.7\lambda_0$ ,  $t = 0.3\lambda_0$ ,  $H_{cav} = 0.5\lambda_0$ ,  $\lambda_0 = 28$  mm.

Fig. 3.24 shows an RCA with a cavity fed by a rectangular slot of dimensions  $14 \times 9.5$  mm in the middle of a circular metal ground plane of diameter  $D = 1.7\lambda_0$ ,  $\lambda_0 = 28$  mm. The superstrate is a dielectric slab of thickness  $t$  composed of ten subwavelength concentric sections, each of width  $w$ . The elements of the superstructure have a permittivity  $\epsilon_i$ ,  $i = 1, 2, \dots, 10$ , where  $\epsilon_1$  is the permittivity of the central disk. The width of each dielectric section in the superstrate is  $w = 2.4$  mm, which is  $0.086\lambda_0$ . Such a fine discretisation of the superstrate eliminates the need to control the width of each section and adds flexibility to the optimizer to find a possibly better solution.

This optimization problem has 11 variables. In order to find the optimal vector of parameters in the superstrate with the design variables

$$\mathbf{x} = (\epsilon_1, \epsilon_2, \dots, \epsilon_{10}, t),$$

as before, a classic PSO with decreasing inertia weight [62] has been applied. The constraints have been defined as

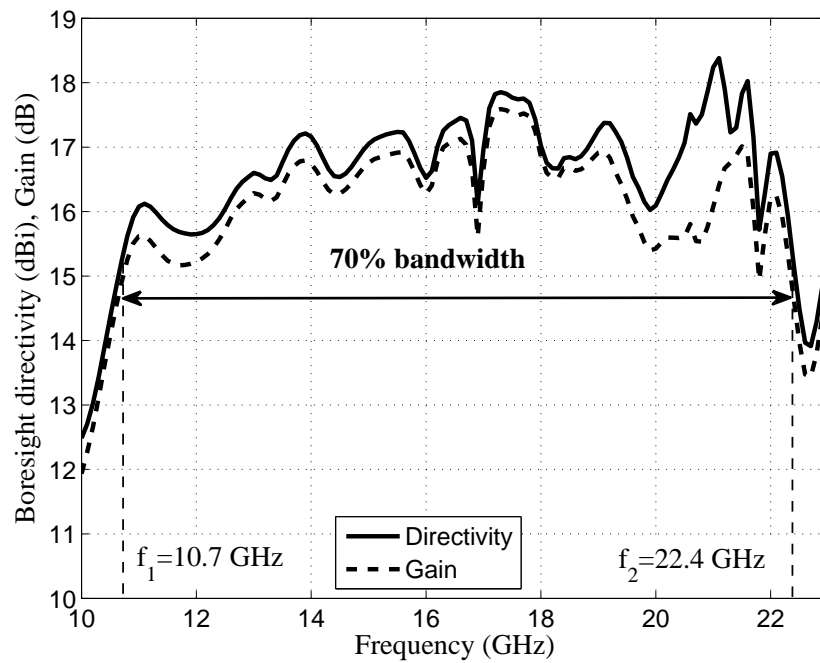
$$\begin{aligned} 2 &\leq (\varepsilon_1, \varepsilon_2, \dots, \varepsilon_{10}) \leq 10, \\ 4 &\leq t \leq 14 \text{ mm}, \\ SLL_{(E,H)} &< -10 \text{ dB}, \end{aligned} \tag{3.10}$$

where  $SLL_{(E,H)}$  is the first side lobe level in both principal planes. The optimization goal is to maximise the expression given in Eq. (3.9) in the frequency band 10–23 GHz.

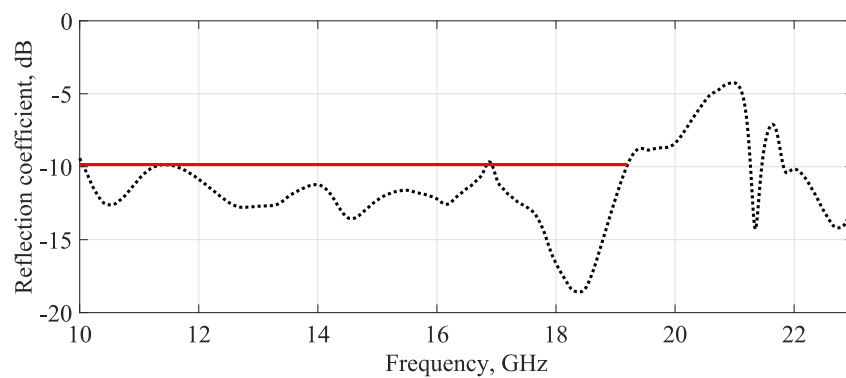
### 3.5.2 Results and Discussion

The parameters of the optimal solution obtained after 30 generations of the swarm of 20 particles are  $\varepsilon_{i=1\dots10}^* = (10, 10, 7.6, 6.9, 10, 5.4, 5.7, 7.4, 2, 4.67)$ ,  $t^* = 8.6 \text{ mm}$ . The boresight directivity, shown in Fig. 3.25, has a maximum value of 18.4 dBi, and its 3-dB bandwidth extends from 10.7 to 22.4 GHz. The peak gain and bandwidth of the optimized RCA are 17.6 dB and 70%, respectively. The optimized antenna produces the largest bandwidth ever obtained by an RCA. Such an extreme bandwidth has been achieved with the diameter of the antenna as small as  $1.7\lambda_0$ .

The input impedance matching, given in Fig. 3.26, shows that the reflection coefficient is less than  $-10 \text{ dB}$  between 10 and 19.2 GHz, which is the majority of the frequency range of interest, but rises at higher frequencies. The goal of impedance matching can be included in the fitness function along with adding the slot dimensions in the design variables in order to ensure an overlap of the radiation and impedance bandwidths, but that was out of the scope of this study.

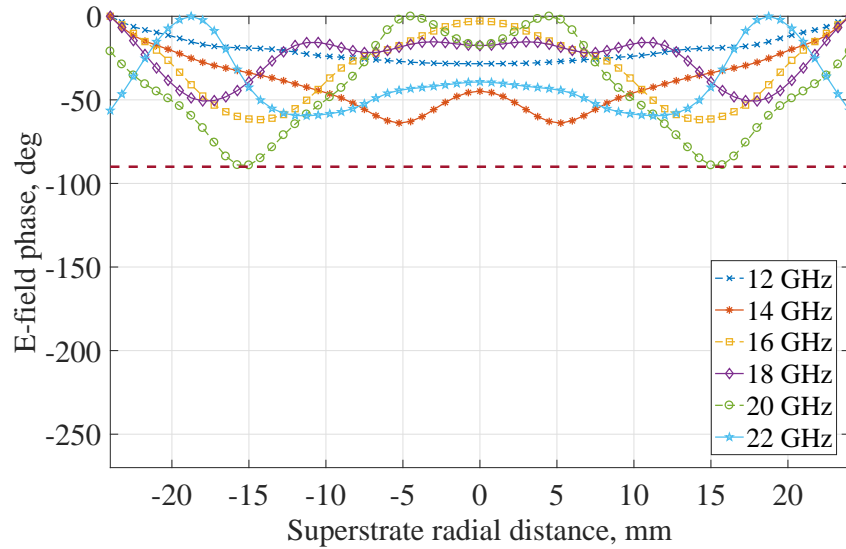


**Figure 3.25:** Bore sight directivity and gain of the optimized RCA.



**Figure 3.26:** Input impedance matching of the optimized RCA.

As suggested in [136], the reason for large directivity bandwidths in compact RCAs is the uniformity of the E-field phase distribution. An effective in-phase aperture was defined in [136] as the aperture within which the phase difference  $\Delta\varphi \leq 90^\circ$ . The E-field phase distribution on the aperture located  $\lambda_0/9=3$  mm above the superstrate of the optimized RCA is given in Fig. 3.27. It can be seen that the effective in-phase radius coincides with the entire superstrate, resulting in a 100% in-phase aperture. For the clarity of the figure, the phase distributions at 12, 14, 16, 18, 20 and 22 GHz are shown, but the phase difference is less than  $90^\circ$  for all frequencies in the band 11–22 GHz. The results suggest that the extremely wide 3-dB directivity bandwidth of 70% has been achieved by finding an optimal permittivity distribution in the superstrate that produces a uniform aperture phase distribution in a wide frequency band.

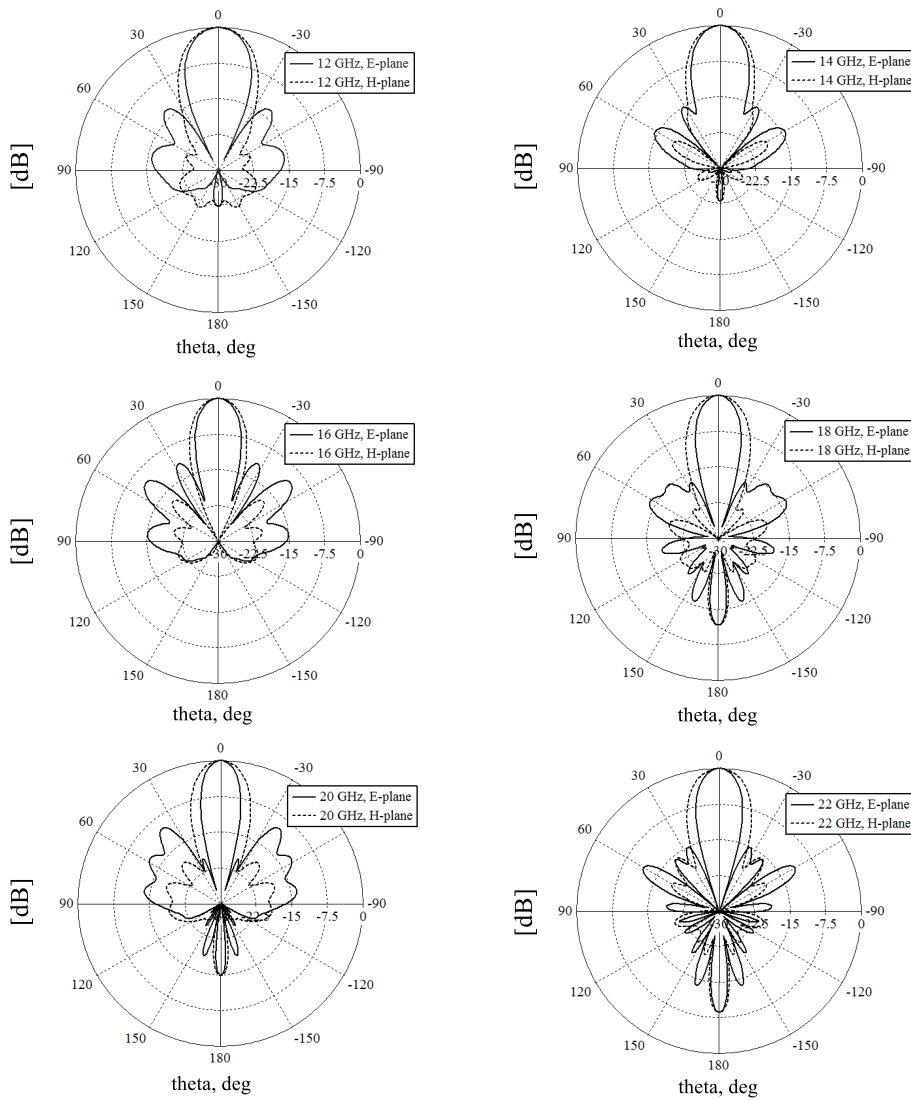


**Figure 3.27:** E-field phase distribution probed 3 mm above the optimized superstrate of the extremely wideband RCA.

As opposed to the RCA with a three-sectional superstrate, this superstrate has much higher level of the discretization of permittivity. Also, the optimal permittivity profile of this superstrate does not demonstrate a gradual decrease of permittivity from the centre of the superstrate towards the edges as suggested in [136]. It may only be important that the spatial phase distribution lies within  $90^\circ$ . Since materials with the dielectric constants required for building the prototype of the optimized RCA are not commercially available,

either additive manufacturing or artificially engineered materials [153] can be used for realisation of the design.

The radiation patterns at six frequencies within the directivity bandwidth are shown in Fig. 3.28. It can be seen that the patterns remain directive throughout the operating frequency range 10.7–22.4 GHz with the  $SLL_{(E,H)}$  less than  $-10$  dB. The front-to-back ratio, which becomes significant at the frequencies 18–22 GHz, can be reduced by increasing the size of the ground plane without affecting other parameters.



**Figure 3.28:** Normalised radiation patterns of the optimized RCA at six frequencies within the operating frequency range.

### 3.6 Summary

Novel RCAs offer attractive properties for microwave and millimetre-wave wireless communication systems. High gain, compact size and simple configuration make them an appealing alternative to the conventional solutions such as parabolic antennas, horns and arrays. In this chapter, a number of RCAs with different radiation characteristics and design complexity have been presented.

Fig. 3.29 summarises the designs proposed in this chapter in the order in which they have been presented. The designed RCAs have very small footprints with diameters of  $1.7\text{--}2.2\lambda_0$  and superstrate areas of  $2.27\text{--}3.8\lambda_0^2$ . Cavities of different height ( $H_{cav} = 11, 12, 13$  and  $14$  mm) have been investigated, and from the optimized results it can be seen that  $H_{cav}$  corresponds to  $f_1$  of the half-power directivity bandwidth. All optimized RCAs demonstrate further improvement in radiation performance, along with the advantages, as compared to recent advances in the development of wideband high-gain RCAs, of a single planar unprinted superstrate. Taking DBP per unit area (DBP/A) as a figure-of-merit for the comparison, the best performance is provided by the ten-sectional RCA with a peak gain of 17.6 dB and a 3-dB bandwidth of 70%. This extremely wideband and directive radiation performance can be especially useful for building high-speed wireless backhaul networks.

A disadvantage of PSO is that it operates with continuous variables and, therefore, yields permittivity values not available from off-the-shelf dielectric materials. Potentially, some dielectric materials can be obtained using additive manufacturing technology. However, it is desirable to have an optimization method that operates with discrete variables and produces a design containing the materials from the list of RF laminates at hand. In the next chapter, an optimization approach based on the CE method will be proposed for problems with both continuous and discrete variables.

RCA Design	Peak Directivity, dB	3-dB Bandwidth, %	Area, $\lambda_0^2$	DBP/Area, dB*%/ $\lambda_0^2$
<u><b>Section 3.4.2 Design I: Ten-Sectional Superstrate</b></u> $(\epsilon_1, \dots, \epsilon_{10}) = (11, 11, 11, 11, 11, 6.9, 11, 2, 8.7, 6.5)$ $t = 4.2 \text{ mm}$ $D_{\text{RCA}} = 2.2 \lambda_0, H_{\text{cav}} = 11 \text{ mm} = 0.5\lambda_0$	19.1	24	3.8	120.6
<u><b>Section 3.4.3 Design II: Four-Sectional Superstrate</b></u> $(\epsilon_1, \dots, \epsilon_4) = (10, 10, 6.6, 3.03)$ $t = 6.35 \text{ mm}$ $D_{\text{RCA}} = 1.85 \lambda_0, H_{\text{cav}} = 13 \text{ mm} = 0.5\lambda_0$	18.3	50	2.7	338.8
<u><b>Section 3.4.4 Design III: Three-Sectional Superstrate</b></u> $(\epsilon_1, \dots, \epsilon_3) = (7.26, 5.24, 3.19)$ $t = 10 \text{ mm}$ $D_{\text{RCA}} = 2 \lambda_0, H_{\text{cav}} = 12 \text{ mm} = 0.5\lambda_0$	19.6	55	3.14	343.3
<u><b>Section 3.5 Extremely Wideband RCA With a Slot Feed</b></u> $(\epsilon_1, \dots, \epsilon_{10}) = (10, 10, 7.6, 6.9, 10, 5.4, 5.7, 7.4, 2, 4.67)$ $t = 8.6 \text{ mm}$ $D_{\text{RCA}} = 1.7 \lambda_0, H_{\text{cav}} = 14 \text{ mm} = 0.5\lambda_0$	17.6	70	2.27	542.7

**Figure 3.29:** Summary of the RCA design parameters and their performance characteristics presented in this chapter.





*The secret of change is to focus all of your  
energy not on fighting the old, but on building  
the new.*

— Socrates

## Chapter 4

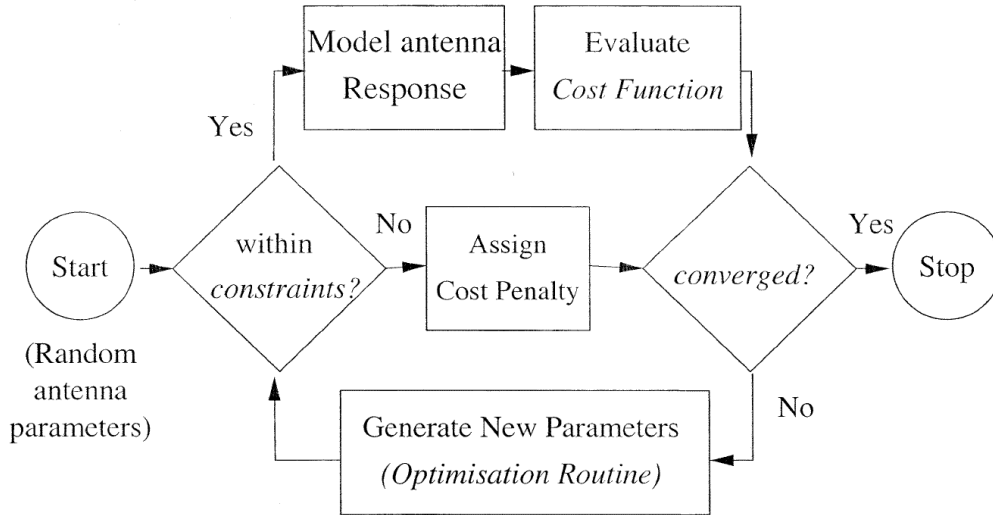
# CE Method for EM Optimization With Constraints and Mixed Variables

A brief introduction to the CE optimization method was given in Chapter 2. In this chapter, the basic principle of the CE method is described from the perspective of its application to real-world EM engineering problems. Then, a novel approach to optimization of designs with constraints and mixed variables is proposed. It is then interfaced with a full-wave EM solver in order to improve the performance of compact RCAs with single-slab all-dielectric TPG superstrates. Commercially available dielectric materials and real-world constraints are considered in optimization.

The main contribution of this chapter is a new, elegant, yet simple approach for the optimization of EM structures with mixed variables and constraints using the CE method. To the best of the author’s knowledge, this is the first time the CE method has been coupled with full-wave simulations. This is also the first time it has been used to optimize mixed-variable constrained EM design problems.

---

The material in this chapter is published as: M. Kovaleva, D. Bulger, B. A. Zeb and K. P. Esselle, “Cross-Entropy Method for Electromagnetic Optimization With Constraints and Mixed Variables”, *in IEEE Transactions on Antennas and Propagation*, vol. 65, no. 10, pp. 5532-5540, Oct. 2017.



**Figure 4.1:** Flow chart of a common general approach to optimization of constrained antenna design problems [154].

## 4.1 Introduction

Electronic and EM engineering designs frequently make use of commercially available elements, such as electronic components and dielectric RF laminates. For example, resistors, inductors and capacitors are available in standard values, and dielectric materials are sold in specific thickness and permittivity values. From the optimization point of view, a problem containing variables that can only take specific values (as opposed to any value from an interval) is called a discrete or combinatorial optimization problem. EM optimization problems can consist of only discrete variables, but more often they include a combination of both types of variables, i.e. discrete and continuous. Problems with both continuous and discrete variables are called *mixed-variable* or *mixed-integer* optimization problems. There are many designs of microwave components, such as waveguides, filters and antennas, which fall into this category. Particularly, antenna design examples include microstrip patch antennas, dielectric horn antennas, lens antennas, wire antennas and dielectric resonator antennas, to name a few.

The overall dimensions of many modern antenna designs are constrained by space limitations. To ensure that the optimized designs are within the space requirements, the constraints have to be taken into account. The most common approach to solving

constrained optimization problems is to use a penalty function (Fig. 4.1). It has to be implemented because most optimization methods cannot intrinsically generate populations of designs that are located within the imposed constraints. Therefore, the constrained problem is transformed to an unconstrained problem, and constraints are handled outside the algorithm update procedures by penalising the designs that violate them. A similar approach is an “acceptance-rejection method”, which also results in inefficient optimization schemes [155].

Constraints and mixed variables pose a significant challenge for the current optimization algorithms available for EM problems. In terms of design parameters, Genetic Algorithms (GAs) and Ant Colony Optimization (ACO) handle discrete variables intrinsically, while most other algorithms, including the popular Particle Swarm Optimization (PSO), Differential Evolution (DE), Cuckoo Search (CS), Invasive Weed Optimization (IWO) and Evolutionary Strategies (ES), were originally developed for problems with a continuous domain.

## 4.2 Optimization Approach using the CE Method

The first application of the CE algorithm to EM problems was in antenna array synthesis in 2008 [87], and little research has been done since then on its application to other EM problems [88–90, 93, 156]. However, all previous applications were based on closed-form expressions, and no simulation-driven optimization using the CE method has been reported. It has been discussed in Section 2.6.3 that full-wave analysis is a standard approach nowadays, and, therefore, to make the CE method useful for practical applications, it has to be tested in a real-world environment. The advantage of the CE approach is its fast convergence and the adaptive update procedure, which makes it inherently capable of optimizing mixed-variable and constrained problems in a much simpler way than hybrid real-binary techniques, such as [44, 46–48, 50].

### 4.2.1 Convergence Properties of the CE Method

The CE method is a stochastic optimization technique based on minimizing the cross-entropy (or Kullback-Leibler divergence) between probability distributions to solve difficult multi-modal, multi-objective optimization problems. The idea of the optimizer evolved from a method to estimate the probability of rare events. Detailed explanations and possible modifications of the CE method can be found in Chapter 2 and in the literature [157]. Recent studies [158] have shown some similarities between the CE approach and the ACO and Estimation of Distribution algorithms, all of which belong to a *model-based search paradigm*. These methods differ from traditional heuristics in that they adjust a solution-reproducing mechanism instead of directly manipulating solutions. Recent stochastic runtime analyses show excellent runtime results and asymptotic convergence properties of the CE method [94, 159]. Below, the CE algorithm will be briefly discussed from the standpoint of its application to practical optimization problems.

### 4.2.2 Basic Principle of the CE Method

In statistics, the probability distribution of a random variable  $x$  is a description of the probability of each possible value, or range of values, that  $x$  could take. This probability is specified by the probability density function (PDF)  $p(x; v)$ , where  $v$  is a vector of shape parameters identifying the distribution within the family. For instance, the well-known normal (Gaussian) distribution of a random variable  $x \in R$  is characterised by its mean  $\mu$  and variance  $\sigma^2$ , and its PDF is expressed as:

$$p(x; v) = \frac{1}{\sigma\sqrt{2\pi}} e^{-(x-\mu)^2/2\sigma^2}, \quad v = (\mu, \sigma^2). \quad (4.1)$$

At each iteration, CE produces new solutions by sampling from the PDF. In any specific implementation of the CE method, only a finite-dimensional family of probability distributions is used, and it is often called a *model*. CE aims to produce a sequence of sampling distributions that are increasingly concentrated around the optimal design.

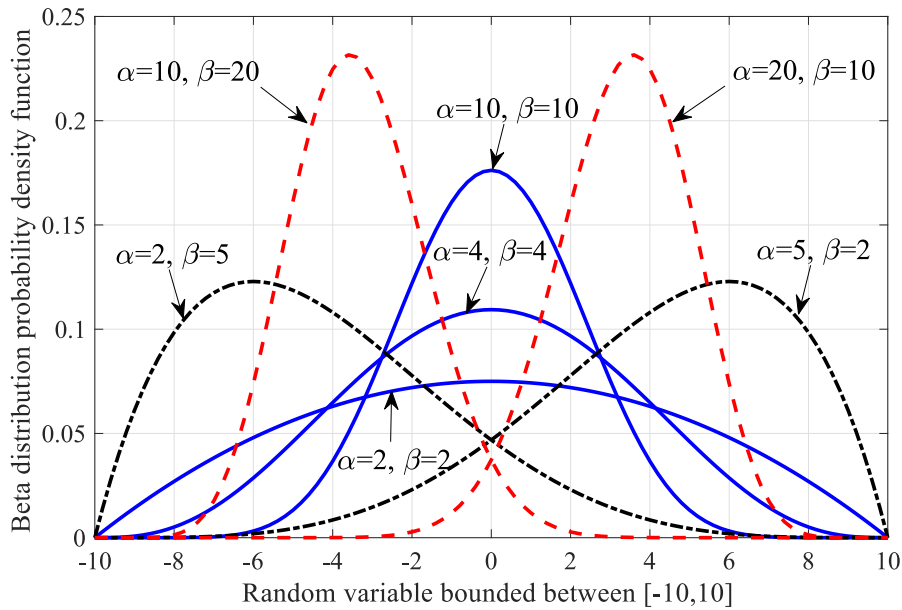
The choice of a probability distribution family in the CE method strongly depends on the nature of the design variables. For optimization problems with continuous variables,

normal and beta distribution families can be used to generate possible solutions. As discussed previously, the beta distribution, which has the PDF given by:

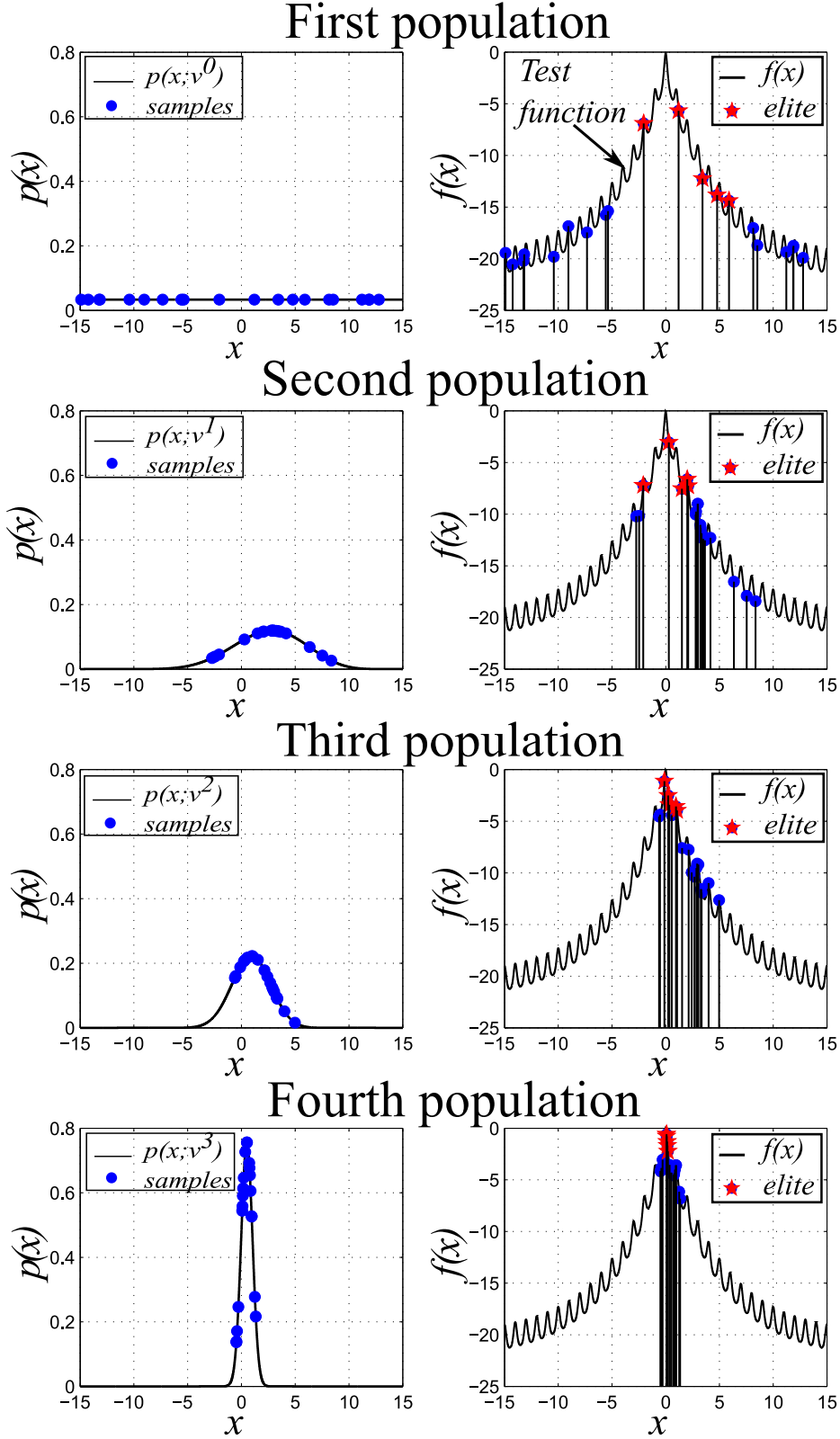
$$B(x; v) = \frac{x^{\alpha-1}(1-x)^{\beta-1}}{\int_0^1 x^{\alpha-1}(1-x)^{\beta-1} dx}, \quad v = (\alpha, \beta), \quad (4.2)$$

is particularly useful in describing continuous bounded variables. Fig. 4.2 demonstrates how shape parameters affect the PDF of a variable enclosed in an interval  $[-10, 10]$ . For optimization problems with discrete variables, discrete probability distribution families such as binomial, Poisson, Bernoulli, discrete uniform and geometric can be applied. For optimization problems with mixed variables, consisting of both discrete and continuous parameters, a combination of appropriate distribution families can be used. Thus, optimization of mixed-variable problems is intrinsic in the CE method.

Let us consider an engineering optimization problem where we wish to determine the values of several design variables in order to optimise some user-defined performance measure called the fitness function. As with any other evolutionary optimization method, the CE evaluates batches of designs at a time, called populations. Each population consists of  $N$  designs, called candidates. Each candidate is characterised by the vector of design



**Figure 4.2:** Beta distribution PDF of a random variable bounded between  $[-10, 10]$  for various shape parameters  $(\alpha, \beta)$ .



**Figure 4.3:** Illustration of selection and evaluation procedure in the CE method. The figure shows the first four iterations in the optimization of the univariate Ackley test function, with PDF shown on the left and fitness function on the right.

variables  $\mathbf{x} = (x_1, x_2, \dots, x_d)$ , where  $d$  is the number of variables or the problem dimensionality. Each candidate should be evaluated, usually by simulation, to calculate its fitness function. Thus, the total number of function evaluations in a complete optimization process equals the number of candidates  $N$  multiplied by the number of populations that is required to achieve the defined goal.

Optimization of the univariate (1D) Ackley test function is illustrated in Fig. 4.3. The algorithm is initialised by selecting the first population of  $N$  candidates from the initial sampling distribution  $p(x; v^0)$ . It can be seen that the initial beta distribution (left-hand side in Fig. 4.3) with  $v^0 = (1, 1)$  is used to characterise the continuous variable  $x$  bounded between  $-15$  and  $15$ . Subsequently, the initial population is created by randomly sampling  $N$  candidates from  $p(x; v^0)$ . The performance of every candidate is evaluated according to the fitness function  $f(x)$ , and the  $N_{el}$  best candidates are selected (right-hand side in Fig. 4.3) as the elite subpopulation. Depending on the type of the optimization, whether it is a maximisation or minimisation problem, the fitness values are sorted in descending or ascending order, respectively. The elite subpopulation of the  $N_{el}$  best performing candidates is used to construct a new distribution  $p(x; v^1)$ . In particular, the algorithm estimates distributional parameters  $v^1$  that best describe the current elite subpopulation according to the Kullback-Leibler distance, or the cross-entropy minimisation [84]. These empirical shape parameters describe the distribution  $p(x; v^1)$ , which is used to generate the next population. Selection, evaluation and updating procedures are repeated until the stopping criterion is satisfied. In the illustrated example, the elite subpopulation of the fourth population reached the global solution.

A number of techniques can be used to avoid premature convergence of the CE method to local instead of global solutions. First, the initial sampling distribution can be very wide (as  $p(x; (2, 2))$  in Fig. 4.2) or even uniform (as  $p(x; (1, 1))$  in Fig. 4.3, top left), to cover all plausible designs. Second, the population size  $N$  can be defined large enough to maximise the chance that good designs will appear in a random sample. Third, the smoothing parameter  $\alpha_S$  given by Eq. (2.5) can be applied in order to slow down the convergence. Last, if the best fitness value has not been improved for a number of

iterations, a mutation operator [88] can be used to add small random perturbations to the shape parameters.

### 4.3 RCAs Optimized by the CE Method

The proposed approach of the CE optimization is used to improve the performance of a compact RCA described in the previous chapter (Fig. 4.4) and overcome the limitations that are attributed to the designs optimized by continuous PSO. RCAs are not only a prominent antenna design for future communication systems, they also represent an optimization problem that well illustrates the benefits of CE, in particular, its ability to handle simultaneously both mixed variables and design constraints without complexity.

The constraint in this design example is the total diameter  $D$  of the antenna. Although the widths  $w_i$  of the dielectric sections shown in Fig. 4.4 can take any positive value, their sum ( $\sum_{i=1}^N w_i$ ), i.e. the total superstrate radius, is fixed to a particular value. Some design variables, such as  $w_i$  and  $t$ , are continuous, but the permittivities,  $\varepsilon_i$ , are discrete, because they can take only commercially available values.

#### 4.3.1 Algorithm Implementation

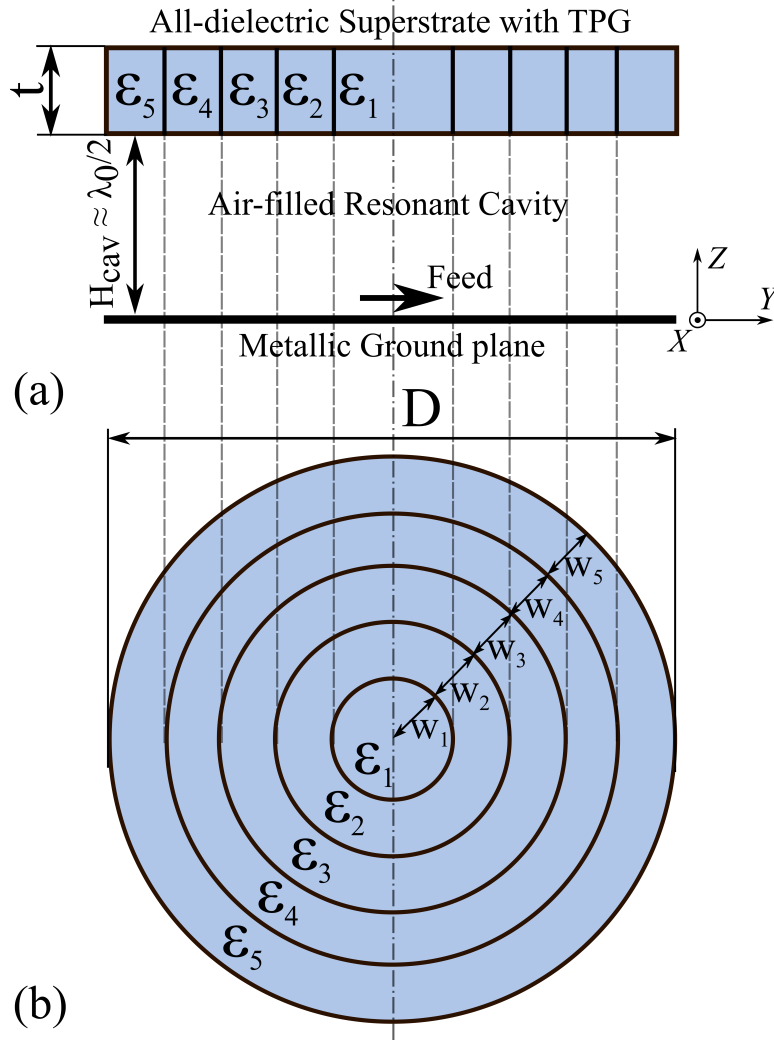
The given RCA with a TPG superstrate is a combinatorial and constrained optimization problem. We approach it by combining discrete and continuous variables in a single parameter vector. *Discrete variables* describe those parameters of the superstrate that can only take values from a given catalogue, for example, nominal permittivity and thickness values of Rogers materials. *Continuous variables* describe the width of each section ( $w_i$ ) in the superstrate under the constraint that they sum to  $D/2$ . The permittivities  $\varepsilon_i$  and section widths  $w_i$  of the superstrate form the design vector

$$\mathbf{x} = (\varepsilon_1, \varepsilon_2, \dots, \varepsilon_n, w_1, w_2, \dots, w_n), \quad (4.3)$$

where

$$\varepsilon_1, \varepsilon_2, \dots, \varepsilon_n \in S, \quad (4.4)$$





**Figure 4.4:** (a) Side view and (b) top view of an RCA with a TPG superstrate. The superstrate is made out of five dielectric segments.

and the section widths  $w_i$  are constrained by

$$w_1 + w_2 + \cdots + w_n = D/2, \quad (4.5)$$

$S$  is a catalogue of discrete commercially available permittivities and  $n$  is the number of sections in the TPG superstrate.

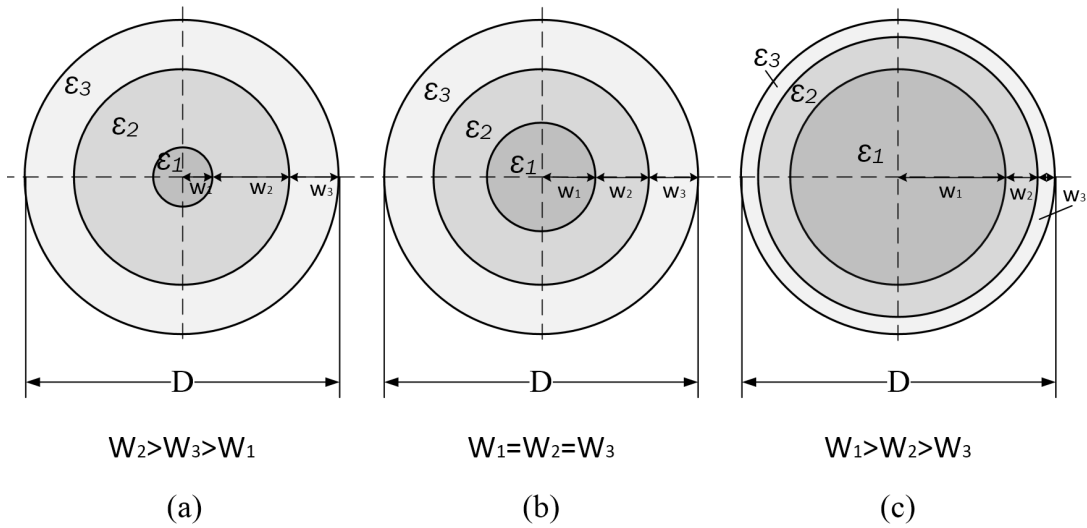
The uniqueness of the proposed CE optimization approach lies in the use of the general discrete distribution family for the discrete variables, and the Dirichlet distribution family for the continuous constrained variables. The sampling distribution for  $\varepsilon_i$  is described by a stochastic vector of length  $q_p$ , which is the number of elements in the catalog. These vectors are stored in an  $n \times q_p$  matrix. During initialisation, this matrix is uniform,

meaning that every permittivity has equal probability to occur in each section. Then, based on fitness function evaluations, those permittivities that lead to better results earn a higher probability of occurrence in the next population. Specifically, each row in the parameter matrix is replaced by the sample proportion vector of that section's permittivities in the elite subpopulation.

The widths  $w_i$  cannot be sampled independently, due to the constraint that they sum to  $D/2$ . For fabrication simplicity and to avoid physically meaningless designs, we assume  $w_i > 0.1\lambda_0$  for each section. Thus, the vector  $(w_1 - 0.1\lambda_0, \dots, w_n - 0.1\lambda_0)/(D/2 - 0.1n\lambda_0)$  (abbreviated as  $(x_1, \dots, x_n)$ ) must be elementwise nonnegative and sum to 1, and therefore can be sampled from a multivariate Dirichlet distribution, with parameter vector  $(\alpha_1, \dots, \alpha_n)$ . For convenience, we used a simple method-of-moments update of the Dirichlet parameter vector at each iteration [160], rather than minimising the Kullback-Leibler distance, replacing the parameter  $\alpha_i$  at each iteration with

$$\alpha_i = \bar{x}_i \left( \frac{1 - \sum_{j=1}^n \bar{x}_j^2}{\sum_{j=1}^n \text{Var}[x_j]} \right) - 1,$$

where the sample mean, denoted by the overbar, and variance  $\text{Var}$  are taken over the elite subpopulation. Fig. 4.5 illustrates different combinations of widths in a superstrate made of three sections when  $w_i, i=1\dots3$ , are sampled from the Dirichlet distribution. It can be seen that in every case the constraint in Eq. (4.5) is satisfied.



**Figure 4.5:** Three possible combinations of widths.

First, we optimized the design of an RCA with a three-sectional superstrate of fixed thickness  $t$  (Case-I). The design vector in this case is  $\mathbf{x} = (\varepsilon_1, \varepsilon_2, \varepsilon_3, w_1, w_2, w_3)$ . The optimization was repeated for three values of  $t$ , and three RCAs were designed. The catalogue of available materials included five laminates with permittivity 3.27, 4.5, 6, 9.2 and 9.8. The overall diameter of the TPG superstrate and the ground plane was constrained to  $D = 48$  mm, which is  $1.85\lambda_0$ , where  $\lambda_0$  is the free-space wavelength corresponding to the first resonance frequency of the cavity  $f_0 = 11.5$  GHz. The cavity height  $H_{cav}$  is 13 mm.

Then we optimized an RCA with a six-sectional superstrate of variable thickness  $t$  (Case-II) with design vector  $\mathbf{x} = (\varepsilon_1, \varepsilon_2, \varepsilon_3, \varepsilon_4, \varepsilon_5, \varepsilon_6, w_1, w_2, w_3, w_4, w_5, w_6, t)$ . Here the catalogue of substrates had ten permittivity and five thickness values. Superstrates with diameters  $D_1 = 1.5\lambda_0$ ,  $D_2 = 1.85\lambda_0$  and  $D_3 = 2.2\lambda_0$  were considered, and three more RCAs have been designed in Case-II optimization. Design parameters for both cases, Case-I and Case-II, are summarised in Table 4.1.

### 4.3.2 Fitness Function Definition

The aim of optimization is to achieve a high directivity-bandwidth product (DBP) and low side lobe levels (SLLs) in the band 10–20 GHz. Hence, the product of the peak directivity  $Dir_{peak}$  (in dBi) and the 3-dB directivity percentage bandwidth  $BW$  (%),

**Table 4.1:** Design parameters for RCA optimization.

	Case-I	Case-II
Number of sections, $n$	3	6
Catalogue of available permittivity values, $q_p$	5	10
Catalogue of available thickness values, $q_t$	1	5
Number of candidates in a population, $N$	45	70
Number of candidates in elite subpopulation, $N_{el}$	10	10
Smoothing parameter, $\alpha_S$	0.5	0.6
Stopping threshold, $[\delta_{perm}, \delta_{width}]$	$[0, 0.009\lambda_0]$	$[0, 0.009\lambda_0]$

given by

$$F_{DBP} = Dir_{peak} * BW, \quad (4.6)$$

has been considered. As a 40% bandwidth is sufficient for most applications, we restricted the largest  $BW$  to  $BW_{lim}$  as follows:

$$BW = \begin{cases} BW, & \text{if } BW < BW_{lim}. \\ BW_{lim}, & \text{otherwise.} \end{cases} \quad (4.7)$$

This technique, found successful in previous optimizations of wideband antennas [161], is applied here to obtain a design with a high peak directivity  $Dir_{peak}$ , as well as a large percentage  $BW$ . In this example, the desirable  $BW$  has been limited to 40%, however any other value can be specified, which would result in a different superstrate profile and performance.

SLLs in the E-plane are generally much higher than in the H-plane, therefore the fitness of SLLs in the E-plane is included in the objective. Side lobe fitness  $F_{SLL}$  is defined as the average difference between the current and desired values of SLLs over the frequency range from  $f_l$  to  $f_h$ :

$$F_{SLL} = mean(max(0, SLL_{E,(f_l < f < f_h)} - SLL_{E,obj})), \quad (4.8)$$

where the desired SLL in the E-plane is  $SLL_{E,obj} = -20$  dB, and  $SLL_{E,(f_l < f < f_h)}$  is the current SLL between  $f_l$  and  $f_h$  (evaluated with a 0.5 GHz frequency step in the frequency range from 10 to 20 GHz). These objectives were combined into a single objective by a weighted sum:

$$F.F. = F_{DBP} - k * F_{SLL}, \quad (4.9)$$

where  $k$  was set to 20. This coefficient was selected through a trial-and-error process with the goal to reflect the relative importance of combined objectives and to compensate for the difference in their magnitudes as described in Section 2.6.1. There is a linear proportionality between  $k$  and  $F.F.$ . Larger  $k$  would result in lower  $F.F.$  value, thus, placing more importance to the SLL objective. Impedance matching was not included in the objective function as it was beyond the scope of this study.

Since the superstrate is non-periodic and has small lateral dimensions (diameter  $< 2\lambda_0$  at the lowest frequency), classic design approaches involving unit-cell optimizations [144] or transmission-line modelling [162] cannot be used for the analysis of this compact RCA. Instead, full-wave analysis of the complete antenna was performed to accurately predict boresight directivity and SLLs. Thus, the CE algorithm was implemented in MATLAB and linked to the time-domain solver in CST MWS using macro programming. A flowchart for design automation and a macro for the optimization of the RCA are provided in Appendix A. To reduce the simulation time, we exploited the bilateral  $X$ - and  $Y$ -symmetry of the RCA superstrate by applying appropriate boundary conditions in two planes.

### 4.3.3 Stopping Criterion

The optimization cycle continues until the stopping criterion is satisfied. Its definition is frequently based on a maximum number of iterations or on the expected value of the fitness function. If the criterion is too strict, the optimization continues longer than required, which unnecessarily extends the overall optimization time. On the other hand, forcing the optimizer to stop prematurely can prevent the population from finding a significantly better solution. The condition for stopping should be based on *a priori* knowledge of the problem.

Here, the stopping criterion was based on a measure of elite subpopulation diversity, defined as the maximum variation between the candidates in a current subpopulation. Diversity in radii and permittivities were calculated separately, each measuring the maximum deviation of any elite parameter from the corresponding elite mean. The algorithm stopped when the diversity was equal to 0 for permittivities and less than the threshold  $\delta = 0.009\lambda_0 = 0.2$  mm for the section widths.

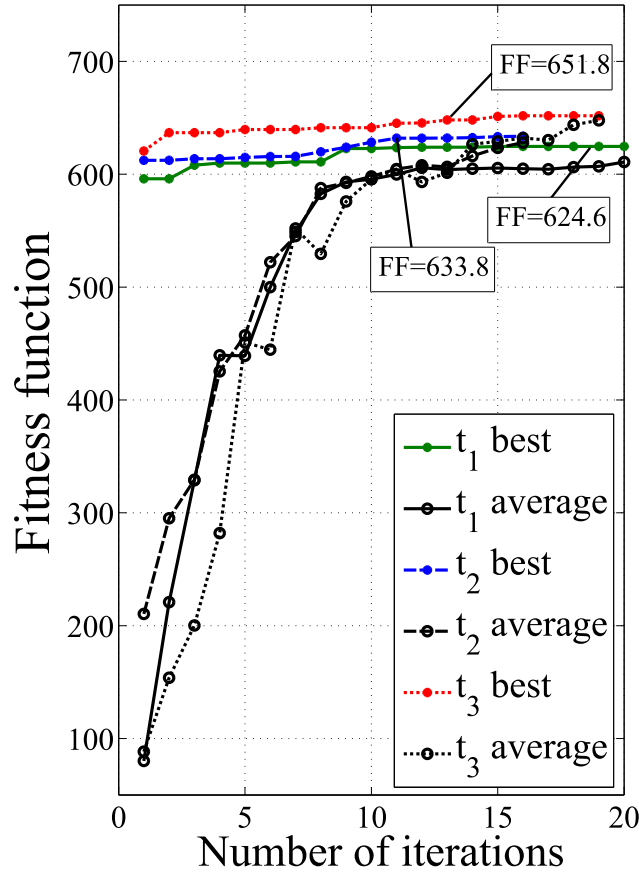
#### 4.3.4 Optimization Case-I: RCA with Three-Sectional TPG

The RCA with three-sectional superstrate was optimized for three fixed thickness values  $t_1$ ,  $t_2$  and  $t_3$ , and the best result for each thickness is summarized in Table 4.2. The catalogue of available dielectric materials contained five Rogers TMM laminates with permittivities  $\{3.27; 4.5; 6; 9.2; 9.8\}$ . It can be seen that the design with the superstrate thickness of 7.62 mm has the highest value of the fitness function (Eq. (4.9)), which is calculated as  $F.F. = 19.38 \times 40 - 20 \times 6.16 = 651.80$ . The lowest average SLLs were obtained for the superstrate with permittivity distribution (9.8, 6, 4.5), widths  $10.8 + 5.28 + 7.92 = 24$  mm and thickness  $t = 6.99$  mm. It is interesting to note that, without any constraint of the decreasing permittivity from the centre towards the edges, the optimal permittivity profiles have a gradual decrease of permittivity. This agrees well with the theoretical arguments made in [136].

Fig. 4.6 shows the convergence plots for Case-I optimization. With parameters  $N=45$ ,  $N_{el}=10$  and  $\alpha_S=0.5$ , the stopping criterion was reached after 20 iterations for  $t_1$ . Evaluation of one population (45 candidates) took approximately 20 minutes on an Intel(R) Core(TM) i7-4790 CPU 3.6 GHz processor with 32 GB of RAM. Approximately 14 hours were required to complete this optimization. Evolution of the design parameters over

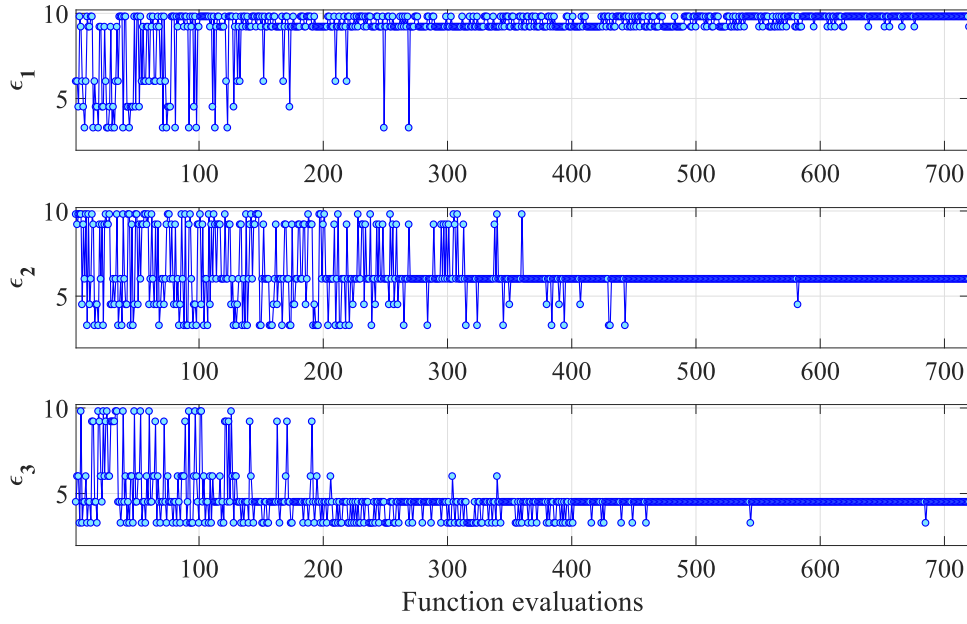
**Table 4.2:** Optimization Case-I results for three predefined superstrate thickness values.

Superstrate thickness	$t_1=6.35$ mm ( $0.24\lambda_0$ )	$t_2=6.99$ mm ( $0.27\lambda_0$ )	$t_3=7.62$ mm ( $0.29\lambda_0$ )
Superstrate section parameters			
$\varepsilon_1, w_1$	9.8, 7.92	9.8, 10.8	9.8, 8.40
$\varepsilon_2, w_2$	9.2, 8.16	6, 5.28	6, 6.96
$\varepsilon_3, w_3$	4.5, 7.92	4.5, 7.92	4.5, 8.64
$Dir_{peak}$ , dBi	18.51	18.32	19.38
BW, %	45.07	41.46	42.39
$F_{SLL}$ , dB	5.79	4.95	6.16
Fitness function, Eq. (4.9)	624.60	633.80	651.80

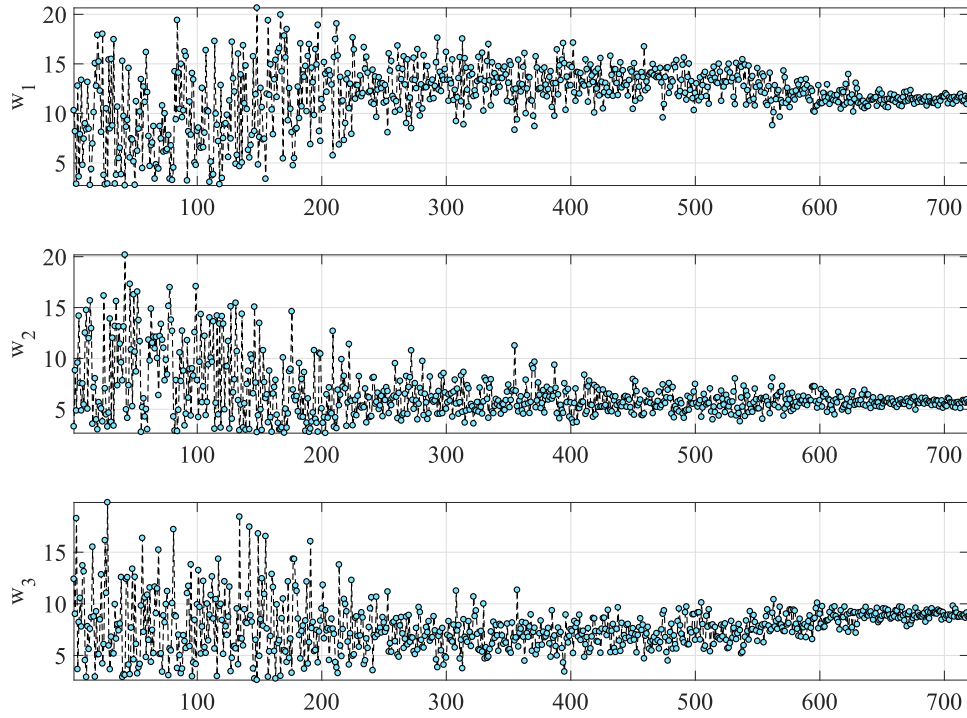


**Figure 4.6:** Convergence results of the CE method for Case-I optimization of three compact RCAs with TPG superstrates, where  $t$  is the superstrate thickness and  $D$  is its diameter. For each optimization run, “best” is the best result observed so far, and “average” is the mean of all results observed at each iteration.

the progress of optimization is shown in Fig. 4.7. It can be seen that the first iterations are characterised by significant variances of the design parameters because the optimizer operates in the exploration mode. Then, the population gradually concentrates around the design parameters that produced the best fitness function. Discrete variables have fewer fluctuations in their parameters than continuous ones.



(a) Evolution of discrete variables  $\epsilon_1$ ,  $\epsilon_2$  and  $\epsilon_3$  over the progress of optimization.



(b) Evolution of continuous variables  $w_1$ ,  $w_2$  and  $w_3$ , mm over the progress of optimization.

**Figure 4.7:** Evolution of design variables for Case-I optimization with superstrate thickness  $t_2 = 6.99$  mm shows the gradual convergence of the population.



For comparison, we calculate the fitness function value of the RCA presented in [136], which has three sections of equal widths in the superstrate, permittivity profile (10.2, 6.15, 3.27) and  $t = 7.62$  mm. The peak directivity of the antenna is 17.2 dBi, the 3-dB bandwidth is 60%, and the fitness of SLLs is 8.5 dB, which yield the fitness function (Eq. (4.9)) value of 516.92, which is much lower than that of all three optimized designs presented in this section.

#### 4.3.5 Optimization Case-II: RCA with Six-Sectional TPG

Case-II presents a more complex optimization problem. The RCA with six-sectional superstrate has been optimized for three different total diameter values  $D_1 = 38$  mm,  $D_2 = 48$  mm and  $D_3 = 58$  mm. An extended catalogue of materials' permittivity and thickness, as shown in Table 4.3, has been provided.

**Table 4.3:** Catalogue of RF laminates for Case-II optimization.

Dielectric constant	[1.96 2.2 2.94 3.27 3.5 4.5 6 9.2 9.8 10.2]
Thickness, mm	[3.81 5.08 6.35 6.99 7.62]

The population size for the Case-II optimization was increased to 70 due to the higher dimensionality of the problem, and the smoothing parameter  $\alpha_S$  was set to 0.6. The best optimization results for each diameter are summarised in Table 4.4. It can be seen that the highest peak directivity of 19.4 dBi and the lowest SLLs were obtained for the largest diameter ( $D_3 = 58$  mm) of the antenna. The optimized permittivity profile of the superstrate is (10.2, 9.2, 6, 4.5, 3.5, 3.5) and thickness is 6.99 mm. For this design, the stopping criterion defined in Section 4.3.3 was reached after 27 iterations in approximately 48 hours. Convergence plots for the Case-II optimization are shown in Fig. 4.8.

Optimization of the RCA with diameter  $D_1$  required 14 iterations, while RCAs with diameters  $D_2$  and  $D_3$  required 26 and 27 iterations, respectively. Fig. 4.9 shows that, over all 26 iterations, the constraint Eq. (4.5) of the fixed diameter is satisfied, i.e.,  $w_1 + w_2 + \dots + w_6 = D_2 = 48$  mm. Use of the Dirichlet distribution for the sampling of

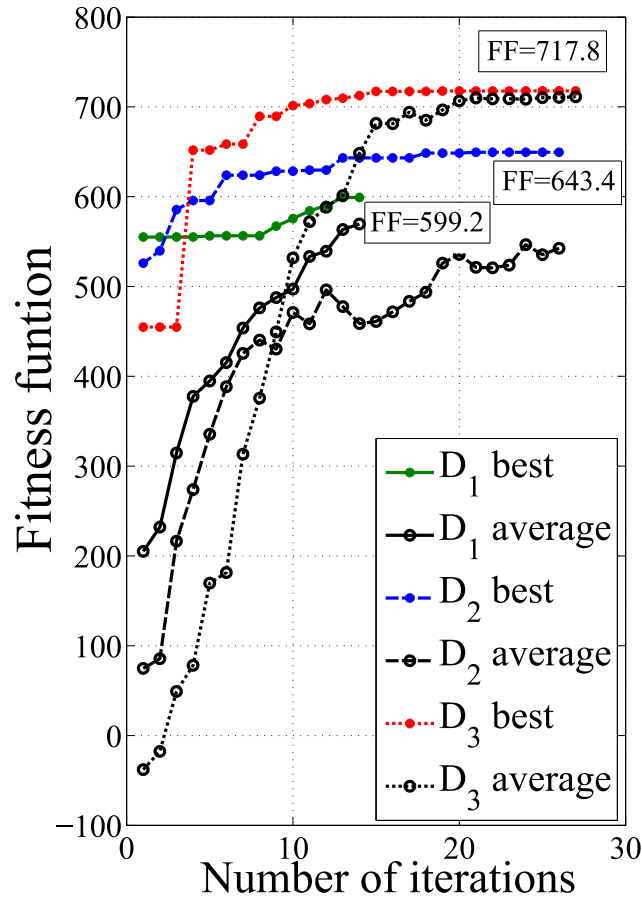
**Table 4.4:** Optimization Case-II Results for Three Predefined Superstrate Diameter Values ( $\lambda_0=26$  mm).

Antenna diameter	$D_1=38$ mm ( $1.5\lambda_0$ )	$D_2=48$ mm ( $1.85\lambda_0$ )	$D_3=58$ mm ( $2.2\lambda_0$ )
Superstrate section parameters			
$\varepsilon_1, w_1$	9.2, 2.59	9.2, 2.54	10.2, 7.92
$\varepsilon_2, w_2$	6, 1.93	9.2, 4.65	9.2, 6.62
$\varepsilon_3, w_3$	9.2, 2.57	9.2, 3.37	6, 4.47
$\varepsilon_4, w_4$	6, 2.35	6, 4.57	4.5, 2.92
$\varepsilon_5, w_5$	4.5, 7.25	4.5, 3.71	3.5, 3.39
$\varepsilon_6, w_6$	3.5, 2.31	3.5, 5.15	3.5, 3.68
$t$	6.99	6.99	6.99
$Dir_{peak}$ , dBi	17.8	18.5	19.4
BW, %	41	43	40
$F_{SLL}$ , dB	5.62	4.9	2.9
Fitness function, Eq. (4.9)	599.2	643.4	717.8

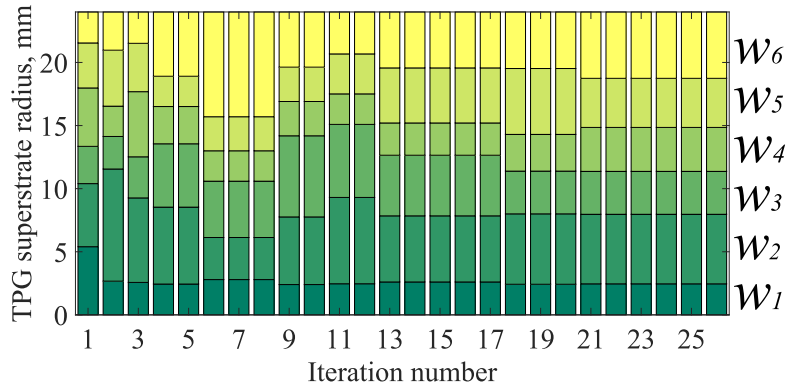
widths ensures an efficient optimization process, which is often not the case when the penalty approach is used.

The evolution of discrete and continuous design parameters over the progress of optimization Case-II is shown in Fig. 4.10. It can be observed from the figures that, as in Case-I, the samples were well spread over the entire search space (which is  $[1.96; 10.2]$  for permittivities), which means that the proposed method has good exploratory abilities. Also, it can be noted that the variance of the discrete variables reduced substantially after approximately 600 function evaluations, while for the continuous variables significant changes in the values continued for at least two times as long.

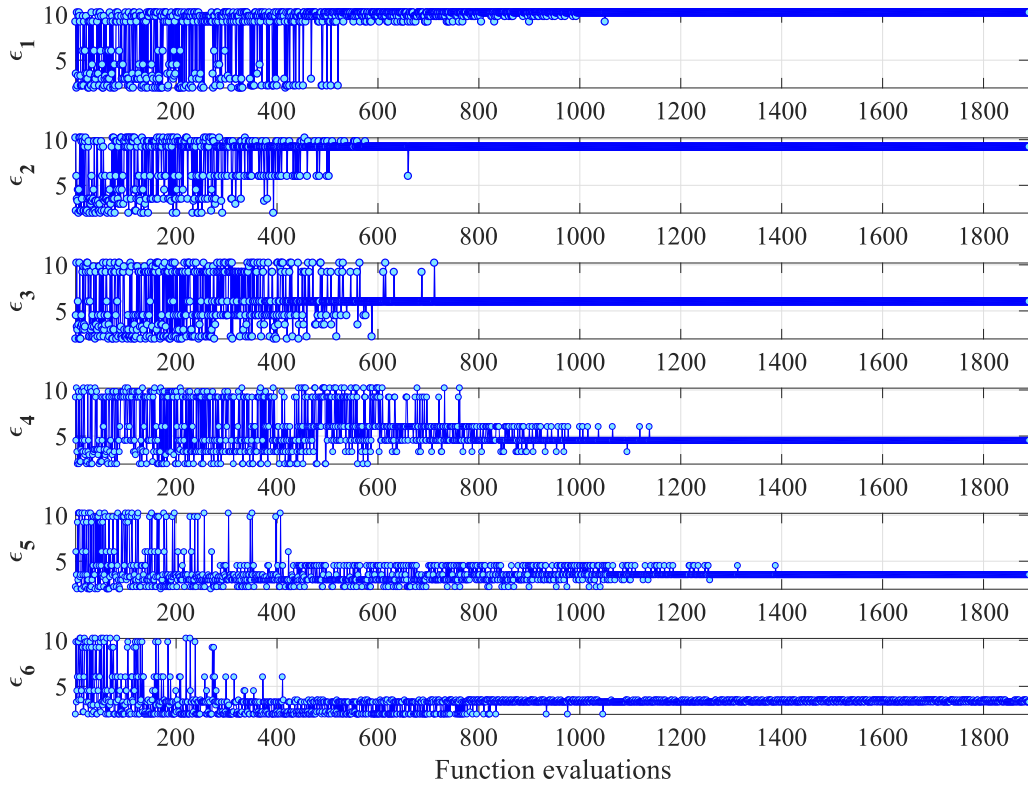
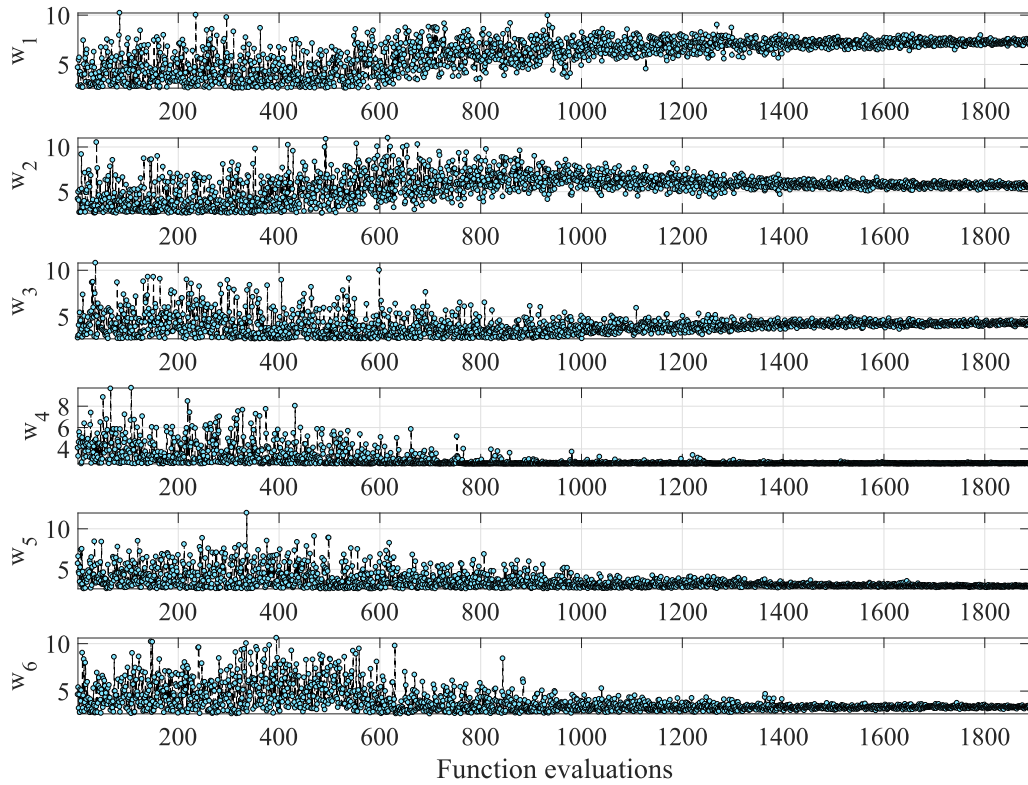
It is worth mentioning that the number of possible permittivity combinations in the superstrate of six sections when the library of RF laminates contains 10 values is one million ( $10^6$ ). Problems of such scale are not practical to handle using traditional grid-search methods with full-wave simulators.



**Figure 4.8:** Convergence results of the CE method for Case-II optimization of three compact RCAs with TPG superstrates, where  $t$  is the superstrate thickness and  $D$  is its diameter. For each optimization run, “best” is the best result observed so far, and “average” is the mean of all results observed at each iteration.



**Figure 4.9:** Case-II total section widths over iterations.

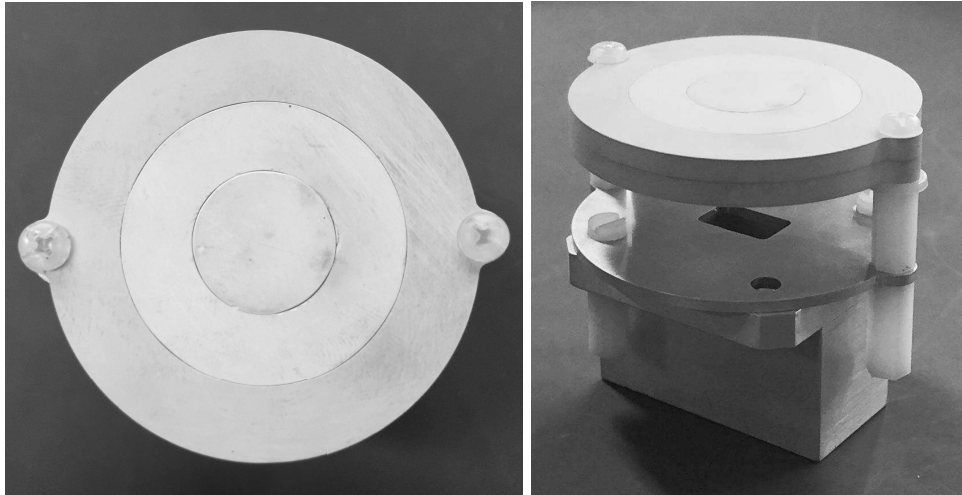
(a) Evolution of discrete variables  $\varepsilon_1, \dots, \varepsilon_6$ .(b) Evolution of continuous variables  $w_1, \dots, w_6$ .

**Figure 4.10:** Evolution of design variables for Case-II optimization with  $D_3$  over the progress of optimization shows the gradual convergence of the population.

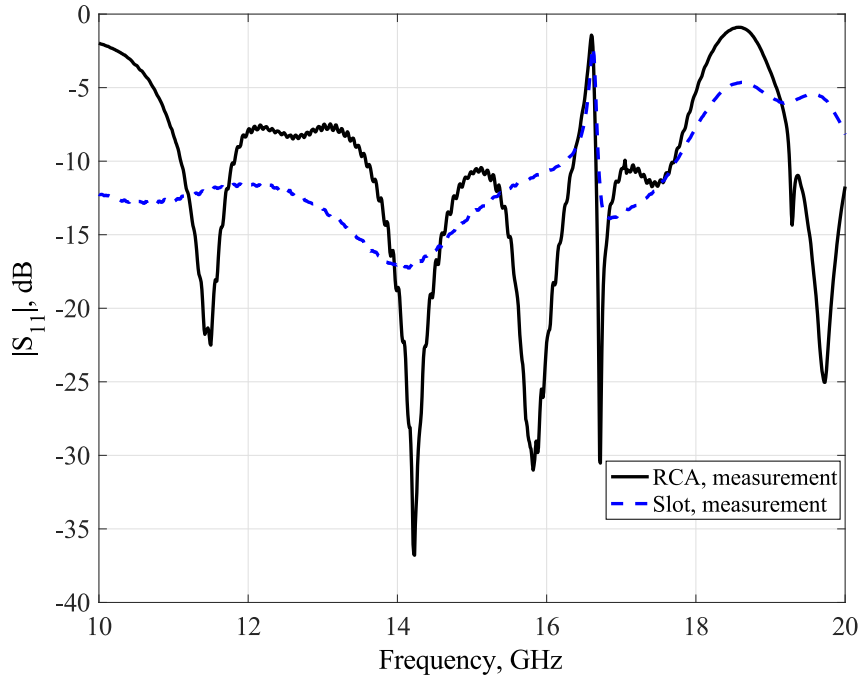
## 4.4 Experimental Results

To demonstrate the validity of the simulated results, one of the optimized RCAs, the design with a three-sectional superstrate with  $t_1=6.35$  mm and  $D = 48$  mm, has been fabricated. The prototype, shown in Fig. 4.11, was built by subtractive manufacturing using TMM10i ( $\epsilon_r = 9.8$ ), TMM10 ( $\epsilon_r = 9.2$ ) and TMM4 ( $\epsilon_r = 4.5$ ) Rogers laminates. Two nylon spacers supported the superstrate above the aluminium ground plane. A rectangular slot in a ground plane was fed by a coaxial-to-waveguide adapter WR-75 to excite the resonant cavity as the feed antenna. The slot dimensions were  $12 \times 7.5$  mm<sup>2</sup> after fine tuning to provide good impedance matching. The diameter of the ground plane was equal to the diameter of the superstrate (48 mm).

The measured input impedance matching for the fabricated RCA prototype and the slot antenna without the substrate is shown in Fig. 4.12. The effect of a superstrate loading on the input impedance of the slot can be observed. The RCA appears well-matched in the frequency range 11–18 GHz with a notch at 16.6 GHz due to the use of the WR-75 adapter as a feed, which can be substituted with a more broadband transition. The improvement of the reflection coefficient was not in the scope of this study and, thus, was not included in the objective function.



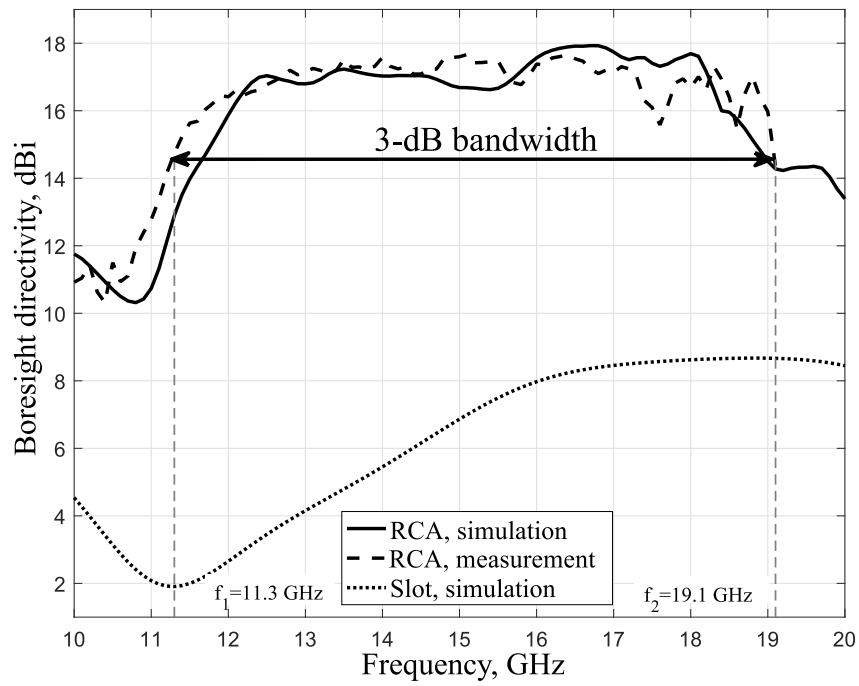
**Figure 4.11:** Fabricated prototype of the optimized RCA from Case-I study with superstrate thickness  $t_1=6.35$  mm. Two nylon spacers support the superstrate above the ground plane.



**Figure 4.12:** Measured reflection coefficient of the RCA prototype from Case-I study with superstrate thickness  $t_1=6.35$  mm. Impedance matching of the slot is shown for comparison.

The radiation characteristics of the prototype were measured in a spherical near-field measurement system at the Australian Antenna Measurement Facility (AusAMF). Fig. 4.13 shows the predicted and measured boresight directivity versus frequency. Overall, good agreement is noted between predicted and measured results. Discrepancy of the results between 17 and 18 GHz is attributed to the use of an approximate simulation model of the WR-75 coaxial-to-waveguide adapter. The measured peak directivity is 17.6 dBi, and the 3-dB directivity bandwidth extends from 11.3 to 19.1 GHz, featuring a 51% percentage bandwidth.

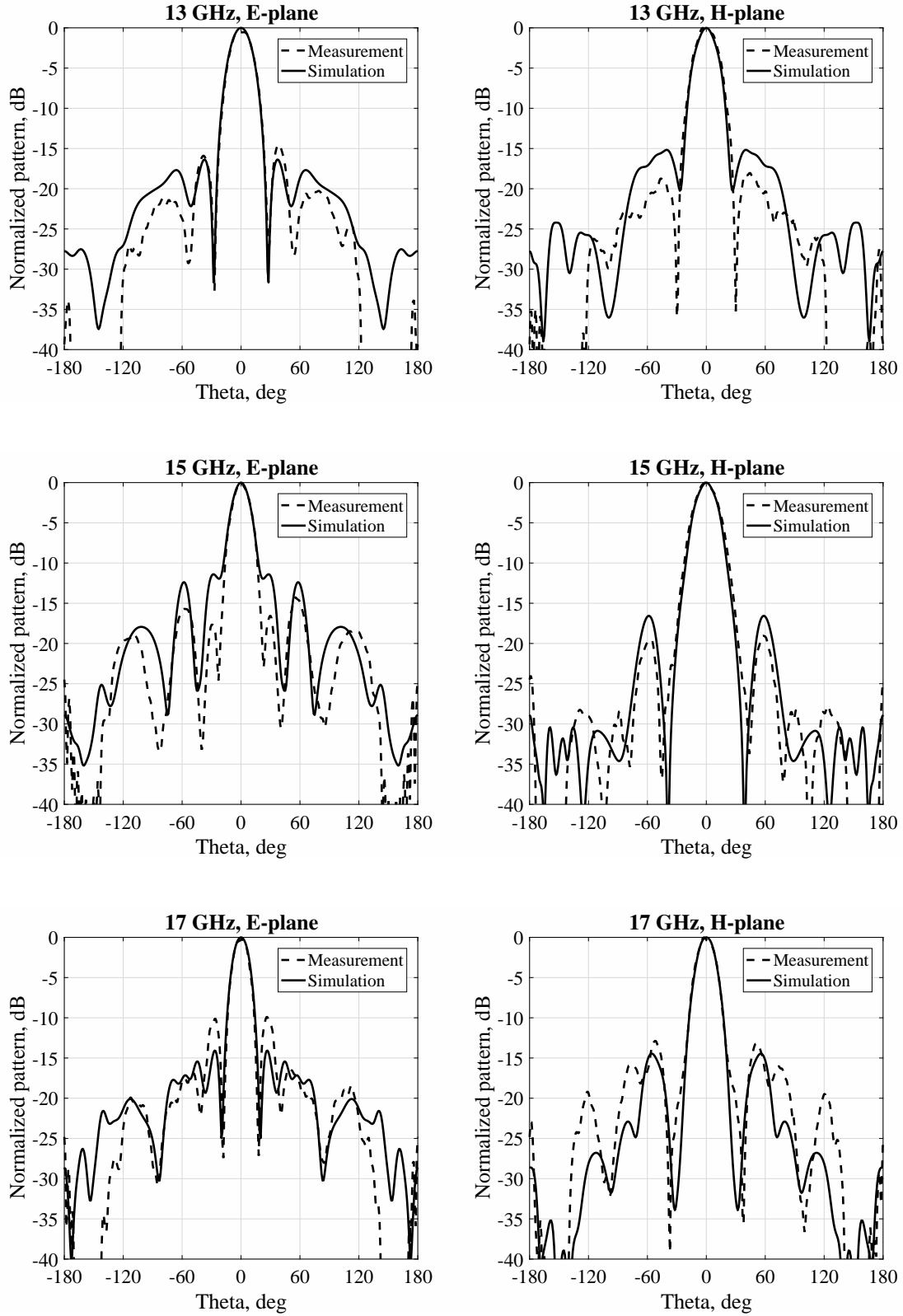
The comparison of the predicted and measured patterns in the E- and H-planes at three selected frequencies within the operating band are shown in Fig. 4.14. The predicted and measured beamwidths agree very well at all frequencies. Overall, the measured SLLs are less than  $-15$  dB in the H-plane, and less than  $-10$  dB in the E-plane (Table 4.5), except for 18 GHz, where SLL in the E-plane rises to  $-7$  dB. The front-to-back ratio is greater than 24 dB at all measured frequencies.



**Figure 4.13:** Measured boresight directivity of the prototype of the optimized RCA with the fitness function  $f(x)=624.6$ . Measured peak directivity is 17.6 dBi, and measured 3-dB directivity bandwidth is 51%.

**Table 4.5:** Measured SLLs of the RCA prototype.

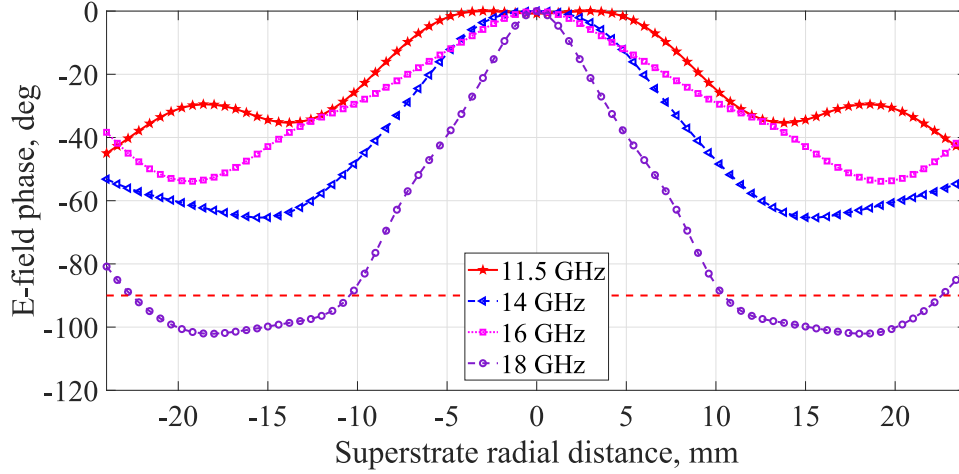
	13 GHz	14 GHz	15 GHz	16 GHz	17 GHz	18 GHz
<i>E-plane</i>	-14.5	-17.7	-16.5	-11.3	-10.2	-7.4
<i>H-plane</i>	-18.1	-16.5	-19.0	-15.0	-13.2	-13.5



**Figure 4.14:** Predicted and measured radiation patterns of the prototyped antenna at 13 GHz, 15 GHz and 17 GHz.



It is interesting to continue the observation of the E-field phase distributions above the superstrates for the optimized RCAs. Fig. 4.15 shows the spatial E-field phase distribution 3 mm above the RCA from Case-I study with  $t_1 = 6.35$  mm at the frequencies within the directivity bandwidth: 11.5, 14, 16 and 18 GHz. An effective in-phase aperture of this RCA is also 100% for the majority of the frequencies, which confirms that the uniformity of the E-field phase is required for large directivity bandwidths.



**Figure 4.15:** E-field phase distribution probed 3 mm above the optimized RCA from Case-I study with  $t_1 = 6.35$  mm.

## 4.5 Summary

A new optimization technique using the CE method is proposed for solving EM optimization problems with mixed variables and constraints. To the best of the author's knowledge, no classical PSO, GA or CMA-ES algorithm can solve the described optimization problem. By using sampling probability distributions that match the variable domain, six compact RCAs with improved performance as compared to the initial design have been produced by the CE method. The measurements of an antenna prototype validated the method and the predicted results. As CE is a universal optimization method, the introduced technique is applicable to any EM and RF optimization problem with both continuous and discrete parameters and/or constraints (for example, the total length of a device has a specified value). The next chapter compares the performance of three optimization algorithms on the continuous optimization problem of designing a broadband aperture-coupled microstrip patch antenna that can be used as a feed for RCAs.

*Be sure that, as you scramble up the ladder of  
success, it is leaning against the right building.*  
— Stephen Covey

## Chapter 5

# CE, PSO and CMA-ES in the Design of Wideband Antennas

In the previous chapters, the optimization of RCAs using PSO and CE has been discussed. In this chapter, the optimization results of an aperture-coupled microstrip patch antenna (ACMPA) using CE, PSO and CMA-ES are provided, and the performance of each algorithm is analysed. The designed wideband ACMPA with a 53% impedance bandwidth is integrated with a six-sectional TPG PRS to create a high-gain and wideband RCA with an improved planar feed antenna.

### 5.1 Introduction

With the constantly increasing demand for high data rates in wireless communication systems, it is essential for antennas to operate at wide bandwidths. At the same time, relentless miniaturisation requirements force antennas to have compact configurations. Although there is a number of alternative compact wideband printed antenna solutions employing monopole or slot antennas, microstrip patch antennas (MPA) offer the advantages of flat profile, low weight, medium gain of 5–10 dB and low cost. According to [163], broadband printed antennas can be classified according to the direction of radiation as bidirectional, when the antenna radiates at both sides of the ground plane, and single-directional, when the radiation is mostly concentrated on one side of the ground

plane. The MPA, which has a hemispherical radiation pattern, is the basic antenna type of the second group. In its simplest form, an MPA antenna consists of a radiating patch on one side of a dielectric substrate and a ground plane on the other side [164]. Since the first introduction in 1953 [165], MPAs have undergone enormous development and have been used in such applications as terrestrial and satellite communications, telemetry, navigation, off-body communications, biomedical and many others [166–170].

Increasing the bandwidth of MPAs has been the major challenge for antenna engineers for a long time, and broadband solutions with bandwidths of up to 60% have been achieved [171, 172]. One of the bandwidth-broadening techniques is to introduce additional resonant elements, such as slots or parasitic patches, with the resonant frequencies adjacent to each other and stack-tune the resonances. An MPA with an indirect excitation of the radiating patch through an aperture coupling (or, simply, slot-coupling) and one or more parasitic patches placed above is known as an aperture-coupled MPA (ACMPA). It has been shown that ACMPAs can have very wide common impedance and gain bandwidths of more than 70% [173–176] but at a cost of low front-to-back ratio.

Any bandwidth-broadening technique introduces additional degrees of freedom to the designs and thus increases their complexity. The strong mutual coupling between closely spaced elements makes it difficult to predict the influence of design parameters on the input impedance using manual design methods. Not only can optimization algorithms find a close-to-optimum solution, but also they can speed up the design process. PSO, DE and CMA-ES have been previously applied to the design of broadband and ultra-wideband antennas, including E-patch [98] and planar monopole [177], and some performance comparisons are available in the literature [20, 41, 109, 178–181]. As discussed in Section 2.5, the comparative studies do not intend to find the best algorithm for all antenna optimization problems, but rather they can shed some light on the question which algorithm steadily produces a better solution in shorter time frames for a particular problem. This knowledge is useful for future optimization of antenna problems that have design similarities.

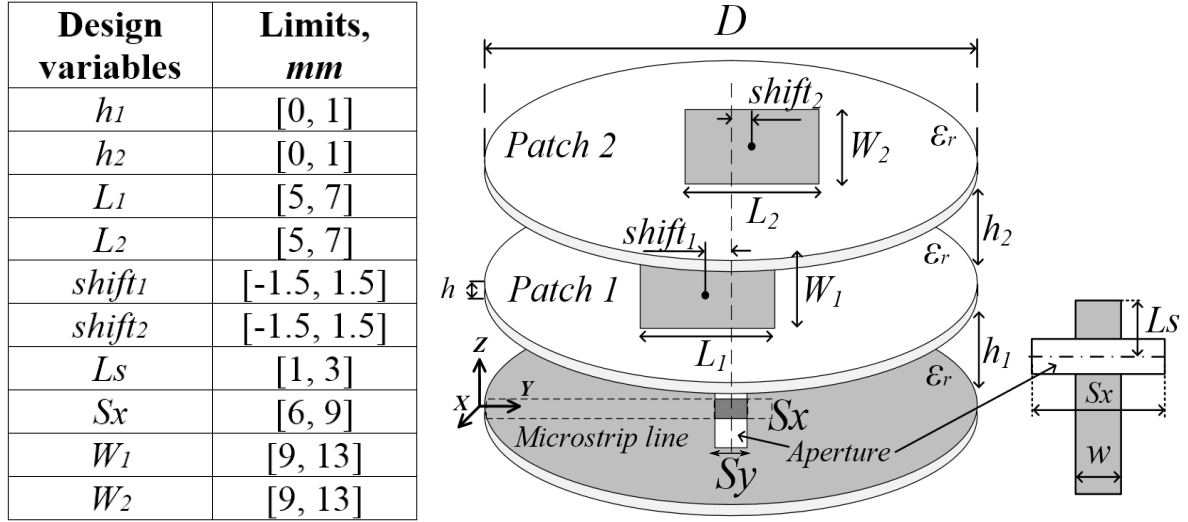
The optimization of an ACMPA and an RCA with an ACMPA as a feed is presented below. CE, PSO and CMA-ES have been implemented to achieve wide impedance bandwidth in the frequency range 12–18 GHz and a low profile of the antennas. First, the ACMPA without a superstrate is optimized, and the obtained results as well as the performance of the algorithms is compared. Then, the ACMPA is combined with the a six-sectional TPG PRS to create a compact wideband RCA, which is optimized using the three aforementioned methods.

## 5.2 Optimization of an ACMPA

This section presents the results of optimization of an ACMPA using CE, PSO and CMA-ES. In this section, we 1) describe the optimization approach using the CE method for a continuous bounded search space and 2) compare the optimization results of an ACMPA obtained by CE, PSO and CMA-ES. As CE is a relatively new optimization method for EM applications, this comparison is required for the assessment of its convergence properties. The comparison will be based on the number of function evaluations required for the convergence to the global solution and on the best fitness value obtained by each algorithm.

### 5.2.1 Problem Formulation

The geometry of the ACMPA is shown in Fig. 5.1, and the lower and upper limits for each design variable are given in the inset table. The antenna with the diameter  $D=60$  mm consists of three Rogers RT5880 laminates with a thickness of  $h=0.787$  mm and a relative permittivity of  $\varepsilon_r=2.2$ . The fixed parameters of the antenna are summarised in Table 5.1. The first substrate has a printed 50- $\Omega$  microstrip line ( $w=2.45$  mm) on one side and a ground plane with a coupling aperture of width  $S_y = 0.5$  mm and length  $S_x$  on the opposite side. The aperture is centred along the  $x$ -coordinate under the patch, to obtain low cross-polarisation levels. The excitation of the aperture is controlled by the length of an open-circuit stub  $L_s$ . The aperture has a significant affect on the coupling to the



**Figure 5.1:** Geometry of the optimized ACMPA. Inset table shows the lower and upper limits of the design variables.

first patch of width  $W_1$  and length  $L_1$ . The size of the first patch is a very important factor in impedance matching as it comes in between the aperture and the top patch of dimensions  $W_2 \times L_2$ .

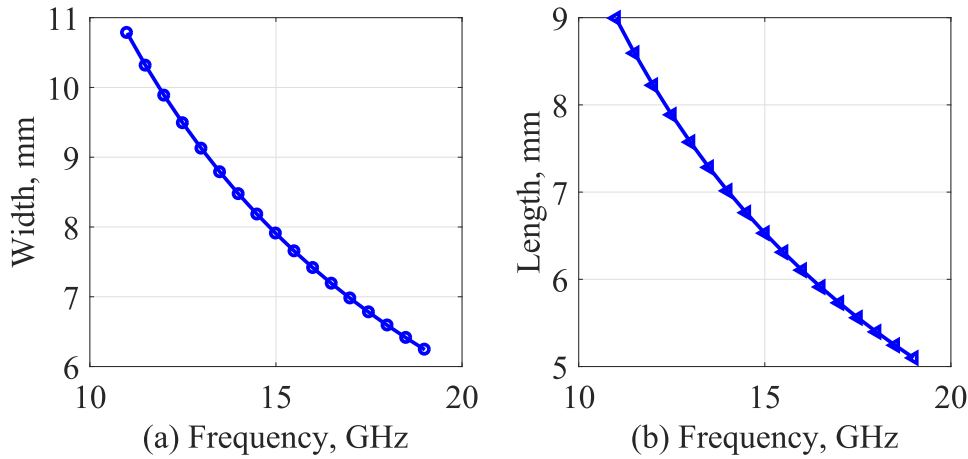
Broadband impedance matching in the ACMPA is achieved by stagger-tuning of the resonances. The aperture in the ground plane has a resonant length and allows the coupling of the resonant patches to the feedline resulting in three closely spaced resonances. For the maximum bandwidth and efficiency, the patches are separated from each other by air gaps  $h_1$  and  $h_2$ , and the thin dielectric substrates are only used for the support of the printed patches. Lower values of  $h_1$  and  $h_2$  are preferred in order to have a low-profile antenna, but they also increase the coupling between the aperture and the patches. It can be seen that two contradicting requirements are imposed on the design, i.e., wide impedance bandwidth and low antenna profile. However, decreasing the thickness of the dielectric layers in microstrip antennas results in less impedance bandwidth. To solve

**Table 5.1:** Fixed ACMPA parameters.

$D$ , mm	$h$ , mm	$\epsilon_r$	$w$ , mm	$S_y$ , mm
60	0.787	2.2	2.45	0.5

this problem, two more variables,  $shift_1$  and  $shift_2$ , have been introduced as proposed in [182]. They determine the shift of the patches in the  $y$  direction from the middle of the superstrates and help to achieve a larger impedance bandwidth with reduced thickness of the antenna.

In order to choose the lower and upper limits, theoretical calculations and a quick sensitivity analysis using a grid search have been performed. The theoretical dimensions of the patches have been calculated using the equations from [183], and the width and length of a microstrip patch on a given substrate as a function of the design frequency are shown in Fig. 5.2. For the frequency band between 10 and 20 GHz, the optimal width of an MPA changes from 11 to 6 mm, and the length changes from 9 to 5 mm. These dimensions can be used as reference values, but they are not accurate because the cavity model, which is a simplification of a patch antenna, has been used to devise the equations.



**Figure 5.2:** Theoretical dimensions of a microstrip patch.

Sensitivity analysis is usually performed to quantify the contribution of the design variables to a possible improvement of a model response. Unfortunately, sufficiently accurate sensitivity methods require huge numerical effort due to the large number of simulations [184]. Therefore, a quick sensitivity check has been performed to find appropriate ranges for the design variables. To meet the requirement of a low profile, the air gaps between the substrates have been limited to the range of  $[0,1]$  mm. It can be seen from Fig. 5.3(a) that even small variations in  $h_1, h_2$  significantly affect the input

impedance. The sensitivity of other design variables is displayed in Fig. 5.3(a)–(e), where the grey dashed lines determine the desired  $|S_{11}|$  response. The widths of patches are less-sensitive parameters and, therefore, their ranges have been extended to [9, 13] mm. According to [165], the two patches are usually very close in size with the top element being slightly larger than the bottom element. Also, it has been previously observed that for impedance matching the relative dimensions of two patches are important as opposed to their absolute dimensions [164]. Parameters  $shift_1$  and  $shift_2$  vary between narrow limits  $[-1.5, 1.5]$  mm to avoid significant asymmetry in the radiation patterns.

The optimization goal is to obtain a magnitude of the reflection coefficient below  $-10$  dB ( $|S_{11}| \leq -10$  dB) across the frequency band 12–18 GHz. To ensure this, the input impedance is analysed in the range 11–19 GHz, and the fitness function to be maximized has been defined as:

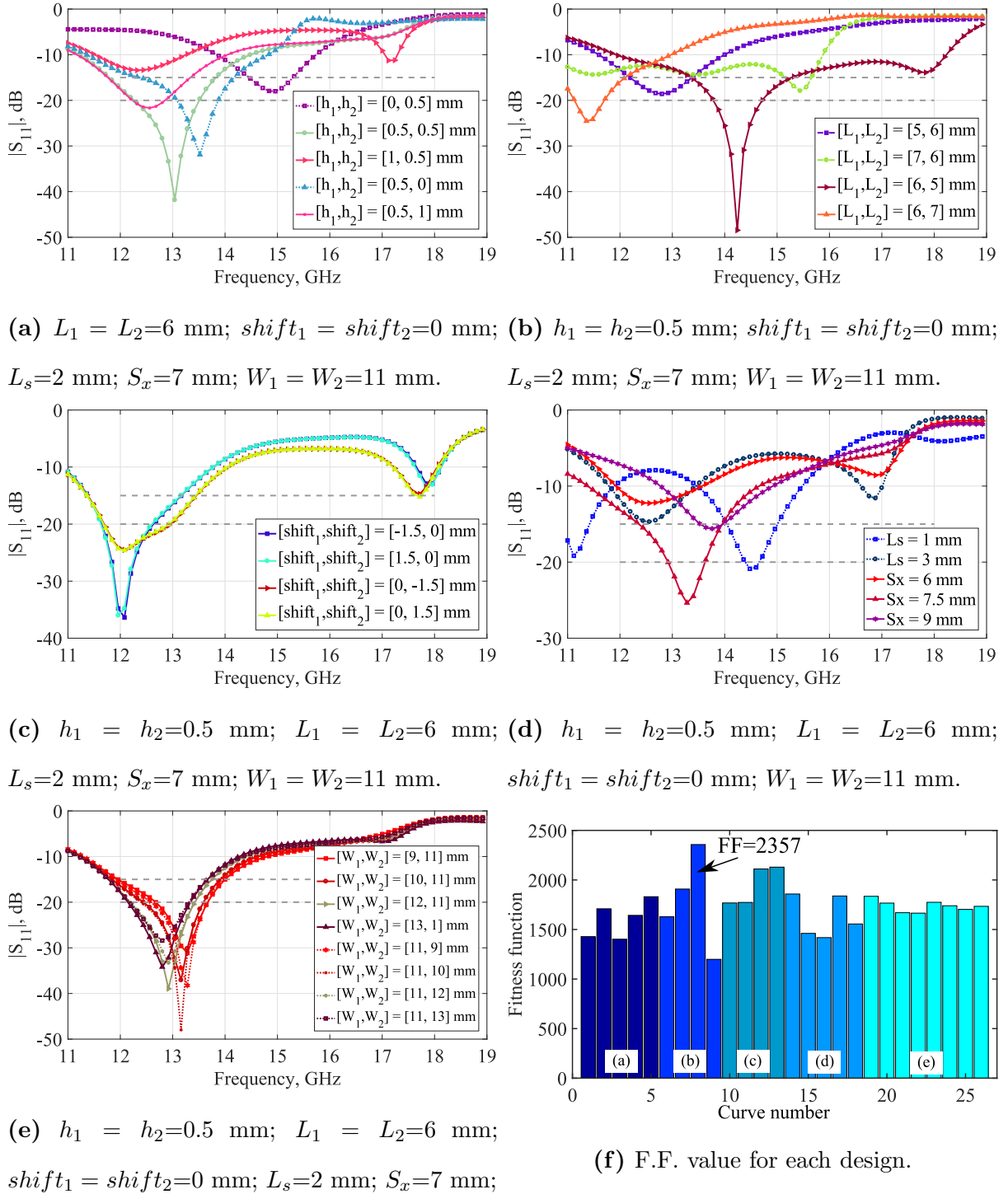
$$F.F. = -\left(\sum_{f_i=11 \text{ GHz}}^{19 \text{ GHz}} L(f_i)\right), \quad (5.1)$$

where

$$L(f_i) = \begin{cases} S_{11}(f_i), & \text{if } S_{11}(f_i) \geq -15 \text{ dB}, \\ -20, & \text{if } -20 \text{ dB} \leq S_{11}(f_i) < -15 \text{ dB}, \\ -35 - S_{11}(f_i), & \text{if } -35 \text{ dB} \leq S_{11}(f_i) < -20 \text{ dB}, \\ 0, & \text{if } S_{11}(f_i) < -35 \text{ dB} \end{cases} \quad (5.2)$$

and  $f_i = 11, \dots, 19$  GHz with  $i=1, \dots, 201$  frequency points. Proposed in [161], Eq. (5.2) gradually penalises designs with the reflection coefficient lower than  $-20$  dB in order to achieve larger impedance bandwidth. This fitness function works well for wideband antennas because the desired  $S_{11}$  is usually between  $-15$  and  $-20$  dB, and it is known in advance that a  $-30$  dB matching level in a wide frequency band is not realistic to obtain. Fig. 5.3(f) shows the calculated fitness function values for all designs from the sensitivity analysis. It can be observed that the best manually found solution has  $F.F. = 2357$ .





**Figure 5.3:** Sensitivity analysis of the design variables. Grey dashed lines show the desired  $S_{11}$  response.

### 5.2.2 Optimization Methodology

The given ACMPA optimization problem is a classic continuous optimization problem with a bounded solution space. It has ten continuous design variables ( $d=10$ ):

$$\mathbf{x} = (h_1, h_2, L_1, L_2, shift_1, shift_2, L_s, S_x, W_1, W_2). \quad (5.3)$$

The optimization has been carried out independently by CE, PSO and CMA-ES with the fitness function given in Eq. (5.1).

As the search space of this optimization problem is continuous and bounded, we used a beta distribution family to sample the populations. Although a normal distribution can also be used for sampling continuous variables, the use of a beta distribution ensures that every sample stays within the defined limits.

The flow of the CE method is as follows:

1. Initialise iteration count  $t = 0$ . Initial distribution parameters  $v^t = (\alpha^t, \beta^t) = 1$ .
2. Create the beta distribution  $B(\mathbf{x}; v^t)$  using Eq. (2.7).
3. Randomly sample  $N_{pop}$  candidates from the beta distribution  $B(\mathbf{x}; v^t)$ .
4. Evaluate the fitness function of each candidate.
5. Sort the candidates and choose the elite of size  $N_{el}$ .
6. Using a maximum likelihood estimation, find such  $(\alpha^{t+1}, \beta^{t+1})$  that best describe the elite distribution.
7. (optional) Smooth  $(\alpha^{t+1}, \beta^{t+1})$  according to the equations:

$$\alpha^{t+1} = \alpha^t + \alpha_s * (\alpha^{t+1} - \alpha^t), \quad (5.4)$$

$$\beta^{t+1} = \beta^t + \alpha_s * (\beta^{t+1} - \beta^t). \quad (5.5)$$

8. Update iteration count  $t = t + 1$ .
9. Repeat the steps 2–8 until the stopping criterion is met.

The input parameters required for CE, PSO and CMA-ES that were set in this optimization are given in Table 5.2. The population size  $N_{pop}$  for CMA-ES was found using

$$N_{pop} = (4 + \text{round}(3 * \log(d))) = 11, \quad (5.6)$$

given that the number of design variables  $d = 10$  in this case. Other parameters were set to their default values.

It is worth mentioning that CE and CMA-ES have some resemblance in operating principles. Both algorithms are model-based, i.e., they use probability distributions (also called models) for sampling the populations, rank the solutions and choose the elite subpopulations. There are two principal differences between CE and CMA-ES. The first difference is in the updating mechanism as discussed in Section 2.5. CMA-ES creates new candidates by learning the covariance matrix, while CE does it using the maximum likelihood estimation. The second difference lies in the population sampling. In CMA-ES, populations are generated by sampling from a multivariate normal distribution, while in CE, any distribution family can be used for sampling.

As in the previous implementation, the stopping criterion for the CE optimization is the population diversity. The run is considered converged when the average difference between the candidates in an elite subpopulation is less than the threshold  $\delta=0.5$  mm. This stopping criterion helps to avoid unnecessary computations of very similar designs and, thus, to reduce the total optimization time. For PSO and CMA-ES, the stopping criterion was a maximum number of iterations  $N_{it}$  equal to 30 and 1000, respectively.

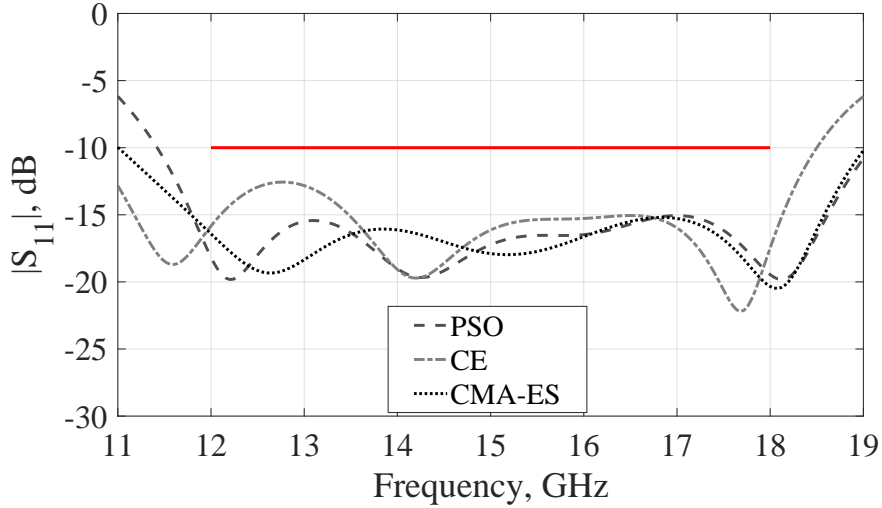
The CE algorithm converged after 24 iterations and 1200 function evaluations. The time required for the full optimization was approximately 32 hours using an Intel Core i7, 3.6 GHz processor with 32 GB of RAM. With the population size 50, the number of function evaluations for PSO has been predefined to 1500. While the population size of CMA-ES was the smallest, the NFE reached 1815.

**Table 5.2:** Input parameters for CE, PSO and CMA-ES.

CE	PSO	CMA-ES
<ul style="list-style-type: none"> <li>Population size</li> </ul> $N_{pop} = 50$	<ul style="list-style-type: none"> <li>Population size</li> </ul> $N_{pop} = 50$	<ul style="list-style-type: none"> <li>Population size</li> </ul> $N_{pop} = 11$
<ul style="list-style-type: none"> <li>Elite subpopulation size</li> </ul> $N_{el} = 10$	<ul style="list-style-type: none"> <li>Acceleration coefficients</li> </ul> $c_1 = c_2 = 1.49$	
<ul style="list-style-type: none"> <li>Smoothing coefficient</li> </ul> $\alpha_S = 0.5$	<ul style="list-style-type: none"> <li>Inertia weight</li> </ul> $w_{max} = 0.9, w_{min} = 0.1$	
	<ul style="list-style-type: none"> <li>Number of iterations</li> </ul> $N_{it} = 30$	
	<ul style="list-style-type: none"> <li>Velocity clamping factor</li> </ul> $V_{cf} = 1.8$	

### 5.2.3 Optimization Results

The input reflection coefficients of the ACMPAs optimized by CE, PSO and CMA-ES for the fitness function given in Eq. (5.1) are shown in Fig. 5.4. It can be seen that all the optimized antennas are well matched in the range of 12–18 GHz with  $|S_{11}| \leq -10$  dB. The best design was achieved by CMA-ES and has a fractional bandwidth of 53%.



**Figure 5.4:** Reflection coefficients of the ACMPAs optimized by PSO, CE and CMA-ES.

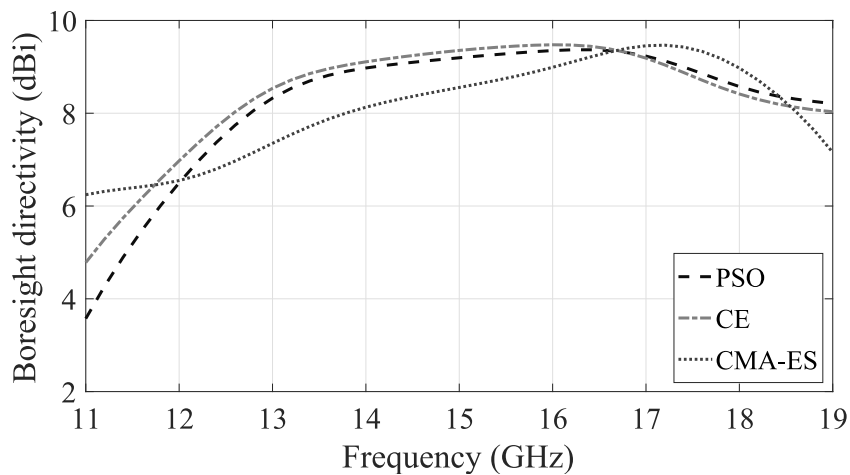
Optimized design parameters of the best ACMPAs obtained by PSO, CE and CMA-ES are given in Table 5.3. Most of the design variables in the solutions obtained by PSO and CE have very similar values. For instance, the resonant lengths of the aperture  $L_s$  and the patches  $W_1, W_2$  have dimensions (6.3, 9.4, 10.8) mm for PSO and (6.8, 9.5, 10.9) mm for CE, and the values of  $shift_1, shift_2$  for PSO and CE are (−0.46, 1.5) mm and (−0.4, 1.3) mm, respectively.

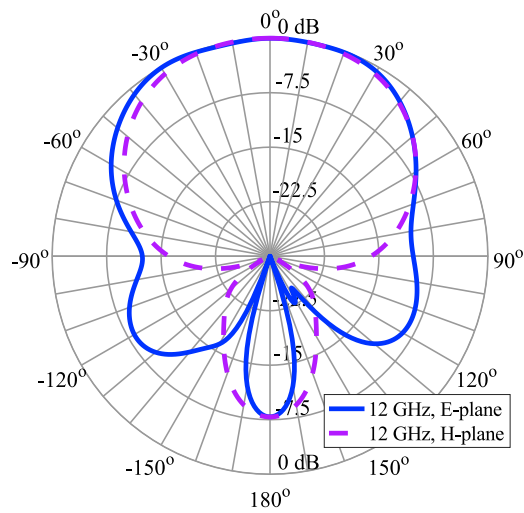
The CE-optimized ACMPA design has a significantly higher fitness function value of 3470.2 compared to the one obtained manually with  $F.F. = 2357$ . Although CMA-ES produced the result with the highest  $F.F.$ , many of the optimal design parameters exceed the given boundaries. This is attributed to use of the Gaussian distribution for sampling in CMA-ES, that intrinsically has an unbounded support.

**Table 5.3:** Dimensions and F.F. of the best ACMPA solutions.

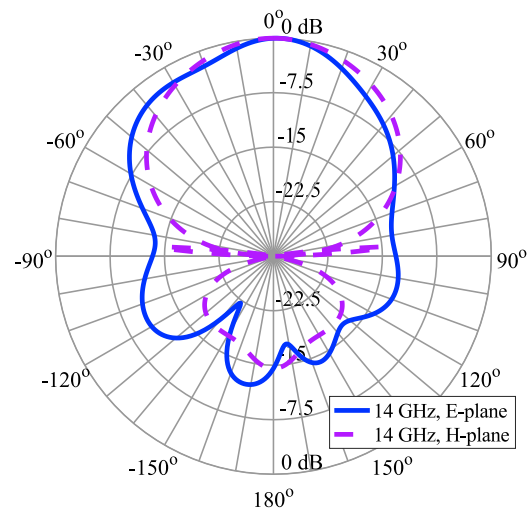
Design variables, mm	CE	PSO	CMA-ES
$h_1, h_2$	0.47, 0.75	0.55, 0.98	1.4, 1.9
$L_1, L_2$	6.2, 5.3	5.94, 5.0	6.9, 4.7
$shift_1, shift_2$	-0.4, 1.3	-0.46, 1.5	-0.92, 3.4
$L_s, S_x$	1.6, 6.8	1.4, 6.3	3.6, 15.9
$W_1, W_2$	9.5, 10.9	9.4, 10.8	12.3, 9.8
<i>F.F.</i> , Eq. (5.1)	3470.2	3743.2	<b>3780.9</b>

The boresight directivity curves of three optimized ACMPAs are shown in Fig. 5.5. The boresight directivity changes from 7 to 9.5 dBi across the frequency range 12–18 GHz. Larger variations in the boresight directivity across the bandwidth can be seen for the CMA-ES solution than for the PSO and CE solutions. This is attributed to the significant shift of the second patch from the middle of the structure. The radiation patterns at 12, 14, 16 and 18 GHz for the CE solution are given in Fig. 5.6. The E-plane corresponds to the zy plane in Fig. 5.1, and the H-plane corresponds to the zx plane. In the majority of the frequency band, the patterns in E plane remain near-broadside. The cross-polarisation levels are below -25 dB for most of the band and rise to -12 dB at 18 GHz.

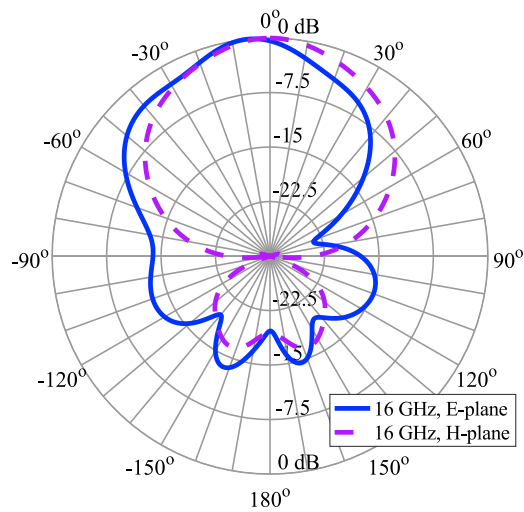
**Figure 5.5:** Boresight directivity of the optimized ACMPAs.



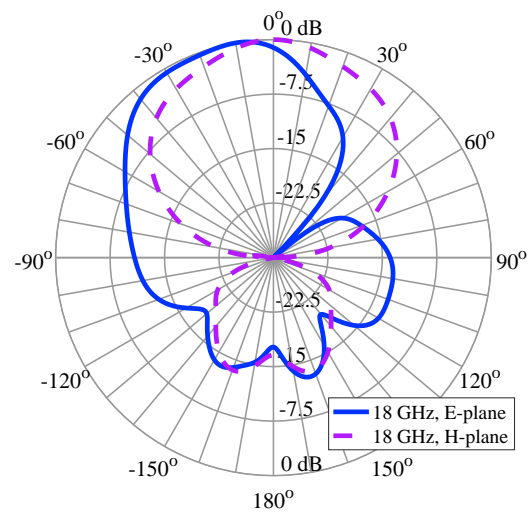
(a) 12 GHz



(b) 14 GHz



(c) 16 GHz



(d) 18 GHz

**Figure 5.6:** Radiation patterns of the CE-optimized ACMPA.

### 5.3 Optimization of RCA with ACMPA Feed

In this section, an ACMPA antenna is proposed as an alternative feed solution for RCAs. A wideband high-gain RCA is designed by integrating the ACMPA described in the previous section with the all-dielectric TPG superstrate from Chapter 4. PSO, CE and CMA-ES have been applied to optimize the input impedance of the proposed design, and the algorithms' performances have been analysed.

For a long time, a narrow bandwidth has been the main limitation of RCAs that impeded their use in wideband communication systems, such as telemetry, point-to-point and satellite communications. A feed antenna that excites a resonant cavity in RCAs has a critical effect on both impedance and radiation bandwidths. While most recent bandwidth-improvement techniques have been concentrated on the radiation characteristics of the RCAs, in practice, a shared radiation and impedance bandwidth is required. In many reported radiation bandwidth improvement techniques, the impedance bandwidth is either shifted in frequency [185,186], or does not cover the full radiation band [187–189]. Therefore, there is a need for a wideband planar feed solution that can accommodate for the wide directivity bandwidths. Some common feed techniques in RCAs include:

- square patch with very narrow impedance bandwidth of  $\approx 1\%$  [190];
- E-patch with the impedance bandwidth of 5.6% [151];
- dual slot fed by a microstrip line with 11% bandwidth [133,191];
- slot-coupled patch with the impedance bandwidth of 26% [129] and 35% [192];
- bowtie antenna with 40% impedance bandwidth and circular polarisation [193];
- waveguide-fed slot antenna with the bandwidth of 35–45% [189,194];

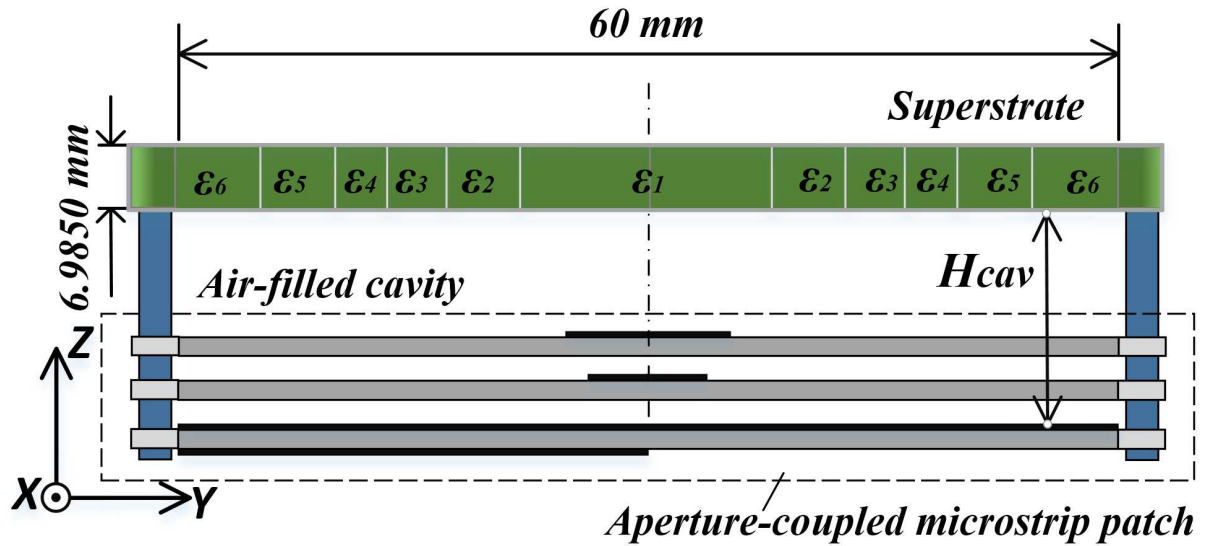
By far the most common feed is a waveguide-fed slot antenna. However, its bandwidth is usually limited to 40%, and it is not a completely planar solution because a waveguide or a coax-to waveguide adapter that is used for the slot excitation protrudes outside the ground plane. ACMPCAs have previously been designed that have up to 60–70%



impedance bandwidths. Therefore, an ACPMA is a potential candidate for use in RCAs. The advantage of using ACPMAs for the cavity excitation is that the ground plane of a microstrip line can also serve as a metal plate of a resonant cavity. Thus, an ACPMA with a PRS placed on top at a half-wavelength distance can form a high-gain wideband RCA with a low-profile feed.

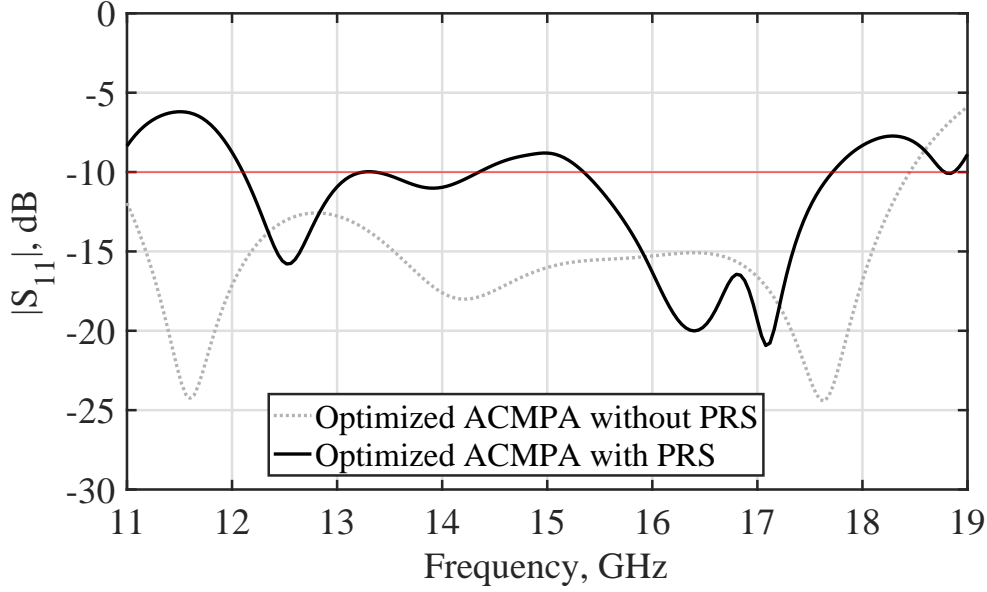
### 5.3.1 Design of an RCA with an ACPMA Feed

Fig. 5.7 shows an RCA constructed from an ACPMA with a six-sectional all-dielectric TPG PRS placed on top.



**Figure 5.7:** Geometry of the RCA with an ACPMA feed. The PRS is an all-dielectric TPG superstrate of diameter  $D=60$  mm and thickness  $t=6.985$  mm.

The fixed design parameters of the ACPMA remain the same as given in Fig. 5.1 and Table 5.1. The TPG superstrate that was presented in Section 4.3.5 with the thickness of  $t=6.985$  mm and the permittivity distribution  $(\varepsilon_1, \dots, \varepsilon_6)=(10.2, 9.2, 6, 4.5, 3.5, 3.5)$  has been taken for this design. The permittivity gradient is created by dividing the superstrate into six circular sections of widths  $(w_1, \dots, w_6)=(7.92, 6.62, 4.47, 2.92, 3.39, 3.68)$  mm. The cavity height  $H_{cav}$  equals 13 mm, which corresponds to  $0.5\lambda_0$ , where  $\lambda_0=26$  mm is the free-space wavelength of the first resonance frequency of the cavity.



**Figure 5.8:** Reflection coefficient of the CE-optimized ACMPA (Table 5.3) before and after placing the PRS on top.

Fig. 5.8 shows that the input impedance of the CE-optimized ACMPA deteriorates when it is loaded with a highly-reflective superstrate. Therefore, to achieve a broadband impedance bandwidth of this RCA, the ACMPA with the presence of the PRS has been optimized again using PSO, CE and CMA-ES.

### 5.3.2 Optimization Details

When the superstrate is placed above the ACMPA, a resonant cavity is created. The strong reflections between the TPG superstrate and the ground plane make impedance matching very difficult. Therefore, the requirements in the fitness function have been relaxed to the following:

$$F.F. = -\left( \sum_{f_i=11 \text{ GHz}}^{19 \text{ GHz}} L(f_i) \right), \quad (5.7)$$

where

$$L(f_i) = \begin{cases} S_{11}(f_i), & \text{if } S_{11}(f_i) \geq -10 \text{ dB}, \\ -15, & \text{if } -15 \text{ dB} \leq S_{11}(f_i) < -10 \text{ dB}, \\ -30 - S_{11}(f_i), & \text{if } -30 \text{ dB} \leq S_{11}(f_i) < -15 \text{ dB}, \\ 0, & \text{if } S_{11}(f_i) < -30 \text{ dB} \end{cases} \quad (5.8)$$

and  $f_i=11, \dots, 19$  GHz with  $i=1, \dots, 201$  frequency points. Again, this formulation of the fitness function intentionally suppresses the candidates with  $S_{11} < -30$  dB at any frequency within the band for the sake of a wideband matching.

The settings for each algorithm are summarised in Table 5.4. The population size  $N_{pop}$  for CMA-ES is calculated using Eq. (5.6) with  $d=10$ .

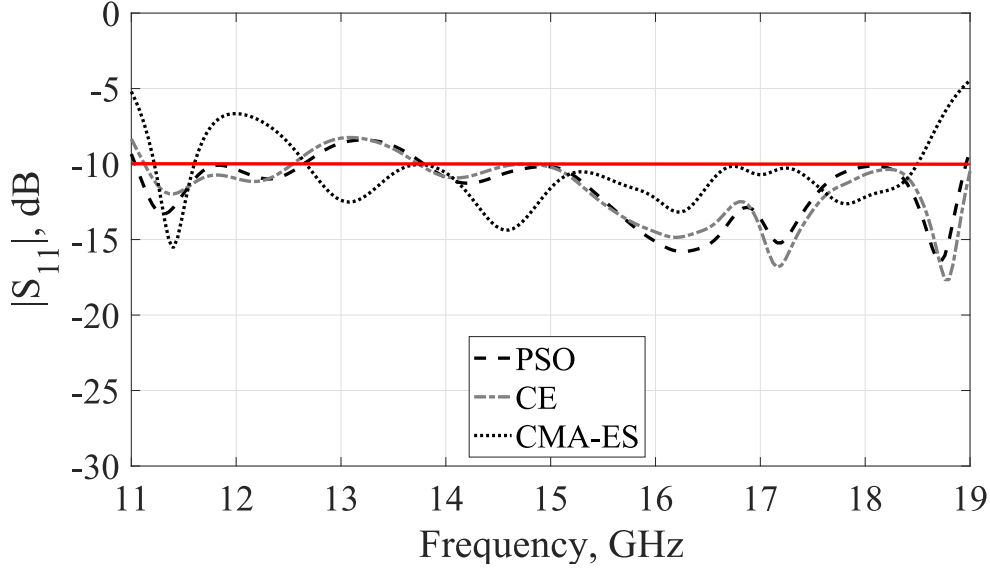
**Table 5.4:** Input parameters for CE, PSO and CMA-ES.

CE	PSO	CMA-ES
<ul style="list-style-type: none"> <li>Population size</li> </ul>	<ul style="list-style-type: none"> <li>Population size</li> </ul>	<ul style="list-style-type: none"> <li>Population size</li> </ul>
$N_{pop} = 50$	$N_{pop} = 30$	$N_{pop} = 11$
<ul style="list-style-type: none"> <li>Elite subpopulation size</li> </ul>	<ul style="list-style-type: none"> <li>Acceleration coefficients</li> </ul>	
$N_{el} = 6$	$c_1 = c_2 = 1.49$	
<ul style="list-style-type: none"> <li>Smoothing coefficient</li> </ul>	<ul style="list-style-type: none"> <li>Inertia weight</li> </ul>	
$\alpha_S = 0.8$	$w_{max} = 0.9, w_{min} = 0.1$	
	<ul style="list-style-type: none"> <li>Number of iterations</li> </ul>	
	$N_{it} = 30$	
	<ul style="list-style-type: none"> <li>Velocity clamping factor</li> </ul>	
	$V_{cf} = 1.8$	

### 5.3.3 Results

Fig. 5.9 provides the impedance matching results of the best optimized RCAs. The CE solution has the reflection coefficient  $S_{11} \leq -10$  dB in the band 11–19 GHz except for the increase to  $-8.5$  dB around 13 GHz. The PSO solution has a very similar input

impedance across the whole frequency band, and the CMA-ES solution has a reflection coefficient increasing up to  $-6.8$  dB between 11.6 and 12.7 GHz.



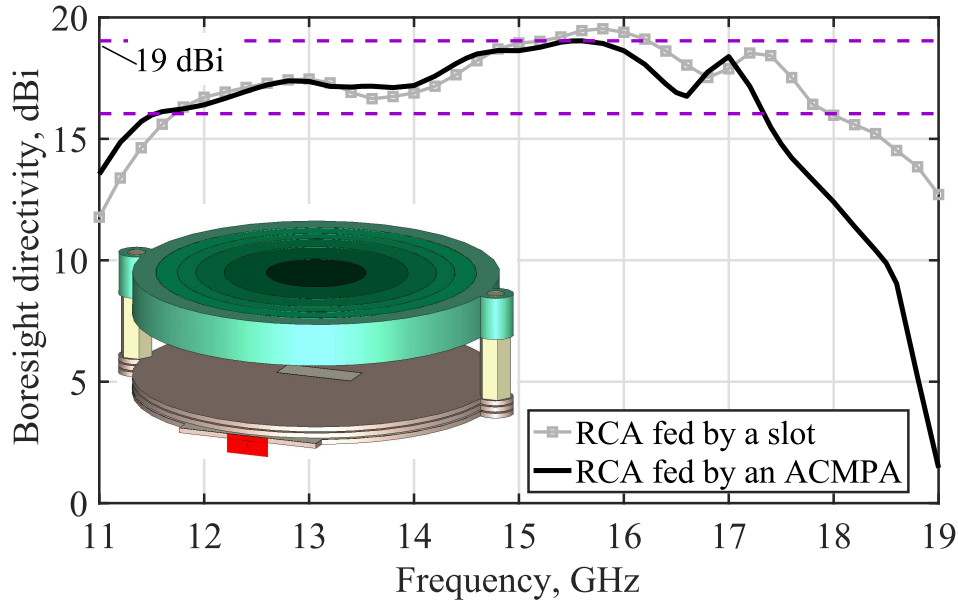
**Figure 5.9:** Reflection coefficient of the RCAs optimized by PSO, CE and CMA-ES.

The dimensions of the best ACMPA designs obtained by PSO, CE and CMA-ES are summarised in Table 5.5. The highest fitness  $F.F. = 2825.8$  is found by PSO, and the CE solution has  $F.F. = 2789.7$ . Both CE and PSO converged after 900 NFE. In comparison to the ACMPA in Section 5.2, the RCA model is much more complex, and its single simulation requires much more time. Particularly, the CE optimization took 241178.15 sec, which is almost 3 days. PSO took approximately the same overall optimization time because of the same number of function evaluations. CMA-ES with  $N_{pop} = 11$  took more than twice longer and was stopped after 205 iterations because of no improvement for 45 consecutive iterations.

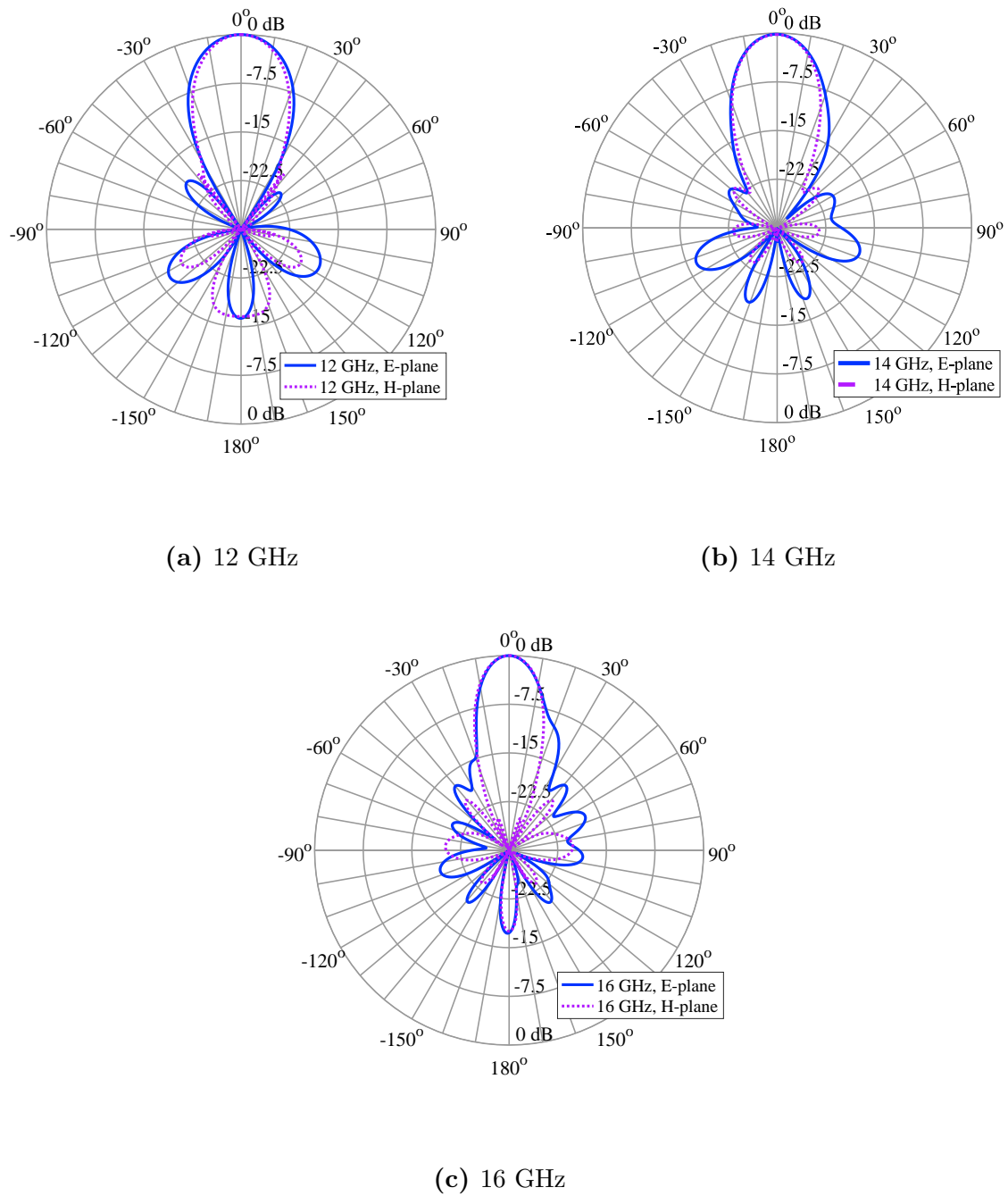
The boresight directivity of the CE solution is shown in Fig. 5.10 with an ACMPA-fed RCA depicted in an inset. The peak directivity is 19 dBi, and the 3-dB bandwidth is from 11.5 to 17.2 GHz, which is 40%. For comparison, the boresight directivity of the slot-fed RCA presented in Section 4.3.5 is also given in the graph. Its peak directivity is 19.4 dBi, and the bandwidth is also 40% (Table 4.4). With just a 0.4 dB reduction in the peak directivity, ACMPA design provides an alternative feed solution resulting in a much lower RCA profile.

**Table 5.5:** Dimensions and F.F. of the best ACMPA-fed RCA solutions.

Design variables (mm)	CE	PSO	CMA-ES
$h_1, h_2$	0.19, 0.56	0.26, 0.24	0.58, 0
$L_1, L_2$	5.75, 5.29	5.82, 5.03	2.75, 4.21
$shift_1, shift_2$	0.41, -0.72	-0.57, -1.5	-2.05, 0.36
$L_s, S_x$	2.0, 6.32	1.83, 6.52	1.16, 6.56
$W_1, W_2$	9.06, 10.87	10.38, 12.99	12.36, 9.54
$F.F.$ , Eq. (5.7)	2789.7	<b>2825.8</b>	2669.4

**Figure 5.10:** Boresight directivity comparison of the slot-fed RCA and the ACMPA-fed RCA optimized by CE (shown in an inset).

Radiation patterns at 12, 14 and 16 GHz of the CE-optimized design are provided in Fig. 5.11. It can be seen that the RCA has a directive beam with low side lobe levels and a front-to-back ratio less than -15 dB.



**Figure 5.11:** Radiation patterns of the CE-optimized RCA with ACMPA.

## 5.4 Discussion

Applied to the ACMPA optimization problems with continuous variables, the CE method converged faster than PSO and CMA-ES. Also, it was found that PSO can outperform CE and CMA-ES in terms of the best fitness function. The comparison of the acquired F.F. and NFE for the ACMPA design and the RCA with an ACMPA feed is given in Table 5.6. In the first example, PSO required 1500 NFE, while CE only needed 1200, and in the second example, both PSO and CE converged after 900 NFE. Although CMA-ES had the smallest population size, it required more function evaluations, and, therefore, a longer optimization time. NFE was 1815 in the first case and 2255 in the second case. Although CMA-ES found the best ACMPA design in the first optimization example, it violated the limits that had been defined for the design variables. The reason is that the Gaussian distribution has an unbounded support, and, therefore, some random samples might appear on the tails of the distribution and exceed the boundary limits. This can be solved by disregarding or penalising designs that are located outside of the search space limits.

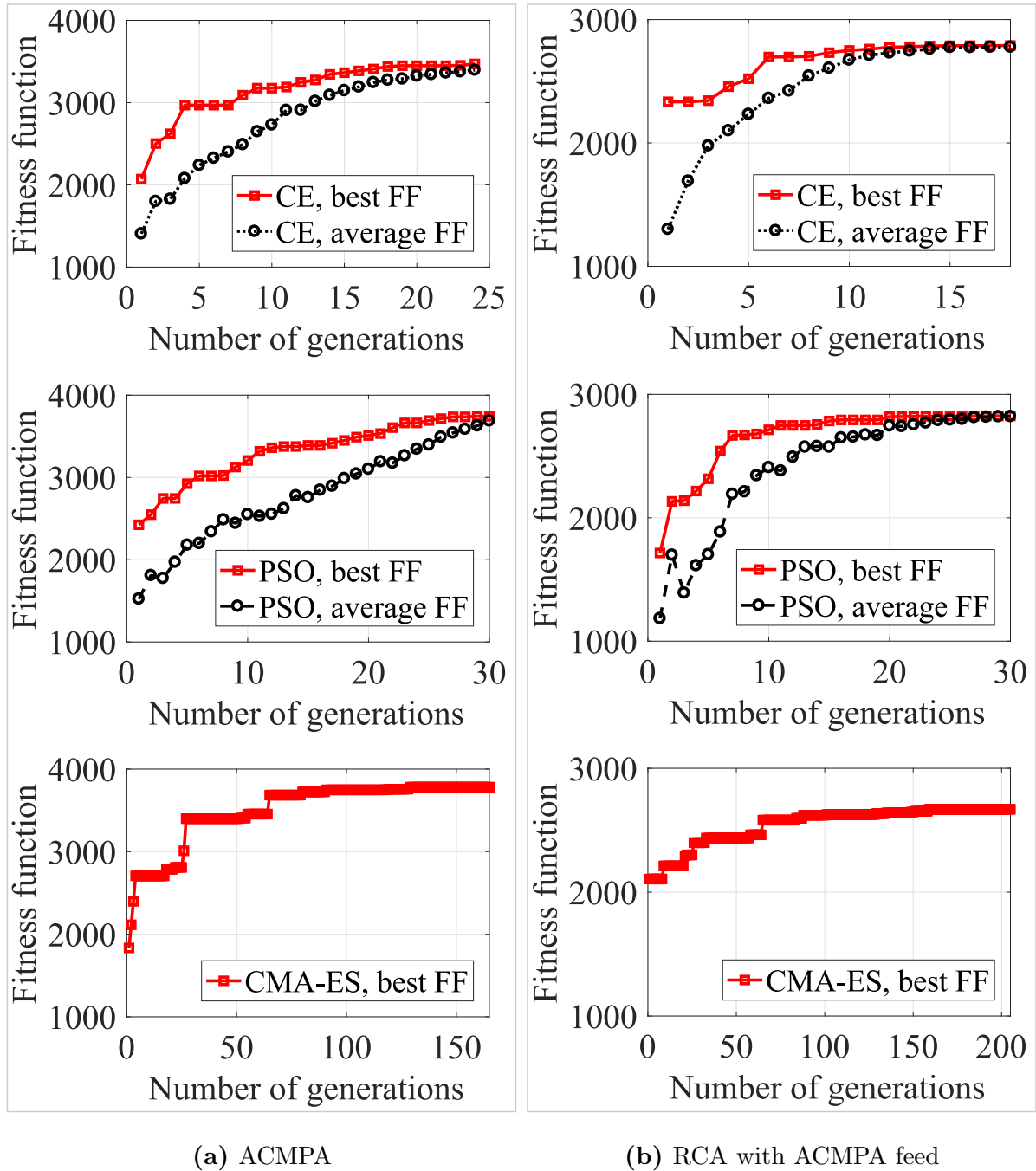
The convergence curves for the optimization of the ACMPA and the RCA with ACMPA can be observed from Fig. 5.12(a) and (b), respectively. Good convergence can be observed for the CE and PSO methods. The convergence of CMA-ES has not been recorded. The effect of smoothing parameters  $\alpha_S$  on the number of iterations in the CE method can be seen. In ACMPA optimization,  $\alpha_S = 0.5$  and  $N_{it} = 24$ , while in the RCA with ACMPA feed optimization, smoothing was increased to  $\alpha_S = 0.8$ , which resulted in  $N_{it} = 18$ .

The limitation of this optimization study is the small number of trials obtained for each algorithm. To obtain a statistically viable performance measure for the comparison study, multiple optimization trials have to be executed. This is a common procedure when test functions are optimized, but in application to real engineering problems when the fitness function is evaluated via simulation, performing multiple repetitive trials is often impractical.

**Table 5.6:** Best obtained fitness function value and NFE of each algorithm applied to the optimization of the ACMPA and the ACMPA-fed RCA.

	Best F.F.	NFE
<b>ACMPA</b>		
CE	3470.2	<b>1200</b>
PSO	3743.2	1500
CMA-ES	<b>3780.9</b>	1815
<b>RCA with ACMPA feed</b>		
CE	2789.7	<b>900</b>
PSO	<b>2825.8</b>	<b>900</b>
CMA-ES	2669.4	2255





**Figure 5.12:** CE, PSO and CMA-ES convergence curves for two design cases.

## 5.5 Summary

In this chapter, the optimization results of CE, PSO and CMA-ES in application to an ACMPA optimization problem with ten continuous variables were provided. An ACMPA with a peak directivity of 9.5 dBi and a 53% impedance bandwidth was designed. Then, the described ACMPA was integrated with an all-dielectric TPG superstrate to form an RCA. Again, the reflection coefficient was optimised using CE, PSO and CMA-ES. The designed ACMPA-fed RCA has a peak directivity of 19 dBi and a 3-dB radiation bandwidth of 40%, well-covered by an impedance bandwidth. Compared to the alternative solutions for the cavity excitation, the proposed ACMPA results in a reduced RCA profile. In addition, the convergence properties and NFE needed for each algorithm to produce the desired result were compared.

*To guess what to keep and what to throw away takes considerable skill. Actually it is probably merely a matter of luck, but it looks as if it takes considerable skill.*

— Richard Feynman

## Chapter 6

# Optimization of Thin Pixelated EM Surfaces

In the previous chapter, an application of the CE method to continuous design problems has been presented. It was shown that the method is capable of locating a near-to-optimal solution and requires fewer function evaluations than PSO and CMA-ES. In this chapter, a general optimization approach to the synthesis of thin pixelated EM surfaces using the CE method will be described. This is the first time that CE has been applied to the optimization of encoded binary EM structures; previously these problems have mostly been handled by GAs.

### 6.1 Introduction

EM surfaces, also called metasurfaces, are planar structures of finite thickness that are composed of sub-wavelength periodic or nonperiodic unit-cells. The unit-cell usually consists of one or more layers of dielectric materials with metallic patterns printed on their opposite sides. The prominent feature of such structures is simultaneous control of the magnitude, phase and polarisation of the EM waves. Interesting properties such as broadband anti-reflection, absorption and polarisation conversion can be achieved through manipulation of their reflection and transmission characteristics. The applications of EM surfaces in antenna and microwave engineering include wideband absorbers, multiband

spatial filters, conformal antenna radomes, reflectarrays and transmitarrays, EM shielding and radar cross section reduction, to name a few.

Previously, frequency-selective surfaces (FSSs), PRSs, high-impedance surfaces (HIS) and artificial magnetic conductors (AMCs) have been realised using metallic squares, loops, cross-type elements and their combinations [129, 195–197]. The required reflection and transmission characteristics of the EM surface can be obtained by finding the appropriate geometrical parameters of the element in a unit-cell. When designing either a band-pass or band-stop FSS, the choice of the proper element may be of utmost importance [195].

An alternative approach is to divide a unit-cell into pixels that can be either metallic or non-metallic and use optimization to find the pattern that provides the desired performance. The advantage of pixelated surfaces is the flexibility of the geometry, that is not limited to any element of a canonical shape. Optimization of pixelated EM surfaces has been previously conducted by encoding a pattern of “metal-air” inclusions into a binary string. GAs with their inherent binary representation of design variables were the first methods applied to such optimization. Using GAs, a variety of printed pixelated structures have been designed, such as a microwave absorber composed of multiple dielectric layers with FSS screens [198], a PRS of an RCA for high-Q resonant cavity [24], periodic metamaterials [25] and a double-sided AMC [199].

Apart from GAs, other methods have also been implemented for the optimization of pixelated printed EM surfaces, such as PSO and SA [45, 200]. In the majority of cases, they are real-coded optimization methods that require significant overhead when applied to binary optimization problems. Therefore, considering the fast convergence of the CE method and its flexibility in terms of design variables, it is worth investigating the performance of the CE method in application to the design of binary EM problems, such as pixelated surfaces. Previous research on the CE method in EM applications identified the possibility of using CE for binary EM problems but little work has been done in this direction [91].

In order to investigate the performance of the CE method on binary optimization problems, in this thesis CE has been implemented on the design of thin composite EM structures. Pixelated patterns printed on both sides of a thin dielectric material have been optimized targeting various frequency responses. By controlling the phases and magnitudes of the scattered waves from both sides of the surfaces, AMCs and planar phase shifters have been designed.

## 6.2 The Theory of Thin EM Surfaces

The first realisation of AMCs was demonstrated in [201], where rectangular or hexagonally shaped metallic patches connected to the ground plane through vias, so-called mushroom-like metallic structures, were shown to have a high surface impedance. Another realisation was demonstrated in [202], eliminating the need for vias between the ground plane and the printed layer. As opposed to the PECs, which have surface impedances equal to zero, AMCs are characterised by high absolute values of surface impedances and, therefore, are also called high-impedance surfaces (HISs).

Theoretically, AMCs can be realised by backing a layer of a dielectric material of thickness  $d$  with permittivity  $\varepsilon$  and permeability  $\mu$  by an infinite metallic surface [203]. Then, the input impedance seen by a normally incident plane wave at the top of the dielectric is

$$Z_S = j\sqrt{\frac{\mu}{\varepsilon}} \tan\left(\frac{2\pi}{\lambda}d\right). \quad (6.1)$$

It can be seen that the surface impedance  $|Z_S| \rightarrow \infty$  as  $d \rightarrow \lambda/4$ . However, a quarter-wavelength dielectric layer is prohibitively thick for many practical applications. The thickness of AMCs can be significantly reduced by placing a printed metallic pattern on top of a thin dielectric layer. When the thickness of the dielectric layer is much less than  $\lambda/4$ , the input impedance of the surface is inductive and equals  $Z_S \approx j\omega\mu d$ . If a capacitive grid with impedance  $1/(j\omega C_g)$  is placed on top of the dielectric, the total surface impedance is the parallel connection of the inductive input impedance of the thin layer and the capacitive grid impedance of the FSS:

$$Z_S = \frac{j\omega\mu d}{1 - \omega^2 C_g \mu d}. \quad (6.2)$$

For normally incident plane waves, the surface impedance tends to infinity at the resonance frequency  $\omega_0 = \sqrt{1/(C_g \mu d)}$ , realising an artificial magnetic conductor. One of the practical applications of magnetic conductors is to reduce the profile of wire antennas positioned above a ground plane [203]. As shown in [204], metal backing is not a necessary condition for achieving the required values of reflection and transmission phases. Moreover, the anticipated benefits of an AMC surface without a completely metallic ground plane in an antenna application include the absence of the associated image and scattering-induced currents on the back side of a finite ground plane, a lowered possibility of surface waves, and lighter weight [204]. Based on these considerations, a unit-cell composed of thin dielectric material of thickness  $d$  with a pixelated pattern printed on both sides has been considered for optimization by the CE method.

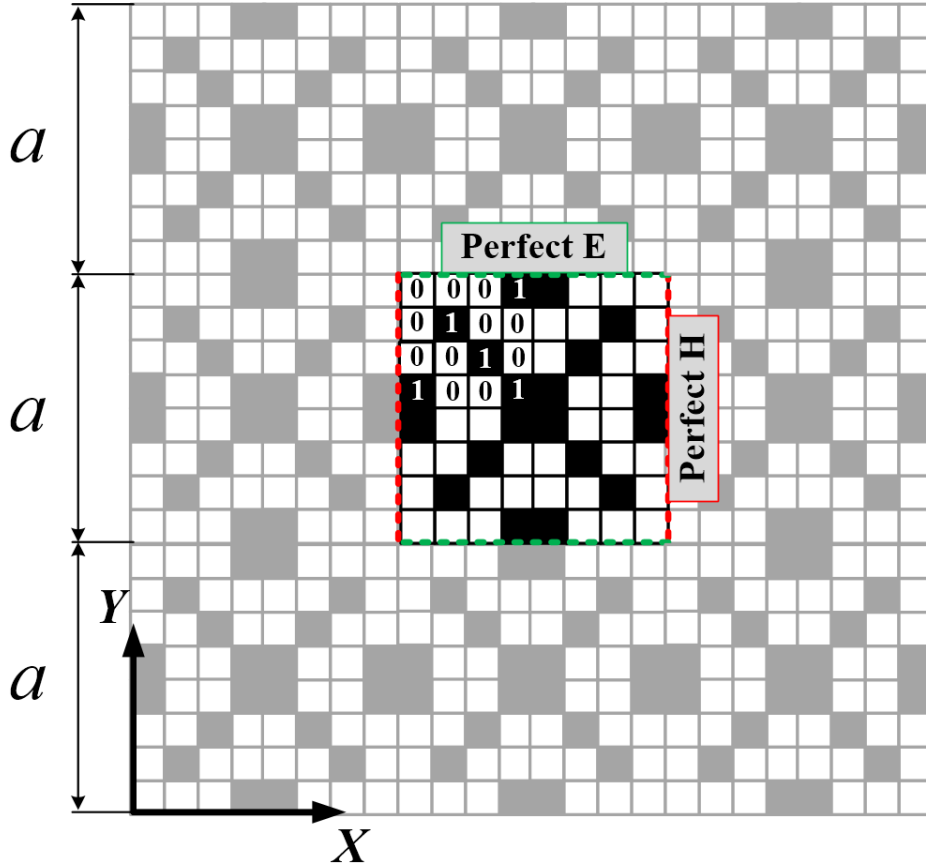
## 6.3 Method of Analysis

The method of analysis and some simplifications that have been considered in order to reduce the overall optimization time are described below. In order to efficiently optimize an EM structure, an accurate simulation model with minimal computational burden has to be established. Accurate prediction of the frequency-dependent reflection and transmission characteristics of the structure can be obtained by numerical analysis in full-wave simulation software.

### 6.3.1 Periodic Analysis

A two-dimensional periodic structure is created by translating a unit-cell in  $x$  and  $y$  directions, as shown in Fig. 6.1. It is sufficient to analyse the fields in a single unit-cell in order to predict the characteristics of the infinitely large periodic EM surface. Periodic boundary conditions should be applied around the unit-cell to imitate the infinite dimensions of the structure. The waveguide simulation method in conjunction with time-

domain analysis in CST MWS has been used to predict the reflection and transmission characteristics of all the cases presented in the following discussion. Illumination by a normal plane wave from two opposite ports with the E-field aligned with  $x$ -axis was considered, and perfect electric and perfect magnetic boundary conditions were assigned to model an ideal parallel-plate waveguide. Taking  $xz$ -plane as a plane of incidence, the applied plane wave is TE-polarized.



**Figure 6.1:** Illustration of a periodic structure having a pixelated unit-cell with  $n = 8$ . By assuming perfect walls surrounding a single unit-cell, infinite repetitions in the  $x$  and  $y$  directions are realised.

A square unit-cell, shown in Fig. 6.1, consists of a dielectric material of thickness  $d$  with two pixelated patterns printed on its opposite sides. The printed surface on both sides of a unit-cell have equal side length  $a$  and level of pixelation  $n$  (number of columns/rows). Each pattern (both top and bottom) is represented by a matrix of  $n^2$  elements that can take value either “1” or “0”, where “1” corresponds to “metal” and

“0” to “air”.

The design variables are expressed as:

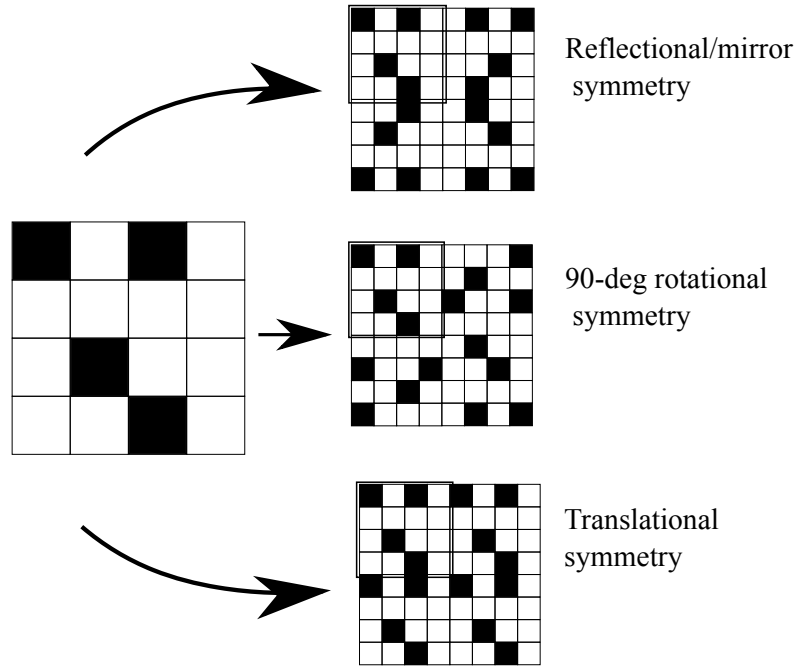
$$X_k = \begin{bmatrix} x_{11} & x_{12} & x_{13} & \dots & x_{1n} \\ x_{21} & x_{22} & x_{23} & \dots & x_{2n} \\ \vdots & \vdots & \vdots & \ddots & \vdots \\ x_{n1} & x_{n2} & x_{n3} & \dots & x_{nn} \end{bmatrix},$$

where  $k = 1$  and  $2$  correspond to the top and bottom pattern, respectively. Therefore, a unit-cell is represented by a binary vector  $X = [X_1, X_2]$  of  $2 * n^2$  elements. The optimization problem is to find the binary combination in  $X$  that corresponds to the unit-cell exhibiting the desired transmission and reflection characteristics.

### 6.3.2 Symmetry Planes

To further reduce the dimensionality of the optimization problem and, therefore, reduce the computational time, symmetry within the unit-cell is imposed. As shown in Fig. 6.2, a quarter of a unit-cell can be transformed to a full pattern using three types of symmetries, i.e. reflectional, rotational and translational. Although there are other possible ways to reduce the number of variables in a unit-cell, a 90-degree rotational symmetry not only reduces the number of design variables by a factor of four, but also ensures polarisation independence of the structure. Thus, in the designs presented further, a 90-degree rotational symmetry in the unit-cell will be considered.





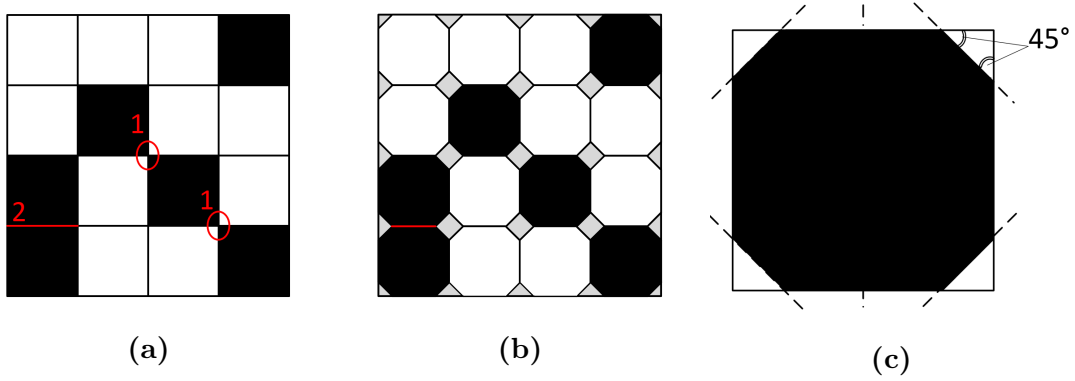
**Figure 6.2:** A quarter of a unit-cell can be converted into three different configurations by applying different symmetry planes. Reducing the unit-cell to a quarter decreases the dimensionality of the optimization problem by a factor of four.

### 6.3.3 Vertices-Removal Technique

Pixelated surfaces are known for the fabrication issue related to the interconnections of the diagonal pixels as in Fig. 6.3 (a). There are two types of possible connections between square pixels: Type 1, when there is only a single infinitely small point (shown in circles) and Type 2, when the squares have a common side. The problem occurs because the pixels with Type 1 connection are treated as not electrically connected by numerical analysis. In practice, an infinitely small point cannot be realised, and the vertices end up being physically connected, allowing current flow between the pixels. This causes disagreement between the predicted and measured results.

A number of techniques have been proposed to deal with this issue. In [205,206], a *vertex breaking technique* separating the vertices of diagonal pixels by the distance 0.04 mm has been applied. The disadvantage of this technique is that geometry modification is required for every generated pattern, which with the numerous simulations required by the optimization, might substantially increase the computational time. A *geometry re-*

*finement technique* proposed in [207, 208] eliminates the diagonal connections of square pixels by analysing the geometry of every solution. However, by disregarding many potential solutions, this approach considerably reduces the search space available for the optimizer. Another approach called *the nonuniform overlapping scheme*, which ensures proper electrical connection of diagonal pixels, has been proposed in [209] and [210]. The idea is to intentionally overlap the metallic pixels in the simulation model by shifting the diagonally adjacent pixels in the  $y$  direction. This ensures the existence of the electrical connection in both numerical analysis and the fabricated prototype. Again, this scheme introduces an additional step to the overall optimization flow.



**Figure 6.3:** (a) Conventional unit-cell with square pixels causing problematic connections of Type 1; (b) unit-cell with octagonal pixels; (c) square-to-octagonal pixel conversion for the elimination of diagonal infinitesimal intersection of pixels.

The described problem can be eliminated by using octagonal pixels instead of rectangular ones. This can be easily achieved by subtracting four isosceles triangles with a base angle  $45^\circ$  from a square pixel, as shown in Fig. 6.3 (c). This approach has the advantage of not adding any complementary steps to the optimization procedure, as the conversion can be done only once. A unit-cell with octagonal pixels is shown in Fig. 6.3 (b). It can be seen that only Type 2 electrical connection remains between the octagonal pixels. The proposed solution comes at a cost of an increased mesh size of the structure in the numerical analysis. To be specific, the number of meshcells increases from 14 000 with squared pixels to 22 500 with octagonal pixels. However, due to the short evaluation time (approximately 60 sec for each unit-cell), the overall optimization time is still acceptable.

## 6.4 Optimization Approach

It has been shown in the previous chapters that the use of the CE method for continuous and mixed-variable optimization problems presents many advantages in application to EM problems due to its fast and versatile nature. In this section, a method to optimize problems with binary variables using CE will be presented.

### 6.4.1 Sampling Binary Variables

The CE method attempts to iteratively approach the global optimal solution by consecutively adapting the shape parameters of the sampling probability distributions. The nature of the design variables guides the choice of the probability distribution used for sampling. For optimization problems with design variables that have only two possible values, a Bernoulli distribution can be used. As is known from statistics, the Bernoulli distribution is a discrete probability distribution of a random variable that takes the value 1 with probability  $p$  and the value 0 with probability  $(1 - p)$ . The probability mass function  $f(x; p)$  of a Bernoulli distribution over possible outcomes  $x$  is

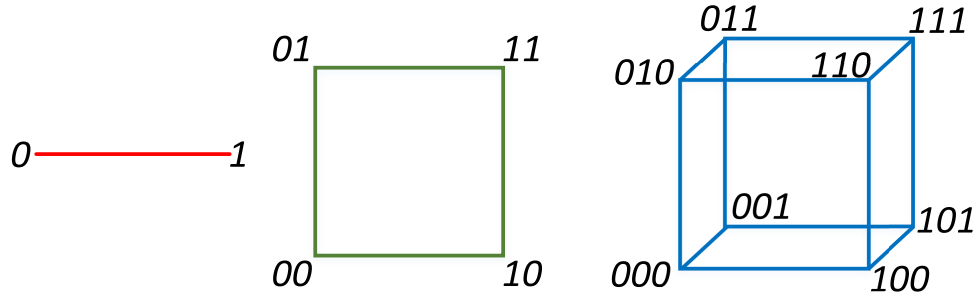
$$f(x; p) = p^x(1 - p)^{1-x}, \quad (6.3)$$

where  $x$  is either 1 or 0, meaning that  $f(x; p) = p$  when  $x = 1$ , and  $f(x; p) = (1 - p)$  when  $x = 0$ .

Therefore, by encoding a pixelated unit-cell into a binary string, the CE method with the Bernoulli sampling distribution can be used for its optimization. Using a 90-degree rotational symmetry in a unit-cell with  $n = 6$ , the quarter of the pattern on top of the dielectric layer is represented by a probability distribution matrix  $P^T$ :

$$P^T = \begin{pmatrix} p_{111} & p_{121} & p_{131} \\ p_{211} & p_{221} & p_{231} \\ p_{311} & p_{321} & p_{331} \end{pmatrix}, \quad (6.4)$$

and the quarter of the pattern on the bottom of the dielectric layer is represented by  $P^B$ :



**Figure 6.4:** Illustration of the exponential increase in the complexity of binary optimization problems.

$$P^B = \begin{pmatrix} p_{112} & p_{122} & p_{132} \\ p_{212} & p_{222} & p_{232} \\ p_{312} & p_{322} & p_{332} \end{pmatrix}. \quad (6.5)$$

The probability  $p_{ijk}$  is the probability that the pixel located at row  $i = 1, \dots, n/2$ , column  $j = 1, \dots, n/2$  and side  $k = \{1; 2\}$  is filled with metal. The quarter of a unit-cell is, therefore, sampled using the sampling distribution parameter matrix  $P = [P^T P^B]$  with number of elements  $D = 2 \times (n/2)^2 = 18$  for  $n = 6$ . The number of parameters  $D$  in the quarter matrix  $P$  is the dimensionality of the optimization problem. Fig. 6.4 illustrates that the difficulty of binary optimization problems increases exponentially with the number of dimensions. If  $D = 1$ , there are only two possible outcomes (straight line), that represent either “air” or “metal”. If  $D = 2$ , the number of outcomes equals the number of vertices of a rectangle, i.e.,  $2^2 = 4$ . For  $D = 3$ , the number of outcomes is  $2^3 = 8$ . In the considered case with  $n = 6$ , the binary optimization problem with 18 design variables has  $2^D = 2^{18} = 262\,144$  possible outcomes.

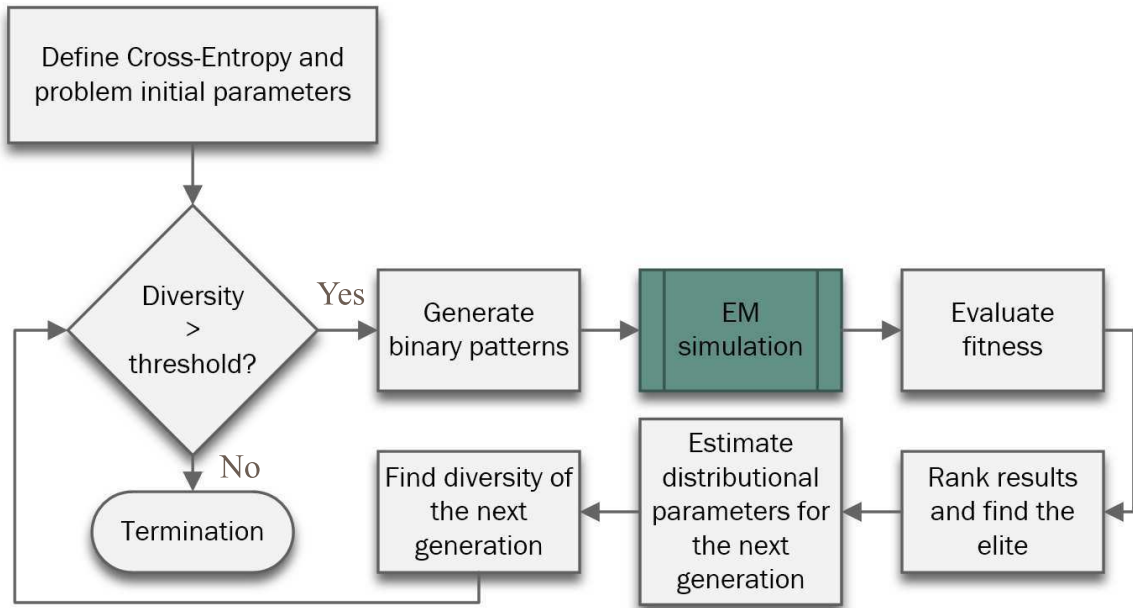
### 6.4.2 CE Algorithm for Optimization of Binary Problems

The principle of the CE method has been explained in Section 2.3, and only the crucial steps of the algorithm implementation on binary problems will be given further. The main idea of the CE optimizer is the minimization of the cross-entropy between two probability distributions: an empirical distribution describing the current elite subpopulation and a

sampling distribution which is used to sample a new population. At each iteration, two important steps must be taken to implement this idea:

- Generate a random population of solutions  $x^t$  with  $N_{pop}$  candidates from the sampling distribution  $f(x^t; p^t)$ , where  $p^t$  are the distributional parameters at the  $t$ -th iteration, and choose the  $N_{el}$  best-performing candidates for the elite subpopulation by evaluating the fitness function.
- Update the shape parameters  $p^{t+1}$  of  $f(x^{t+1}; v^{t+1})$  by minimising its cross-entropy with the empirical distribution  $g(x^t; w^t)$  describing the current elite solutions using the maximum likelihood estimation of  $w^t$ .

The flowchart of the proposed optimization scheme for the design of pixelated printed surfaces by the CE method with a Bernoulli sampling distribution is given in Fig. 6.5. The optimization begins by setting the parameters of the CE method, such as population



**Figure 6.5:** The flowchart for optimization of binary problems using the CE method.

size  $N_{pop}$ , proportion of elite subpopulation  $\rho = N_{el}/N_{pop}$  and smoothing parameter  $\alpha_S$ . Also, it is required to set the parameters of the optimization problem, such as the number of rows  $N_p$  and the number of columns  $M_p$  in the probability matrices  $P^T$  and  $P^B$ . In the discussion, we omit the indices  $(i, j, k)$  for brevity. The initial patterns  $X^0$  are generated

by sampling from the uniform probability mass function  $P^0$  with all probabilities equal 0.5. At each iteration  $t$ , the patterns are generated by the same principle. In particular, for each candidate, a matrix  $E^t$  of random variables from the interval  $[0, 1]$  is compared to the corresponding value of success probability in  $P^t$  according to:

$$\begin{aligned} E_{ijk}^t < p_{ijk}^t &\Rightarrow x_{ijk}^t = 0; \\ E_{ijk}^t \geq p_{ijk}^t &\Rightarrow x_{ijk}^t = 1. \end{aligned} \quad (6.6)$$

If the value of  $E^t$  is less than the probability of success  $P^t$ , the corresponding variable  $x^t$  is equal to “0” (no metal), and otherwise it is “1” (metal).

The next step is to obtain the performance parameters via EM simulation and evaluate the fitness functions for each candidate. If the fitness function is to be maximized, the results are sorted in descending order, and if minimized, in ascending order. In either case, the first  $\rho\% = N_{el} \cdot 100\% / N_{pop}$  constitute the elite subpopulation. These  $N_{el}$  candidates are used to generate new probability mass functions  $P^{(t+1)}$ , to increase the probability that the best-performing candidates occur in the next generation. This is achieved by maximum likelihood estimation, which for the Bernoulli distribution is simply the mean of the best-performing candidates [82]:

$$\hat{P} = \frac{1}{N_{pop}} \sum_{c=1}^{N_{pop}} X_c. \quad (6.7)$$

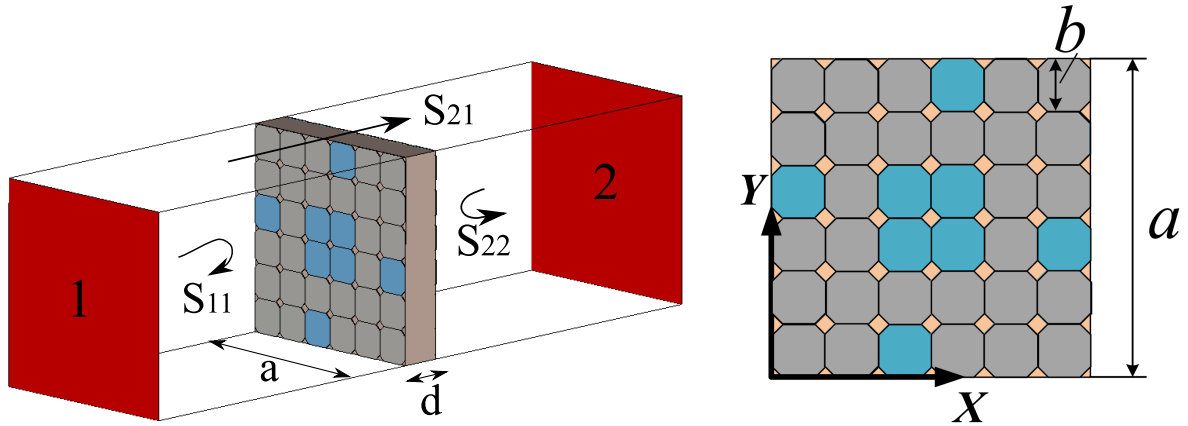
An optional smoothing procedure described in Section 2.3 and given by Eq. (2.5) has been applied.

The termination condition has been defined as the diversity of the elite subpopulation. If the variance of the elite candidates equal to or goes below the threshold, the optimization stops. For binary variables, the threshold is  $\delta=0$ , which implies that optimization stops when the elite subpopulation has converged to the same solution.

A script for the optimization of a pixelated unit-cell is provided in Appendix C.

## 6.5 Optimization Results

The square unit-cell with side length  $a$  and thickness  $d$  is shown in Fig. 6.6. Keeping the fabrication tolerance in mind, the printed surface has been divided into 6 by 6 pixels resulting in each pixel having a side length  $b=1.33$  mm. As clarified earlier, only one quarter of each pattern has been optimized due to the use of 90-degree rotational symmetry. After applying the symmetry, the parameter vector of the optimization problem consists of  $D = 2 \cdot 3^2 = 18$  variables. The metallic pixels in Fig. 6.6 are shown in grey and represented by “1” in the  $X$  matrix, whereas the absence of metallic pixels is shown in blue and represented by “0”. Numerical results have been obtained by CST MWS using the waveguide simulation method described in Section 6.3.1. The unit-cell is illuminated by a TE-polarised wave with the  $E$  vector oriented along the  $x$  axis from two waveguide ports. Each port is located at a half-wavelength distance from the unit-cell, and the reference planes are positioned at the opposite sides of the unit-cell in order to acquire the reflection phase values.



**Figure 6.6:** A model of the square unit-cell under optimization.

### 6.5.1 Single-Frequency AMC Surface

The first AMC design was optimized for X-band operation at 10 GHz. The side length of the unit-cell was set to  $a=8$  mm, and the dielectric material Rogers RO4003 with  $\epsilon_r = 3.55$  and thickness  $d=1.58$  mm has been used. The target phase and magnitude (on

a linear scale) of the reflection and transmission coefficients at the required frequency are the following

$$\angle S_{11} = 0^\circ, \angle S_{22} = 180^\circ, |S_{21}| \leq 0.3. \quad (6.8)$$

The optimization goal was to minimise the objective function  $F.F.$ , which is the sum of three terms:

$$F.F. = F_1 + F_2 + 100 * F_3, \quad (6.9)$$

where

$$F_1 = |0^\circ - \angle S_{11}|^2, \quad (6.10)$$

$$F_2 = |180^\circ - \angle S_{22}|^2, \quad (6.11)$$

$$F_3 = \begin{cases} 0, & \text{if } |S_{21}| \leq 0.3 \\ |S_{21}|, & \text{otherwise.} \end{cases} \quad (6.12)$$

As the transmission coefficient magnitude  $|S_{12}|$  of 0.3 is sufficient, all the designs with  $|S_{12}| \leq 0.3$  have  $F_3=0$ .

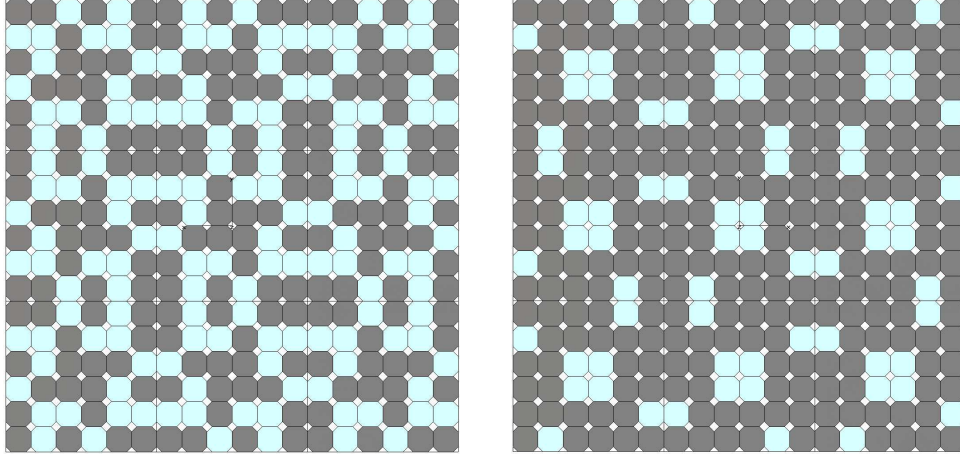
The parameters of the CE method were set to the following values: population size  $N_{pop}=30$ , elite subpopulation size  $N_{el}=10$  and smoothing parameter  $\alpha_S=0.6$ . The time required for a single simulation is between 30 and 60 s using a PC with Intel Core i7-4790 processor and 32 GB of memory. Five optimization runs were conducted to keep the balance between the statistical certainty of the results and the computational cost. The best obtained solution has  $F.F.=6.8$  and is represented by the following solution matrix:

$$X^T = \begin{pmatrix} 1 & 0 & 1 \\ 1 & 0 & 0 \\ 0 & 1 & 1 \end{pmatrix}, X^B = \begin{pmatrix} 1 & 1 & 1 \\ 0 & 1 & 1 \\ 1 & 1 & 0 \end{pmatrix}.$$

The top and bottom patterns of the surface with  $3 \times 3$  unit-cells, obtained after CE optimization for the goal given in Eq. (6.8), are shown in Fig. 6.7. To construct the geometry of a periodic EM surface from the optimized unit-cell, the image theory has been applied. The mirror image of a current element flowing parallel (perpendicular) to the PEC boundary should be formed in the opposite (same) direction. The image of a

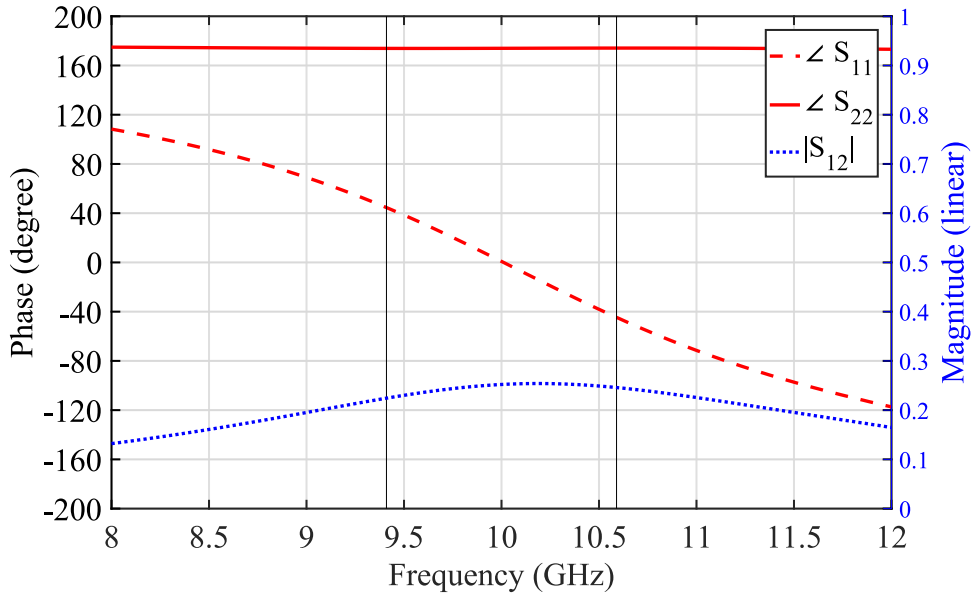


current element flowing parallel (perpendicular) to a PMC boundary is formed in the same (opposite) direction [211].



**Figure 6.7:** A part of the optimized single-frequency AMC: top pattern (*left*) and bottom pattern (*right*) of 9 unit-cells.

The transmission and reflection results are given in Fig. 6.8, where  $S_{11}$  and  $S_{22}$  represent reflections from the top and the bottom surface, respectively.



**Figure 6.8:** Reflection phase of TE-polarised incident wave from the top and bottom sides of the optimized AMC, as well as the transmission magnitude.

As required,  $\angle S_{11} = 0$ ,  $|S_{12}| = 0.25$  ( $-12$  dB) and  $\angle S_{22} = 174^\circ$  at 10 GHz. Therefore, the top surface of the designed EM structure behaves as an AMC at the specified fre-

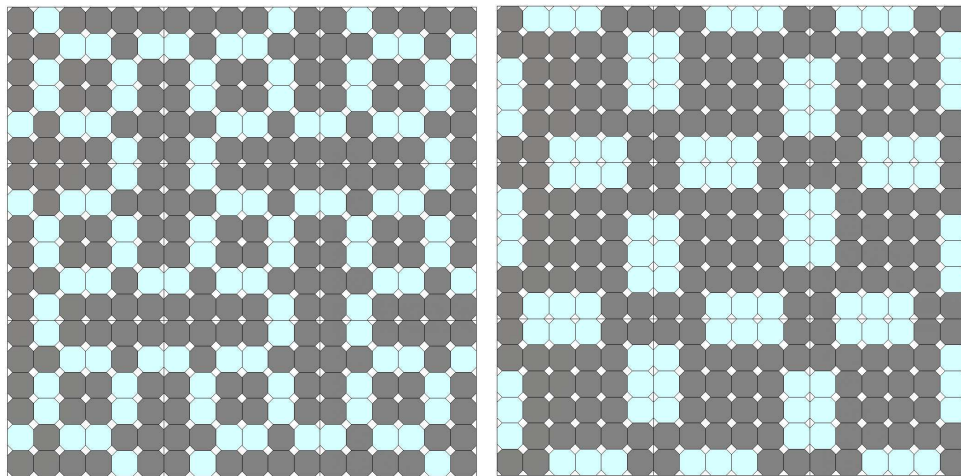
quency. An in-phase reflection bandwidth, which is commonly defined as the frequency band with the phase of the reflection coefficient being within  $\pm 45^\circ$ , is from 9.41 GHz to 10.59 GHz.

It is also worth noting that, to obtain this AMC, a complete metallic backing was not required. As shown in Table 6.1, in comparison to the pixelated surfaces obtained through GA in [25,199], the thickness of this AMC is merely the same but the level of discretisation is significantly lower,  $6 \times 6$  pixels as opposed to  $16 \times 16$ , which is advantageous for fabrication purposes. The side length of the unit-cell in [25] is  $0.1\lambda_0$  at 5 GHz, which is 6.6 mm, and thus the dimensions of each pixel are  $0.4 \times 0.4$  mm. Neither of the designs from Table 6.1 have been fabricated due to the focus of the work being on the optimization methodologies. However, practical considerations should be taken into account. The side length  $a = 8$  mm and coarser discretisation in the unit-cell have been chosen due to anticipated fabrication limits. The thickness  $t = 1.58$  mm has been considered because the AMC surface of  $100\lambda_0 \times 100\lambda_0$  has to be rigid for the measurement purposes.

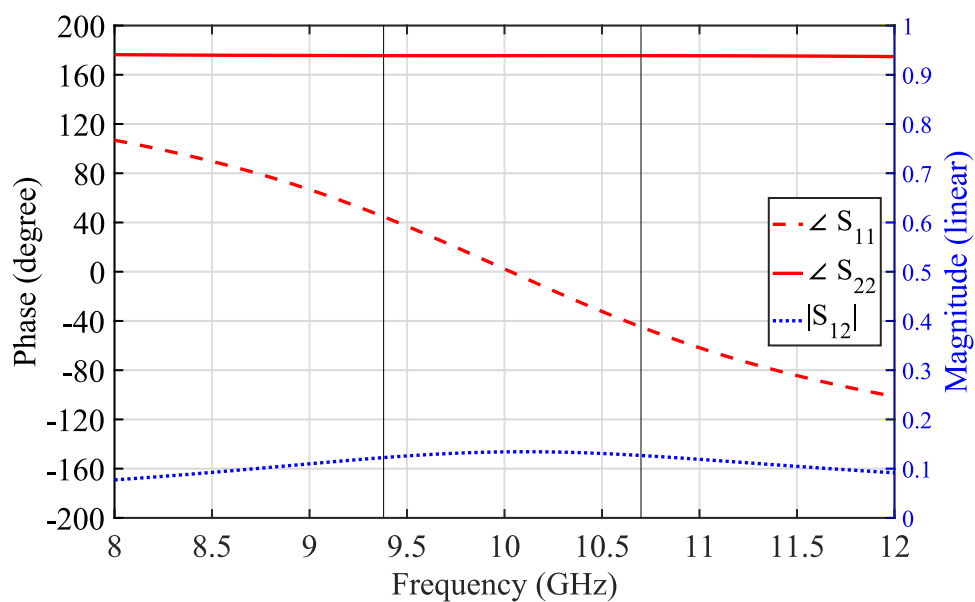
To demonstrate that AMC design with  $a = 0.1\lambda_0$  is also possible, a unit-cell with  $a = 3$  mm and 36 pixels (each pixel having  $b=0.5$  mm) on each side has been optimized. The  $3 \times 3$  surface is shown in Fig. 6.9, and its reflection and transmission characteristics are given in Fig. 6.10. The desired specifications have been satisfied, as  $|S_{12}| = 0.14$ ,  $\angle S_{11} = 2.2^\circ$  and  $S_{22} = 175.5^\circ$  at 10 GHz. The best obtained solution is represented by the following solution matrix:

$$X^T = \begin{pmatrix} 1 & 1 & 1 \\ 0 & 1 & 0 \\ 1 & 0 & 1 \end{pmatrix}, X^B = \begin{pmatrix} 1 & 0 & 0 \\ 1 & 1 & 1 \\ 0 & 1 & 1 \end{pmatrix}.$$

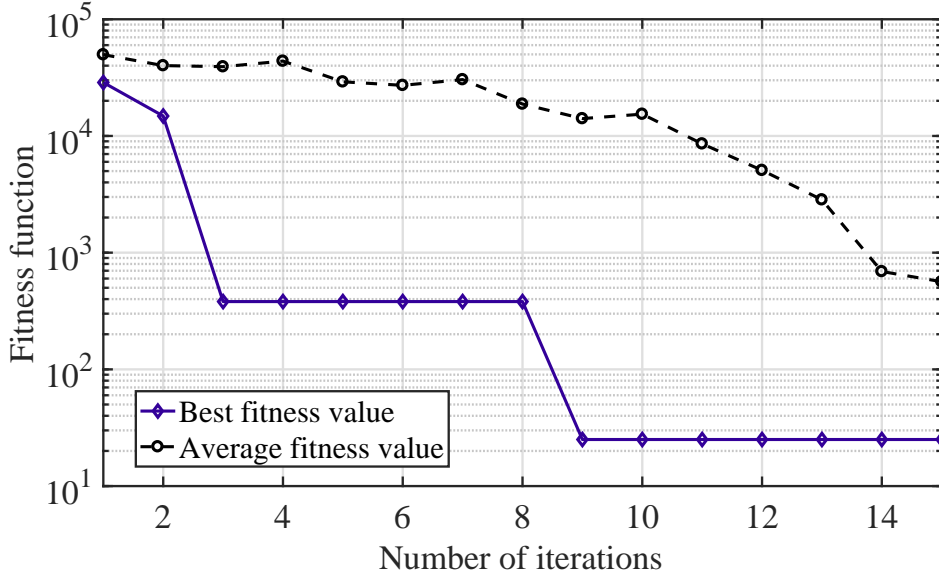
The optimization of the single-frequency AMC only took from 8 to 15 iterations, which is three times less computational effort than that required by GA in [25]. The convergence curve of the optimization of the single-frequency AMC with  $a = 0.1\lambda_0$  is shown in Fig. 6.11. A more detailed visualisation of the fitness function improvement can be observed in Fig. 6.12, which compares the fitness function values calculated by Eq. (6.9) for every candidate at the first and the last iteration of the optimization for



**Figure 6.9:** A part of the optimized single-frequency AMC with  $a = 0.1\lambda_0$ : top pattern (*left*) and bottom pattern (*right*) of 9 unit-cells.

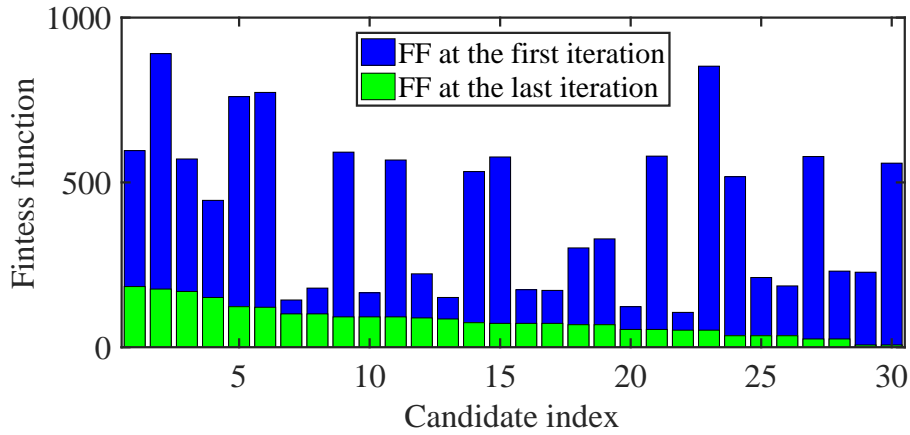


**Figure 6.10:** Reflection phase of TE-polarised incident wave from the top and bottom sides of the AMC with  $a = 0.1\lambda_0$ , as well as the transmission magnitude.




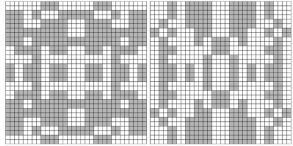
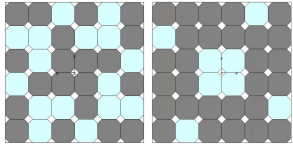
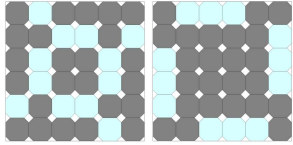
**Figure 6.11:** Convergence curve for the optimization of a single-frequency AMC with  $a = 0.1\lambda_0$ .

$a = 0.27\lambda_0$ . The candidates are sorted in descending order of their final  $F.F.$  value. A significant reduction can be seen in the fitness function of all candidates, from the highest value of 890 at the first iteration to the lowest of 6.8 at the last iteration.



**Figure 6.12:** Distribution of the F.F. value (Eq. (6.9)) over all candidates for the first and the last iteration of the optimization of the AMC with  $a = 0.27\lambda_0$ .

**Table 6.1:** A comparison table of the presented work with the GA-optimized single-frequency AMC surfaces.

Ref.	Unit-cell geometry	Method	$a$	$t$	Polarisation dependency
Single-frequency AMC					
[25]		GA	$0.1\lambda_0$	$0.08\lambda_r$	No
[199]		GA	$0.3\lambda_0$	$0.09\lambda_r$	Yes
This work		CE	$0.27\lambda_0$	$0.09\lambda_r$	No
This work		CE	$0.1\lambda_0$	$0.09\lambda_r$	No

### 6.5.2 Dual-Frequency AMC Surface

The second AMC design, with the unit-cell dimensions  $a = 8$  mm and  $d = 3.16$  mm, was optimized to operate at 8 GHz and 12 GHz. The target characteristics were defined as in Eq. (6.8) at these two frequencies. The optimization goal was to minimise the objective function

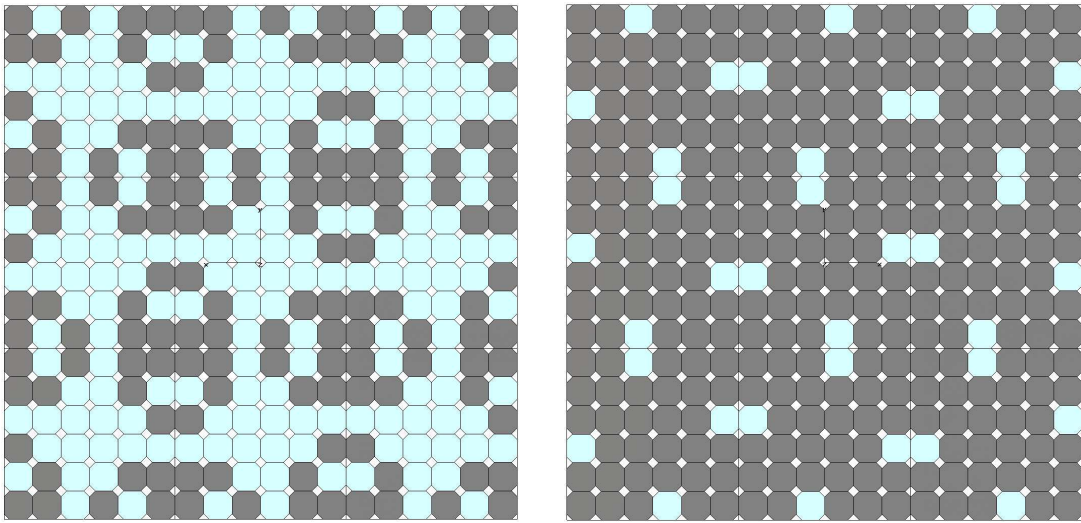
$$F.F. = F.F.^{8GHz} + F.F.^{12GHz}, \quad (6.13)$$

where  $F.F.^{8GHz}$  and  $F.F.^{12GHz}$  are calculated using Eq. (6.9) – (6.12).

Out of five consecutive optimization runs, each with population size  $N_{pop}=30$ , elite subpopulation size  $N_{el}=10$  and smoothing parameter  $\alpha_S=0.1$ , the two best solutions had almost the same  $F.F.$  value and design parameters. The solution shown in Fig. 6.13 with  $F.F.=41.3$  has the following solution matrix:

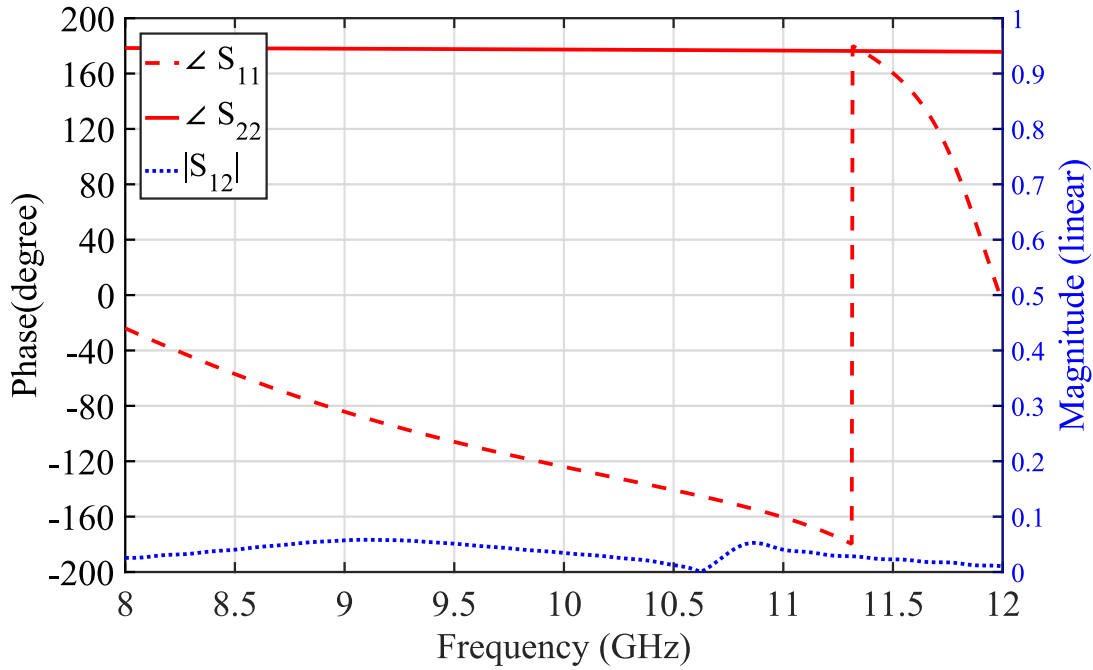
$$X^T = \begin{pmatrix} 1 & 1 & 0 \\ 0 & 1 & 0 \\ 1 & 0 & 0 \end{pmatrix}, X^B = \begin{pmatrix} 1 & 1 & 0 \\ 1 & 1 & 1 \\ 1 & 1 & 1 \end{pmatrix}.$$

The second solution has  $F.F. = 35.2$ , and the only difference in the solution matrix is a single bit in the bottom pattern, which has all “1s”. It suggests that for dual-band performance, a complete or nearly complete metallic backing is required.



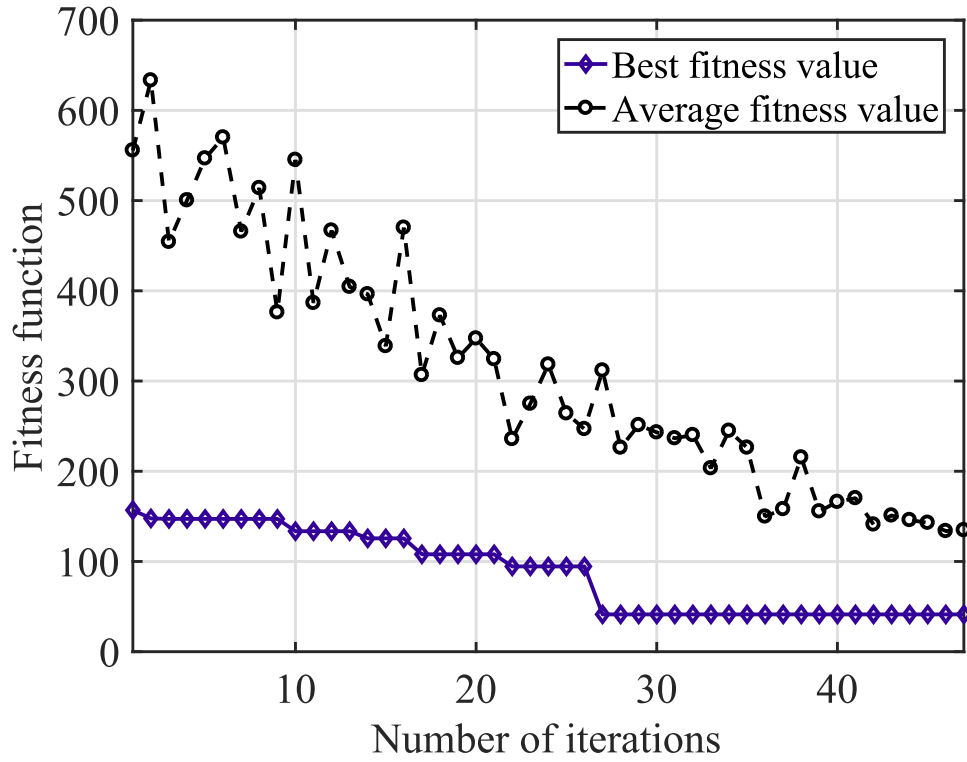
**Figure 6.13:** A part of the optimized dual-frequency AMC showing 9 unit-cells: top view (*left*) and bottom view (*right*) of the optimized patterns.

The transmission and reflection results are given in Fig. 6.14. Phase  $\angle S_{22}$  is  $177^\circ$  and  $175^\circ$ , and  $|S_{12}|$  is  $-32$  dB and  $-40$  dB at 8 and 12 GHz, respectively. Phase  $\angle S_{11}$  is  $-25^\circ$  at 8 GHz, which is within the in-phase reflection bandwidth ( $\pm 45^\circ$ ), and it passes through  $0^\circ$  at 12 GHz. Therefore, the optimized surface behaves as an AMC at both target frequencies of 8 and 12 GHz. In comparison to the pixelated surface obtained through GA in [25], this AMC is electrically thinner,  $t = 0.09\lambda_r$  versus  $0.13\lambda_r$ , and has a larger side length,  $a = 0.27\lambda_0$  versus  $0.11\lambda_0$ . As in the previous case, a comparison given in Table 6.2 shows that the thickness and the side length of this AMC are merely the same as in [199] but the level of discretisation of the optimized unit-cell is significantly lower due to the fabrication considerations.

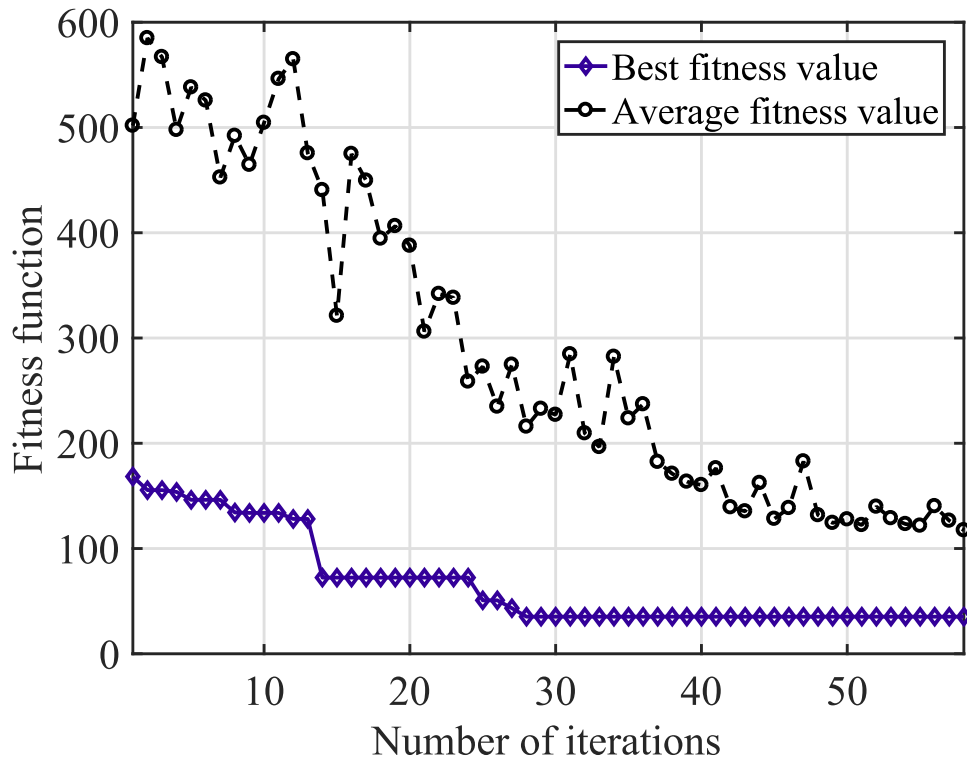


**Figure 6.14:** Reflection phase of TE-polarised incident wave from the top and bottom sides of the optimized AMC, as well as the transmission magnitude.

The optimization run that produced the design in Fig. 6.13 continued for 47 iterations. Its convergence curve is given in Fig. 6.15. The best result was obtained after the 27th iteration, and the optimization was terminated after not producing any better solution for as long as 20 iterations.



(a)


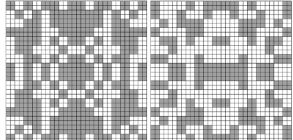
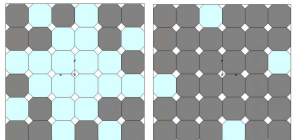


(b)

**Figure 6.15:** Convergence curves for the optimization of a dual-frequency AMC. The stopping criterion was satisfied after (a) 47 iterations for the first run and (b) 58 iterations for the second run. The unit-cell with octagonal pixels has the side length  $a=8$  mm and thickness  $t=3.15$  mm.



**Table 6.2:** A comparison table of the presented work with the GA-optimized dual-frequency AMC surfaces.

Ref.	Unit-cell geometry	Method	$a$	$t$	Polarisation dependency
<b>Dual-frequency AMC</b>					
[25]		GA	$0.1\lambda_0$	$0.08\lambda_r$	No
[199]		GA	$0.22\lambda_0$	$0.19\lambda_r$	Yes
This work		CE	$0.27\lambda_0$	$0.19\lambda_r$	No

### 6.5.3 Thin Phase-Correcting Metasurfaces

Other applications of EM surfaces are found in the design of low-profile planar phase correcting structures [212,213] and beam steering metasurfaces [214]. Using the proposed optimization methodology by means of the CE method, phase-shifting structures made of a single dielectric layer with pixelated surfaces printed on the two sides have been designed. The unit-cells (as in Fig. 6.6) were optimized to provide a required phase shift without introducing significant losses to the transmitted wave. Eleven optimization problems have been formulated to obtain phase shifters covering a range of phases from  $180^\circ$  to  $360^\circ$  with  $10^\circ$  to  $20^\circ$  steps.

The same unit-cell as in the design of AMCs, with 36 pixels on each side, has been used for realisation of the phase shifters. Motivated by practical considerations for operation at 20 GHz ( $\lambda_0 = 15$  mm), the side length of the unit-cell has been set to  $a = 0.3\lambda_0 = 5$  mm. The pixelated patterns are printed on a commercially available dielectric material Taconic TLY-5 with  $\varepsilon_r = 2.2$  and  $t = 1.58$  mm.

The optimization goal for all phase-shift values has been defined as:

$$F.F. = 1000 \cdot F_{phase}^2 + 0.01 * F_{mag}^2, \quad (6.14)$$

where

$$F_{phase} = \begin{cases} 0, & \text{if } |\angle S_{12obj} - \angle S_{12}| \leq 2^\circ \\ |\angle S_{12,obj} - \angle S_{12}|, & \text{otherwise} \end{cases} \quad (6.15)$$

and

$$F_{mag} = \begin{cases} 0, & \text{if } |S_{12}| \geq 0.9 \\ 0.9 - |S_{12}|, & \text{otherwise.} \end{cases} \quad (6.16)$$

The coefficients in Eq. (6.14) have been chosen to reflect the relative importance of the phase and magnitude objectives and to compensate for the difference in their units. The threshold values 0.9 for magnitude and  $2^\circ$  for phase are optional, and the target phase shift  $\angle S_{12,obj}$  takes eleven values:  $\{180^\circ, 200^\circ, 220^\circ, 240^\circ, 260^\circ, 280^\circ, 300^\circ, 320^\circ, 330^\circ, 350^\circ, 360^\circ\}$ .

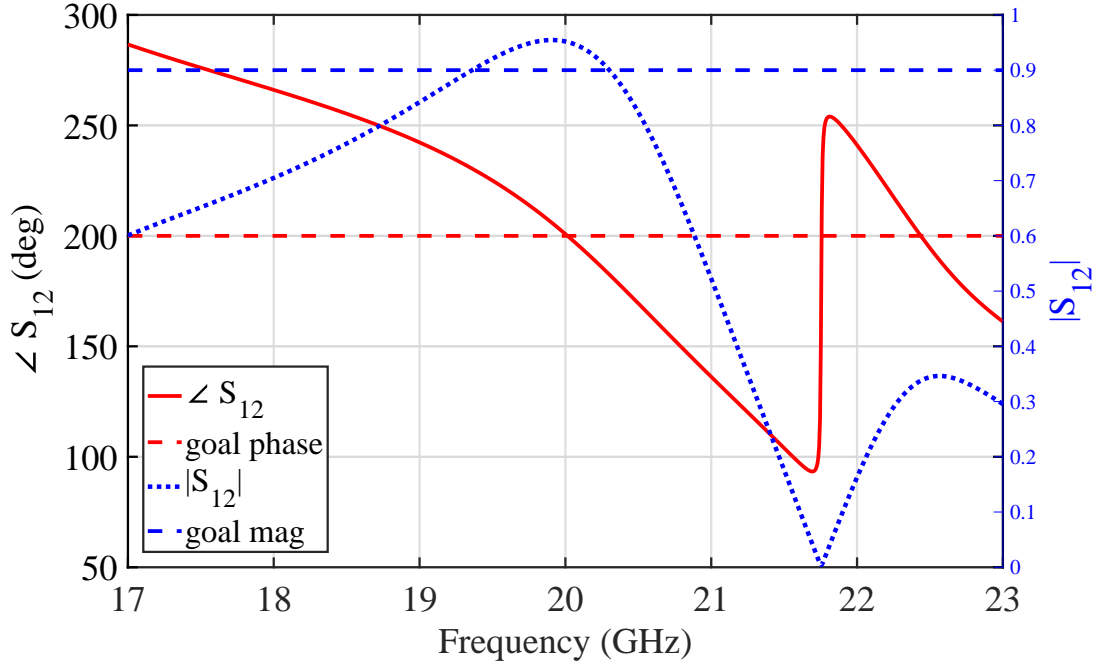
The optimized results are summarised in Table 6.3, where the target transmission-phase  $\angle S_{12}$  values and the ones obtained after optimization can be compared. For all

solutions, the magnitude of the transmission phase  $|S_{12}|$  is  $\geq 0.9$  (linear scale), which ensures transmission losses of less than  $-1$  dB. The largest difference between the desired and obtained phase shift is  $5.67^\circ$ , which is assumed to introduce only minor errors in application to phase correction. A more precise phase-shifting element might be obtained by optimizing a unit-cell with an increased level of discretisation. Other phase values can be obtained by defining the desired  $\angle S_{12,obj}$  in the optimization goal.

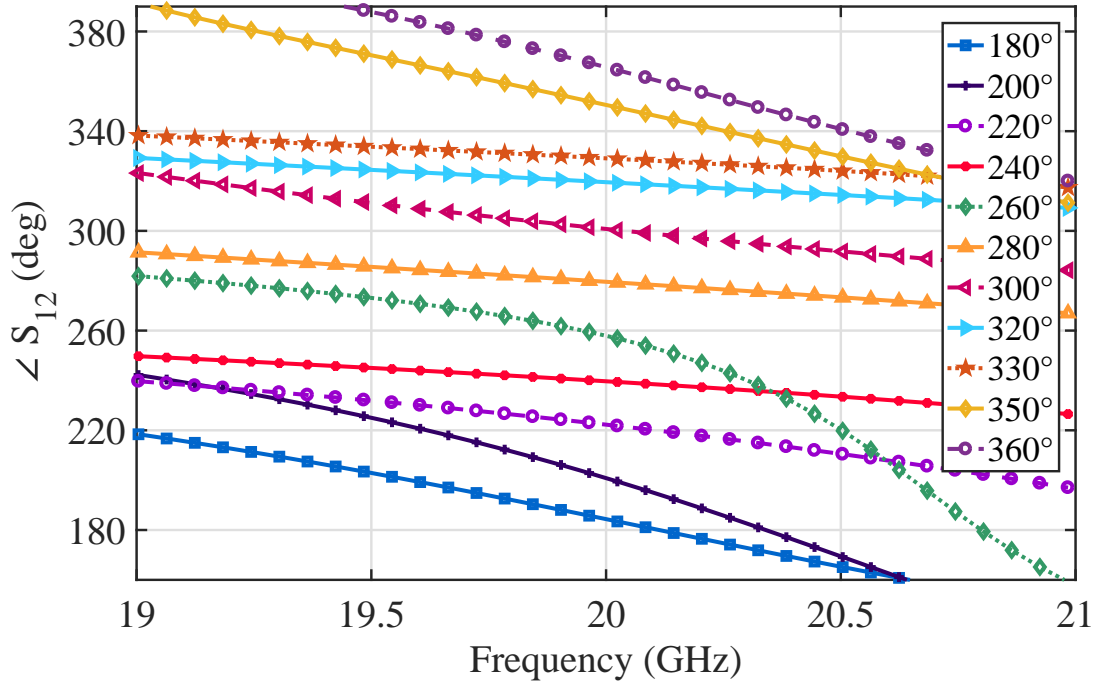
**Table 6.3:** Obtained phase shifts of the optimized pixelated unit-cells.

Desired $\angle S_{12}$	Obtained $\angle S_{12}$	Obtained $ S_{12} $	Design variables
$180^\circ$	$184.36^\circ$	0.92	$X^T = [000001110]$ , $X^B = [111110000]$
$200^\circ$	$200.83^\circ$	0.95	$X^T = [100101110]$ , $X^B = [110010101]$
$220^\circ$	$222.26^\circ$	0.93	$X^T = [001001110]$ , $X^B = [110100100]$
$240^\circ$	$239.66^\circ$	0.90	$X^T = [011100011]$ , $X^B = [110001101]$
$260^\circ$	$257.94^\circ$	0.91	$X^T = [001011001]$ , $X^B = [100101001]$
$280^\circ$	$279.57^\circ$	0.90	$X^T = [000000011]$ , $X^B = [010011011]$
$300^\circ$	$300.76^\circ$	0.95	$X^T = [111001110]$ , $X^B = [100000000]$
$320^\circ$	$319.79^\circ$	0.93	$X^T = [000010000]$ , $X^B = [101011010]$
$330^\circ$	$329.11^\circ$	0.90	$X^T = [000000000]$ , $X^B = [101001101]$
$350^\circ$	$350.52^\circ$	0.95	$X^T = [000101111]$ , $X^B = [001100111]$
$360^\circ$	$365.67^\circ$	0.90	$X^T = [101100101]$ , $X^B = [011011010]$

The transmission phase and magnitude of the unit-cell for a  $200^\circ$  phase shift is shown in Fig. 6.16, with the top and bottom unit-cell patterns given in the inset. Fig. 6.17 demonstrates the phase shifts provided by the optimized designs given in Table 6.3. It can be seen that a thin double-sided single-layer metasurface is capable of providing a  $180^\circ$  phase-shifting range at 20 GHz. The optimized unit-cells with pixelated patterns are half the thickness of the metasurface with square patches in [214] and can be used to improve the beam-steering solution by decreasing the profile, weight and complexity of the turning metasurfaces. The proposed optimization methodology and the obtained unit-cells can also be used in the design of transmitarrays [215].



**Figure 6.16:** Transmission coefficient magnitude and phase of the phase correcting metasurface. Optimized design meets the target of  $\angle S_{12,obj} = 200^\circ$ ,  $|S_{12}| \geq 0.9$  at 20 GHz.



**Figure 6.17:** The phase of the transmission coefficient of the optimized phase-shifting unit-cells with  $|S_{12}| \geq 0.9$ .

## 6.6 Summary

In this section, a novel methodology has been introduced for the synthesis of thin printed EM surfaces. The CE method has been used to optimize the double-sided pixelated unit-cell of a periodic structure. To the best of the author's knowledge, this is the first time CE has been used in application to the optimization of pixelated metallo-dielectric EM surfaces. The proposed approach has been demonstrated in application to the synthesis of thin double-sided AMCs and planar phase shifters, and it can be extended to any design of thin metallo-dielectric structures, for example metasurfaces and coding metamaterials [216]. Although only narrowband structures have been considered in the optimization, the bandwidth of the AMC can be increased by cascading two or more layers of periodic surfaces. The next chapter presents a simple and novel approach to the optimization of a microstrip lowpass filter by the CE method.



*The best and most beautiful things in the world  
cannot be seen or even touched. They must be  
felt with the heart.*

— Helen Adams Keller

## Chapter 7

# Optimization of Microstrip Low-Pass Filters

This chapter presents a simple approach for handling constraints using the CE method that strictly satisfies the linear equality and inequality constraints of an optimization problem. The feasibility of the proposed approach is demonstrated in application to the design of a microstrip low-pass filter. The formulated linear equality and inequality design constraints are strictly satisfied in each evaluated design, which is ensured by the use of appropriate sampling distributions. The desired cut-off frequency of the filter is achieved by incorporating a mask function in the optimization goal.

### 7.1 Introduction

A filter is a two-port device that allows signals of a certain desired band of frequencies to pass through it with very little attenuation or loss, while stopping the transmission of other undesired bands of frequencies [217]. A low-pass filter (LPF) allows the transmission of low frequencies while rejecting high frequencies. The recent advances in fabrication technologies and computer-aided design tools such as full-wave EM simulators revolutionised filter design [218]. Particularly, EM simulators can provide more accurate performance prediction than traditional linear models, as they can account for effects that are very difficult to simulate using linear modelling techniques. This is because the

microstrip circuitry is quasi-TEM, with some portion of the EM fields in the free space above the dielectric material. The design of high-performance microwave filters by interfacing EM simulation packages with global optimization algorithms is a vital modern research topic [219–222].

To obtain an optimal design in a reasonable time frame, local optimization from the starting point of a known initial design has become a routine approach for filter design optimization during the last decade [223]. However, when the initial design is not near the optimal solution, global optimization methods are necessary. In [10], it is stated that EAs require a prohibitive amount of time to complete a single optimization run. However, it will be shown in this chapter that a microstrip filter can be optimized within a reasonable period of time.

Although nowadays the computational time might not be such a problem due to the progress in computing capabilities and numerical analysis techniques, other challenges are present for optimization algorithms. In engineering problems, it is often required that additional restrictions are fulfilled by the optimal design. Such restrictions can be formulated by equality and inequality constraints. The constraint functions can include the design variables, the performance parameters and any mathematical combination of both. Equality constraints are very difficult to treat by optimization methods [224]. The reason is that the EAs randomly sample populations from a continuous solution space, which require minimal and maximal allowed values, also called lower and upper boundaries. These are, therefore, the only strict constraints that can be put on the design variables.

For the sufficiently accurate fulfilment of other constraints, additional modifications in the optimization flowchart are required as described in Section 2.6.2. However, such “tweaks” negatively affect the convergence of the optimizer, i.e. slow down or distort the search. Neither PSO nor CMA-ES in their pure forms can handle constraints [51, 225]. The advantage of the CE method is its flexibility with regard to the probability distribution family that is used for sampling the candidates. This advantage can be exploited for the consideration of design constraints. In order to demonstrate its feasibility, the



method was applied to the optimization of an improved microstrip LPF design.

In the design of microstrip filters, constraints are often required due to package considerations and space limitations. The description of the proposed optimization approach to tackle equality and inequality constraints will be addressed below. The design challenge is to preserve the cut-off frequency and the selectivity of the proposed filter design and improve its rejection bandwidth.

## 7.2 The CE Method for LPF Optimization

Classical stepped-impedance microstrip LPFs are realised by cascading low- and high-impedance transmission lines. The low-impedance wide lines act as shunt capacitors, and the high-impedance narrow lines act as series inductors. The recommended impedance of the capacitive microstrip sections is between 20–25 ohms, restricting the size of capacitive microstrip sections.

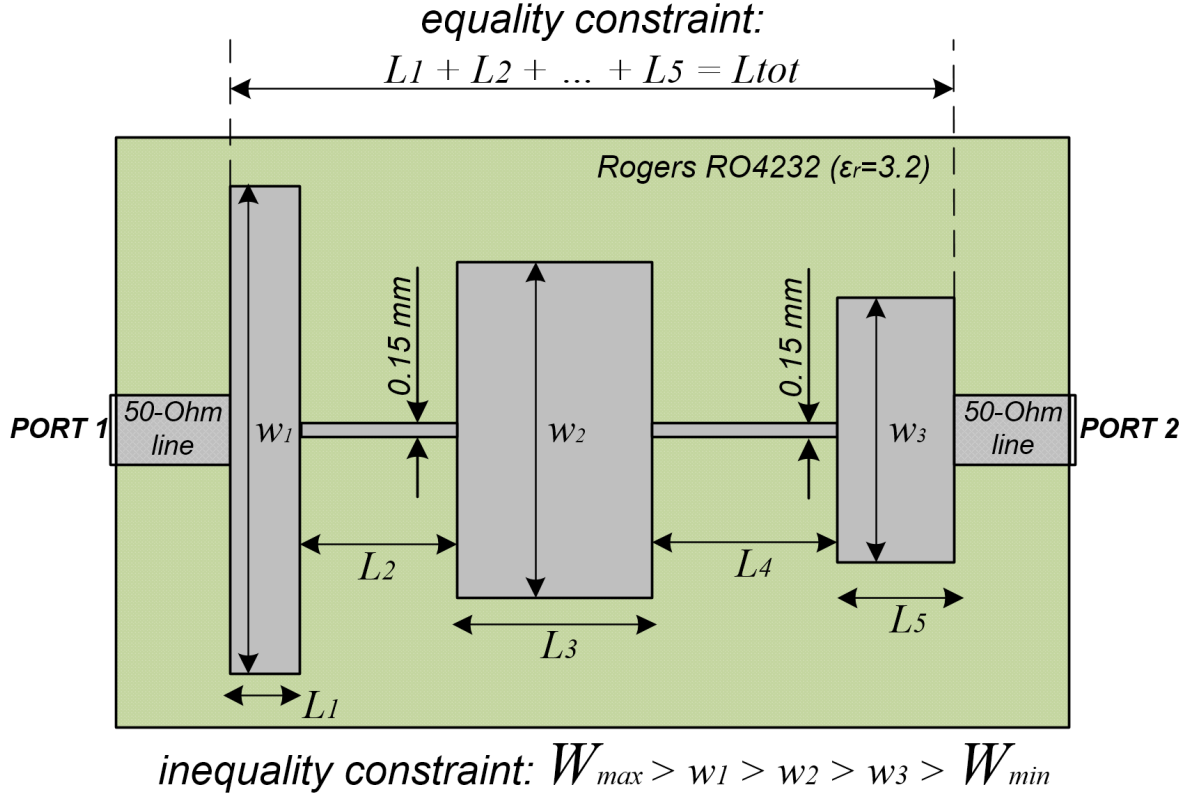
In [226], a new approach to the design of the classical stepped-impedance microstrip LPFs was adopted. It was shown that, by introducing a transverse resonance in a capacitive section, a transmission zero can be added in the stopband of the filter. This improves the sharpness of rejection, attenuation depth and rejection bandwidth. The design of this filter is known as the transverse resonance LPF (TR-LPF). It has been implemented using the Butterworth prototype, but the Chebyshev prototype can also be used. However, the limitation of the initial TR-LPF was the trade-off between the high selectivity and wide rejection bandwidth, due to a single transmission zero (TZ) frequency that was the same for all capacitive sections.

To overcome this limitation, linearly-distributed multiple TZ frequencies have been introduced in the stopband [227]. When TZ frequencies are placed closer to the cut-off frequency, higher selectivity with a very high attenuation level is obtained, but at a cost of limited rejection bandwidth. On the other hand, when TZ frequencies are spread out more in the stopband, it results in the large rejection bandwidth but with lower attenuation levels and poor selectivity. This filter, called a linear TR-LPF, has multiple

design variables and seems an ideal candidate for optimization.

### 7.2.1 Non-Uniform Microstrip Transverse Resonance LPF

Instead of linearly distributing the TZ frequencies in the stopband, we aim at optimizing the filter dimensions so that the TZ frequencies can be placed at arbitrary locations while preserving the transverse resonance. A 5-pole TR-LPF with cut-off frequency  $f_c = 2.5$  GHz is considered as an example for applying the proposed optimization approach. The widths of the capacitive sections depend on the TZ frequencies, and their lengths depend on the capacitance required to obtain the Butterworth response. In order to maintain the cut-off frequency, the lengths of the inductive sections have to be adjusted. The widths of the inductive sections are fixed at 0.15 mm. While wider inductive sections can handle more power, lower widths suppress the harmonics in the stopband. A layout of a 5-pole parametrised TR-LPF consisting of alternating capacitive and inductive elements is shown in Fig. 7.1.



**Figure 7.1:** Layout of a 5-pole transverse resonance Butterworth microstrip LPF.

The substrate Rogers RO4232 with  $t=0.762$  mm and  $\varepsilon_r=3.2$  is used for the realisation of the design. Each capacitive section is defined by two parameters,  $L_i$  and  $w_i$ , and each inductive section is defined only by length  $L_j$ , where  $i = 1, 3, 5$ ,  $j = 2, 4$ . For the case of the 5-pole filter, the design vector has 8 continuous variables. To incorporate *a priori* knowledge of this filter design, we formulate the optimization problem subject to two constraints, the equality constraint  $L_1 + L_2 + \dots + L_5 = L_{tot}$  and the inequality constraint  $W_{max} > w_1 > w_2 > w_3 > W_{min}$ . The total length of the filter  $L_{tot}=18$  mm, and the minimal and maximal widths of the capacitive sections are  $W_{min}=10$  mm and  $W_{max}=35$  mm (substrate width), respectively.

The equality constraint ensures that the total length of the filter is within the required dimensions. The inequality constraints arise out of the physics of the problem. Since transverse resonance occurs along the width of the capacitive section, its wavelength cannot be more than the half wavelength at the first TZ frequency. Since the TZ frequency will always be greater than the cut-off frequency  $f_c$ ,  $W_{max}$  will always correspond to  $\lambda_c/2\sqrt{\varepsilon_{r,eff}}$ , where  $\varepsilon_{r,eff}$  can be calculated using the Hammerstad-Jensen formula [228]. The practical  $W_{min}$  limit is slightly larger than the width of a 50-ohm microstrip line. Below this width, the capacitance of the 50-ohm lines dominates, and the capacitive sections behave as inductors.

### 7.2.2 Optimization Approach

The design parameters of this filter are defined by the design vector

$$\mathbf{x} = (L_1, L_2, L_3, L_4, L_5, w_1, w_2, w_3).$$

Two constraints have been previously formulated for the optimization problem:

- Length requirement:  $L_1 + L_2 + \dots + L_5 = L_{tot}$ ,
- Width requirement:  $W_{max} > w_1 > w_2 > w_3 > W_{min}$ .

To ensure that each generated design inherently satisfies the formulated constraints, the Dirichlet distribution has been used for sampling. The Dirichlet distribution has the

PDF given by

$$f(x_1, \dots, x_k; \alpha_1, \dots, \alpha_k) = \frac{\Gamma(\sum_{i=1}^k \alpha_i)}{\prod_{i=1}^k \Gamma(\alpha_i)} \prod_{i=1}^k x_i^{\alpha_i-1}, \quad (7.1)$$

where the sum of the design variables  $\sum_{i=1}^k x_i = 1$  and  $x_i \geq 0$  for all  $i \in [1, k]$  dimensions,  $\Gamma$  is the gamma function and  $(\alpha_1, \dots, \alpha_k)$  are the distributional parameters. It is important to note that the support of the Dirichlet distribution includes real numbers from the interval  $(0, 1)$ , but it can be converted to any simplex defined by the design variables. To do that, a linear transformation can be applied to the Dirichlet simplex.

The lengths have been sampled directly from PDF  $f_1(x_1, \dots, x_5; \alpha_1, \dots, \alpha_5)$ , where  $x_1 + x_2 + \dots + x_5 = 1$  and  $(\alpha_1, \dots, \alpha_5)$  are the distributional parameters. The minimal limitation of  $L_{min} = 0.1$  mm has been applied considering fabrication tolerances. Thus, the sampled values  $(x_1, \dots, x_5)$  are transformed to the required simplex by

$$L_1, \dots, L_5 = L_{min} + (L_{tot} - 5 * L_{min}) * (x_1, \dots, x_5). \quad (7.2)$$

Due to the fact that  $\sum_{i=1}^k x_i = 1$ , the equality constraint is automatically fulfilled.

The widths are sampled from PDF  $f_2(y_1, \dots, y_4; \alpha_6, \dots, \alpha_9)$ , with the further transformation according to:

$$w_3 = w_{min} + (w_{max} - w_{min}) * y_1, \quad (7.3)$$

$$w_2 = w_{min} + (w_{max} - w_{min}) * (y_1 + y_2), \quad (7.4)$$

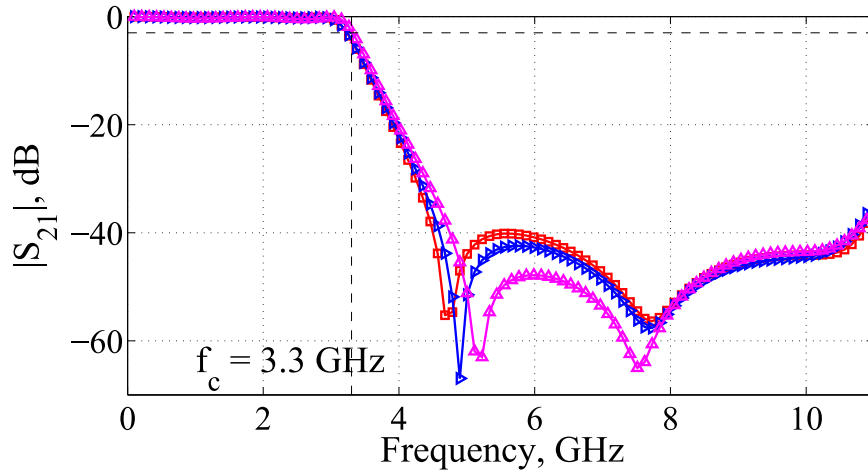
$$w_1 = w_{min} + (w_{max} - w_{min}) * (y_1 + y_2 + y_3), \quad (7.5)$$

ensuring the inequality condition. The parameters of the CE method that were set in the optimization of this LPF are summarised in Table 7.1.

**Table 7.1:** The CE method parameters for optimization of 5-pole LPF problem.

Population size	Elite subpopulation size	Smoothing
$N_{pop}$	$N_{el}$	$\alpha_S$
30	10	0.1

The major difficulty of broadband filter response optimization is to obtain an optimized solution with a cut-off frequency of exactly 2.5 GHz. Initially, a traditional approach was taken to the formulation of the fitness function, specifying the desired levels of attenuation in the passband and in the rejection band. The cost function increases proportionally to the difference between the desired level and the actual result. Many designs optimized using this cost function have excellent stopband response in terms of the selectivity and/or the rejection bandwidth, but with a cut-off frequency different from 2.5 GHz. Fig. 7.2 shows the transmission characteristics of some of the optimized cases. It can be seen that the passband and rejection-band requirements are fulfilled, but the cut-off frequency is shifted from 2.5 to 3.3 GHz.



**Figure 7.2:** Transmission characteristics of the designed 5-pole TR-LPF with a cut-off frequency at 3.3 GHz using the traditional cost function formulation.

In order to achieve the desired transmission characteristics of the filter, a new approach has been taken to the fitness formulation. The optimization goal was expressed using a mask function given by the following expression:

$$mask(fr) = \begin{cases} 0, & fr < 2.4 \text{ GHz} \\ 147 - 60 \times fr, & 2.4 \text{ GHz} \leq fr < 3 \text{ GHz} \\ -35, & fr \geq 3 \text{ GHz} \end{cases} \quad (7.6)$$

The mask has separate sections for the passband, cut-off and rejection bands. The coefficient in front of the frequency variable corresponds to the desired selectivity 60 dB/GHz,

and another coefficient is selected to smooth out the sharp corners of the piecewise function. The optimization goal is to minimise the cost function given below:

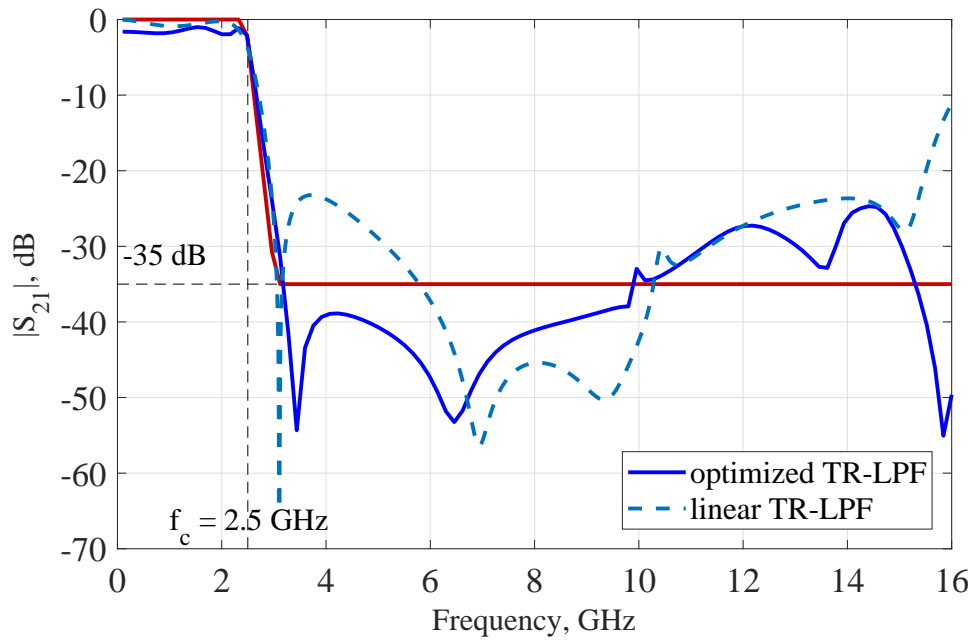
$$F.F. = \sum_{0.1 \text{ GHz}}^{2.4 \text{ GHz}} 20 * (S_{21}(fr_i) - mask(fr))^2 + \sum_{2.4 \text{ GHz}}^{3 \text{ GHz}} (S_{21}(fr_i) - mask(fr))^2 + \sum_{3 \text{ GHz}}^{16 \text{ GHz}} (S_{21}(fr_i) - mask(fr))^2, \quad (7.7)$$

where  $S_{21}(fr_i)$  is a transmission coefficient given in dB at  $i = 1, \dots, 101$  frequency points in the range 0.1–16 GHz. Due to the filter symmetry and even-mode excitation, a magnetic wall was placed into the plane of symmetry in order to reduce the simulation time by half.

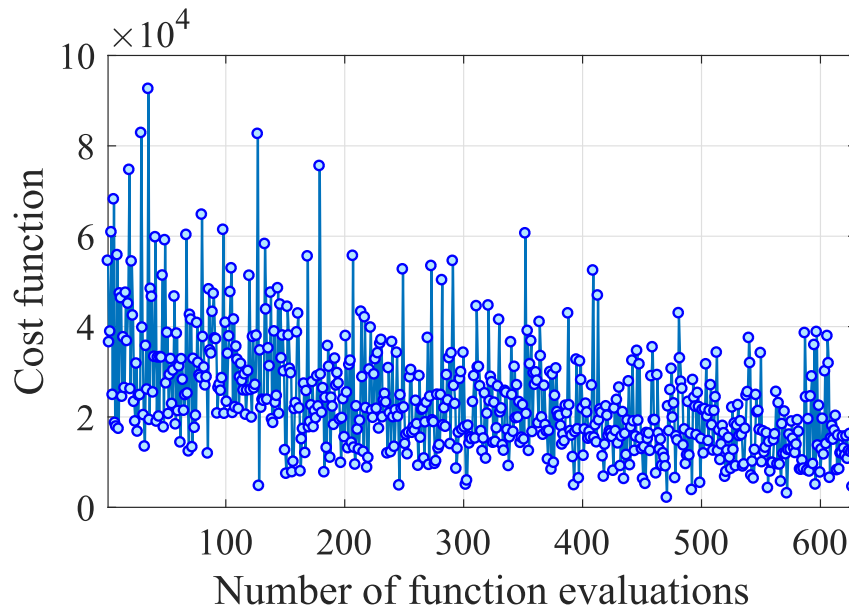
### 7.3 Optimization Results

The best result obtained after five optimization runs is shown in Fig. 7.3. The cut-off frequency of the filter is at 2.5 GHz, as desired. As a result of the optimization, the rejection bandwidth has been improved from 0.5 GHz [227] to 8.5 GHz, preserving the selectivity of the filter and its cut-off frequency. Considering the low order of the filter, the attenuation level is compared at the level of  $-30$  dB. Although the level of  $|S_{21}|$  in the passband degraded from  $-1.3$  dB for the initial filter to  $-2.2$  dB for the optimized one, the required insertion loss level depends on the application. The weight of the first term in the cost function might be increased, but also decreasing the width of inductive sections (which has been fixed to 0.15 mm) can minimize the ripple in the passband.

CST MWS time-domain solver was used to model the filter response. On an Intel Core i7 3.6 GHz processor with 32 GB of RAM, the optimization takes around 4.5 hours. Fig. 7.4 shows the evolution of the cost function over the function evaluations for the run that produces the best result. The stopping criterion was satisfied after 21 iterations, resulting in 630 function evaluations. The dimensions of the initial design, with a linear distribution of the TZ frequencies, and the optimized design are summarised in Table 7.2.



**Figure 7.3:** Comparison of the optimized TR-LPF and the linear TR-LPF. The transmission mask (*red line*) defines the desired filter response. The optimization goal was to minimise the squared difference between the mask and the result.



**Figure 7.4:** Convergence curve for the optimization of a 5-pole TR-LPF.

**Table 7.2:** Parameter values for the 5-pole TR-LPF before and after optimization.

Design Parameters, mm	Before optimization	After optimization
$L_1, w_1$	0.55, 33.23	1.58, 30.34
$L_2$	3.5	2.75
$L_3, w_2$	4.05, 16.46	4.89, 17.17
$L_4$	3.5	3.93
$L_5, w_3$	1.77, 10.87	4.84, 11.14
–30 dB rejection bandwidth, GHz	0.5	8.5
Selectivity, dB/GHz	60.2	60.3



## 7.4 Summary

This chapter presents the results of applying the CE method to the design of a stepped-impedance TR-LPF. The initially proposed design of the 5-pole TR-LPF with the cut-off frequency at 2.5 GHz had a limitation of a narrow rejection bandwidth if the selectivity was 60 dB/GHz. The CE optimization method incorporates the design considerations in the form of equality and inequality constraints. The novel approach ensures that the constraints are satisfied for each design solution, which cannot be realised by PSO or CMA-ES in their pure forms. The optimization goal was formulated by means of a mask function representing the desired response. By optimizing the lengths and widths of capacitive and inductive microstrip sections, the rejection bandwidth of the 5-pole TR-LPF was improved from 0.5 GHz to 8.5 GHz.



*Success is not final, failure is not fatal: it is the courage to continue that counts. Success consists of going from failure to failure without loss of enthusiasm.*

— Winston Churchill

# Chapter 8

## Conclusions

This chapter summarises and concludes the thesis by highlighting the key findings of the conducted research. Avenues for future work are proposed that can advance optimization technology for EM engineering problems.

### 8.1 Summary

This thesis investigated the functionality of evolutionary optimization algorithms in application to EM engineering problems. Three algorithms were considered: particle swarm optimization (PSO), cross-entropy (CE) and covariance matrix adaptation evolutionary strategy (CMA-ES). PSO was selected because it is simple to implement and a very popular optimization method. CE is a new method for EM problems, and was found to have attractive properties, especially for simulation-driven optimization. In particular, it has fast convergence, and it can be easily adapted to any type of optimization problem, such as continuous, discrete (including binary), mixed-parameter and constrained. CMA-ES was selected because it is an emerging popular algorithm and does not require adjustment of its internal parameters.

The optimization problems considered in this thesis are cutting-edge research topics and offer novel promising capabilities for many applications in wireless communication systems. Chapter 3, 4 and 5 describe the optimization of compact resonant cavity antennas (RCAs) and aperture-coupled microstrip patch antennas (ACMPAs) using PSO,

CE and CMA-ES. Chapter 6 introduces the CE optimization method for the synthesis of pixelated EM surfaces and metasurfaces, and Chapter 7 shows the approach to design constrained microstrip low-pass filters with improved characteristics.

In Chapter 3, the designed RCAs have superstrates (of either pre-defined or optimized thickness) constructed from annular dielectric sections of equal widths and different permittivity values. Since these design problems are continuous and unconstrained, PSO was employed for their optimization. Four different formulations of the objective functions yielded four antenna designs with high-gain performance of 17.6–19.6 dB and small footprint of  $1.7\text{--}2.2\lambda_0$ . The antennas have 3-dB radiation bandwidths of 24%, 50% and 70%, which makes them good candidates for wideband communication systems including high data-rate wireless local area networks and point-to-point communications.

The problem of constrained mixed-variable optimization is addressed in Chapter 4 using the CE method. Previously, CE applications to EM designs have utilised only the normal distribution, thus not taking advantage of its flexible updating rules. Discrete and Dirichlet probability distribution families are employed to optimize both constrained continuous parameters of the widths in the superstrates of fixed diameter and their discrete permittivity values. The method accounts for the list of available dielectric constants, which results in ready-to-fabricate optimized designs. Six compact wideband RCAs are obtained with optimal superstrate profiles and diameters of  $1.5\lambda_0$ ,  $1.85\lambda_0$  and  $2.2\lambda_0$ . Compared to the initial design obtained manually, the optimized RCAs have higher gain and lower side lobe levels in the frequency band of interest. The best obtained RCA design has a peak directivity of 19.4 dBi, 3-dB radiation bandwidth of 40% and side lobe levels close to  $-20$  dB at all frequencies in the operating band.

Chapter 5 presents the results of ACMPA design by PSO, CE and CMA-ES. The optimization problem is continuous and unconstrained. The design objective is to provide input impedance matching with  $S_{11} \leq -10$  dB in the band 12–18 GHz. First, a stand-alone ACMPA is optimized. Then, it is optimized in the resonant cavity offering an advantage of a planar feed for RCAs. Comparing the performance of three optimization methods, it is concluded that CE is an efficient and fast optimization technique for unconstrained

continuous problems. It yielded designs with performance similar to PSO in much less time.

A novel methodology for the optimization of pixelated EM surfaces is proposed in Chapter 6. The optimization problem has binary design variables. As in the optimization of such problems by GAs, the pixels are encoded by “0s” and “1s”, but instead of genetic operators, a Bernoulli probability distribution is used to produce next generations. The proposed methodology yielded two types of EM surfaces: artificial magnetic conductors (AMCs) and phase-shifting metasurfaces. A single-frequency AMC operates at 10 GHz, and dual-band AMC operates at 8 and 12 GHz, both featuring polarisation independence. Eleven thin transparent metasurfaces operate at 20 GHz and produce phase shifts from 180 to 360°.

Most real-world EM engineering problems are constrained. Commonly, constraints are handled by applying penalties to designs which fall outside of the constrained area, which reduces the chance that these candidates will occur in the next generations. This procedure is, however, inefficient. In Chapter 7, it is shown how to incorporate constraints in the definition of design parameters using the CE method. The Dirichlet probability distribution is used to generate continuous constrained variables, which by design satisfy all predefined constraints. Using the proposed technique, a microstrip low-pass filter with transverse resonance in the capacitive sections is designed. The optimized filter outperforms the initial design, offering a wide rejection bandwidth and preserving the filter size, selectivity and a cut-off frequency.

## 8.2 Avenues for Future Work

The findings of this research and proposed methodologies can be applied to other EM design problems. Possible directions for future study are given below.

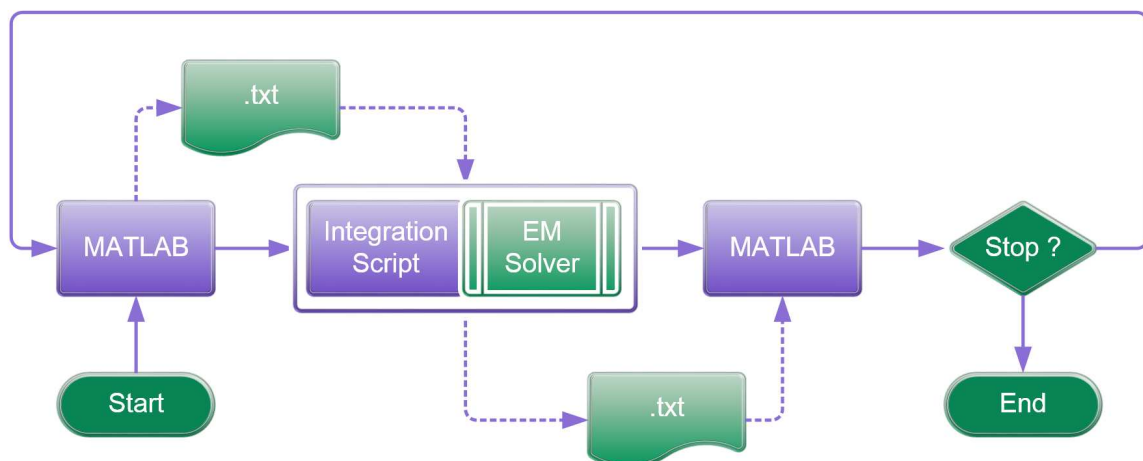
- The methodology for combinatorial optimization using the CE method can be used in the design of lens antennas, such as Maxwell fish-eye lens as a beam splitter described in [229].

- The proposed methodology for constrained design problems using the Dirichlet distribution can be applied to microwave devices, such as filters and couplers, in order to achieve miniaturisation or weight reduction by reducing the number of elements [230].
- The methodology for binary optimization using the CE method can be applied to the synthesis of other thin metallo-dielectric structures, such as metasurfaces, coding metamaterials, reflectarrays, transmitarrays and polarisation converters [231].
- Modifications can be sought to further improve the convergence rate of the CE algorithm and/or improve the algorithm's resistance to premature convergence. Also, other probability distributions can be used in CE optimization, discovering new capabilities of the method.
- It is interesting to compare the performance of other emerging algorithms such as IWO and BBO with CE, PSO and CMA-ES on some common antenna design problems and identify the common features. As the topography of fitness functions in simulation-driven EM optimization is usually unknown, it would be useful to match the algorithms with problems of similar type. Also, it is important to create a common figure-of-merit for the comparison that combines both mean number of function evaluations and the value of the fitness function. Alternatively, the comparison can be based on the characteristics of the EM problems.
- Following from the previous suggestion, it seems useful to create a standard set of benchmark EM problems (continuing the work initiated in [232–235]). The demand for evolutionary optimization in electromagnetics will continue to grow, and therefore, a systematic approach to their study is necessary.

# Appendix A

## Interfacing MATLAB and CST MWS

A general workflow for interfacing a MATLAB-based optimization algorithm (a custom-built or from the Optimization Toolbox) with an external EM solver is shown in Fig. A.1. In this thesis, CST MWS has been used for all simulations, and, therefore, it will be mentioned as an example EM solver in the further discussion.



**Figure A.1:** The flowchart for interfacing MATLAB and CST MWS.

The important implementation steps are:

- *MATLAB environment*: a new population is generated by an optimization algorithm, and the values of the design parameters for each candidate are stored in

a text file. MATLAB initiates the execution of a macro script to launch CST simulations.

- *CST MWS environment*: the values of the design parameters for each candidate are transferred to a project for simulation. To store the simulation results of each candidate, a user-defined watch is used. It creates another text file in a Result folder and stores the results after each simulation. When all simulations are completed, control returns to MATLAB.
- *MATLAB environment*: the results stored in the Result folder are accessed for further evaluations of the fitness function. The iterations continue until the stopping condition is satisfied.

The described implementation employs **ParameterSweep Object** to speed up the evaluation process. In particular, the information about all candidates in a generation is loaded into CST MWS to perform continuous simulations. This is faster than simulating each candidate separately due to the minimized number of software launches. Although optimization problems are ideal for parallel computing, the described technique is beneficial in case of computationally inexpensive problems or unavailable high performance computing resources.

In order to launch CST MWS, the following command has to be executed from MATLAB environment:

```
system('C:\...\CST STUDIO SUITE 2016\CST
DESIGN ENVIRONMENT.exe" -m "E:\...\Macro.bas"');
```

The file “Macro.bas” is a macro script written using Visual Basic for Applications (VBA). Below an example of a script used for the optimization problem Case-I from Chapter 4 is provided.

```
Sub Main
Dim popSize As Integer, N As Integer
Dim eps() As Double, radii() As Double
```



---

```
Dim FilePath1 As String, FilePath2 As String
Dim sequenceName As String, candidate As String, strPopSize As String
Dim i As Integer, j As Integer, k As Integer
FilePath1 = "E:\...\eps.txt"
FilePath2 = "E:\...\radii.txt"

'Set number of sections in a superstrate
N=3

'Set population size
popSize = 25

'Preallocate arrays for eps and radii
ReDim eps(popSize,N), ReDim radii(popSize,N)
'Read data for the current generation from the text files
Open FilePath1 For Input As #1
For i = 1 To popSize
For j = 1 To N
    Input#1, eps(i,j)
Next j
Next i
Close #1
Open FilePath2 For Input As #2
For i = 1 To popSize
For j = 1 To N
    Input#2, radii(i,j)
Next j
Next i
Close #2
```

```
'Open CST model
openfile("E:\...\File_name.cst")
Rebuild

'Define parameters for each candidate
With ParameterSweep
.DeleteAllSequences
For k = 1 To popSize
candidate = "Candidate"
strPopSize = CStr (k)
sequenceName = candidate & strPopSize
.AddSequence sequenceName
.AddParameter_Samples sequenceName, "e1", eps(k,1), eps(k,1), "1", "False"
.AddParameter_Samples sequenceName, "e2", eps(k,2), eps(k,2), "1", "False"
.AddParameter_Samples sequenceName, "e3", eps(k,3), eps(k,3), "1", "False"
.AddParameter_Samples sequenceName, "w_1", radii(k,1), radii(k,1), "1", "False"
.AddParameter_Samples sequenceName, "w_2", radii(k,2), radii(k,2), "1", "False"
.AddParameter_Samples sequenceName, "w_3", radii(k,3), radii(k,3), "1", "False"
'Write result about each candidate into a result text file
.AddUserdefinedWatch
Next k
'Start solver
.Start
End With
save
End Sub
```

# Appendix B

## Sample Code for the Implementation of the CE method

A MATLAB implementation of the CE method for the optimization of Ackley and Sum of Squares functions using the beta distribution family is provided below.

```
1  %%% Copyright 2016, Maria Kovaleva, David Bulger
2  %%% Macquarie University. All rights reserved.%%
3  clear all; clc
4  %% Set the number of Monte-Carlo simulations
5  for N_trial=1:20
6  %% %%%%%%%%%%% Set parameters %%%%%%%%%%%
7  D = 5; % Set dimensionality of the problem
8  variable_range=15.*repmat([-1 1],1,D); % Set search space bounds
9  variable_range=reshape(variable_range, [2,D]);
10 genSize=100; % Set population size
11 qElite=10; % Set elite subpopulation size
12 smooting=0.9; % Set smoothing parameter
13 % Set initial distribution parameters:
14 Beta_alpha=ones(D,1); % uniform Beta distribution, *optional
15 Beta_beta=ones(D,1); % uniform Beta distribution, *optional
16 %% Preallocation for speed:
17 average_fitness_plot=zeros(1,100);
```

```

18 fBestResult_plot=zeros(1,100);
19 fBestResult= -inf;
20 % Initialize history
21 history={};
22 fitness = zeros(1, genSize);
23 variable = zeros(D,genSize);
24 variable_real = zeros(D,genSize);
25 %% Start Cross-Entropy Optimization Algorithm
26 threshold= - 0.1; % Set stopping criterion
27 i=1; % Set iteration count
28 tic % Display elapsed time
29 while fBestResult < threshold
30 %% Sample variables from the beta-distribution
31 Beta_alpha_r= repmat(Beta_alpha,1,genSize); ...
    Beta_beta_r= repmat(Beta_beta,1,genSize);
32 for c=1:D % in each dimension
33 variable(c,:) = betarnd (Beta_alpha_r(c,:),Beta_beta_r(c,:));
34 variable_real(c,:) = ...
    diff(variable_range(:,c)).*variable(c,:)+variable_range(1,c); % ...
    transform into the search space bounds
35 end
36 %% Start fitness function evaluation
37 % Option to switch between Ackley and Sum of Squares
38 for gen=1:genSize
39 %hist.fitness_raw(1,gen) = -sumsqu (variable_real(:,gen),D);
40 hist.fitness_raw(1,gen) = -ackley (variable_real(:,gen),D); % inverted ...
    for maximization
41 end
42 %% Sort fitness values, choose elite
43 [fitness, sortOrder] = sort(hist.fitness_raw, 2, 'descend'); % in ...
    descending order for maximization
44 sortOrder = sortOrder(1:qElite);
45 % The elite, in descending order of fitness:
46 elite_x = variable(:, sortOrder);

```

---

```

47 elite_real=variable_real(:, sortOrder); % transformed into the search ...
    space bounds
48 %% HAS THIS GENERATION PRODUCED A NEW BEST RESULT?
49 if fitness(1) > fBestResult
50 fBestResult = fitness(1);
51 best_x = elite_real(:, 1);
52 end
53 average_fitness=mean(fitness);
54 % Plot fitness evolution over generations
55 average_fitness_plot(i)=average_fitness;
56 fBestResult_plot(i)=fBestResult;
57 figure (1)
58 xlabel('Number of generations')
59 ylabel('Fitness function')
60 title('Fitness over generations'); grid on
61 plot(1:i, fBestResult_plot(1:i), 'r*-'); hold on
62 plot(1:i, average_fitness_plot(1:i), 'ko:');
63 %% From the elite, estimate distrib. parameters for the next generation
64 for c=1:D
65 p_x(c,:) = betafit(elite_x(c,:)); % beta parameter estimates
66 end
67 new_Beta_alpha=p_x(:,1); new_Beta_beta=p_x(:,2);
68 %% Apply smoothing *optional
69 Beta_alpha=Beta_alpha+smooting*(new_Beta_alpha-Beta_alpha);
70 Beta_beta=Beta_beta+smooting*(new_Beta_beta-Beta_beta);
71 %% Writing history file *optional
72 hist.Beta_alpha=Beta_alpha; hist.Beta_beta=Beta_beta; ...
    hist.fitness=fitness;
73 hist.average_fitness=average_fitness; hist.fBestAntenna = fBestResult;
74 hist.variable=variable_real; hist.elite=elite_real;
75 history = {history{:}, hist};
76 %% Generation count
77 i=i+1;
78 end
79 toc

```

```

80 best_solution = sprintf('%f\n', best_x);
81 fprintf('Best location:\n %s\n', best_solution)
82 fprintf('Global best with fitness %f was reached at generation %d.\n', ...
    fBestResult, i-1);
83 stats_AckleyBeta.MNFE(N_trial) = genSize*(i-1);
84 stats_AckleyBeta.Iter(N_trial) = i;
85 end
86 fprintf('After repeting %d trials, FINAL statistics: \n Average MNFE is ...
    %.2f, Average number of generations %.1f.\n', N_trial, ...
    mean(stats_AckleyBeta.MNFE), mean(stats_AckleyBeta.Iter));
88 figure; boxplot(stats_AckleyBeta.MNFE)

1 function y = ackley(x,n) % Ackley function.
2 % Initial Matlab Code by A. Hedar (Sep. 29, 2005) but modified to
3 % include the number of variables in the input parameters.
4 a = 20; b = 0.2; c = 2*pi;
5 s1 = 0; s2 = 0;
6 for i=1:n
7     s1 = s1+x(i)^2;
8     s2 = s2+cos(c*x(i));
9 end
10 y = -a*exp(-b*sqrt(1/n*s1)) -exp(1/n*s2) +a +exp(1);

1 function y = sumsqu(x,n) % SUM SQUARES FUNCTION
2 % Copyright 2013. Derek Bingham, Simon Fraser University.
3 sum = 0;
4 for i = 1:n
5     xi = x(i);
6     sum = sum + i*xi^2;
7 end
8 y = sum;
9 end

```

# Appendix C

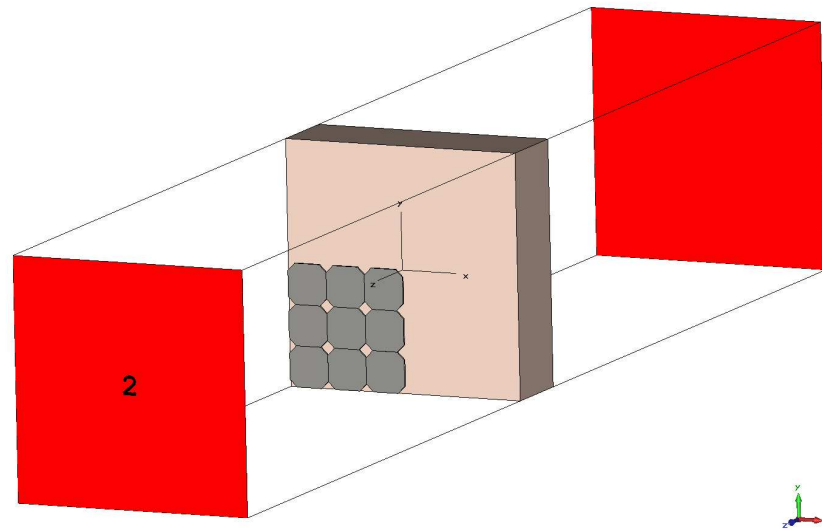
## VBA Program for the Optimization of Pixelated Unit-Cells

The following VBA program has been used for the optimization of pixelated unit-cells. For parallel simulations on a local machine, `matlabpool` has been used. The designs are sent to *CST MWS environment* from *MATLAB* by the following command:

```
parfor k=1:popSize
fprintf(' Simulating %f particle.\n ', k);
system(['C:\...\CST DESIGN ENVIRONMENT.exe" -m "E:\...
...\macro_pixelated_uc',num2str(k),'.bas"']);
end
```

Each script has a name starting from “macro\_pixelated\_uc.bas” and ending with the candidate index. The scripts call *.cst* files with a unit-cell model shown in Fig. C.1. The contents of “macro\_pixelated\_uc1.bas” are provided below:

```
Sub Main
Dim genSize As Integer, m_bits As Integer, n_bits As Integer
Dim length As Double, t_pec As Double, th_s As Double, h_cav As Double
Dim top_bits() As Double, bot_bits() As Double
Dim FilePath1 As String, FilePath2 As String
```



**Figure C.1:** Initial unit-cell model with only the quarter of the pixels on each side of the superstrate.

```

Dim sequenceName As String, candidate As String, strPopSize As String
Dim i As Integer, j As Integer, k As Integer, c As Integer, cand As Integer
FilePath1 = "E:\...\top_bits_data_can1.txt"
FilePath2 = "E:\...\bot_bits_data_can1.txt"

' Define Unit-Cell Parameters
m_bits=3 ' Number of rows/2
n_bits=3 ' Number of columns/2

' Set population size
genSize=30

' Read data for the current generation from the text files
ReDim top_bits(m_bits-1,n_bits-1,genSize-1)
Open FilePath1 For Input As #1
For i = 0 To m_bits-1
    For j = 0 To n_bits-1
        Input#1, top_bits(i,j,genSize-1)
    
```



---

```

        Next j
    Next i
Close #1
ReDim bot_bits(m_bits-1,n_bits-1,genSize-1)
Open FilePath2 For Input As #2
    For i = 0 To m_bits-1
        For j = 0 To n_bits-1
            Input#2, bot_bits(i,j,genSize-1)
        Next j
    Next i
Close #2

' Open CST model
OpenFile ("E:\...\pixelated_design_1.cst")
Rebuild

' Substitute zero bits by vacuum
For j = 1 To n_bits
    For i = 1 To m_bits
        If top_bits(i-1,j-1,genSize-1) = 0 Then
            Solid.ChangeMaterial "Unit-cell:top_element_"+cstr(i)+cstr(j), "Vacuum"
        End If
        If bot_bits(i-1,j-1,genSize-1) = 0 Then
            Solid.ChangeMaterial "Unit-cell:bot_element_"+cstr(i)+cstr(j), "Vacuum"
        End If
    Next i
Next j

```

```
'Rotate the quarter of the unit-cell to form the full structure
```

```
With Transform
```

```
.Reset:.Name "Unit-cell":.Origin "Free":.Center "0", "0",
```

```
"0":.Angle "0", "0", "90"
```

```
.MultipleObjects "True":.GroupObjects "False":.Repetitions
```

```
"3":.MultipleSelection "False"
```

```
.Destination "":.Material "":.Transform "Shape", "Rotate"
```

```
End With
```

```
Solver.Start
```

```
' Write the results into the results folder
```

```
Dim filename1 As String, filename2 As String
```

```
filename1 = "E:\...\Result_UC_magS12_can1.txt"
```

```
filename2 = "E:\...\Result_UC_phaseS12_can1.txt"
```

```
SelectTreeItem ("Tables\1D Results\S1,2mag")
```

```
With ASCIIExport
```

```
.FileName (filename1):.Execute
```

```
End With
```

```
SelectTreeItem ("Tables\1D Results\arg(S1,2)")
```

```
With ASCIIExport
```

```
.FileName (filename2):.Execute
```

```
End With
```

```
End Sub
```

# Appendix D

## List of Publications

Some of the presented work has been published in peer-reviewed journal and conference proceedings, while the remaining work is in preparation for submission. I am the main contributor to the following publications:

- ***Patents:***

1. **M. Kovaleva**, D. Bulger, K.P. Esselle, B.A. Zeb, International Patent Application PCT/AU2017/050873. *Title: Optimisation of designs of electromagnetic devices*, date of filing: 16 August 2017.
2. **M. Kovaleva**, D. Bulger, K.P. Esselle, B.A. Zeb, Australian Patent Application (AU) 2016903249. *Title: Optimisation of designs of electromagnetic devices*, date of filing: 16 August 2016.

- ***Academic journals:***

1. **M. Kovaleva**, D. Bulger, B.A. Zeb and K.P. Esselle, “Cross-Entropy Method for Electromagnetic Optimization with Constraints and Mixed Variables”, *IEEE Transactions on Antennas and Propagation*, vol. 65, no. 10, pp. 5532-5540, Oct. 2017.
2. **M. Kovaleva**, D. Bulger and K. P. Esselle, “A Comparative Study of CE, PSO and CMA-ES in Wideband Antenna Design”, *IEEE Transactions on Evolutionary Computation*, in preparation.

3. **M. Kovaleva**, D. Bulger and K. P. Esselle, “A Novel Fast Optimization Method for Pixelated Metasurface Design”, *IEEE Transactions on Antennas and Propagation*, in preparation.

• **Conference proceedings:**

1. **M. Kovaleva**, D. Bulger, R. P. Khokle, K.P. Esselle, “Application of the Cross-Entropy Method to Electromagnetic Optimisation Problems”, *2018 IEEE International Symposium on Antennas and Propagation (AP-S/USNC-URSI)*, Boston, MA, 2018, pp. 1595-1596.
2. K. Singh, **M. Kovaleva**, K.P. Esselle and J. Kot, “Cross-Entropy Method for Optimization of a Dielectrically Loaded Wideband Waveguide Polarizer”, *Third Australian Microwave Symposium (AMS 2018)*, Brisbane, Australia, Feb. 6-7, 2018.
3. **M. Kovaleva**, D. Bulger and K.P. Esselle, “Efficient Optimization of a Simple Compact Resonant Cavity Antenna”, *2017 IEEE International Symposium on Antennas and Propagation (AP-S/USNC-URSI)*, San Diego, California, July 9-14, 2017, pp. 45-346.
4. **M. Kovaleva**, D. Bulger, B.A. Zeb and K.P. Esselle, “Modern Global Optimization Methods for Electromagnetic Devices”, *Fifteenth Australian Symposium on Antennas (ASA 2017)*, Sydney, Australia, Feb. 7-8, 2017.
5. **M. Kovaleva**, B.A. Zeb, D. Bulger, K.P. Esselle, “An Extremely Wideband Fabry-Perot Cavity Antenna for Superfast Wireless Backhaul Applications”, *2016 International Symposium on Antenna Technology and Applied Electromagnetics (ANTEM)*, Montreal, Canada, July 10-13, 2016.
6. **M. Kovaleva**, B.A. Zeb, D. Bulger, K.P. Esselle, “Simulation-Driven Optimization of a Compact Fabry-Perot Cavity Antenna”, *2016 IEEE International Symposium on Antennas and Propagation (AP-S/USNC-URSI)*, Fajardo, Puerto Rico, June 26-July 1, 2016.

7. **M. Kovaleva**, B.A. Zeb, D. Bulger, K.P. Esselle, “Radiation Performance Enhancement of a Compact Fabry-Perot Cavity Antenna Using Particle Swarm Optimization”, *2015 IEEE International Symposium on Antennas and Propagation (ISAP)*, Hobart, Australia, Nov. 9-12, 2015.
8. **M. Kovaleva**, D. Bulger and K.P. Esselle, “Directivity-Bandwidth Enhancement of EBG Resonator Antennas Using a Particle Swarm Optimization Algorithm”, *Fourteenth Australian Symposium on Antennas (ASA 2015)*, Sydney, Australia, Feb. 18-19, 2015.



# Bibliography

- [1] X.-S. Yang and S. Koziel, Eds., *Computational optimization and applications in engineering and industry*. Springer Science and Business Media, 2011, vol. 359.
- [2] H. W. Katsuki Fujisawa, Yuji Shinano, Ed., *Optimization in the Real World: Toward Solving Real-World Optimization Problems*. Springer Japan, 2016, vol. 13.
- [3] X.-S. Yang, *Nature-Inspired Metaheuristic Algorithms*. Luniver press, 2010.
- [4] A. S. Fraser, “Simulation of genetic systems by automatic digital computers i. introduction,” *Australian Journal of Biological Sciences*, vol. 10, no. 4, pp. 484–491, 1957.
- [5] D. B. Fogel, “An introduction to simulated evolutionary optimization,” *IEEE Transactions on Neural Networks*, vol. 5, no. 1, pp. 3–14, Jan 1994.
- [6] S. Forrest and M. Mitchell, “Adaptive computation: The multidisciplinary legacy of John H. Holland,” *Commun. ACM*, vol. 59, no. 8, pp. 58–63, Jul. 2016.
- [7] F. Gross, *Smart Antennas with MATLAB, Second edition: Principles and Applications in Wireless Communication*. McGraw-Hill Professional, Feb 2015.
- [8] V. Agrawal, V. Chandwani, and R. Nagar, “Swarm intelligence assisted optimization in structural engineering: a review,” *INROADS-An International Journal of Jaipur National University*, vol. 3, no. 1, pp. 173–180, 2014.
- [9] S. Koziel and X.-S. Yang, *Computational optimization, methods and algorithms*. Springer, 2011, vol. 356.

- 
- [10] S. Koziel, X.-S. Yang, and Q.-J. Zhang, *Simulation-driven design optimization and modeling for microwave engineering*. World Scientific, 2013.
  - [11] B. Liu, G. Gielen, and F. V. Fernández, “Electromagnetic design automation: Surrogate model assisted evolutionary algorithm,” in *Automated Design of Analog and High-frequency Circuits*. Springer, 2014, pp. 133–151.
  - [12] S. Koziel and S. Ogurtsov, *Antenna Design by Simulation-Driven Optimization*. Springer Publishing Company, Incorporated, 2014.
  - [13] E. E. Altshuler, “Electrically small self-resonant wire antennas optimized using a genetic algorithm,” *IEEE Transactions on Antennas and Propagation*, vol. 50, no. 3, pp. 297–300, Mar 2002.
  - [14] G. S. Hornby, A. Globus, D. S. Linden, and J. D. Lohn, “Automated antenna design with evolutionary algorithms,” in *AIAA Space*, 2006, pp. 19–21.
  - [15] J. D. Lohn, G. Hornby, and D. S. Linden, “Tools for automated antenna design and optimization,” *JACIC*, vol. 4, no. 5, pp. 853–864, 2007.
  - [16] A. B. S. Koziel, *Multi-Objective Design of Antennas Using Surrogate Models*, 2017.
  - [17] Scopus database. [Online]. Available: <https://www.scopus.com>
  - [18] A. Minasian and T. Bird, “Particle swarm optimization of microstrip antennas for wireless communication systems,” *IEEE Transactions on Antennas and Propagation*, vol. 61, no. 12, pp. 6214–6217, Dec 2013.
  - [19] A. Mitchell, M. Lech, D. Kokotoff, and R. Waterhouse, “Search for high-performance probe-fed stacked patches using optimization,” *IEEE Transactions on Antennas and Propagation*, vol. 51, no. 2, pp. 249–255, Feb 2003.
  - [20] D. Boeringer and D. Werner, “Particle swarm optimization versus genetic algorithms for phased array synthesis,” *IEEE Transactions on Antennas and Propagation*, vol. 52, no. 3, pp. 771–779, March 2004.



- [21] M. Bray, D. Werner, D. Boeringer, and D. Machuga, "Optimization of thinned aperiodic linear phased arrays using genetic algorithms to reduce grating lobes during scanning," *IEEE Transactions on Antennas and Propagation*, vol. 50, no. 12, pp. 1732–1742, Dec 2002.
- [22] R. Haupt, "Optimized element spacing for low sidelobe concentric ring arrays," *IEEE Trans. on Antennas and Propagation*, vol. 56, no. 1, pp. 266–268, 2008.
- [23] E. Afacan, "Location optimization for square array antennas using differential evolution algorithm," *International Journal of Antennas and Propagation*, 2016.
- [24] Y. Ge, K. Esselle, and Y. Hao, "Design of low-profile high-gain EBG resonator antennas using a genetic algorithm," *IEEE Antennas and Wireless Propagation Letters*, vol. 6, pp. 480–483, 2007.
- [25] Y. Ge and K. Esselle, "GA/FDTD technique for the design and optimisation of periodic metamaterials," *IET Microwaves, Antennas and Propagation*, vol. 1, no. 1, pp. 158–164, February 2007.
- [26] F. Yang and Y. Rahmat-Samii, *Electromagnetic Band Gap Structures in Antenna Engineering*. Cambridge University Press, 2008.
- [27] Y. Rahmat-Samii, "Modern antenna designs using nature inspired optimization techniques: Let Darwin and the bees help designing your multi band MIMO antennas," in *2007 IEEE Radio and Wireless Symposium*, Jan 2007, pp. 463–466.
- [28] N. Chase, M. Redemacher, E. Goodman, R. Averill, and R. Sidhu, "A benchmark study of optimization search algorithms," *MI, USA: Red Cedar Technology*, 2010.
- [29] X.-S. Yang, *Engineering Optimization: An Introduction with Metaheuristic Applications*. Wiley Publishing, 2010.
- [30] B. Xing and W.-J. Gao, *Introduction to Computational Intelligence*. Cham: Springer International Publishing, 2014, pp. 3–17.

- [31] J. Brownlee, “Clever algorithms: Nature-inspired programming recipes,” 2011.
- [32] B. Xing and W.-J. Gao, *Innovative computational intelligence: a rough guide to 134 clever algorithms*. Springer, 2014.
- [33] R. L. Haupt, “Thinned arrays using genetic algorithms,” *IEEE Transactions on Antennas and Propagation*, vol. 42, no. 7, pp. 993–999, July 1994.
- [34] J. M. Johnson and Y. Rahmat-Samii, “Genetic algorithm optimization and its application to antenna design,” in *IEEE Antennas and Propagation Society International Symposium*, vol. 1, June 1994, pp. 326–329 vol.1.
- [35] D. S. Weile and E. Michielssen, “Genetic algorithm optimization applied to electromagnetics: a review,” *IEEE Transactions on Antennas and Propagation*, vol. 45, no. 3, pp. 343–353, Mar 1997.
- [36] J. M. Johnson and V. Rahmat-Samii, “Genetic algorithms in engineering electromagnetics,” *IEEE Antennas and Propagation Magazine*, vol. 39, no. 4, pp. 7–21, 1997.
- [37] J. H. Barton, C. R. Garcia, E. A. Berry, R. Salas, and R. C. Rumpf, “3-D printed all-dielectric frequency selective surface with large bandwidth and field of view,” *IEEE Transactions on Antennas and Propagation*, vol. 63, no. 3, pp. 1032–1039, March 2015.
- [38] S. Karimkashi and A. A. Kishk, “Invasive weed optimization and its features in electromagnetics,” *IEEE Transactions on Antennas and Propagation*, vol. 58, no. 4, pp. 1269–1278, April 2010.
- [39] A. Foudazi and A. R. Mallahzadeh, “Pattern synthesis for multi-feed reflector antennas using invasive weed optimisation,” *IET Microwaves, Antennas and Propagation*, vol. 6, no. 14, pp. 1583–1589, November 2012.

- [40] Z. Bayraktar, M. Komurcu, J. Bossard, and D. Werner, “The wind driven optimization technique and its application in electromagnetics,” *IEEE Transactions on Antennas and Propagation*, vol. 61, no. 5, pp. 2745–2757, May 2013.
- [41] M. Gregory, S. Martin, and D. Werner, “Improved electromagnetics optimization: The covariance matrix adaptation evolutionary strategy,” *IEEE Antennas and Propagation Magazine*, vol. 57, no. 3, pp. 48–59, June 2015.
- [42] D. H. Wolpert and W. G. Macready, “No free lunch theorems for optimization,” *IEEE Transactions on Evolutionary Computation*, vol. 1, no. 1, pp. 67–82, Apr 1997.
- [43] Y.-C. Ho and D. L. Pepyne, “Simple explanation of the no-free-lunch theorem and its implications,” *Journal of optimization theory and applications*, vol. 115, no. 3, pp. 549–570, 2002.
- [44] S. Goudos, “Antenna design using binary differential evolution: Application to discrete-valued design problems,” *IEEE Antennas and Propagation Magazine*, vol. 59, no. 1, pp. 74–93, 2017.
- [45] N. Jin and Y. Rahmat-Samii, “Advances in particle swarm optimization for antenna designs: Real-number, binary, single-objective and multiobjective implementations,” *IEEE Transactions on Antennas and Propagation*, vol. 55, no. 3, pp. 556–567, March 2007.
- [46] ———, “Hybrid real-binary particle swarm optimization (HPSO) in engineering electromagnetics,” *IEEE Transactions on Antennas and Propagation*, vol. 58, no. 12, pp. 3786–3794, Dec 2010.
- [47] R. L. Haupt, “Antenna design with a mixed integer genetic algorithm,” *IEEE Transactions on Antennas and Propagation*, vol. 55, no. 3, pp. 577–582, March 2007.

- [48] E. BouDaher and A. Hoorfar, “Electromagnetic optimization using mixed-parameter and multiobjective covariance matrix adaptation evolution strategy,” *IEEE Transactions on Antennas and Propagation*, vol. 63, no. 4, pp. 1712–1724, April 2015.
- [49] T. Liao, K. Socha, M. A. M. de Oca, T. Stützle, and M. Dorigo, “Ant colony optimization for mixed-variable optimization problems,” *IEEE Transactions on Evolutionary Computation*, vol. 18, no. 4, pp. 503–518, Aug 2014.
- [50] L. Xie and Y.-C. Jiao, “Hybrid real-binary differential evolution algorithm applied to antenna optimization,” *Microwave and Optical Technology Letters*, vol. 54, no. 6, pp. 1460–1463, 2012.
- [51] V. V. de Melo and G. Iacca, “A CMA-ES-based 2-stage memetic framework for solving constrained optimization problems,” in *2014 IEEE Symposium on Foundations of Computational Intelligence (FOCI)*, Dec 2014, pp. 143–150.
- [52] D. Simon, *Evolutionary Optimization Algorithms: Biologically-Inspired and Population-Based Approaches to Computer Intelligence*. Wiley, 2013.
- [53] K. Deb, *Multi-Objective Optimization Using Evolutionary Algorithms*. New York, NY, USA: John Wiley & Sons, Inc., 2001.
- [54] T. C. Bora, V. C. Mariani, L. dos Santos Coelho, and P. Alotto, “Multiobjective cross entropy for electromagnetic optimization,” in *2016 IEEE Conference on Electromagnetic Field Computation (CEFC)*, Nov 2016, pp. 1–1.
- [55] J. Kennedy and R. Eberhart, “Particle swarm optimization,” in *Proceedings IEEE International Conference on Neural Networks*, vol. 4, Nov 1995, pp. 1942–1948 vol.4.
- [56] M. Clerc and J. Kennedy, “The particle swarm - explosion, stability, and convergence in a multidimensional complex space,” *IEEE Transactions on Evolutionary Computation*, vol. 6, no. 1, pp. 58–73, Feb 2002.

- [57] J. Robinson, S. Sinton, and Y. Rahmat-Samii, "Particle swarm, genetic algorithm, and their hybrids: optimization of a profiled corrugated horn antenna," in *IEEE Antennas and Propagation Society International Symposium*, vol. 1, 2002, pp. 314–317.
- [58] X. Hu and R. Eberhart, "Multiobjective optimization using dynamic neighborhood particle swarm optimization," in *Evolutionary Computation, 2002. CEC '02. Proceedings of the 2002 Congress on*, vol. 2, 2002, pp. 1677–1681.
- [59] G. I. Evers and M. Ben Ghalia, "Regrouping particle swarm optimization: A new global optimization algorithm with improved performance consistency across benchmarks," in *IEEE International Conference on Systems, Man and Cybernetics*, 2009, pp. 3901–3908.
- [60] H. Garg, "A hybrid PSO-GA algorithm for constrained optimization problems," *Applied Mathematics and Computation*, vol. 274, no. Supplement C, pp. 292 – 305, 2016.
- [61] D. Simon, *Evolutionary optimization algorithms*. John Wiley & Sons, 2013.
- [62] J. Robinson and Y. Rahmat-Samii, "Particle swarm optimization in electromagnetics," *IEEE Transactions on Antennas and Propagation*, vol. 52, no. 2, pp. 397–407, Feb 2004.
- [63] M. Kovaleva, B. A. Zeb, D. Bulger, and K. P. Esselle, "Radiation performance enhancement of a compact Fabry-Perot cavity antenna using particle swarm optimization," in *IEEE Antennas and Propagation Society International Symposium*, 2015.
- [64] R. C. Eberhart and Y. Shi, "Comparing inertia weights and constriction factors in particle swarm optimization," in *Proceedings of the 2000 Congress on Evolutionary Computation*, vol. 1, 2000, pp. 84–88 vol.1.

- [65] Y. Rahmat-Samii, J. Kovitz, and H. Rajagopalan, "Nature-inspired optimization techniques in communication antenna designs," *Proceedings of the IEEE*, vol. 100, no. 7, pp. 2132–2144, July 2012.
- [66] N. Jin and Y. Rahmat-Samii, "Parallel particle swarm optimization and finite-difference time-domain (pso/fdtd) algorithm for multiband and wide-band patch antenna designs," *IEEE Transactions on Antennas and Propagation*, vol. 53, no. 11, pp. 3459–3468, Nov 2005.
- [67] D. Sun, Z. Zhang, X. Yan, and X. Jiang, "Design of broadband dual-polarized patch antenna with backed square annular cavity," *IEEE Transactions on Antennas and Propagation*, vol. 64, no. 1, pp. 43–52, Jan 2016.
- [68] J. M. Kovitz, H. Rajagopalan, and Y. Rahmat-Samii, "Design and implementation of broadband MEMS RHCP/LHCP reconfigurable arrays using rotated e-shaped patch elements," *IEEE Transactions on Antennas and Propagation*, vol. 63, no. 6, pp. 2497–2507, June 2015.
- [69] X. F. Liu, Y. C. Jiao, and F. S. Zhang, "Conformal array antenna design using modified particle swarm optimization," *Journal of Electromagnetic Waves and Applications*, vol. 22, no. 2-3, pp. 207–218, 2008.
- [70] S. Soltani, M. Azarmanesh, and P. Lotfi, "Design of small acs-fed band-notch uwb monopole antenna using particle swarm optimization," *Microwave and Optical Technology Letters*, vol. 52, no. 7, pp. 1510–1513, 2010.
- [71] M. M. Khodier and C. G. Christodoulou, "Linear array geometry synthesis with minimum sidelobe level and null control using particle swarm optimization," *IEEE Transactions on Antennas and Propagation*, vol. 53, no. 8, pp. 2674–2679, Aug 2005.
- [72] M. Donelli, R. Azaro, F. G. B. D. Natale, and A. Massa, "An innovative computational approach based on a particle swarm strategy for adaptive phased-arrays

- control,” *IEEE Transactions on Antennas and Propagation*, vol. 54, no. 3, pp. 888–898, March 2006.
- [73] P. J. Bevelacqua and C. A. Balanis, “Minimum sidelobe levels for linear arrays,” *IEEE Transactions on Antennas and Propagation*, vol. 55, no. 12, pp. 3442–3449, Dec 2007.
- [74] J. Kennedy and R. C. Eberhart, “A discrete binary version of the particle swarm algorithm,” in *1997 IEEE International Conference on Systems, Man and Cybernetics*, vol. 5, Oct 1997, pp. 4104–4108.
- [75] N. Jin and Y. Rahmat-Samii, “Particle swarm optimization for antenna designs in engineering electromagnetics,” *J. Artif. Evol. App.*, vol. 2008, Jan. 2008.
- [76] F. Afshinmanesh, A. Marandi, and M. Shahabadi, “Design of a single-feed dual-band dual-polarized printed microstrip antenna using a boolean particle swarm optimization,” *IEEE Transactions on Antennas and Propagation*, vol. 56, no. 7, pp. 1845–1852, July 2008.
- [77] P. Nayeri, F. Yang, and A. Z. Elsherbeni, “Design of single-feed reflectarray antennas with asymmetric multiple beams using the particle swarm optimization method,” *IEEE Transactions on Antennas and Propagation*, vol. 61, no. 9, pp. 4598–4605, Sept 2013.
- [78] T. H. Nguyen, H. Morishita, Y. Koyanagi, K. Izui, and S. Nishiwaki, “A multi-level optimization method using pso for the optimal design of an l-shaped folded monopole antenna array,” *IEEE Transactions on Antennas and Propagation*, vol. 62, no. 1, pp. 206–215, Jan 2014.
- [79] R. Y. Rubinstein, “Optimization of computer simulation models with rare events,” *European Journal of Operational Research*, vol. 99, no. 1, pp. 89 – 112, 1997.
- [80] S. Kullback and R. A. Leibler, “On information and sufficiency,” *The Annals of Mathematical Statistics*, vol. 22, no. 1, pp. 79–86, 1951.

- 
- [81] Z. I. Botev, D. P. Kroese, R. Y. Rubinstein, P. L'Ecuyer *et al.*, "The cross-entropy method for optimization," *Machine Learning: Theory and Applications*, V. Govindaraju and CR Rao, Eds, Chennai: Elsevier BV, vol. 31, pp. 35–59, 2013.
- [82] D. C. Montgomery and G. C. Runger, *Applied statistics and probability for engineers*. John Wiley & Sons, 2003.
- [83] D. P. Kroese, T. Taimre, and Z. I. Botev, *Handbook of monte carlo methods*. John Wiley & Sons, 2013, vol. 706.
- [84] R. Y. Rubinstein and D. P. Kroese, *The Cross Entropy Method: A Unified Approach To Combinatorial Optimization, Monte-carlo Simulation (Information Science and Statistics)*. Secaucus, NJ, USA: Springer-Verlag New York, Inc., 2004.
- [85] S. Surjanovic and D. Bingham. (2013) Virtual library of simulation experiments: Test functions and datasets. [Online]. Available: <http://www.sfu.ca/~ssurjano>
- [86] D. P. Kroese, S. Porotsky, and R. Y. Rubinstein, "The cross-entropy method for continuous multi-extremal optimization," *Methodology and Computing in Applied Probability*, vol. 8, no. 3, pp. 383–407, 2006.
- [87] J. Connor, S. Foo, and M. Weatherspoon, "Synthesizing antenna array sidelobe levels and null placements using the cross entropy method," in *34th Annual Conference of IEEE Industrial Electronics*, Nov 2008, pp. 1937–1941.
- [88] S. Ho and S. Yang, "The cross-entropy method and its application to inverse problems," *IEEE Transactions on Magnetism*, vol. 46, no. 8, pp. 3401–3404, Aug 2010.
- [89] P. Minvielle, E. Tantar, A. Tantar, and P. Berisset, "Sparse antenna array optimization with the cross-entropy method," *IEEE Transactions on Antennas and Propagation*, vol. 59, no. 8, pp. 2862–2871, Aug 2011.
- [90] M. H. Weatherspoon, J. D. Connor, and S. Y. Foo, "Shaped beam synthesis of phased arrays using the cross entropy method," *International Journal of Numerical*



- Modelling: Electronic Networks, Devices and Fields*, vol. 26, no. 6, pp. 630–642, 2013.
- [91] J. D. Connor, *Antenna array synthesis using the cross entropy method*. The Florida State University, 2008, PhD Thesis.
- [92] Y. Zhang, C. Ji, W. Malik, D. O’Brien, and D. Edwards, “Cross-entropy optimisation of multiple-input multiple-output capacity by transmit antenna selection,” *IET Microwaves, Antennas and Propagation*, vol. 1, pp. 1131–1136(5), December 2007.
- [93] L. Bian, X. Che, and D. Yang, “Pattern null steering using the cross entropy method by controlling the current phases,” *International Journal of Advancements in Computing Technology*, vol. 3, no. 4, May 2011.
- [94] A. Costa, O. D. Jones, and D. Kroese, “Convergence properties of the cross-entropy method for discrete optimization,” *Operations Research Letters*, vol. 35, no. 5, pp. 573–580, 2007.
- [95] N. Hansen and A. Ostermeier, “Completely derandomized self-adaptation in evolution strategies,” *Evol. Comput.*, vol. 9, no. 2, pp. 159–195, 2001.
- [96] M. Gregory, Z. Bayraktar, and D. Werner, “Fast optimization of electromagnetic design problems using the covariance matrix adaptation evolutionary strategy,” *IEEE Transactions on Antennas and Propagation*, vol. 59, no. 4, pp. 1275–1285, April 2011.
- [97] D. Werner, M. Gregory, Z. H. Jiang, and D. E. Brocker, “Optimization methods in antenna engineering,” *Handbook of antenna technologies*, pp. 321–376, 2016.
- [98] J. M. Kovitz and Y. Rahmat-Samii, “Ensuring robust antenna designs using multiple diverse optimization techniques,” in *2013 IEEE Antennas and Propagation Society International Symposium (APSURSI)*, July 2013, pp. 408–409.

- [99] L. Zhang, Y.-C. Jiao, B. Chen, and Z.-B. Weng, "Optimization of non-uniform circular arrays with covariance matrix adaptation evolutionary strategy," *Progress In Electromagnetics Research C*, vol. 28, pp. 113–126, 2012.
- [100] X. S. Fang, C. K. Chow, K. W. Leung, and E. H. Lim, "New single-/dual-mode design formulas of the rectangular dielectric resonator antenna using covariance matrix adaptation evolutionary strategy," *IEEE Antennas and Wireless Propagation Letters*, vol. 10, pp. 734–737, 2011.
- [101] Z. Li and Q. Zhang, "A simple yet efficient evolution strategy for large scale black-box optimization," *IEEE Transactions on Evolutionary Computation*, 2017.
- [102] X. Hu, Y. Shi, and R. Eberhart, "Recent advances in particle swarm," in *Congress on Evolutionary Computation*, vol. 1, June 2004, pp. 90–97 Vol.1.
- [103] N. Hansen and A. Auger, *Principled Design of Continuous Stochastic Search: From Theory to Practice*. Berlin, Heidelberg: Springer Berlin Heidelberg, 2014, pp. 145–180.
- [104] J. R. Perez and J. Basterrechea, "Comparison of different heuristic optimization methods for near-field antenna measurements," *IEEE Transactions on Antennas and Propagation*, vol. 55, no. 3, pp. 549–555, March 2007.
- [105] S. K. Goudos, K. Siakavara, T. Samaras, E. E. Vafiadis, and J. N. Sahalos, "Self-adaptive differential evolution applied to real-valued antenna and microwave design problems," *IEEE Transactions on Antennas and Propagation*, vol. 59, no. 4, pp. 1286–1298, April 2011.
- [106] P. I. Lazaridis, E. N. Tziris, Z. D. Zaharis, T. D. Xenos, J. P. Cosmas, P. B. Gallion, V. Holmes, and I. A. Glover, "Comparison of evolutionary algorithms for LPDA antenna optimization," *Radio Science*, vol. 51, no. 8, pp. 1377–1384, 2016.

- [107] C. K. Sotirios K. Goudos and R. Mittra, “Evolutionary algorithms applied to antennas and propagation: A review of state of the art,” *International Journal of Antennas and Propagation*, 2016.
- [108] C. M. Coleman, E. J. Rothwell, and J. E. Ross, “Investigation of simulated annealing, ant-colony optimization, and genetic algorithms for self-structuring antennas,” *IEEE Transactions on Antennas and Propagation*, vol. 52, no. 4, pp. 1007–1014, April 2004.
- [109] A. Deb, J. S. Roy, and B. Gupta, “Performance comparison of differential evolution, particle swarm optimization and genetic algorithm in the design of circularly polarized microstrip antennas,” *IEEE Transactions on Antennas and Propagation*, vol. 62, no. 8, pp. 3920–3928, Aug 2014.
- [110] M. M. Stevanetic, D. I. Olcan, and B. M. Kolundzija, “Comparison of differential evolution and cuckoo optimization for antenna array problems,” in *Proceedings of the 2012 IEEE International Symposium on Antennas and Propagation*, July 2012, pp. 1–2.
- [111] T. P. Runarsson and X. Yao, “Search biases in constrained evolutionary optimization,” *IEEE Transactions on Systems, Man, and Cybernetics, Part C (Applications and Reviews)*, vol. 35, no. 2, pp. 233–243, May 2005.
- [112] B. Tessema and G. G. Yen, “An adaptive penalty formulation for constrained evolutionary optimization,” *IEEE Transactions on Systems, Man, and Cybernetics - Part A: Systems and Humans*, vol. 39, no. 3, pp. 565–578, May 2009.
- [113] U. Diwekar, *Introduction to applied optimization*. Springer Science & Business Media, 2008, vol. 22.
- [114] M. F. Pantoja, A. R. Bretones, F. G. Ruiz, S. G. Garcia, and R. G. Martin, “Particle-swarm optimization in antenna design: Optimization of log-periodic dipole arrays,” *IEEE Antennas and Propagation Magazine*, vol. 49, no. 4, pp. 34–47, Aug 2007.

- [115] N. T. Hung and H. Morishita, "Sizing optimization of small antenna design by pso linking matlab and cst-microwave studio," in *National Defense Academy, Yokosuka, Japan, International Conference on Simulation Technology, JSST*, 2012, pp. 27–28.
- [116] S. Koziel and S. Ogurtsov, "Robust microwave design optimization using manifold mapping with adjoint sensitivity," in *7th European Microwave Integrated Circuits Conference*, 2012, pp. 238–241.
- [117] O. M. Bucci, M. D'Urso, and T. Isernia, "Some facts and challenges in array antenna synthesis," in *2007 19th International Conference on Applied Electromagnetics and Communications*, Sept 2007, pp. 1–4.
- [118] A. Feresidis and J. Vardaxoglou, "High gain planar antenna using optimised partially reflective surfaces," *IEE Proceedings Microwaves, Antennas and Propagation*, vol. 148, no. 6, pp. 345–350, Dec 2001.
- [119] B. A. Zeb, N. Nikolic, and K. P. Esselle, "A high-gain dual-band EBG resonator antenna with circular polarization," *IEEE Antennas and Wireless Propagation Letters*, vol. 14, pp. 108–111, 2015.
- [120] G. Trentini, "Partially reflecting sheet arrays," *IRE Transactions on Antennas and Propagation*, vol. 4, no. 4, pp. 666–671, October 1956.
- [121] Z.-g. Liu, Z.-c. Ge, and X.-y. Chen, "Research progress on Fabry-Perot resonator antenna," *Journal of Zhejiang University SCIENCE A*, vol. 10, no. 4, pp. 583–588, 2009.
- [122] H. Yang and N. Alexopoulos, "Gain enhancement methods for printed circuit antennas through multiple superstrates," *IEEE Transactions on Antennas and Propagation*, vol. 35, no. 7, pp. 860–863, Jul 1987.
- [123] D. R. Jackson and A. A. Oliner, "A leaky-wave analysis of the high-gain printed antenna configuration," *IEEE Transactions on Antennas and Propagation*, vol. 36, no. 7, pp. 905–910, Jul 1988.

- [124] D. R. Jackson, A. A. Oliner, and A. Ip, "Leaky-wave propagation and radiation for a narrow-beam multiple-layer dielectric structure," *IEEE Transactions on Antennas and Propagation*, vol. 41, no. 3, pp. 344–348, Mar 1993.
- [125] M. Thevenot, C. Cheype, A. Reineix, and B. Jecko, "Directive photonic-bandgap antennas," *IEEE Transactions on Microwave Theory and Techniques*, vol. 47, no. 11, pp. 2115–2122, Nov 1999.
- [126] C. Cheype, C. Serier, M. Thevenot, T. Monediere, A. Reineix, and B. Jecko, "An electromagnetic bandgap resonator antenna," *IEEE Transactions on Antennas and Propagation*, vol. 50, no. 9, pp. 1285–1290, Sep 2002.
- [127] A. R. Weily, K. P. Esselle, B. C. Sanders, and T. S. Bird, "High-gain 1D EBG resonator antenna," *Microwave and Optical Technology Letters*, vol. 47, no. 2, pp. 107–114, 2005.
- [128] A. P. Feresidis and J. C. Vardaxoglou, "A broadband high-gain resonant cavity antenna with single feed," in *First European Conference on Antennas and Propagation (EuCAP)*, 2006, pp. 1–5.
- [129] N. Wang, Q. Liu, C. Wu, L. Talbi, Q. Zeng, and J. Xu, "Wideband Fabry-Perot resonator antenna with two complementary FSS layers," *IEEE Transactions on Antennas and Propagation*, vol. 62, no. 5, pp. 2463–2471, May 2014.
- [130] R. Hashmi, B. Zeb, and K. Esselle, "Wideband high-gain EBG resonator antennas with small footprints and all-dielectric superstructures," *IEEE Transactions on Antennas and Propagation*, vol. 62, no. 6, pp. 2970–2977, June 2014.
- [131] K. Konstantinidis, A. Feresidis, and P. Hall, "Dual subwavelength Fabry-Perot cavities for broadband highly directive antennas," *IEEE Antennas and Wireless Propagation Letters*, vol. 13, pp. 1184–1186, 2014.

- 
- [132] —, “Multilayer partially reflective surfaces for broadband Fabry-Perot cavity antennas,” *IEEE Transactions on Antennas and Propagation*, vol. 62, no. 7, pp. 3474–3481, 2014.
- [133] K. Konstantinidis, A. P. Feresidis, and P. S. Hall, “Broadband sub-wavelength profile high-gain antennas based on multi-layer metasurfaces,” *IEEE Transactions on Antennas and Propagation*, vol. 63, no. 1, pp. 423–427, 2015.
- [134] Z. Liu, W. Zhang, D. Fu, Y. Gu, and Z. Ge, “Broadband Fabry-Perot resonator printed antennas using FSS superstrate with dissimilar size,” *Microwave and Optical Technology Letters*, vol. 50, no. 6, pp. 1623–1627, 2008.
- [135] M. Al-Tarifi, D. Anagnostou, A. Amert, and K. Whites, “Bandwidth enhancement of the resonant cavity antenna by using two dielectric superstrates,” *IEEE Transactions on Antennas and Propagation*, vol. 61, no. 4, pp. 1898–1908, April 2013.
- [136] R. M. Hashmi and K. P. Esselle, “A class of extremely wideband resonant cavity antennas with large directivity-bandwidth products,” *IEEE Transactions on Antennas and Propagation*, vol. 64, no. 2, pp. 830–835, Feb 2016.
- [137] Z.-C. Ge, W.-X. Zhang, Z.-G. Liu, and Y.-Y. Gu, “Broadband and high-gain printed antennas constructed from Fabry-Perot resonator structure using EBG or FSS cover,” *Microwave and Optical Technology Letters*, vol. 48, no. 7, pp. 1272–1274, 2006.
- [138] Z.-G. Liu, R. Qiang, and Z. xin Cao, “A novel broadband Fabry-Perot resonator antenna with gradient index metamaterial superstrate,” in *2010 IEEE Antennas and Propagation Society International Symposium*, July 2010, pp. 1–4.
- [139] A. A. Baba, R. M. Hashmi, and K. P. Esselle, “Wideband gain enhancement of slot antenna using superstructure with optimised axial permittivity variation,” *Electronics Letters*, vol. 52, no. 4, pp. 266–268, 2016.

- [140] H. Boutayeb and T. A. Denidni, "Internally excited Fabry-Perot type cavity: Power normalization and directivity evaluation," *IEEE Antennas and Wireless Propagation Letters*, vol. 5, no. 1, pp. 159–162, 2006.
- [141] H. Boutayeb, K. Mahdjoubi, A.-C. Tarot, and T. A. Denidni, "Directivity of an antenna embedded inside a Fabry-Perot cavity: Analysis and design," *Microwave and Optical Technology Letters*, vol. 48, no. 1, pp. 12–17, 2006. [Online]. Available: <http://dx.doi.org/10.1002/mop.21249>
- [142] Y. J. Lee, J. Yeo, R. Mittra, and W. S. Park, "Application of electromagnetic bandgap (EBG) superstrates with controllable defects for a class of patch antennas as spatial angular filters," *IEEE Transactions on Antennas and Propagation*, vol. 53, no. 1, pp. 224–235, Jan 2005.
- [143] —, "Application of electromagnetic bandgap (EBG) superstrates with controllable defects for a class of patch antennas as spatial angular filters," *IEEE Transactions on Antennas and Propagation*, vol. 53, no. 1, pp. 224–235, Jan 2005.
- [144] B. A. Zeb, R. M. Hashmi, K. P. Esselle, and Y. Ge, "The use of reflection and transmission models to design wideband and dual-band Fabry-Perot cavity antennas (invited paper)," in *Proceedings of 2013 URSI International Symposium on Electromagnetic Theory (EMTS)*, 2013.
- [145] D. Jackson and N. Alexopoulos, "Gain enhancement methods for printed circuit antennas," *IEEE Transactions on Antennas and Propagation*, vol. 33, no. 9, pp. 976–987, Sep 1985.
- [146] M. Rahman and M. A. Stuchly, "Transmission line-periodic circuit representation of planar microwave photonic bandgap structures," *Microwave and Optical Technology Letters*, vol. 30, no. 1, pp. 15–19, 2001.
- [147] M. García-Vigueras, P. DeLara-Guarch, J. L. Gómez-Tornero, R. Guzmán-Quirós, and G. Goussetis, "Efficiently illuminated broadside-directed 1D and 2D tapered

- Fabry-Perot leaky-wave antennas,” in *6th European Conference on Antennas and Propagation (EUCAP)*, March 2012, pp. 247–251.
- [148] C. Mateo-Segura, A. Feresidis, and G. Goussetis, “Bandwidth enhancement of 2-D leaky-wave antennas with double-layer periodic surfaces,” *IEEE Transactions on Antennas and Propagation*, vol. 62, no. 2, pp. 586–593, Feb 2014.
- [149] C. Mateo-Segura, M. Garcia-Vigueras, G. Goussetis, A. Feresidis, and J. Gomez-Tornero, “A simple technique for the dispersion analysis of Fabry-Perot cavity leaky-wave antennas,” *IEEE Transactions on Antennas and Propagation*, vol. 60, no. 2, pp. 803–810, Feb 2012.
- [150] B. Zeb, K. Esselle, and R. Hashmi, “Computational models for bandwidth enhancement of electromagnetic bandgap (EBG) resonator antennas and their limitations,” in *IEEE International Conference on Computational Electromagnetics (ICCEM)*, Feb 2015, pp. 19–21.
- [151] D. Kim, J. Ju, and J. Choi, “A mobile communication base station antenna using a genetic algorithm based Fabry-Perot resonance optimization,” *IEEE Transactions on Antennas and Propagation*, vol. 60, no. 2, pp. 1053–1058, Feb 2012.
- [152] R. M. Hashmi, K. P. Esselle, and S. G. Hay, “Achieving high directivity-bandwidth through flat GRIN superstrates in Fabry-Perot cavity antennas,” in *IEEE Antennas and Propagation Society International Symposium (APS-URSI)*, 2014, pp. 1748–1749.
- [153] R. Arya, S. Pandey, and R. Mittra, “A technique for designing flat lenses using artificially engineered materials,” in *IEEE Antennas and Propagation Society International Symposium (APSURSI)*, July 2014, pp. 769–770.
- [154] W. E. Lillo, S. Hul, M. H. Loh, and S. H. Zak, “On solving constrained optimization problems with neural networks: A penalty function method approach,” in *1992 American Control Conference*, June 1992, pp. 968–972.



- [155] C. G. A. L. G. L. V. P. Peter R. Wiecha, Arnaud Arbouet, “Evolutionary multi-objective optimization of colour pixels based on dielectric nanoantennas,” *Nature Nanotechnology*, 2017.
- [156] L. Hadj Abderrahmane and B. Boussouar, “New optimisation algorithm for planar antenna array synthesis,” *International Journal of Electronics and Communications*, vol. 66, no. 9, pp. 752–757, 2012.
- [157] P.-T. de Boer, D. P. Kroese, S. Mannor, and R. Y. Rubinstein, “A tutorial on the Cross-Entropy method,” *Annals of Operations Research*, vol. 134, no. 1, pp. 19–67, 2005.
- [158] M. Zlochin, M. Birattari, N. Meuleau, and M. Dorigo, “Model-based search for combinatorial optimization: A critical survey,” *Annals of Operations Research*, vol. 131, no. 1, pp. 373–395, Oct 2004.
- [159] Z. Wu and M. Kolonko, “Asymptotic properties of a generalized cross-entropy optimization algorithm,” *IEEE Transactions on Evolutionary Computation*, vol. 18, no. 5, pp. 658–673, 2014.
- [160] T. P. Minka, “Estimating a Dirichlet distribution,” Tech. Rep., 2000.
- [161] J. Jayasinghe, J. Anguera, and D. Uduwawala, “On the behavior of several fitness functions for genetically optimized microstrip antennas,” *International Journal of Scientific World*, vol. 3, no. 1, pp. 53–58, 2015.
- [162] A. Hosseini, F. Capolino, F. De Flaviis, P. Burghignoli, G. Lovat, and D. Jackson, “Improved bandwidth formulas for Fabry-Perot cavity antennas formed by using a thin partially-reflective surface,” *IEEE Transactions on Antennas and Propagation*, vol. 62, no. 5, pp. 2361–2367, May 2014.
- [163] A. Katyal and A. Basu, “Compact and broadband stacked microstrip patch antenna for target scanning applications,” *IEEE Antennas and Wireless Propagation Letters*, vol. 16, pp. 381–384, 2017.

- 
- [164] G. Kumar and K. Ray, *Broadband microstrip antennas*. Artech House, 2003.
- [165] D. M. Pozar and D. H. Schaubert, *Microstrip antennas: the analysis and design of microstrip antennas and arrays*. John Wiley & Sons, 1995.
- [166] B. Biglarbegian, M. Fakharzadeh, D. Busuioc, M. R. Nezhad-Ahmadi, and S. Safavi-Naeini, “Optimized microstrip antenna arrays for emerging millimeter-wave wireless applications,” *IEEE Transactions on Antennas and Propagation*, vol. 59, no. 5, pp. 1742–1747, May 2011.
- [167] N. R. Labadie, S. K. Sharma, and G. M. Rebeiz, “A circularly polarized multiple radiating mode microstrip antenna for satellite receive applications,” *IEEE Transactions on Antennas and Propagation*, vol. 62, no. 7, pp. 3490–3500, July 2014.
- [168] M. Li and K. M. Luk, “Low-cost wideband microstrip antenna array for 60-GHz applications,” *IEEE Transactions on Antennas and Propagation*, vol. 62, no. 6, pp. 3012–3018, June 2014.
- [169] S. J. Chen, T. Kaufmann, D. C. Ranasinghe, and C. Fumeaux, “A modular textile antenna design using snap-on buttons for wearable applications,” *IEEE Transactions on Antennas and Propagation*, vol. 64, no. 3, pp. 894–903, March 2016.
- [170] J. Zhang, S. Yan, and G. A. E. Vandenbosch, “A miniature feeding network for aperture-coupled wearable antennas,” *IEEE Transactions on Antennas and Propagation*, vol. 65, no. 5, pp. 2650–2654, May 2017.
- [171] M. A. Matin, B. S. Sharif, and C. C. Tsimenidis, “Probe fed stacked patch antenna for wideband applications,” *IEEE Transactions on Antennas and Propagation*, vol. 55, no. 8, pp. 2385–2388, Aug 2007.
- [172] V. P. Sarin, N. Nassar, V. Deepu, C. K. Aanandan, P. Mohanan, and K. Vasudevan, “Wideband printed microstrip antenna for wireless communications,” *IEEE Antennas and Wireless Propagation Letters*, vol. 8, pp. 779–781, 2009.

- [173] S. D. Targonski, R. B. Waterhouse, and D. M. Pozar, "Wideband aperture coupled stacked patch antenna using thick substrates," *Electronics Letters*, vol. 32, no. 21, pp. 1941–1942, Oct 1996.
- [174] ———, "Design of wide-band aperture-stacked patch microstrip antennas," *IEEE Transactions on Antennas and Propagation*, vol. 46, no. 9, pp. 1245–1251, Sep 1998.
- [175] K. Ghorbani and R. B. Waterhouse, "Ultrabroadband printed (UBP) antenna," *IEEE Transactions on Antennas and Propagation*, vol. 50, no. 12, pp. 1697–1705, Dec 2002.
- [176] H. Oraizi and R. Pazoki, "Radiation bandwidth enhancement of aperture stacked microstrip antennas," *IEEE Transactions on Antennas and Propagation*, vol. 59, no. 12, pp. 4445–4453, Dec 2011.
- [177] Y. S. Chen, W. H. Chou, and S. Y. Chen, "Applications of optimization techniques to designs of ultra-wideband planar monopole antennas," in *2012 Asia Pacific Microwave Conference Proceedings*, Dec 2012, pp. 714–716.
- [178] M. A. Panduro and C. A. Brizuela, "A comparative analysis of the performance of GA, PSO and DE for circular antenna arrays," in *2009 IEEE Antennas and Propagation Society International Symposium*, June 2009, pp. 1–4.
- [179] L. Zhang, Z. Cui, Y.-C. Jiao, and F.-S. Zhang, "Broadband patch antenna design using differential evolution algorithm," *Microwave and Optical Technology Letters*, vol. 51, no. 7, pp. 1692–1695, 2009.
- [180] T. Datta and I. S. Misra, "A comparative study of optimization techniques in adaptive antenna array processing: The bacteria-foraging algorithm and particle-swarm optimization," *IEEE Antennas and Propagation Magazine*, vol. 51, no. 6, pp. 69–81, Dec 2009.

- [181] H. J. Mohammed, F. Abdulsalam, A. S. Abdulla, R. S. Ali, R. A. Abd-Alhameed, J. M. Noras, Y. I. Abdulraheem, A. Ali, J. Rodriguez, and A. M. Abdalla, "Evaluation of genetic algorithms, particle swarm optimisation, and firefly algorithms in antenna design," in *2016 13th International Conference on Synthesis, Modeling, Analysis and Simulation Methods and Applications to Circuit Design (SMACD)*, June 2016, pp. 1–4.
- [182] N. Ghassemi, J. Rashed-Mohassel, M. H. Neshati, S. Tavakoli, and M. Ghassemi, "A high gain dual stacked aperture coupled microstrip antenna for wideband applications," *Progress in Electromagnetics Research B*, vol. 9, pp. 127–135, 2008.
- [183] C. A. Balanis, *Antenna Theory: Analysis and Design, 3rd Edition*. Hoboken, NJ: John Wiley., 2005.
- [184] Y. Zhang, O. S. Ahmed, and M. H. Bakr, "Wideband FDTD-based adjoint sensitivity analysis of dispersive electromagnetic structures," *IEEE Transactions on Microwave Theory and Techniques*, vol. 62, no. 5, pp. 1122–1134, May 2014.
- [185] B. A. Zeb, Y. Ge, K. P. Esselle, Z. Sun, and M. E. Tobar, "A simple dual-band electromagnetic band gap resonator antenna based on inverted reflection phase gradient," *IEEE Transactions on Antennas and Propagation*, vol. 60, no. 10, pp. 4522–4529, Oct 2012.
- [186] G. N. Tan, X. X. Yang, and B. Han, "A dual-polarized Fabry-Perot cavity antenna at millimeter wave band with high gain," in *2015 IEEE 4th Asia-Pacific Conference on Antennas and Propagation (APCAP)*, June 2015, pp. 621–622.
- [187] A. R. Weily, K. P. Esselle, T. S. Bird, and B. C. Sanders, "Dual resonator 1-D EBG antenna with slot array feed for improved radiation bandwidth," *IET Microwaves, Antennas Propagation*, vol. 1, no. 1, pp. 198–203, February 2007.
- [188] N. Wang, J. Li, G. Wei, L. Talbi, Q. Zeng, and J. Xu, "Wideband Fabry-Perot resonator antenna with two layers of dielectric superstrates," *IEEE Antennas and Wireless Propagation Letters*, vol. 14, pp. 229–232, 2015.

- [189] F. Wu and K. M. Luk, "Wideband high-gain open resonator antenna using a spherically modified, second-order cavity," *IEEE Transactions on Antennas and Propagation*, vol. 65, no. 4, pp. 2112–2116, April 2017.
- [190] N. Guerin, S. Enoch, G. Tayeb, P. Sabouroux, P. Vincent, and H. Legay, "A metallic Fabry-Perot directive antenna," *IEEE Transactions on Antennas and Propagation*, vol. 54, no. 1, pp. 220–224, Jan 2006.
- [191] K. Konstantinidis, A. P. Feresidis, and P. S. Hall, "Dual-slot feeding technique for broadband Fabry-Perot cavity antennas," *IET Microwaves, Antennas Propagation*, vol. 9, no. 9, pp. 861–866, 2015.
- [192] A. Chaabane, F. Djahli, H. Attia, L. Mohamed Abdelghani, and T. Ahmed Denidni, "Wideband and high-gain EBG resonator antenna based on dual layer PRS," *Microwave and Optical Technology Letters*, vol. 59, no. 1, pp. 98–101, 2017.
- [193] H. H. Tran and I. Park, "Compact wideband circularly polarised resonant cavity antenna using a single dielectric superstrate," *IET Microwaves, Antennas Propagation*, vol. 10, no. 7, pp. 729–736, 2016.
- [194] B. A. Zeb, R. M. Hashmi, and K. P. Esselle, "Wideband gain enhancement of slot antenna using one unprinted dielectric superstrate," *Electronics Letters*, vol. 51, no. 15, pp. 1146–1148, 2015.
- [195] B. A. Munk, *Frequency selective surfaces: theory and design*. Wiley Online Library, 2000, vol. 29.
- [196] G. I. Kiani, K. L. Ford, K. P. Esselle, A. R. Weily, and C. J. Panagamuwa, "Oblique incidence performance of a novel frequency selective surface absorber," *IEEE Transactions on Antennas and Propagation*, vol. 55, no. 10, pp. 2931–2934, Oct 2007.
- [197] Z. Liu, W. Zhang, D. Fu, Y. Gu, and Z. Ge, "Broadband Fabry-Perot resonator printed antennas using FSS superstrate with dissimilar size," *Microwave and Optical Technology Letters*, vol. 50, no. 6, pp. 1623–1627, 2008.

- [198] S. Chakravarty, R. Mittra, and N. R. Williams, “On the application of the microgenetic algorithm to the design of broad-band microwave absorbers comprising frequency-selective surfaces embedded in multilayered dielectric media,” *IEEE Transactions on Microwave Theory and Techniques*, vol. 49, no. 6, pp. 1050–1059, Jun 2001.
- [199] Z. Bayraktar, M. D. Gregory, X. Wang, and D. H. Werner, “A versatile design strategy for thin composite planar double-sided high-impedance surfaces,” *IEEE Transactions on Antennas and Propagation*, vol. 60, no. 6, pp. 2770–2780, June 2012.
- [200] Y. Zhao, X. Cao, J. Gao, Y. Sun, H. Yang, X. Liu, Y. Zhou, T. Han, and W. Chen, “Broadband diffusion metasurface based on a single anisotropic element and optimized by the simulated annealing algorithm,” *Scientific Reports*, vol. 6, pp. 23 896–, Apr. 2016.
- [201] D. Sievenpiper, L. Zhang, R. F. J. Broas, N. G. Alexopolous, and E. Yablonovitch, “High-impedance electromagnetic surfaces with a forbidden frequency band,” *IEEE Transactions on Microwave Theory and Techniques*, vol. 47, no. 11, pp. 2059–2074, Nov 1999.
- [202] K. P. Ma, K. Hirose, F. R. Yang, Y. Qian, and T. Itoh, “Realisation of magnetic conducting surface using novel photonic bandgap structure,” *Electronics Letters*, vol. 34, no. 21, pp. 2041–2042, Oct 1998.
- [203] S. Tretyakov, *Analytical modeling in applied electromagnetics*. Artech House, 2003.
- [204] A. Erentok, P. L. Luljak, and R. W. Ziolkowski, “Characterization of a volumetric metamaterial realization of an artificial magnetic conductor for antenna applications,” *IEEE Transactions on Antennas and Propagation*, vol. 53, no. 1, pp. 160–172, Jan 2005.

- [205] J. L. T. Ethier, D. A. McNamara, M. R. Chaharmir, and J. Shaker, "Reflectarray design with similarity-shaped fragmented sub-wavelength elements," *IEEE Transactions on Antennas and Propagation*, vol. 62, no. 9, pp. 4498–4509, Sept 2014.
- [206] J. L. T. Ethier and D. A. McNamara, "Antenna shape synthesis without prior specification of the feedpoint locations," *IEEE Transactions on Antennas and Propagation*, vol. 62, no. 10, pp. 4919–4934, Oct 2014.
- [207] M. Ohira, H. Deguchi, M. Tsuji, and H. Shigesawa, "Multiband single-layer frequency selective surface designed by combination of genetic algorithm and geometry-refinement technique," *IEEE Transactions on Antennas and Propagation*, vol. 52, no. 11, pp. 2925–2931, Nov 2004.
- [208] Y. Aoki, H. Deguchi, and M. Tsuji, "Reflectarray with arbitrarily-shaped conductive elements optimized by genetic algorithm," in *2011 IEEE International Symposium on Antennas and Propagation (APSURSI)*, July 2011, pp. 960–963.
- [209] J. Jayasinghe, J. Anguera, D. N. Uduwawala, and A. Andújar, "Nonuniform overlapping method in designing microstrip patch antennas using genetic algorithm optimization," *International Journal of Antennas and Propagation*, vol. 2015, 2015.
- [210] M. Lamsalli, A. El Hamichi, M. Boussouis, N. Amar Touhami, and T. Elhamadi, "Genetic algorithm optimization for microstrip patch antenna miniaturization," *Progress In Electromagnetics Research Letters*, vol. 60, pp. 113–120, 2016.
- [211] O. Turkmen, E. Ekmekci, and G. Turhan-Sayan, "Effects of using different boundary conditions and computational domain dimensions on modeling and simulations of periodic metamaterial arrays in microwave frequencies," *International Journal of RF and Microwave Computer-Aided Engineering*, vol. 23, no. 4, pp. 459–465. [Online]. Available: <https://onlinelibrary.wiley.com/doi/abs/10.1002/mmce.20734>

- [212] M. U. Afzal, K. P. Esselle, and B. A. Zeb, "Dielectric phase-correcting structures for electromagnetic band gap resonator antennas," *IEEE Transactions on Antennas and Propagation*, vol. 63, no. 8, pp. 3390–3399, Aug 2015.
- [213] M. U. Afzal and K. P. Esselle, "A low-profile printed planar phase correcting surface to improve directive radiation characteristics of electromagnetic band gap resonator antennas," *IEEE Transactions on Antennas and Propagation*, vol. 64, no. 1, pp. 276–280, Jan 2016.
- [214] —, "Steering the beam of medium-to-high gain antennas using near-field phase transformation," *IEEE Transactions on Antennas and Propagation*, vol. 65, no. 4, pp. 1680–1690, April 2017.
- [215] C. Jouanlanne, A. Clemente, M. Huchard, J. Keignart, C. Barbier, T. L. Nadan, and L. Petit, "Wideband linearly polarized transmitarray antenna for 60 GHz backhauling," *IEEE Transactions on Antennas and Propagation*, vol. 65, no. 3, pp. 1440–1445, March 2017.
- [216] T. J. Cui, M. Q. Qi, X. Wan, J. Zhao, and Q. Cheng, "Coding metamaterials, digital metamaterials and programmable metamaterials," *Light: Science and Applications*, vol. 3, pp. e218–, Oct. 2014.
- [217] P. Pramanick and P. Bhartia, *Modern RF and Microwave Filter Design*. Artech House, 2016.
- [218] J.-S. G. Hong and M. J. Lancaster, *Microstrip filters for RF/microwave applications*. John Wiley & Sons, 2004, vol. 167.
- [219] M.-I. Lai and S.-K. Jeng, "Compact microstrip dual-band bandpass filters design using genetic-algorithm techniques," *IEEE Transactions on Microwave Theory and Techniques*, vol. 54, no. 1, pp. 160–168, Jan 2006.
- [220] D. Swanson and G. Macchiarella, "Microwave filter design by synthesis and optimization," *IEEE Microwave Magazine*, vol. 8, no. 2, pp. 55–69, April 2007.



- [221] J. W. Bandler and Q. S. Cheng, “Retrospective on microwave cad and optimization technology,” in *2012 IEEE/MTT-S International Microwave Symposium Digest*, June 2012, pp. 1–3.
- [222] N. Mahdi, S. Bila, M. Aubourg, C. Duroisseau, J. Puech, and D. Baillargeat, “Shape optimization of planar microwave components,” in *2015 IEEE MTT-S International Conference on Numerical Electromagnetic and Multiphysics Modeling and Optimization (NEMO)*, Aug 2015, pp. 1–4.
- [223] B. Liu, H. Yang, and M. J. Lancaster, “Global optimization of microwave filters based on a surrogate model-assisted evolutionary algorithm,” *IEEE Transactions on Microwave Theory and Techniques*, vol. 65, no. 6, pp. 1976–1985, June 2017.
- [224] R. Datta and K. Deb, *Evolutionary constrained optimization*. Springer, 2014.
- [225] L. dos Santos Coelho, “Gaussian quantum-behaved particle swarm optimization approaches for constrained engineering design problems,” *Expert Systems with Applications*, vol. 37, no. 2, pp. 1676–1683, 2010.
- [226] A. K. Verma, N. P. Chaudhari, and A. Kumar, “High performance microstrip transverse resonance lowpass filter,” *Microwave and Optical Technology Letters*, vol. 55, no. 5, pp. 1149–1152, 2013.
- [227] N. P. Chaudhari, R. Khokle, K. P. Esselle, and A. K. Verma, “Improved stopband characteristics of microstrip lowpass filter using linearly distributed transmission zeros,” in *2016 URSI Asia-Pacific Radio Science Conference (URSI AP-RASC)*, Aug 2016, pp. 701–704.
- [228] E. Hammerstad and O. Jensen, “Accurate models for microstrip computer-aided design,” in *1980 IEEE MTT-S International Microwave symposium Digest*, May 1980, pp. 407–409.
- [229] Q. Lei, R. Foster, P. S. Grant, and C. Grovenor, “Generalized maxwell fish-eye lens as a beam splitter: A case study in realizing all-dielectric devices from transforma-

- tion electromagnetics,” *IEEE Transactions on Microwave Theory and Techniques*, vol. PP, no. 99, pp. 1–13, 2017.
- [230] P. Kurgan and S. Koziel, “EM-driven compact cell topology selection for explicit size reduction of hybrid rat-race couplers,” in *2017 47th European Microwave Conference (EuMC)*, Oct 2017, pp. 339–342.
- [231] M. Borgese, F. Costa, S. Genovesi, and A. Monorchio, “Ultra-wideband linear polarization converters based on pixelated reflecting metasurfaces,” in *2017 11th European Conference on Antennas and Propagation (EUCAP)*, March 2017, pp. 1949–1953.
- [232] A. Basak and J. D. Lohn, “A comparison of evolutionary algorithms on a set of antenna design benchmarks,” in *2013 IEEE Congress on Evolutionary Computation*, June 2013, pp. 598–604.
- [233] M. Pantoja, A. Bretones, and R. Martin, “Benchmark antenna problems for evolutionary optimization algorithms,” *IEEE Transactions on Antennas and Propagation*, vol. 55, no. 4, pp. 1111–1121, April 2007.
- [234] I. Brinster, P. D. Wagter, and J. Lohn, “Evaluation of stochastic algorithm performance on antenna optimization benchmarks,” in *Proceedings of the 2012 IEEE International Symposium on Antennas and Propagation*, July 2012, pp. 1–2.
- [235] B. Dadalipour, A. R. Mallahzadeh, and Z. Davoodi-Rad, “Application of the invasive weed optimization technique for antenna configurations,” in *2008 Loughborough Antennas and Propagation Conference*, March 2008, pp. 425–428.